

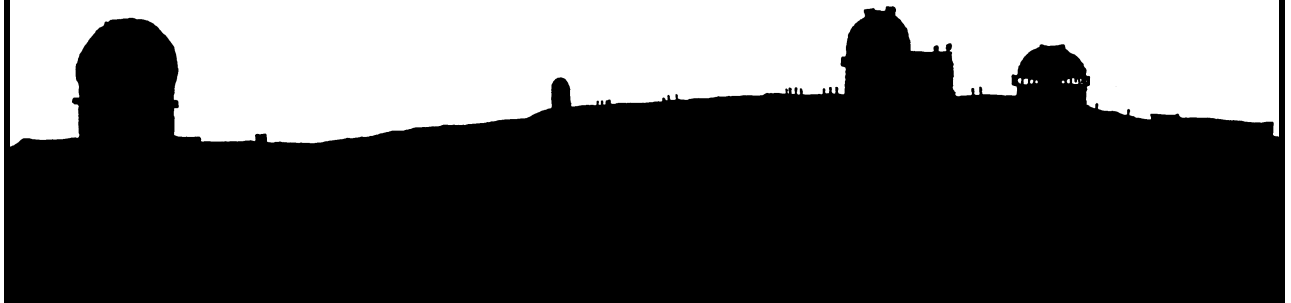
HAWAI'I SPACE GRANT CONSORTIUM

UNDERGRADUATE AND GRADUATE FELLOWSHIP REPORTS

Summer 2011 – Spring 2012



HSGC Report Number 12-21



Compiled in 2012 by
HAWAI'I SPACE GRANT CONSORTIUM

The Hawai'i Space Grant Consortium is one of the fifty-two National Space Grant Colleges supported by the National Aeronautics and Space Administration (NASA).

Material in this volume may be copied for library, abstract service, education, or personal research; however, republication of any paper or portion thereof requires the written permission of the authors as well as appropriate acknowledgment of this publication.

This report may be cited as

Hawai'i Space Grant Consortium (2012) *Undergraduate and Graduate Fellowship Reports*. HSGC Report No. 12-21. Hawai'i Space Grant Consortium, Honolulu.

Individual articles may be cited as

Author, A.B. (2012) Title of article. *Undergraduate and Graduate Fellowship Reports*, pp. xx-xx. Hawai'i Space Grant Consortium, Honolulu.

This report is distributed by:

Hawai'i Space Grant Consortium
Hawai'i Institute of Geophysics and Planetology
University of Hawai'i at Mānoa
1680 East West Road, POST 501
Honolulu, HI 96822

Table of Contents

Foreword	i
----------------	---

FELLOWSHIP REPORTS

THE LIFETIME AND ABUNDANCE OF SLOPE STREAKS ON MARS	1
---	---

Justin M. R. Bergonio
University of Hawai‘i at Mānoa

IDENTIFICATION AND PHOTOMETRY OF CANDIDATE TRANSITING EXOPLANET SIGNALS	8
--	---

Emily K. Chang
University of Hawai‘i at Mānoa

TESTSAT STRUCTURE AND INTERFACE DESIGN AND FABRICATION	16
--	----

Jonathan R. Chinen
University of Hawai‘i at Mānoa

MINERALOGICAL STUDY OF VOLCANIC SUBLIMATES FROM HALEMA‘UMA‘U CRATER, KILAUEA VOLCANO.....	24
--	----

Liliana G. DeSmither
University of Hawai‘i at Hilo

DETERMINING DIMENSIONAL RATIOS FOR FRESH, DEGRADED, AND FLOOR-FRACTURED LUNAR CRATERS	31
--	----

Elyse K. M. Iseke
University of Hawai‘i at Mānoa

EDUCATION IN 3 DIMENSIONS: USING INTERACTIVE SPHERICAL PROJECTION PRESENTATIONS TO TEACH ABOUT THE MOON	40
--	----

Brian P. James
University of Hawai‘i at Mānoa

COTS ADAPTABLE MODULE FOR ATTITUDE DETERMINATION IN CUBESATS.....	46
--	----

Tristan C. J. E. Martinez
University of Hawai‘i at Mānoa

DESIGNING SPACE CRAFT MISSIONS TO NEOS	52
--	----

Reina M. Ojiri
University of Hawai‘i at Mānoa

DEVELOPMENT OF A DEPLOYABLE 3U CUBESAT SOLAR PANEL ARRAY	59
Nathan K. Walsh University of Hawai‘i at Mānoa	

AIR BEARING ADCS TEST BEDS	66
Daniel E. Wukelic University of Hawai‘i at Mānoa	

NOVASOL INTERNSHIP PROGRAM – FALL 2011

FINAL REPORT FOR SOFTWARE INTERNSHIP AT NOVASOL	75
Kale A. Y. Nakata University of Hawai‘i at Mānoa	

MASTER’S APPRENTICESHIP PROGRAM 2009-2011

CONTROL DESIGN FOR A SMALL SATELLITE REACTION WHEEL FOR ATTITUDE CONTROL	79
Zachary K. Lee-Ho University of Hawai‘i at Mānoa	

SUMMER 2011 REPORTS:

GODDARD SPACE FLIGHT CENTER (GSFC) INTERNSHIP PROGRAM

A CROSS-EXAMINATION OF SATURNIAN KILOMETRIC RADIATION EMISSION OBSERVED BY CASSINI AND ULUSSES	104
Robert M. Albarran University of Hawai‘i at Hilo	

JET PROPULSION LABORATORY (JPL) INTERNSHIP PROGRAM

SIMULATIONS AND GUIs: A NEW LOOK TO RADIO SCIENCE.....	110
Michael R. C. Andonian University of Hawai‘i at Mānoa	

NASA AMES ACADEMY INTERNSHIP PROGRAM

LUNAR MICRO ROVER CAMERA SYSTEM DEVELOPMENT.....	119
Adria S. Fung NASA AMES Robotics Internship Program	

LADEE DECOMMISSIONING IMPACT DISPERSION ANALYSIS	124
Arlen M. Kam	
Stanford University	

LUNAR MICRO ROVER PROJECT	130
Carissa C. Nakao	
University of Hawai‘i at Mānoa	

NOVASOL INTERNSHIP PROGRAM

DEFENSE APPLICATION IN HYPERSPECTRICAL REMOTE SENSING	135
James M. Bishop	
University of Hawai‘i at Mānoa	

OPTICAL COMMUNICATION AT NOVASOL	141
Amber K. R. Imai	
University of Hawai‘i at Mānoa	

INTERNSHIP AT INNOVATIVE TECHNICAL SOLUTION (NOVASOL).....	146
Kevin Shin	
University of Hawai‘i at Mānoa	

MARSHALL SPACE FLIGHT CENTER (MSFC) INTERNSHIP PROGRAM

STRUCTURAL OPTIMIZATION OF SPACE SYSTEMS USING GENETIC ALGORITHMS	151
John G. Furumo	
University of Hawai‘i at Mānoa	

Foreword

This volume contains twenty-one reports from Hawai'i Space Grant undergraduate and graduate fellows and interns that worked on their projects in the Summer 2011, Fall 2011 and Spring 2012 semesters under the guidance of their faculty mentors and supervisors. We congratulate all of the students for their outstanding reports and warmly thank their faculty mentors and supervisors for generously supporting the Hawai'i Space Grant Consortium Undergraduate and Graduate Fellowship Programs.

The Hawai'i Space Grant Consortium is supported by NASA through its National Space Grant College and Fellowship Program with matching funds from the University of Hawai'i. The goal of the program is to strengthen the national capabilities in space-related science, technology, engineering, and mathematics (STEM) and to prepare the next generation of space scientists. All of the students' projects are related to the goals of NASA's Strategic Plan.

For more information about the Fellowship Program, please visit our website: <http://www.spacegrant.hawaii.edu/fellowships.html>

Edward R.D. Scott
Associate Director, Fellowships

THE LIFETIME AND ABUNDANCE OF SLOPE STREAKS ON MARS

Justin M. R. Bergonio
Department of Physics and Institute of Astronomy
University of Hawai'i at Mānoa
Honolulu, HI 96822

ABSTRACT

One of few active geological features on Mars today is slope streaks. Slope streaks are dark, fan-shaped avalanches that occur along escarpments on Mars. The first slope streaks were observed in the late 1970's in high resolution Viking images provided by the Viking spacecraft. Later spacecraft such as the Mars Global Surveyor and the Mars Reconnaissance Orbiter (MRO) acquired more high-resolution images. Using the images obtained from these spacecrafts, we were able to determine the lifetime of slope streaks on Mars. The research project's first focus was to determine the lifetime of the streaks by observing changes between Viking images and the more recent Context Camera (CTX) images. The second focus of the project was to determine the number of observable slope streaks as a function of image resolution based on images by the High Resolution Science Experiment (HiRISE) camera in order to better estimate the number of slope streaks on Mars. The first study revealed that the rate of formation and the rate of disappearance are comparable, indicating the population is balanced over long periods of time. The second study revealed that depending on the region being observed, the number of observable slope streaks can increase rapidly with image resolution.

INTRODUCTION

Slope streaks are characterized as either dark (young) or bright (old), fan-shaped surficial mass movements that typically occur in the mid-equatorial, dust-covered regions of Mars (Sullivan et al., 2001); see Figure 1. First discovered in 1978, they were observed in especially high-resolution Viking images transmitted by the Viking Orbiters. Although several mechanisms have been proposed, the leading hypothesis in the formation of these streaks is the removal of brighter surface material via dust avalanche, revealing a darker subsurface beneath (Chuang et al., 2007). Dark slope streaks are usually observed in regions of high albedo, where the streak contrasts the material surrounding it. This allows us to distinguish streaks from mere shadows along escarpment peaks.

In 1996, nearly two decades after the Viking missions, the Mars Global Surveyor (MGS) was launched ("Mars Global Surveyor: Overview"). A study using overlaps of Mars Orbital Camera images (MOC), obtained from the MGS, and Viking images documented slope streak changes over thirty years

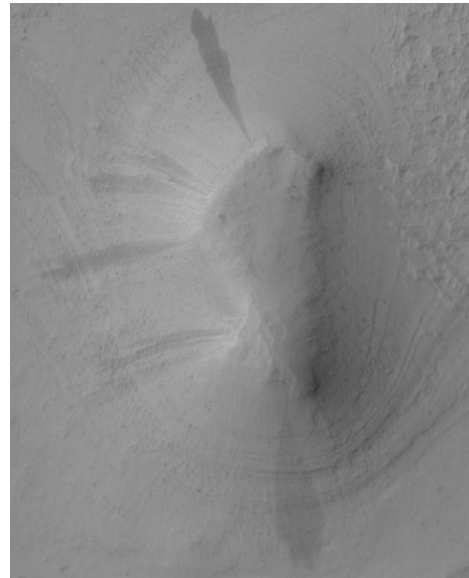


Figure 1: Slope streaks in HiRISE image PSP_008599_1910.

(Schorghofer et al., 2007). The study found that the slope streak population consisted more of persisting streaks than disappeared streaks. It was also revealed that brighter streaks were actually faded, old dark streaks that had transitioned to be brighter over time.

A few years after the success of the MGS, the Mars Reconnaissance Orbiter was launched. On board the MRO were the Context Camera (CTX) and the High Resolution Science Experiment (HiRISE) camera. Context Camera's main mission was to provide context to geological features on Mars by surveying the surface by giving high-resolution images (~5 m/pixel) with a wide field of view, while HiRISE images have been used to study Martian features in greater detail ("Mars Reconnaissance Orbiter: Instruments").

METHODS

Viking-CTX Overlaps

The first semester focused on comparing Viking-CTX image overlaps. First a site with Viking images with a high enough resolution of ~8 m/pixel was selected. Then newly released CTX images with as high as ~5 m/pixel resolution that overlapped these sites were obtained. Once the appropriate images were obtained, a mosaic was constructed using the obtained Viking images as well as the CTX images using Adobe Photoshop Elements 9. The mosaics were overlapped, and changes were observed and recorded using a color-coding system: disappeared streaks were marked by red dots, persisting streaks marked by green dots, partially faded streaks marked in yellow, and newly formed slope streaks in blue (Figure 2). Disappeared (faded) streaks were characterized as being present in Viking images, but completely gone in CTX. Persisting streaks were defined as being present in Viking, and present in CTX by maintaining consistent shape and length. New streaks were defined as not appearing in Viking, but present in CTX. Streaks were considered partially faded if they were present in Viking, but not maintaining shape or length in CTX. The overlaps were compared and looked over carefully to study the changes. Although similar to MOC images in that they both span a large period of time since the Viking images, CTX images differ in that they cover a larger area than MOC. A master mosaic consisting of the previous study conducted by Kim Rottas was merged with the mosaic obtained by our current study.

HiRISE Study

The second portion of the project primarily used HiRISE images. Two HiRISE images were used in this study: ESP_016636_1880 and PSP_008599_1910. The ESP region contained more sand dunes shaped by Martian winds, while in the PSP region the area studied was less active wind-wise, focusing more on the slope streaks along a crater. The images were then resized resolution-wise. The ESP image downsampled to 16th and 4th of its full resolution; hence three images were studied, while the PSP image was downsampled to 64th, 16th, and 4th of its full resolution, obtaining four images to be studied. The ESP region was studied first. The lowest resolution image was taken and the number of observable streaks was counted for several rounds. Once the number of streaks converged for at least three rounds, the average was taken for those rounds. The same process was repeated for each image. Once the counts were completed and the averages were calculated, the data was plotted. After the first count of the lowest resolution image it was found that for both images the extrapolated number of streaks in the highest resolution image would near 10,000 streaks, thus both sets of images were resized to half their full image size.

Viking-HiRISE Overlaps

With time permitting, another study was conducted using HiRISE images that overlapped the previously studied Viking-CTX overlaps. Similar to the Viking-CTX overlaps, Viking-HiRISE overlaps were surveyed to study slope streak changes over long periods of time. Unlike CTX images, HiRISE images cover very small areas due to their high-resolution nature. Hence only a small portion of the full Viking-CTX study site is available from HiRISE. For the most part, only the observable persisting disappeared, and partially faded streaks are taken into count for this portion of the study. These streaks were again looked at in the HiRISE image to reexamine if they are still persisting, disappeared, and/or partially faded at much finer resolution.

RESULTS & DISCUSSION

Viking-CTX Overlaps

For the first portion of the project, it was found that the formation rate of slope streaks was nearly comparable to the disappearance rate. Overall with the incorporation of Kim Rottas' study, 197 slope streaks were found: 25 classified as persisting, 70 as disappeared, 99 as newly formed, and 5 as partially faded. Table 1 is a basic summary of the data collected.

My mentor Dr. Norbert Schorghofer was able to calculate the rate of formation and rate of disappearance. It was found that in my portion of the Lycus Sulci region, the rate of disappearance was found to be 2.6% slope streaks per Earth year, while the rate of formation was 2.8% slope streaks per Earth year. Through this study, it is found that the rate of slope streak disappearance and the rate of slope streak formation is nearly comparable, indicating a more balanced slope streak population than previously thought.

Along with the balanced slope streak population, we discovered islands of persisting and disappearing streaks. There were several slopes in which three or more disappeared or persisting streaks were found as can be seen in Figure 3. These "islands" indicate that no large event wiped out the entire surveyed area, and that the disappearances occur locally. It is also found that the lifetime of a slope streak ranged from 30 to 40 Earth years.

Table 1: Summary of data collected from Viking-CTX overlaps in Lycus Sulci site.

Viking Image ID	441B01 - 441B09	441B10, 441B11	441B12, 441B13	Total
CTX Image ID	B02_010346_2072, B19_016926_2066	B02_010346_2072, B19_016926_2066	B02_010346_2072	
CTX Date	2008-10-10 2010-03-07	2008-10-10 2010-03-07	2008-10-10	
Δ Time (years)	31, 33	31, 33	31	31-33
# persisting	16	2	7	25
# new	32	31	36	99
# disappeared	26	29	15	70
# partially disappeared	3	1	1	5

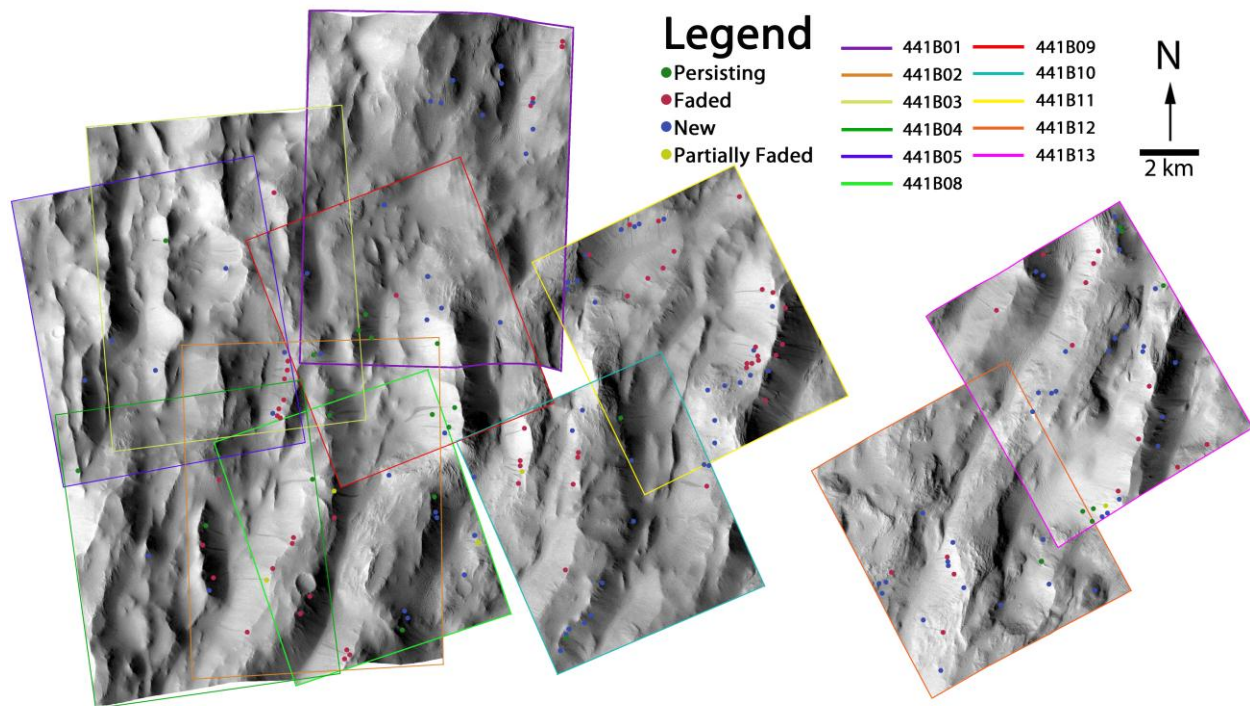


Figure 2: Lycus Sulci Viking-CTX overlap mosaic. Viking images 441B01, 441B08, and 441B10 – 441B13 were studied this semester, while the rest were incorporated from previous study by Kim Rottas.

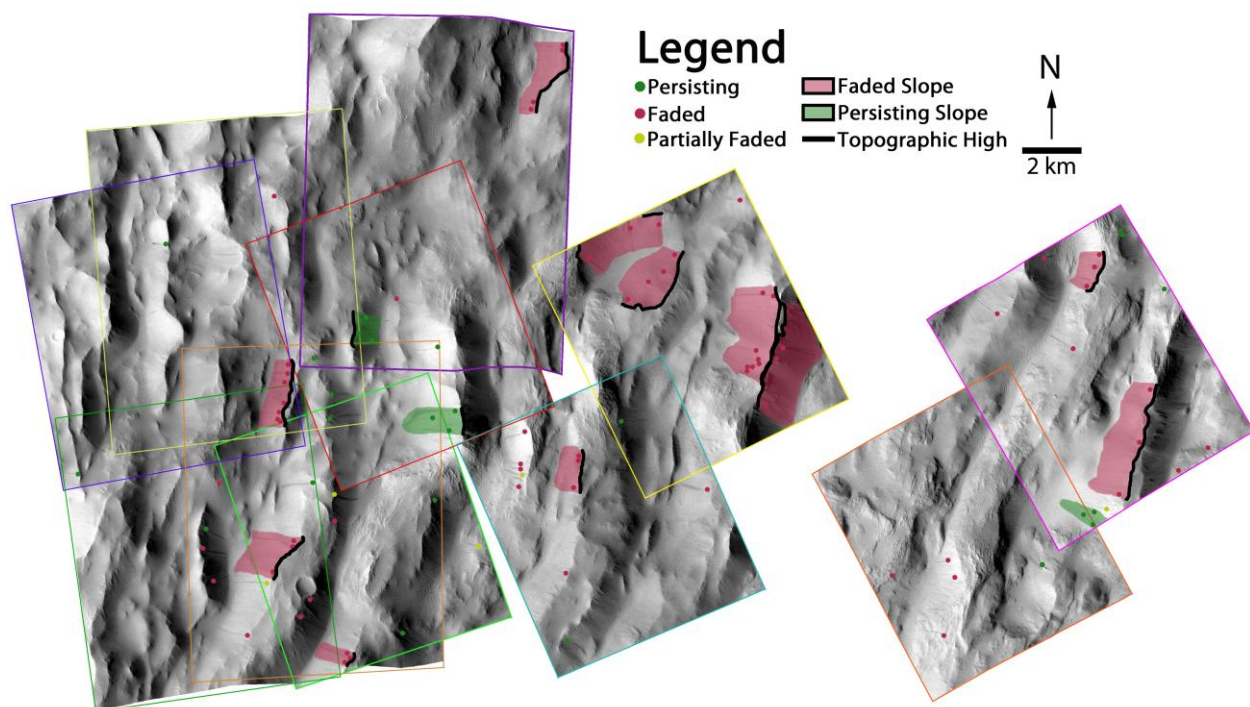


Figure 3: Lycus Sulci Viking-CTX overlap mosaic with “islands” of persistence (green) and disappearance (red).

HiRISE Study

A total of nearly 2,300 slope streaks were counted, repeatedly, over an area of nearly 87 km² in HiRISE image ESP_016636_1880. In the downsampled image of 8.9 m/pixel resolution (16th of the full resolution) the number of slope streaks is 43.3±1.3. (The error is calculated by standard deviation of the mean of the last three rounds.) For the image of 2.2 m/pixel resolution (4th of the full resolution) an average number of 318±6 slope streaks are found. At full resolution (0.55 m/pixel) an average number of 2,257±103 slope streaks is obtained. The number of slope streaks plotted against image resolution reveals a power-relationship as seen in Figure 4. When extrapolated to other areas on Mars, the power-relationship suggests that there could be millions more slope streaks on Mars than previously thought.

In HiRISE image PSP_008599_1910, after 30 rounds of counts about 170 slope streaks were counted, repeatedly, over an area of nearly 99 km². In the downsampled image of 16 m/pixel resolution (64th of the full resolution) a number of 43.3±0.3 slope streaks were found. For the downsampled image of 4 m/pixel resolution (16th of the full resolution) a number of 118.7±0.7 slope streaks were obtained. For the downsampled image of 1 m/pixel resolution (4th full resolution) an average number of 139.0±1.2 slope streaks were observed. In the full resolution image of 0.25 m/pixel 170.0±0.6 slope streaks were counted. In the PSP image, the number of slope streaks does not increase as rapidly with resolution as in the ESP image. When the average number of slope streaks is plotted against the image resolution it is found that the two displayed a more linear relationship as can be seen in Figure 5. This linear-relationship indicates that even at higher resolutions, not many more slope streaks may be found.

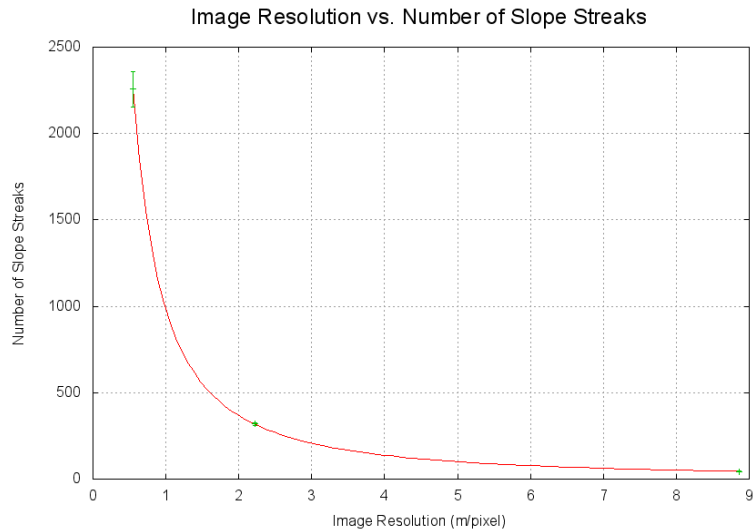


Figure 4: A graph of image resolution against average number of slope streaks in HiRISE image ESP_016636_1880.

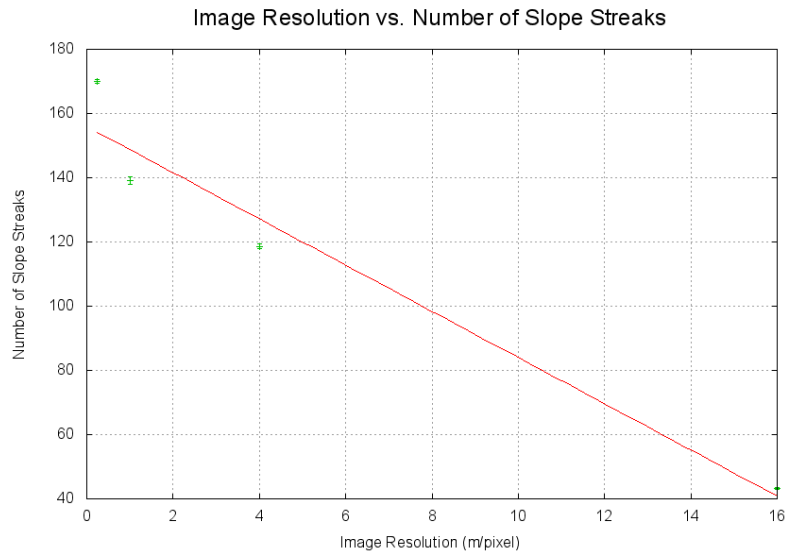


Figure 5: A graph of image resolution against average number of slope streaks in HiRISE image PSP_008599_1910

The two different relationships displayed by studying each HiRISE image can be partly explained by the regions studied. In ESP_016636_1880, the region is covered in sand dunes and is continuously shaped by Martian winds; hence formation of slope streaks may occur more often. While in PSP_008599_1910 the majority of the streaks are found along large, long slopes or in deep craters, while the rest of the terrain is relatively leveled. The region in the PSP image is relatively calm in a sense that only a few slopes are present in the studied site; thus the site may be more inactive in slope streak formation

Viking-HiRISE Overlaps

The third portion of our project found that using Viking-HiRISE overlaps, only 4 of the 15 previously confirmed disappeared streaks had convincingly disappeared. HiRISE revealed that at finer resolution, ambiguity in slope streak placement occurred, and thus many of the previously classified disappeared streaks were not as convincingly disappeared as compared to the resolutions in CTX. One of the most interesting findings of this portion of the project was of a slope streak that had been re-classified several times, shown in Figure 6. Previous MOC studies had classified this streak as having “brightened”, however in the Viking-CTX study it was classified as persisting. In HiRISE image ESP_012258_2080 it was again classified as persisting. It appears as if this streak went from dark (Viking) to bright (MOC) and then back to dark (CTX and HiRISE). Zooming into the HiRISE image however reveals ripples within the streak.

My mentor then pulled up the angle of incidence in which the images for this streak were taken and found that with the MOC image there was a greater angle of incidence in comparison to CTX and HiRISE. This revealed that the darkness of this streak may not be attributed to dark material in the streak but to the illumination of the ripples within the streak.

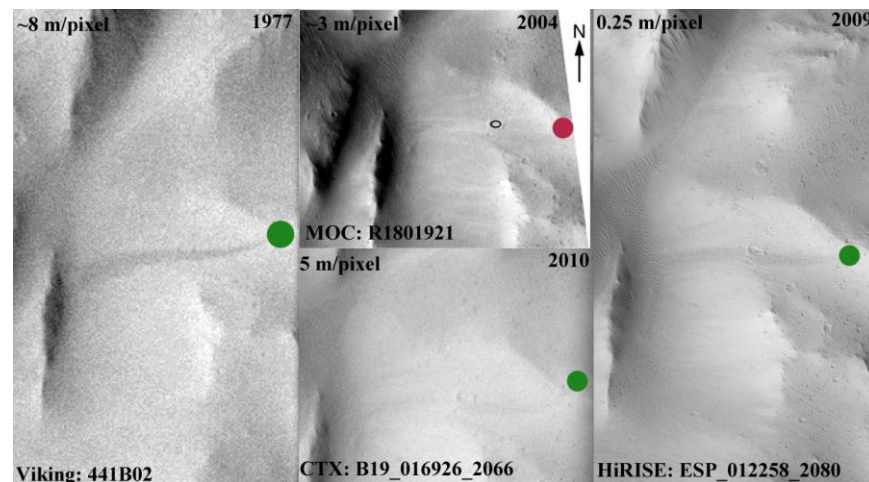


Figure 6: The back-and-forth “brightening” slope streak in Lycus Sulci.

CONCLUSION

This research project revealed many interesting findings about slope streaks. In the Viking-CTX overlap study it was found that the slope streak population is generally balanced with the rates of formation and the rates of disappearance being comparable. Through this the slope streak lifetime was narrowed down to range between 30 to 40 Earth years. Along with narrowing the lifetime range of slope streaks, it was also found that “islands” of persistence and disappearance existed along some slopes indicating there is no single large event responsible for wiping out entire slopes (Schorghofer et al., 2012). In the HiRISE study we found that the

number of slope streaks may increase rapidly with image resolution. In the heavily sand-duned regions a power-relationship between the number of slope streaks and the image resolution was found, while in the leveled, plane-like region there was more of a linear relationship. Finally, through a survey of Viking-HiRISE overlaps, it was found that with the back-and-forth “brightening” streak, the darkness of the streak may have been attributed to the illumination of the ripples within the streak illuminated at different angles by the Sun when the images were taken.

Although much has been done these two semesters, more can be done for years to come as long as MRO is still up and running. With hopes of obtaining requested images of the Lycus Sulci region through the HiWish program, a Viking-HiRISE study can be done in the future allowing for better observations and a closer look at disappeared, persisting, and partially faded slope streaks, extending our understanding of one of few active geological features on Mars.

REFERENCES

Chuang, F.C., R.A. Beyer, A.S. McEwen, and B.J. Thompson (2007). HiRISE observations of slope streaks on Mars. *Geophysical Research Letters* 34: L20204.

"Mars Global Surveyor: Overview." *NASA: Jet Propulsion Laboratory*. NASA, 27 Jan 2010. Web. 30 May 2012. <<http://mars.jpl.nasa.gov/mgs/overview/>>.

"Mars Reconnaissance Orbiter: Mission." *NASA: Jet Propulsion Laboratory*. NASA, n.d. Web. 30 May 2012. <<http://mars.jpl.nasa.gov/mro/mission/instruments/>>

Schorghofer, N., O. Aharonson, M.F. Gerstell, and L. Tatsumi (2007). Three decades of slope streak activity on Mars. *Icarus* 191(1): 132-140.

Schorghofer, N., K.M. Rottas, and J.R. Bergonio (2012). A balanced slope streak population on Mars: comparison of CTX and Viking images. Proceedings of the Lunar and Planetary Science Conference. The Woodlands, Texas. Abstract #1109.

Sullivan, R., P. Thomas, J. Veverka, M. Malin, and K.S. Edgett (2001). Mass movement slope streaks imaged by the Mars Orbiter Camera. *Journal of Geophysical Research* 106(E10): 23607-23633.

IDENTIFICATION AND PHOTOMETRY OF CANDIDATE TRANSITING EXOPLANET SIGNALS

Emily K. Chang
School of Ocean and Earth Science and Technology
University of Hawai'i at Mānoa
Honolulu, HI 96822

ABSTRACT

Exoplanet detection is important to the science of star and planet formation and the origin of life. For my project, the transit method was utilized in planet detection. First, a list of candidate transiting signals was compiled. Data from 1753 late-K and early M dwarf stars collected by the WASP (Wide Angle Search for Planets) survey were analyzed with a transit-hunting algorithm. 1016 stars were found to have a total of 3946 possible transiting signals. The signals were screened based on statistical analysis. The result was a list of 77 candidate transiting signals. Next, I completed follow-up photometry with the Faulkes-North telescope on 18 of the 77 candidate transiting signals across 22 observation times slots. Analysis included the calculation of an optimal aperture radius to use in photometry. A photometric precision of 4.0×10^{-4} has been achieved. With this RMS, I can detect a planet 2.83 times the radius of the Earth. Data from the Kepler Mission was used to predict 1-3 planets should be detected around the Super-WASP late-K and early M dwarf stars. So far, no transits have been observed.

1. INTRODUCTION

Exoplanet detection is important in planetary evolution science and the search for extraterrestrial life (1). The ultimate goal of this project is the discovery of metallic, Earth-like planets with habitable conditions. There are various ways to identify orbiting planets such as use of the Doppler shift, which excels at detecting massive, Jupiter-sized planets (2). In this project, we identify planets with the transit method.

The transit method is the best technique to identify our target sized planets (Neptune-to-Earth sized planets). A transit event occurs when the planet passes in front of the host star. As the planet intercepts the light from the star to the telescope, the brightness of the star decreases a fraction of a percent (0.01 - 10%). Every time the planet transits the star, there is an observable dip in the brightness of the star, creating a period signal. While the transit method can identify planets of the size we are interested in, the star and orbiting planet must be in on the line of sight with the telescope.

The goal of this project is the detection of smaller Neptune-sized exoplanets around certain nearby late K and early M dwarf stars. Late-K and early M dwarf stars are <0.6 solar masses and have temperatures $<4200\text{K}$. They are relatively faint with luminosities of 0.02% - 6% of the sun (3). Late-K and early M dwarf stars are ideal candidates for research because their smaller sizes increase the probability of planet detection.

2. METHODS

2.1. Creating a list of candidate signals.

We obtain data on late K and M dwarf stars from the WASP (Wide Angle Search for Planets) Survey (4). The WASP survey consists of two telescopes, one in each of the hemispheres: Super-WASP-North, located at La Palma in the Canary Islands, and Super-WASP-South, housed at the South African Astronomical Observatory (4). Each telescope has an impressive wide field of view of 7.8×7.8 degrees and a 2048×2048 CCD (4).

Data were limited in sky position to the 2004 inaugural fields of view of the SuperWASP- North survey. 1753 late K and early M dwarf stars were identified in the SUPERBLINK catalog. Data from all subsequent observations after 2004 of the 1753 objects in the inaugural fields of view were analyzed for periodic signals using a transit-detection algorithm called HUNTER; see Figure 1 for a summary of candidate selection.

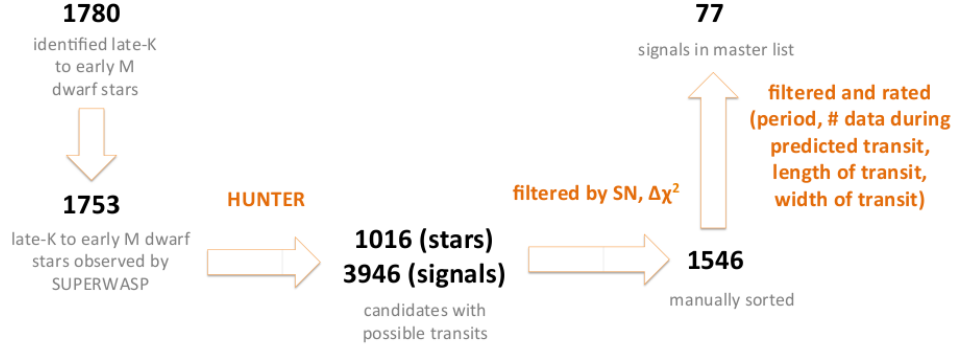


Figure 1. Schematic of candidate selection. The pool of candidate targets was whittled down from 1780 late-K to early M dwarf stars to 77 signals of possible transits. The filtered and rated step is summarized in Table 1.

HUNTER uses the Box-fitting Least Squares algorithm (BLS). The algorithm fits a periodic box-shaped function to the lightcurves. The box-shaped function is made up of 2 step functions of opposite sign which together, resemble a transit signal (5). HUNTER folds the lightcurves at possible periods (0.3-20 days) of the transit signals to increase the signal-to-noise ratio (SN). Up to 5 potential periodic signals per star were identified as possible transiting signals. The resulting list contained 3943 signals from 1042 stars.

We first filtered HUNTER signals by sorting by signal-to-noise (SN) and deviation from linear fit ($\Delta\chi^2$). We kept signals that have a $SN > 6$ or if the $SN > 3$ and a $\Delta\chi^2 > 50$. Signals that did not meet SN and $\Delta\chi^2$ requirements were rejected, leaving 1546 signals. Signals with periods < 1.1 days were rejected to minimize false positives due to aliasing. Table 1 summarizes the criteria for candidate selection.

Manual Filter
$(SN > 6) \cup (\Delta\chi^2 > 50 \cap SN > 3)$
removal of $P < 1.1$ days; 2, 3 ($\pm 5\%$); 5 ($\pm 10\%$) days
$N > 3$
$\frac{1}{2} P^{\frac{1}{3}}$ days $< \text{width (hours)} < 2 P^{\frac{1}{3}}$ days
SN ellipsoidal variation < 8
appearance in more than one camera (for a B rating)

Table 1. Manually applied filters to HUNTER signals. Signals were run through the filters in the above order.

2.2. Follow up with the Faulkes telescope.

The Faulkes North telescope is part of a two- telescope array called the Faulkes Telescope Project. We have access to the Faulkes North Telescope on Haleakala on the island of Maui. The telescope uses the Ritchey-Chrétien Cassegrain optics set up. The telescopes have a 2.0 m primary mirror and a 0.62 secondary mirror. Faulkes uses the SpectraCAM which has a Fairchild CCD486 BI camera. I observe with the PanSTARSS Z filter which transmits in the red range (wavelengths 800-950 nm).

I calculated transit predictions with a GDL (Gnu Data Language) program called transit.pro using ephemeris data from HUNTER (E. Gaidos, pers. comm.) and used the Aladin Sky Atlas software (<http://aladin.u-strasbg.fr/>) to set up the telescope pointing. The pointing is determined by plotting the optimum RA and Dec and roll angle of the telescope to include reference and guide stars (both of similar brightness to the target star) in the field of view of Faulkes and avoid hot pixels; see Figure 2.

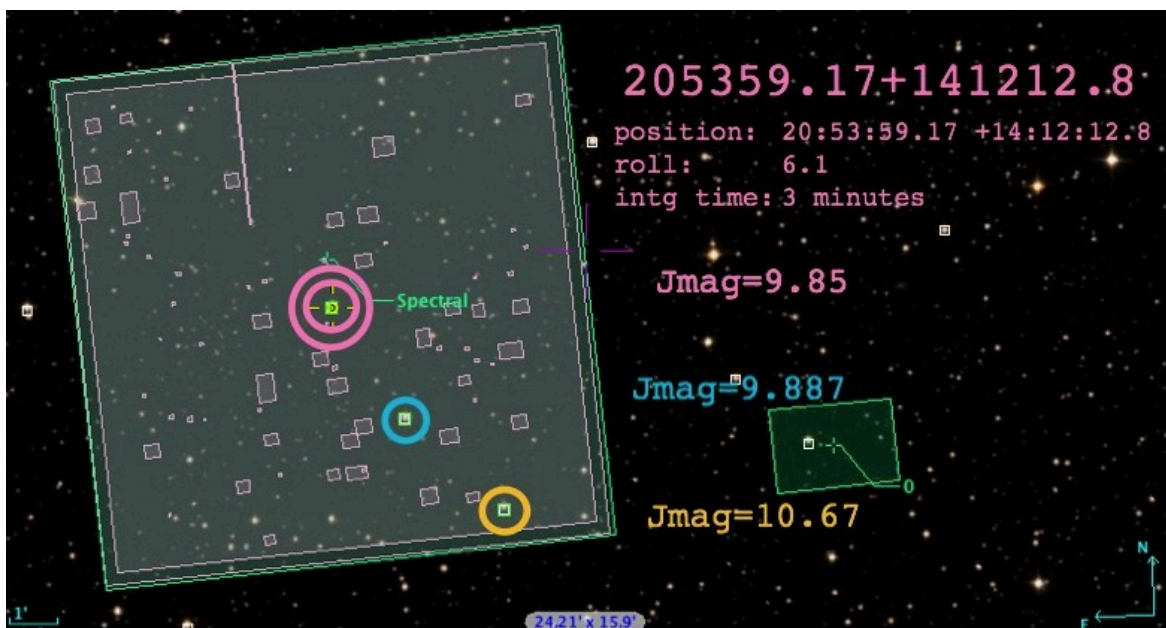


Figure 2. Faulkes telescope pointing. This image is a screenshot from Aladin. The green outline is the mapped field of view of Faulkes. We position the target (marked in pink) around the artifacts. Reference stars (blue and orange) are used during photometry and a guide star (in the box “0”) is utilized to keep the telescope position. The position, roll of telescope, integration time, and brightness of the stars are noted.

Several programs written in GDL (E. Gaidos, pers. comm.) were used to analyze data collected with the Faulkes telescope; see Table 2. We first used photo.pro to process the raw data and produce lightcurves. Plotit.pro uses output from photo.pro to identify the best combination of reference stars to maximize the signal to noise ratio. The program detect limit.pro calculates the smallest real planet that can be detected (with a false alarm probability of 1%) using the lightcurve data obtained from photo.pro.

3. RESULTS

3.1. Final list of candidate signals.

The SUPERBLINK catalog identified 1780 late-K to early M dwarf stars via proper motion from the Super-WASP database (Figure 1 summarizes the steps). The remaining signals were manually inspected to get a shortlist of 77 candidate signals (Figure 3 is a graphical representation of the 77 signals).

Signals produced by HUNTER

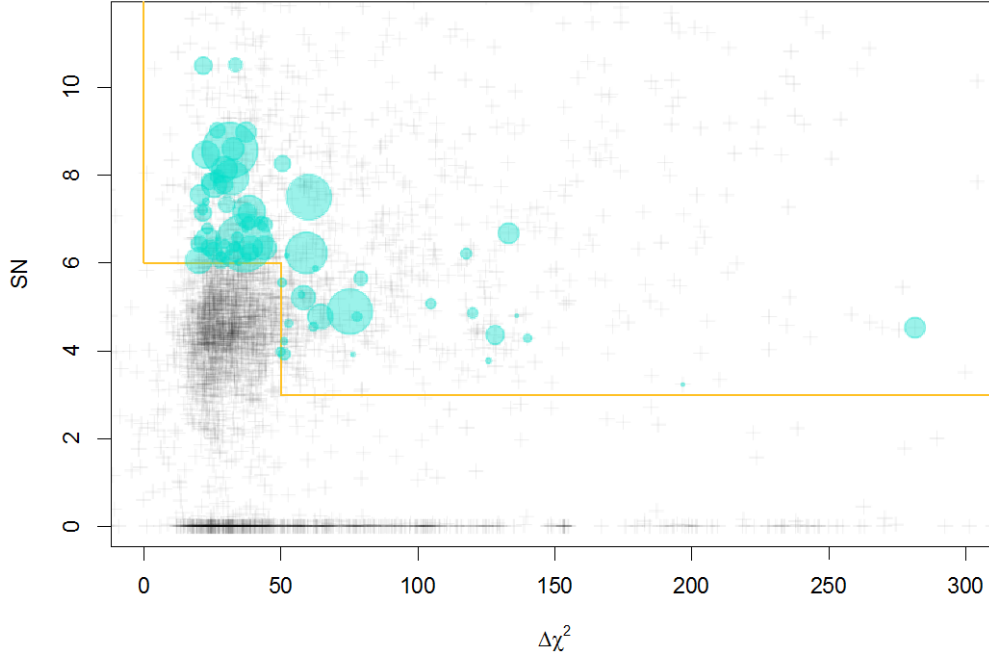


Figure 3. Candidates from HUNTER database. HUNTER found a total of 3946 transiting signals (seen as black crosses). The yellow lines are boundaries of the first 2 restrictions, $\Delta\chi^2$ and SN. The 1016 signals above the yellow line passed the $\Delta\chi^2$ and SN restriction and were manually inspected. The turquoise points are the 77 signals that passed all the criteria. The size of the point corresponds to the radius of the “detected planet.”

3.2. Summary of Faulkes observations.

6 out of the 22 observation sessions investigated signals on the final list of 77 signals. The 22 observation sessions were spread across 20 nights and included 18 unique target signals with the Faulkes telescope. Observations were taken from April 2011 to April 2012. The final list of candidate signals was compiled on January 25, 2012. As a result, some stars that were observed earlier are no longer being considered as transit candidates.

4. ANALYSIS

4.1. Optimization of analysis.

Photo.pro calculates an optimum radius of aperture to use in analysis based on the theoretical lower noise limit from the Poisson noise produced while counting and read noise. After detrending with a fourth order polynomial, we achieved an RMS of 4.0×10^{-4} ; Figure 4. Other studies have detected planets with an RMS of $3\text{--}5 \times 10^{-3}$ (6).

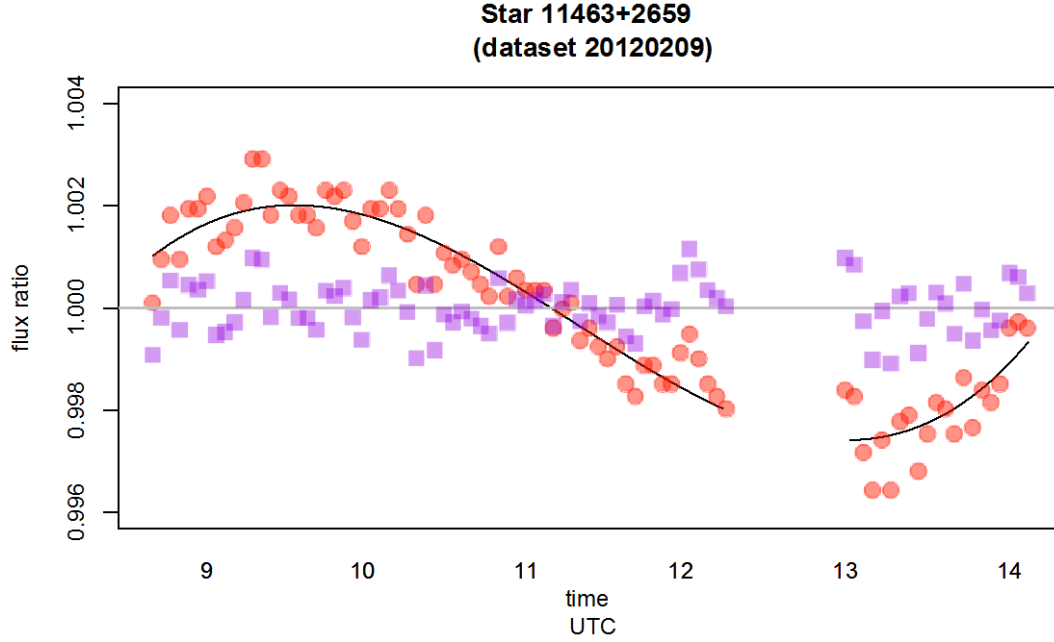


Figure 4. Lightcurve and polynomial fit for 11463+2659. Star 11463+2659 observed on 2/9/2012. The lightcurve of raw data (red) is the ratio between the flux of target star and the flux of the reference star (flux ratio), and plotted against time. A polynomial ($n=4$) was fit to the raw data using R Statistics ($y = 0.81776 + 0.04704x - 0.75550x^2 + 2.01867x^3 + 1.22813x^4$). The difference between the polynomial fit and raw data is plotted in purple. The residual curve has an RMS calculated at 4.0×10^{-4} .

4.2. Detection limit: smallest detectable planet.

I also ran the program detect limit.pro to calculate the minimum detectable transit signal. The output was a histogram of depths of “false positive” transits that could be found in random lightcurve noise with statistical properties similar to what lightcurve data we obtained. The smallest detectable transit using noise from the 20120209 dataset was a transit depth of 0.00490 with a false alarm probability of 1%; Figure 5. The transit depth of 0.00490 corresponds to a planet of 2.83 Earth radii transiting across the center of the star.

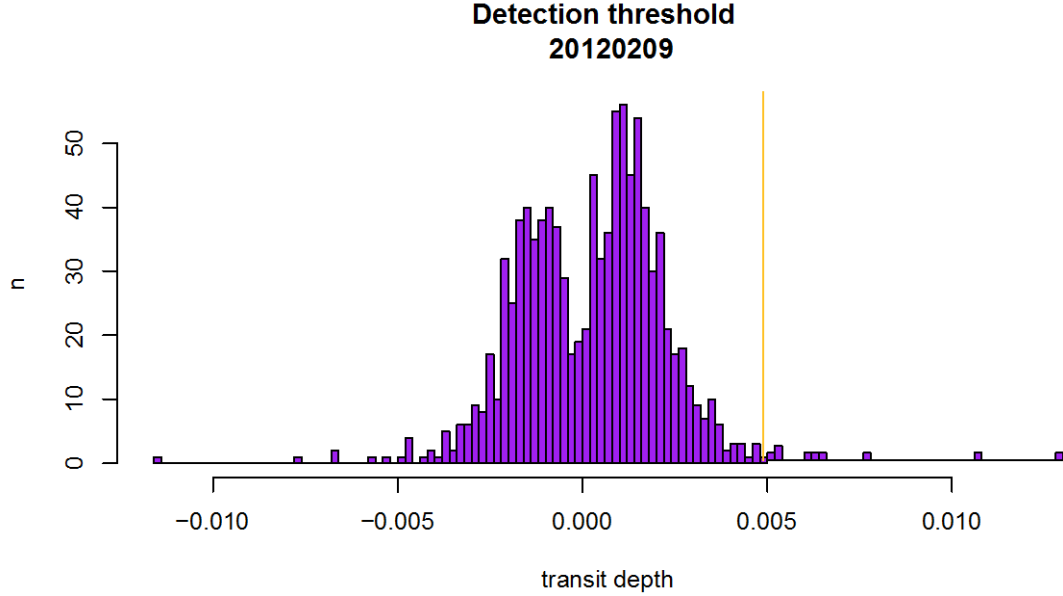


Figure 5. Detection threshold for 20120209. The GDL program detection limit was used to calculate the smallest possible planet using the 20120209 dataset. We set the polynomial fit, $n=4$, and constructed 1000 lightcurves. The smallest possible transit depth with a false alarm probability of 1% is 0.0049, which corresponds to a planet of 2.83 Earth radii.

4.3. Expected results based on Kepler data.

As of yet, no transits have been observed with Faulkes. However, we can predict the number of expected detectable planets from the 2004 fields of view using data from the Kepler Mission. The Kepler Mission is run by NASA to survey 100 square degrees of sky in hopes of finding Earth-like planets in habitable zones (<http://kepler.nasa.gov/Mission/QuickGuide/>). The Kepler Mission features an orbiting 1.4 m telescope. Kepler photometry is superior to ground-based telescopes because the atmosphere does not interfere with observations. So far, Kepler has discovered 2321 candidate planets among >150000 stars.

I can estimate the number of detectable planets by using candidate Kepler planets as analogs for planets around SUPERBLINK stars using a GDL program (E. Gaidos, pers. comm.). We assume stars in the Kepler field of view have similar properties to stars in the Super-WASP fields of view. In essence, the signal-to-noise ratio can be calculated using the signal from the Kepler transiting planet and the noise from the Super-WASP lightcurve. If the signal-to-noise ratio is above the sensitivity of Super-WASP, the analog Kepler planet is detectable.

Kepler planets around SUPERWASP stars

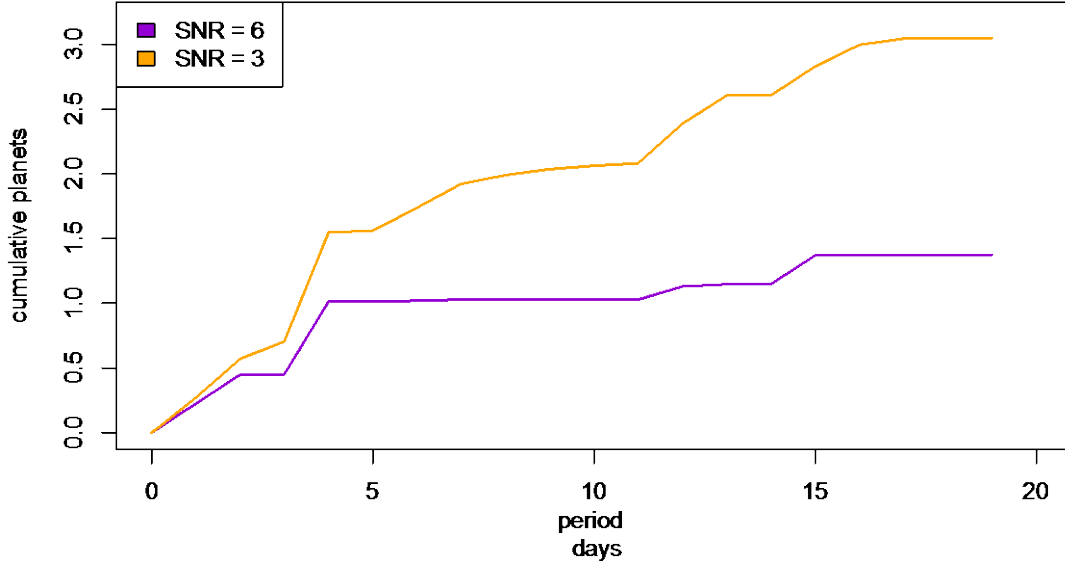


Figure 7. Cumulative detections with different signal-to-noise thresholds. Kepler planets have been placed around late-K and early M dwarf Super-WASP stars at the same occurrence rates. The turquoise line represents a signal-to-noise ratio detection threshold of 3. The purple line represents cumulative detections with a signal-to-noise ratio of 6. Detections level off as the periods of transiting stars go to 20 days. As a result, we investigated signals with periods of 1.1 - 20 days.

I can change the SN threshold used by the program; see Figure 7. A SN >6 yields 1.25 planets and SN >3 yields 3 detectable planets. Most planets are small and do not produce a large signal and thus fall under the SN threshold we chose.

5. CONCLUSION

WASP survey supplied data for 1753 stars. I used targets from the 2004 inaugural field of view and was given all subsequent data taken from the 2004 targets. However, Super-WASP does not obtain much signal from their faint stars. Longer integration times would increase the signal from these fainter stars. One could also expand the survey to more of the sky.

The transit-hunting algorithm HUNTER was essential in identifying transit signals from SuperWASP targets. HUNTER produced 3946 possible transit signals. However, as a result of a high number of alias signals around $\frac{1}{3}$, $\frac{1}{2}$, $\frac{2}{3}$, $\frac{3}{4}$, and 1 day, I rejected signals with a period <1.1 days. One could reexamine HUNTER signals with periods <1.1 days that do not fall within 5% of the aliases.

While Faulkes is a large telescope with a 2.0 m mirror, the detector has a low response in the red range. I look at signal in the Z band, which is near red. As a result, one could obtain higher quality data if the detector is sensitive to the region we observe in. Additionally, a more sensitive detector will allow for a shorter integration time. With a longer integration time, one could obtain more signal.

6. ACKNOWLEDGEMENTS

Thank you University of Hawai'i - NASA Space Grant and the NASA Origins of Solar Systems Program for support, David Anderson, James Armstrong, Jenn Beyer, Eric Hilton, Andrew Mann, and Rachel Street. Thanks to the Las Cumbres Global Telescope Network. And much Mahalos to Eric Gaidos!!

7. REFERENCES

- [1] Des Marais, D. J., et al. (2008) The NASA Astrobiology Roadmap. *Astrobiology*, 8, 715–30.
- [2] Gaidos, E., Haghighipour, N., Agol, E., Latham, D., Raymond, S., and Rayner, J. (2007) New Worlds on the Horizon: Earth-Sized Planets Close to Other Stars. *Science*, 318, 210, 213.
- [3] Tarter, J. C., et al. (2007) A reappraisal of the habitability of planets around M dwarf stars. *Astrobiology*, 7, 30–65.
- [4] Pollacco, D. L., et al. (2006) The WASP project and the SuperWASP cameras. *The Publications of the Astronomical Society of the Pacific*, 118, 1407–1418.
- [5] Collier Cameron, A., et al. (2006) A fast hybrid algorithm for exoplanetary transit searches. *Monthly Notices of the Royal Astronomical Society*, 373, 799–810.
- [6] Pont, F., Sasselov, D. D., and Holman, M. (2008) Transiting planets : proceedings of the 253rd Symposium of the International Astronomical Union. IAU symposium and colloquium proceedings series, Cambridge, Cambridge University Press.

TESTSAT STRUCTURE AND INTERFACE DESIGN & FABRICATION

Jonathan R. Chinen
College of Engineering
University of Hawai'i at Mānoa
Honolulu, HI 96822

ABSTRACT

Under the Hawai'i Space Flight Laboratory (HSFL), the Hawai'i Space Grant Consortium (HSGC), and guidance from mentor Jeremy Chan, and co-mentor Miguel Nunes, the student has researched, designed, constructed, tested, and integrated a functional and reproducible testbed. This testbed, called a "TestSat", is a structure capable of performing a single axis rotation of a 100 kg satellite. The purpose of the TestSat is to calibrate the attitude determination and control subsystem (ADCS). The project required the student to research space exploration related technologies while developing occupational and technical skills. The biggest design challenge of this project was creating an interface for a drive shaft and a satellite mounting plate. By completing the TestSat, the student has gained experience in mechanical and structural subsystem design and fabrication methods as well as graphical user interface and software design.

INTRODUCTION

Satellites are equipped with an attitude determination and control subsystem (ADCS). This subsystem is crucial to satellite operation because it allows us to know the satellite's orientation. The TestSat will support a satellite up to 100 kg. In order to calibrate the ADCS of a satellite we must be able to mount the satellite to a rotating plate. The satellite and plate will interface with each other via set of through holes as specified by the Planetary Systems Corporation 15" Motorized Lightband hole pattern. This satellite mounting plate will interface with the underside of the satellite's base.

In order to calibrate the ADCS, we must be able to accurately rotate the satellite through a manually input angular displacement. An optical encoder and adapter will measure the actual displacement experienced by a drive shaft rotating the satellite mounting plate. A motor that is controlled by a motor controller and computer will rotate the drive shaft. [Fig. 1]

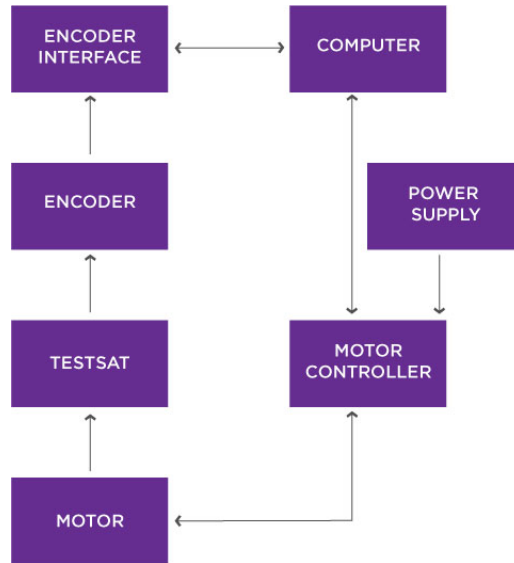


Figure 1, Functional Block Diagram

METHODS

Preliminary research was done to determine the best method to rotate the satellite. Mentor Jeremy Chan and Co-mentor Miguel Nunes suggested I research servomechanism motors and stepper motors. A cost-benefit analysis between the two motor technologies revealed that a stepper motor would be a better choice for its relatively low price, and precise position control when used with a planetary gearbox. For these reasons, the Phidgets 42BYGH40(M)-160-4A NEMA 17 bipolar stepper motor was chosen. This particular motor model is equipped with a planetary gearbox capable of a resolution of 0.02 degrees / step. It should be noted the motor can be substituted with a different motor technology should the need arise.

Using the equation for torque ($\tau = I\alpha$) and moment of inertia ($I = \frac{m}{2}(r_1^2 + r_2^2)$),

Calculations were done to determine the respective moments of inertia and whether the motor would be able to provide enough torque to rotate a 100 kg load. For the purpose of simplifying the analysis, the satellite was evaluated as a cylinder. The moment of inertia was calculated for a hollow cylinder with an inner radius that varied from 0.2921 [m] to 0 [m] (a solid cylinder). An arbitrary angular acceleration of 0.002 was chosen.

The stepper motor has a total allowable torque rating of 3.9228 [N-m]. It is apparent from Table 1 the stepper motor will be able to provide an adequate torque to rotate the 100 kg load.

Inner Radius	Outer Radius	Moment of Inertia	Torque Required	Torque Allowable
r1 [m]	r2 [m]	[kg*m2]	[N*m]	[N*m]
0	0.2921	4.2661	0.0085	3.9228
0.1	0.2921	4.7661	0.0095	
0.12	0.2921	4.9861	0.01	
0.14	0.2921	5.2461	0.0105	
0.16	0.2921	5.5461	0.0111	
0.18	0.2921	5.8861	0.0118	
0.2	0.2921	6.2661	0.0125	
0.22	0.2921	6.6861	0.0134	
0.24	0.2921	7.1461	0.0143	
0.26	0.2921	7.6461	0.0153	
0.28	0.2921	8.1861	0.0164	
0.2921	0.2921	8.5322	0.0171	
Mass [kg]				
100				
Angular Accel [rad/s2]				
0.002				

Table 1, Torque Calculations 1

When determining the diameter of the main drive shaft, various materials were considered. The following equation: $(D = (\frac{32M}{\pi\sigma})^{1/3})$ was used to determine the necessary main drive shaft diameter to support a 100 kg load. Each material had their respective yield rating. Calculations were performed using factors of safety ranging from 1.2, 1.5, and 2.0.

For the sake of working with a practical diameter size, ease of coupling with the stepper motor drive shaft, and sufficient mechanical strength, it was determined a 5/8" diameter ASTM-A 108 steel shaft could be used. A factor of safety of 2.0 was used when solving for this value. The 5/8" drive shaft is coupled to the stepper motor's 8 mm drive shaft. The coupler between the 5/8" drive shaft and stepper motor drive shaft was also designed and made from a 1" diameter ASTM-A 108 steel shaft. The coupler secures to both drive shafts through two sets of set screws.

Satellites are made up of many components. It is often the case the center of mass for any given satellite will not be at the geometric center. The TestSat structure was designed to accommodate this fact and prevent resulting moments or bending on the structure. Scenarios of varying centers of mass were calculated in order to ensure structural stability. Due to relatively slow rotation speeds, resultant forces due to different center of mass positions were assumed to act only in the z-direction. [Table 3]

Material	Yield Strength	Sigma		
		FS = 1.2	FS = 1.5	FS = 2.0
Steel	[MPa]	[MPa]	[MPa]	[MPa]
ASTM-A913 Grade 450	450	375	300	225
ASTM-1992 Grade 345	345	287.5	230	172.5
ASTM-A 108	370	308.333	246.667	185
Stainless Steel AISI 302				
Cold-rolled	520	433.333	346.667	260
Annealed	260	216.667	173.333	130
Aluminum				
Alloy 1100-H14 (99% Al)	95	79.167	63.333	47.5
Alloy 5456-H116	230	191.667	153.333	115
Alloy 6061-T6	240	200	160	120

Table 2, Mechanics of Evaluated Material

Material: ASTM-A 108 Steel				
r	M	Shaft Diameter		
[m]	[N*m]	[m]	[m]	[m]
		FS = 1.2	FS = 1.5	FS = 2.0
0.0032	3.1137	0.0047	0.005	0.0056
0.0064	6.2274	0.0059	0.0064	0.007
0.0095	9.3412	0.0068	0.0073	0.008
0.0127	12.4549	0.0074	0.008	0.0088
0.0159	15.5686	0.008	0.0086	0.0095
0.0191	18.6823	0.0085	0.0092	0.0101
0.0222	21.7961	0.009	0.0097	0.0106
0.0254	24.9098	0.0094	0.0101	0.0111
0.0286	28.0235	0.0097	0.0105	0.0116
0.0318	31.1372	0.0101	0.0109	0.012
0.0349	34.2509	0.0104	0.0112	0.0124
0.0381	37.3647	0.0107	0.0116	0.0127
0.0413	40.4784	0.011	0.0119	0.0131
0.0445	43.5921	0.0113	0.0122	0.0134
0.0476	46.7058	0.0116	0.0124	0.0137
0.0508	49.8196	0.0118	0.0127	0.014
0.054	52.9333	0.012	0.013	0.0143
0.0572	56.047	0.0123	0.0132	0.0146
0.0603	59.1607	0.0125	0.0135	0.0148
0.0635	62.2745	0.0127	0.0137	0.0151
0.0667	65.3882	0.0129	0.0139	0.0153
0.0699	68.5019	0.0131	0.0141	0.0156
0.073	71.6156	0.0133	0.0144	0.0158
0.0762	74.7293	0.0135	0.0146	0.016

Table 3, Shaft Diameter Calculations 1

In order to accurately measure the satellite displacement as a result of motor operation, Dr. Brian Bingham of the Mechanical Engineering Department suggested use of an optical encoder with QSB Quadrature to USB adapter based on his own experiences with these products. Based on Dr. Bingham's suggestion, we chose to use the QSB-M and E-6 optical encoder kit

from US Digital. The optical encoder will be secured to the main drive shaft. The user will then be able to manually input a desired angle displacement. The motor will then be driven until it has displaced through the desired angle.

A graphical user interface (GUI) was designed and coded to simplify TestSat operation. The GUI was programmed in an open-source coding language, Processing. Processing was chosen because it is free, readily available on multiple operating systems, and has an active online community and libraries available for download. In addition to driving the motor to displace a certain number of steps, the GUI also reads and displays values from the optical encoder.

A user will also be able to set parameters such as final velocity, QSB quadrature mode, acceleration, toggle stepper motor on or off, and run or brake the stepper motor. The GUI validates the optical encoder values with the desired input displacement value. The program then drives the stepper motor, adjusting rotation direction accordingly, until the values match. Once these values match, the program stops running. [Fig. 2]

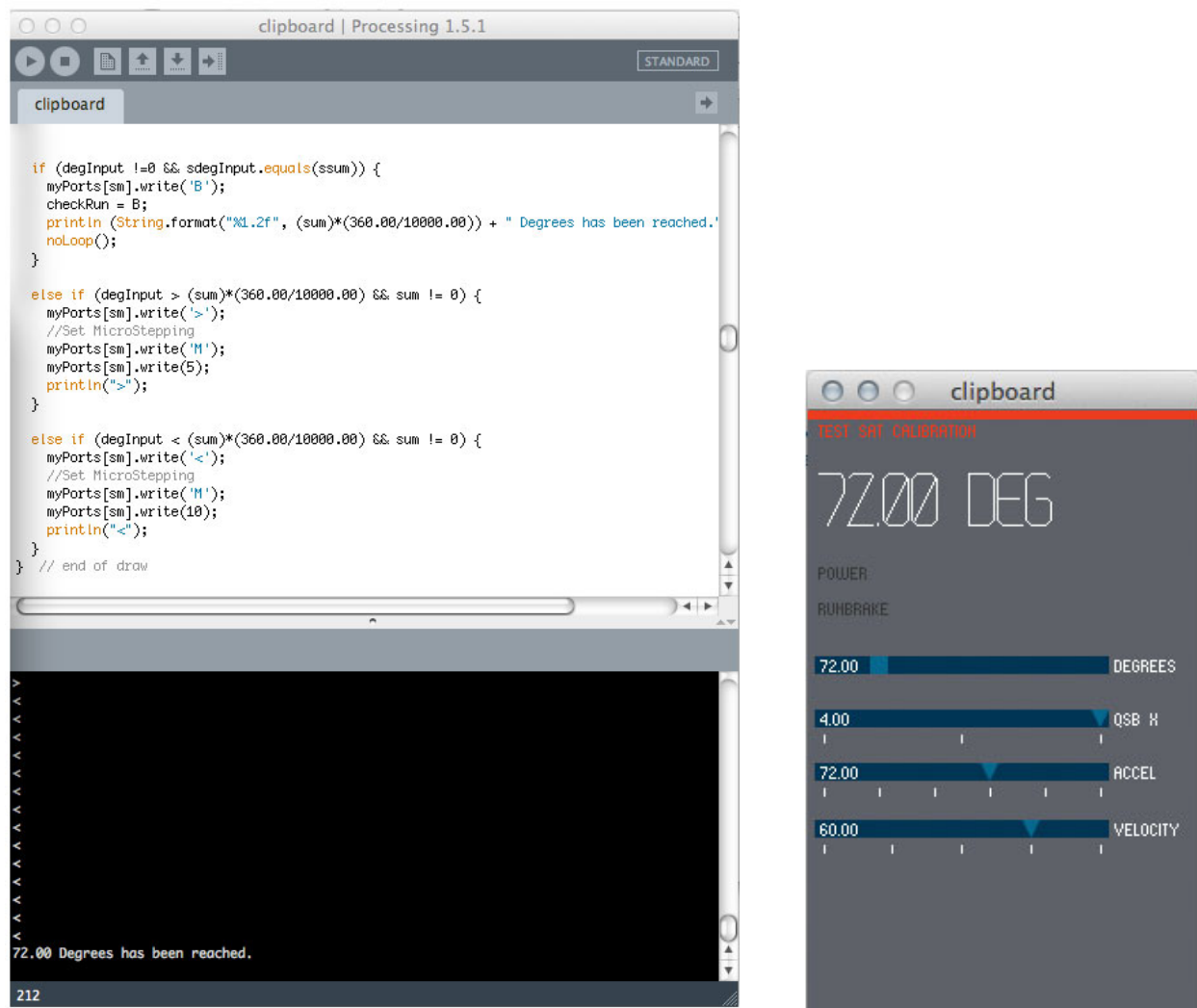


Fig. 2, GUI and Console

RESULTS & DISCUSSION

The biggest challenge in designing the TestSat structure was deciding how to interface the main drive shaft with the satellite's mounting plate. Washers and bolts will secure the satellite and a 0.5" thick mounting plate via through-holes. These through-holes will be placed according to a 15" diameter light band hole pattern.

The mounting plate will be secured to a large-diameter ring style turntable that will be mounted to a table surface. A drive shaft will interface with the base of the satellite mounting plate and go through a hole in the table surface where it will be coupled with a stepper motor drive shaft. Although the primary purpose of the TestSat is to calibrate the ADCS, the main challenge that needed to be addressed was how the structure would be designed – not how the ADCS would be calibrated. [Fig. 2]

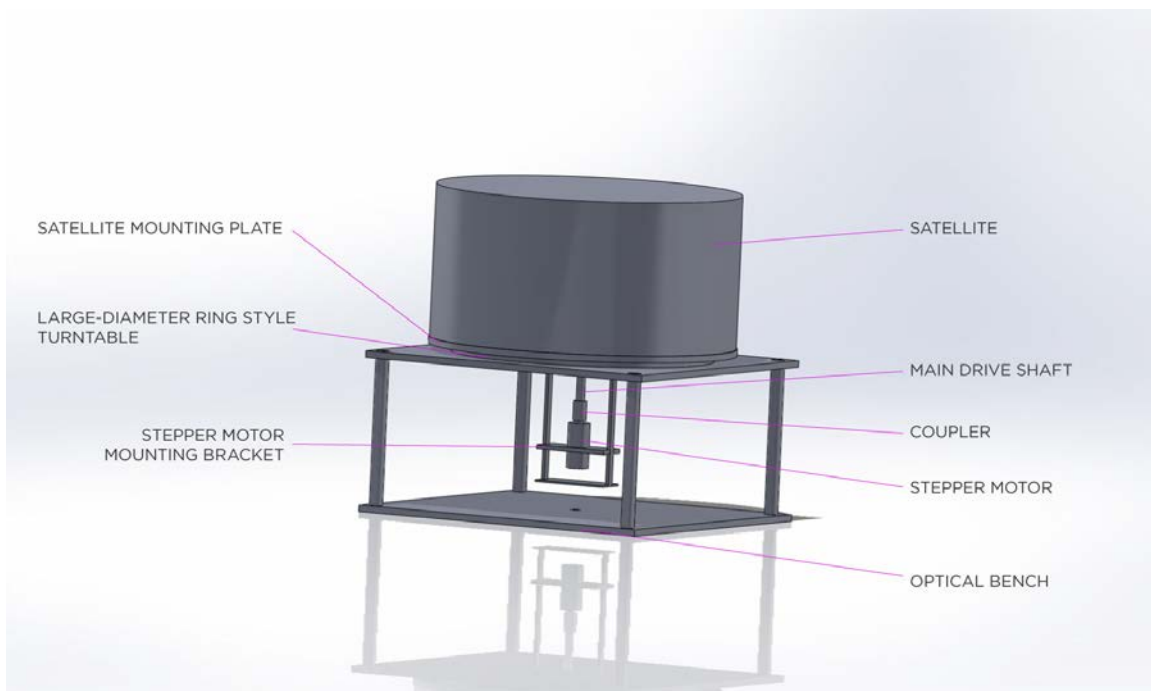


Fig. 2, TestSat Structure 1

An adapter plate was designed to interface the main drive shaft with the base of the satellite mounting plate. An end mill was used to create a notch in the shaft 5/16" (1 radius) deep. This notch effectively created a segment in the shaft that is necessary to transfer the shaft's rotational motion to the satellite mounting plate.

The two adapter plate halves will be fixed to the notched section of the drive shaft by a pair of hex screws. The adapter plate is then mounted to the underside of the satellite mounting plate via a second pair of screws. [Fig. 4] A drive shaft registration hole milled into the underside of the mounting plate helps maintain drive shaft and adapter plate alignment.

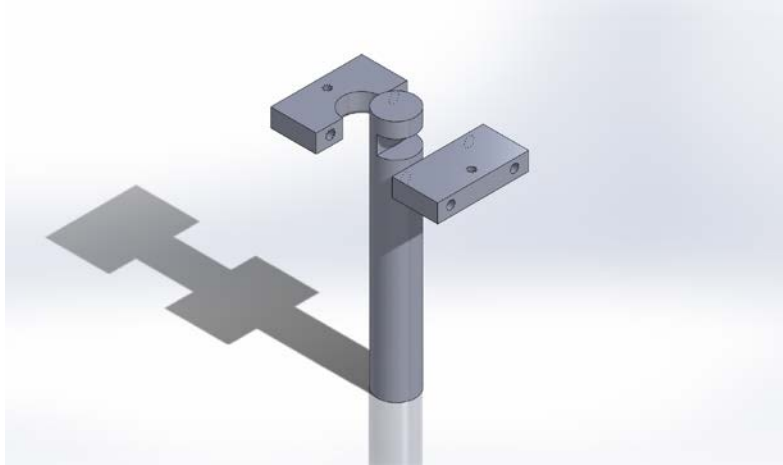


Fig. 4, Adapter Plate

The final design of the TestSat makes use of an optical bench as the base. The optical bench is intended to minimize vibrations and acts as a sturdy foundation for the structure. The table surface itself is ½" thick baltic birch plywood. The structure and motor were tested under a load exceeding 140 lbs). The TestSat successfully operated under this load. Towards the end of this project we noted the plywood was beginning to warp. Investigation of an alternative material and or design will be considered by a group of high school interns that will be working with this project over the summer.

The GUI had difficulties stepping to the proper position because the stepper motor would displace the same amount of steps as it changed rotation direction. Changing the stepper motor's microstepping mode from ½ for clockwise rotation to 1/10 for counter clockwise rotation solved this. Although the stepper motor driver has an optical encoder built-in, output values for this encoder are limited to absolute values and thus are unable to indicate rotation direction.

It was also determined that the stepper motor would stall while changing rotation direction. The cause of the stall is due to the fact the stepper motor is taking time to re-accelerate each time it changes rotation direction. When the stepper motor stalls, the motor draws excessive current, and the motor controller is unable to limit the current to its specified maximum draw. The switching power supply, set to limit current at 3.0A with a 12V output, will drop its output voltage as the current limit is being exceeded.

When the power supply voltage drops below the motor controller's operating voltage, the motor controller will reset. The reset abruptly cuts off power to the stalled motor. Residual current in the motor's inductive windings will be routed through diodes to dissipate it safely. However, the switching power supply may have continued to push the maximum current to the motor driver, and was too slow to ramp down its current output.

The power supply's overvoltage protection was not configured during testing, thus there was no safety cut-off when an overvoltage condition occurred. This may have resulted in multiple events of overvoltage, causing the motor controller to repeatedly reset, which would cause the motor to stall. This may have been what eventually destroyed the motor controller.

CONCLUSION

The TestSat structure and interface design, fabrication, and testing were successfully completed. We are currently looking into an alternative aluminum structure that will not warp or require use of the optical bench. The new structure will offer improved stability during operation. The designed adapter plate and drive shaft coupler performed well.

Jeremy pointed out to me the acceleration relates more to the change of the tangential velocity rather than directly related to the output torque of the motor. The amount of torque is actually related to the microstepping mode of the stepper motor. Therefore, since acceleration is not an influential parameter when calibrating the ADCS, and operating the TestSat with a non-zero acceleration tends to stall the stepper motor, we decided the final version of the GUI will not allow control of the acceleration.

When the stepper motor stalls, there may be an over-voltage condition at the motor controller's power input, resulting in a broken controller. As mentioned earlier, over voltage protection may prevent this from happening. To prevent damage in the future, if current limits may be exceeded in a stall or similar event, power supply overvoltage protection should be enabled.

ACKNOWLEDGEMENTS

I would like to thank the Hawai'i Space Grant Consortium and Hawai'i Space Flight Laboratory for allowing me to work on this project. I would also like to thank Jeremy Chan, Miguel Nunes, Lance Yoneshige, and Daniel Wukelic for their time and patience.

MINERALOGICAL STUDY OF VOLCANIC SUBLIMATES FROM HALEMA‘UMA‘U CRATER, KILAUEA VOLCANO

Liliana G. DeSmither
Department of Geology
University of Hawai‘i at Hilo
Hilo, HI 96720

ABSTRACT

Anatase and silica-rich deposits found around Halema‘uma‘u Crater, within the Kilauea Caldera, are thought to be similar to those that have been found at Home Plate on Mars. The deposits found at Halema‘uma‘u Crater on Kilauea Volcano have been altered by acid sulfate steam leaching around the fumaroles. These fumarole deposits at Kilauea have been used as an analog site for the deposits at Home Plate, but there is also recent suggestion that the deposits are hot springs-related silica sinter (Ruff et al., 2011).

Comparison of altered and unaltered deposits around Halema‘uma‘u crater show that the only elemental oxides left in the rocks are silica (as opal-A) and titanium (as poorly crystalline anatase). Both Si and Ti are mobile in this environment and show a strong zoning. In the outer zone, the rock is largely replaced by opal, but retains its original vesicular texture. Comparison of major element chemistry suggests that titanium was lost from this zone. In the inner zone, the rock has broken down into loosely consolidated, friable material high in Si and Ti that also frequently contains scattered native sulfur crystals. The concentrations of Ti in these deposits is roughly double the amount that should be present if all elements other than Si and Ti were leached from the rock. The decomposed state of the rocks suggest that silica was also leached from the central altered zones, leaving titanium enriched in these samples.

The outer silica-rich zone appears to be a good analog for the Si-rich Gertrude Weise deposits near Homeplate, whereas the Ti- and S-rich deposits in the core of the alteration are analogs for the S-rich Tyrone soils found nearby. The zonation of the acid sulfate deposits at Halema‘uma‘u Crater seems similar

INTRODUCTION

Kilauea Volcano on the Island of Hawai‘i has been used as a terrestrial analog for the Home Plate deposits found on Mars. *Morris et al.* (2009) discussed how silica rich materials at Home Plate tend to also have titanium enrichment. Other elements have been significantly leached from the area because they are more soluble than SiO₂ and TiO₂. They interpreted that the system had undergone acid sulfate leaching. Two types of deposits in particular that have been found at Home Plate, sulfur-rich Tyrone soils and silica-rich Gertrude Weise soils, are believed to have formed during the same process (Wang et al., 2008). Both soils deposits are found in an area that is topographically low, and contain other Si-rich outcrops within them. They believe the two soils are both end members of the same hydrothermal process and that they had been sorted chemically, transported by water and then deposited at some point during this process. However, *Ruff et al.* (2011) noted that a hydrothermal hot springs also form deposits with high opal-A concentrations, and may show enrichments in titanium. Ruff et al. 2011 suggest that the absence of sulfur in the Home Plate soils, suggesting this chemical signature is not unique to one

hydrothermal system over the other, and the lack of sulfur enriched deposits contrast with the idea of acid sulfate leaching.

SUBLIMATE SAMPLES

In May of 2009 Ken Hon and Lopaka Lee collected 73 samples from around the rim of Halema'uma'u Crater under a National Park Service research permit. Ryan Bishop chose 10 sublimates and one ejecta sample from the 2008 eruption for this mineralogical study. Samples from the most intensely altered zones, HM-15 and HM-18, were found to be composed primarily of opaline silica with variable amounts of anatase. These samples appear similar to silica-rich materials at Home Plate by the MER Spirit (Chemtob, 2010). I have expanded Ryan Bishop's work by looking at the core of 3 additional fumarolic alteration zones.

The goal was to find altered materials that have similar silica and anatase alteration, and to look at the surrounding materials. Analyses of the samples illustrates a better image of what the area surrounding Halema'uma'u crater looks like on a larger scale, so it can be compared to Home Plate deposits. During the course of this project a large number of samples were looked at from four principal alteration sites around Halema'uma'u crater. The main samples being analyzed for this project due to the anatase and silica content were: HM-15, HM-18, HM-24, HM-45, HM-51, HM-52, HM-54, and HM-56.

Minerals and other phases were identified by X-ray diffraction on the UH-Hilo Pharmacy Bruker D-8 diffractometer and on the Hitachi S3400 Scanning Electron Microscope with an Oxford EDS detector. X-ray Fluorescence (XRF) for major elements has been used for bulk analysis of four samples consisting of pairs of altered and unaltered spatter, and an additional four samples of altered powdery materials all collected from sites around Halema'uma'u. These analyses were run by the Washington State University GeoAnalytical Lab.

The major element XRF analyses allow us to evaluate how Si and Ti have been transported in the environment and to determine whether or not they are immobile residues. Loss On Ignition (LOI) analysis has also been done on the samples and measures the weight of the material that has been lost during the heating process. Many samples contain significant amounts of native sulfur and water-rich opal. Both compounds have low vaporization points and are lost during the during heating and contributed to the LOI. Samples were also analyzed for S and SO₃ which can be subtracted from the LOI to determine the amount of water in the samples. The samples that were selected to compare the composition of fresh and altered spatter. The samples are: HM-15 unaltered spatter, HM-15 altered spatter, HM-18, HM-51, HM-52, HM-54 unaltered spatter, HM-54 altered spatter, and HM-56.

All of samples were recalculated with only SiO₂ and TiO₂, as these were the only elements left above trace levels in the altered samples. Comparison of the recalculated analyses for fresh and altered samples allows the assessment of leaching versus precipitation during alteration.

Table 1: Whole rock XRF analysis of altered materials (italicized) and unaltered materials (bold).

	Sept-1971 HM-15	Sept-1971 HM-15 alt	1919 Avg ¹	1919 HM-18	Sept-1974 Avg ²	Sept-1974 HM-51	Sept-1974 HM-52	Aug-1971 HM-54	Aug-1971 HM-54 alt	Aug-1971 HM-56
SiO ₂	51.85	80.05	50.02	76.95	50.40	65.32	65.03	52.18	79.00	70.88
Al ₂ O ₃	13.14	0.20	13.96	0.64	13.60	0.84	0.40	12.43	0.19	0.49
FeO*	11.09	0.29	11.06	1.15	11.08	0.51	0.16	10.96	0.23	0.25
MgO	7.16	0.05	7.24	0.09	7.37	0.05	0.05	6.80	0.03	0.05
CaO	11.05	0.05	11.47	0.16	11.20	0.04	0.29	10.77	0.06	0.06
Na ₂ O	2.27	0.05	2.29	0.02	2.22	0.01	0.02	2.18	0.03	0.02
K ₂ O	0.51	0.02	0.55	0.02	0.48	0.00	0.02	0.52	0.01	0.02
TiO ₂	2.63	1.86	2.72	7.81	2.50	18.94	3.00	2.73	1.61	3.40
P ₂ O ₅	0.27	0.13	0.27	0.08	0.25	0.23	0.06	0.27	0.10	0.04
MnO	0.17	0.00	0.17	0.00	0.17	0.00	0.00	0.16	0.00	0.00
Sum	100.14	82.71	99.74	86.92	99.27	85.95	69.02	99.00	81.28	75.22
LOI (%)	-0.27	15.79	0.18	11.38	0.14	13.18	28.98	-0.23	17.38	23.09
Sum w LOI	99.87	98.50	99.92	98.30	99.41	99.14	98.00	98.77	98.66	98.31
~S (wt%)	0.3	1.5		2.70		7.5	28.8	1.2	2.9	15.9
~SO ₃ >=	0.21	0.53		0.39		0.38	0.33	0.43	0.90	0.43

¹: 1919 average from Wright, 1971, ²: 1974 average from Lockwood, 1999.

Table 2: SiO₂ and TiO₂ recalculated to 100% to show the loss (-) and gain (+) of each and the mobility between them.

	Sept-1971 HM-15	Sept-1971 HM-15 alt	1919 Avg ¹	1919 HM-18	Sept-1974 Avg ²	Sept-1974 HM-51	Sept-1974 HM-52	Aug-1971 HM-54	Aug-1971 HM-54 alt	Aug-1971 HM-56
SiO ₂	95.17	97.73	94.84	90.79	95.27	77.52	95.59	95.03	98.00	95.43
TiO ₂	4.83	2.27	5.16	9.21	4.73	22.48	4.41	4.97	2.00	4.57
Total	100.00	100.00	100.00	100.00	100.00	100.00	100.00	100.00	100.00	100.00
SiO ₂	-	2.55	-	-4.05	-	-17.75	0.32	-	2.97	0.40
TiO ₂	-	-2.55	-	4.05	-	17.75	-0.32	-	-2.97	-0.40



Figure 1: Map of the Halema'uma'u Crater sampling sites.

1892-94 Lava Flow Site: Samples HM1

A sample of gray crust, HM-1, is representative of most of the other crusts around Halema'uma'u crater. This sample contains sulfur, gypsum and opal-CT concentrated in a relatively thin (1 cm) layer.

1971 Fissure Site: Sample HM13-HM20

Fresh black spatter (HM15) and altered white spatter (HM-15 alt) were collected from the 1971 fissure rampart (Table 1). The altered sample is nearly pure opal and has very high silica contents. There is very little sulfur in the altered sample and most of the LOI can be attributed to water within the opal.

1919 Shelly Pahoeohoe Channel Site: Samples HM18-HM29

Sample HM-18, analyzed by Ryan Bishop, was a salmon colored soft material that was altered to form silica spheres mostly consisting of opal with some anatase. XRF analysis (Table 1) shows that the altered material has highly leached all of the elements it contained in the unaltered analysis except for SiO_2 and TiO_2 . The crust above HM-18, HM-19, was a white and yellow sulfur crust that was found to have an abundance of opal-CT along with some anatase. HM-24, a very soft and porous sample found filled with sulfur, was found beneath a gray crust. XRD analysis on the sample identified opal and sulfur peaks. Small amounts of anatase were detecting using the SEM.

North Pit Area: Samples HM31-HM36

From the samples taken in the North Pit Area, three crust samples were analyzed with the XRD. HM-31, white crust that forms over 10-20% of the area, HM-34 yellowish orange crust that surrounds lithic bombs, and HM-36, a gray hardpan crust that coats much of the area all contain both anatase and opal CT., Samples HM-31 and HM-36 also contain sulfur, whereas gypsum was found in HM-34 and HM-36.

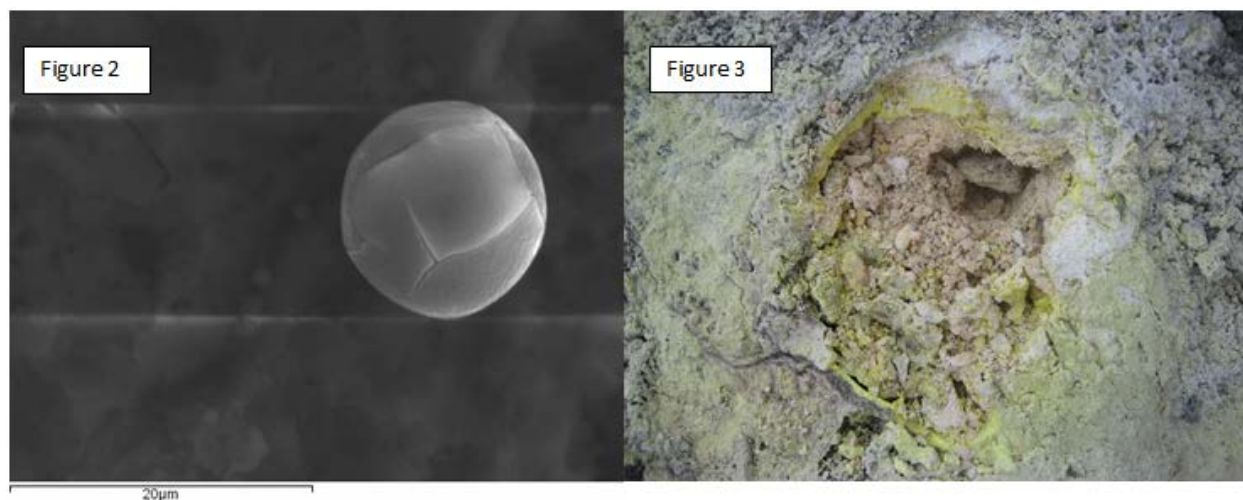


Figure 2: SEM image of an opal sphere at 20 microns.

Figure 3: HM-51 pinkish opal and anatase.

1971-1974 Fissure SW of Halema'uma'u: Samples HM45-HM52

Covering about 80% of the area south of the 1974 fissure is a grayish green hardpan crust, HM-45. The crust has opal-CT and anatase with some sulfur and iron as well, and an SEM image shows the form of the opal spheres (Figure 2). The other crust in the area south of the fissure was HM-47, which was comprised of opal-CT and gypsum. The sulfur crusts around the active fumaroles, HM-50, also had opal-CT, gypsum and anatase. Beneath this sulfur crust was pink-salmon altered clay material, HM-51, which looks very similar to the other anatase rich deposits found (Figure 3). Looking at the XRF data found on table 1, the TiO_2 increased over seven and a half times from the unaltered data, and the SiO_2 slightly increased as well while everything else was significantly leached from the sample. Just above the pink-salmon clays was a layer of white material that was abundant in sulfur, HM-52. After removing as much of the sulfur as possible from the sample, XRD and SEM results showed that Opal-CT, anatase and gypsum were also in the sample. XRF analyses (Table 1) show that all of the elements have been leached almost to zero, except for SiO_2 and TiO_2 which increased slightly in the sample

1971 Fissure E of Halema'uma'u: Samples HM54 and HM-56

Fresh and completely altered spatter found on the 1971 rampart show differences in composition similar to HM-15 altered and fresh spatter with a gain in silica and a loss of titanium. All other elements were almost completely leached out. White totally replaced spatter, HM-54, found on the west end of the 1971 fissure system contains opal, anatase and sulfur. SEM results found olive shaped spheres made up of anatase and silica with the inside being almost entirely anatase (Figure 4). HM-56, white-pink soft material found under crust, also has abundance of opal-CT and anatase. SiO_2 is highly concentrated in this sample, where as TiO_2 is roughly equivalent to the fresh sample, and everything else has been leached out (Table 1).

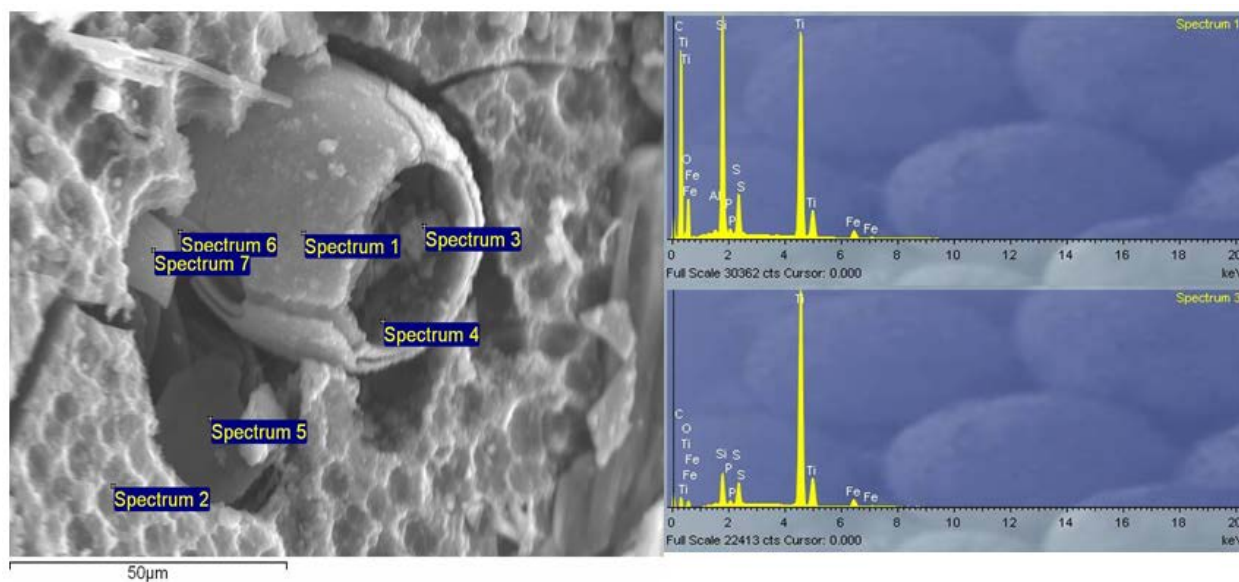


Figure 4: SEM image showing the anatase (Ti) within opalized vesicular spatter.

RESULTS AND CONCLUSIONS

All of the lava flows originally had very similar chemical compositions (Table 1). The XRF analyses show that almost all of the major and trace elements, with the exception of SiO₂ and TiO₂, have been depleted in the altered samples compared to the fresh ones. The variable contents of SiO₂ and TiO₂ indicate that they are relatively insoluble and cannot easily be leached out of their environments. Throughout the samples taken around the crater, most of the crust samples, unless otherwise specified as a sulfur crust, were largely made up of opal-CT. Beneath these crusts is white clay-like material. Samples of this material, HM-52 and HM-56, have gained about the same amount of SiO₂ and TiO₂ as the fresh samples when recalculated (Table 2). Directly below the white material are the pink/salmon colored soft material, HM-18 and HM-51. These deposits have gained the highest concentrations of TiO₂ out of the samples with respective gains of 4% and 18%. HM-15 and HM-54 are the only XRF samples that actually show a loss TiO₂, and they are both samples of altered spatter found on the ground surface. They also have the highest concentrations of SiO₂ and have been able to maintain their original structure, unlike the soft materials. This information suggests that the Ti and Si are mobile during the acid sulfate leaching process, because the Si is concentrated in the upper crusts and ground spatter, whereas the Ti becomes increasingly more concentrated in the layers under the surface crust. The powdery material found in samples HM-18 and HM-51, fit the description of the Gertrude Weise soils found at Home Plate being that they are both light-toned and have high concentrations of Si and Ti. With the Ti and Si becoming mobile in the system and the other elements being highly depleted, the process of acid sulfate leaching caused by fumaroles seems to be a reasonable explanation for the formation of the deposits found at Home Plate on Mars.

ACKNOWLEDGEMENTS

I would like to thank Dr. Ken Morris for all of his help, and allowing me the time I needed using the XRD, John Coney for all of his help assisting me with the SEM and the Washington State University GeoAnalytical Lab for completing XRF analysis on selected samples. I would also like to thank the NASA Space Grant Consortium for giving me the opportunity to work on this research project. I would like to thank my advisor Dr. Ken Hon most of all, for all of his help and guidance throughout this project.

REFERENCES

- Chemtob, S. M., B. L. Jolliff, G. R. Rossman, J. M. Eiler, and R. E. Arvidson (2010) Silica coatings in the Ka'u Desert, Hawaii, a Mars analog terrain: a micro-morphological, spectral, chemical and isotopic study. *JGR*, 115, E04001, doi:10.1029/2009JE003473.
- Lockwood, J. P., Tilling, R. I., Holcomb, R. T., Klein, F., Okamura, A. T., Peterson, D. W. (1999), *Magma Migration and Resupply During the 1974 Summit Eruptions of Kilauea Volcano, Hawai'i*, U.S. Geological Survey Professional Paper 1613.
- Morris, R. V., Ming, D.W. (2009), *Chemical and Mineralogical Constraints for Modeling Hydrous Environments on Mars from the Mars Exploration Rovers*, Workshop on Modeling Martian Hydrous Environments, NASA Johnson Space Center, Houston TX.

Ruff, S. W., et al. (2011), Characteristics, distribution, origin, and significance of opaline silica observed by the Spirit rover in Gusev crater, Mars, *J. Geophys. Res.*, 116, E00F23, doi:10.1029/2010JE003767.

Wang, A., and 14 colleagues, 2008. Light-toned salty soils and coexisting Si-rich species discovered by the Mars Exploration Rover Spirit in the Columbia Hills. *J. Geophys. Res.* 113, E12S40. doi:10.1029/2008JE003126.

Wright, T. L. (1971), Kilauea and Mauna Loa in Space and Time, Geological Survey Professional Paper 735.

DETERMINING DIMENSIONAL RATIOS FOR FRESH, DEGRADED, AND FLOOR-FRACTURED LUNAR CRATERS

Elyse K. M. Iseke
College of Tropical Agriculture and Human Resources
University of Hawai'i at Mānoa
Honolulu, HI 96822

ABSTRACT

Ratios of lunar crater dimensions, that are measured using lunar altimetry, showed differentiation between fresh, degraded, and floor-fractured crater classifications. More specifically, igneously modified floor-fractured craters that were able to be distinguished well using depth as a parameter in analysis.

OBJECTIVE

To examine whether one or more crater parameter (e.g., depth, diameter, rim height, and rim flank) combinations will allow us to distinguish igneously modified floor-fractured lunar craters from fresh and degraded lunar impact craters.

INTRODUCTION

In his 1976 study, using shadow lengths and sun angles to measure the dimensions of fresh lunar craters, Richard J. Pike found that a strong correlation between diameter and depth for fresh craters. When ratios of these parameters were plotted on a log-log diagram, the data for simple craters could be characterized by a linear trend (Pike 1976). We used Pike's discovery as a basis to investigate whether other types of lunar craters exhibit dimensional proportions that are unique enough differentiate between three main crater types: fresh, degraded, and floor-fractured. Fresh craters exhibit the pristine unchanged crater shape. They are the craters all other craters are compared to. Floor-fractured craters have undergone modification to their impact crater shapes do to magmatic swelling beneath their floors, which cause uplift. Finally, degraded craters have changed due to the lunar erosion process, which is primarily cratering. In this case, their shapes have become more subdued due to the process of impact erosion.

To do this comparison we measured depths, diameters, rim heights, and rim flanks (also called flank width) of fresh, degraded, and floor-fractured craters (Figure 1). These parameters were compared in various combinations (i.e. diameter-to-depth, rim flank-to-depth) as a means to determine an acceptable differentiation among the fresh, degraded, and floor-fractured crater types.

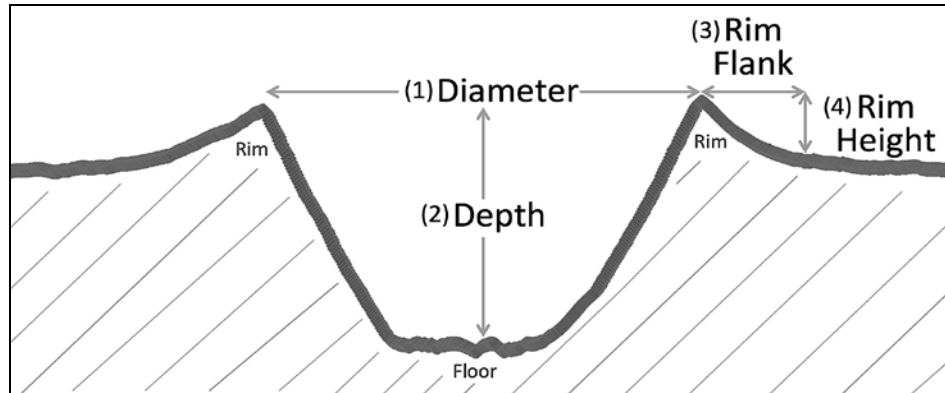


Figure 1: Lunar altimetry profile (cross-section) through a lunar crater illustrating the parameters used in this study. The diameter (1) of the crater is the horizontal distance measured from one rim peak to the other directly across it. Depth (2) is the vertical distance between the averaged elevation of the crater rim and the floor (fluctuating floor elevations may need to be averaged as well). Rim flank (3), also termed flank width is the straight horizontal distance from a peak on the rim directly to its break in slope. A crater's rim height (4) is the vertical measurement from the elevation of the break in slope to the elevation of the rim.

Our hope was to find a set of crater dimensions that allow for good separation of floor-fractured craters from the other classifications. With such a set of crater parameters, we could compare measurements of craters that exhibit ambiguous topographies to test whether they formed by impact erosion or igneous modification.

Fresh lunar craters are the newest, created from impacts that occurred within the last 1 to 2 billion years. Because they are geologically young and experienced almost no modification, their crater features are still very pronounced. The depths of fresh craters are a great deal deeper than other crater types and the rims are noticeably sharp. Some fresh craters are referred to as Copernican craters because they formed from impacts that took place during the most recent geologic period on the Moon, called the Copernican Age. This means that they are the freshest of fresh craters, being younger than 1 billion years. These particular craters display bright white, high-albedo crater rays made up of ejecta and debris from their formation.

In Pike's fresh crater research (Pike 1976) he also established that fresh craters could be further classified as being simple or complex. Simple fresh craters are small in diameter; usually not exceeding 15 kilometers. They are markedly bowl-shaped (fig. 2a), with smooth, curved interiors, and able to maintain their rims. Figure 2b illustrates the topography of a simple fresh crater.

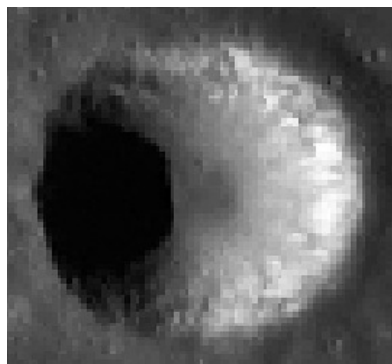


Figure 2a: Overhead view of Taquet

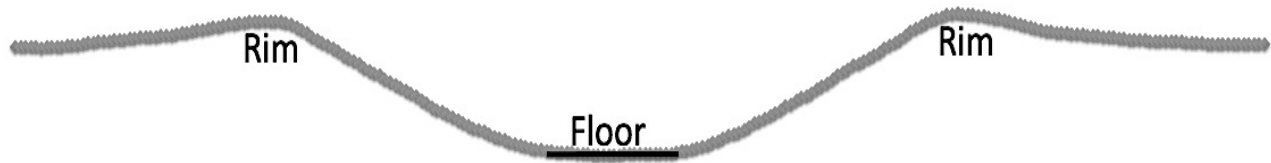


Figure 2b: Altimetry profile simple fresh crater, Taquet (6.43km).

Complexity of fresh craters develops with greater diameters as low as 18 kilometers to much larger sizes. Gravity instigates the morphologies of these craters acting on their vastness. As a result, complex craters are much wider than deep. In addition, they acquire characteristic terracing—formations that look similar to steps—on their inner walls as portions of their rims slide in under gravitational forces.



Figure 3a(above) shows the topography of complex fresh crater, Lalande (23.54km). The shape of the interior is not smooth as a result of terracing (indicated with arrows) and a flat floor.



3b: Overhead view of Lalande.

The degraded classification comprises craters that were made from impacts that occurred more than 3 billion years ago. Degraded craters exhibit reduced topography compared to fresh craters, displaying shallower floors and dull rims. Since they existed over multiple periods of lunar geology, the erosion process transformed once sharp, deep fresh craters into degraded.

Unlike Earth, the Moon has no atmosphere to support weather erosion. It is also no longer geologically active and has never had any form of plate tectonics. Therefore, the main form of erosion acting on lunar craters is other crater formations. The cratering process involves material striking the lunar surface with massive forces that cause energetic explosions; much like a nuclear bomb. Debris, soil, and rock disrupted by the impact process forms ejecta, which is launched outward—sometimes over hundreds of kilometers—and bombards the areas surrounding the impact.

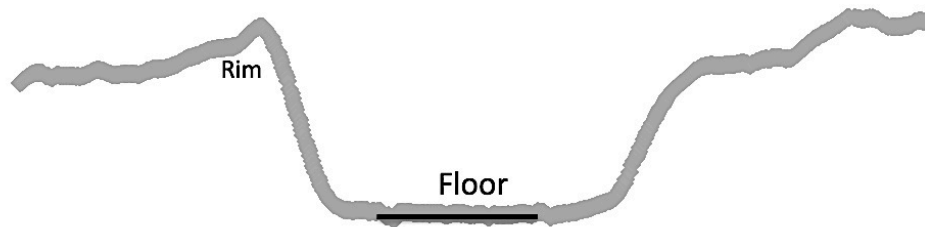
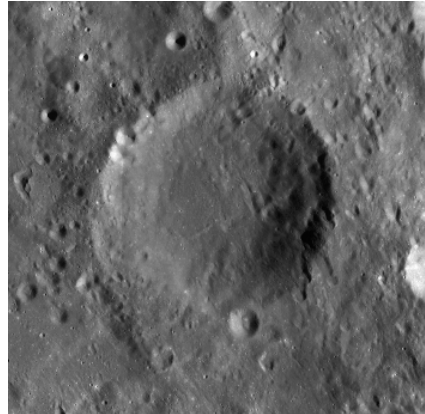


Figure 4a (above): Altimetry profile of a degraded crater (21km). Note that there is only one area on the rim is distinguishable. The opposite rim is extensively degraded and not useful to measure.

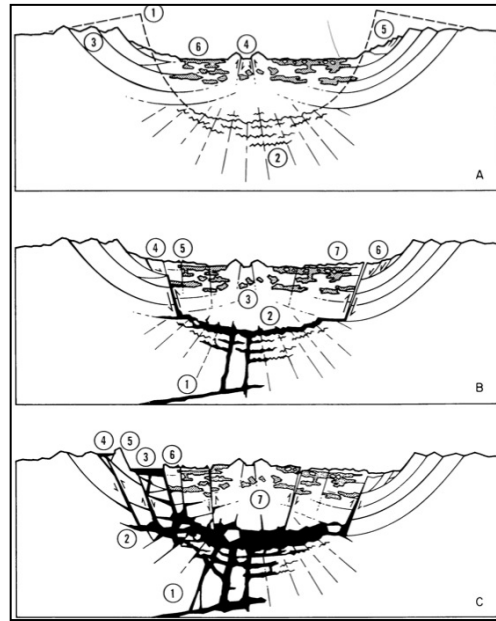


4a (above) shows the overhead view of a degraded crater.

This degradation process affects nearly all the crater shape parameters. Depth is decreased in degraded craters because the repeated ejecta spray, discharged by nearby impacts, fills the interiors making them shallow and flat. Figure 4 a and b show the topography of a degraded crater. Degraded craters also have very diminished rims, which reduce rim flank and rim height as a result of other cratering. Diameter is the one parameter that generally exhibits insignificant changes between fresh and degraded craters. Craters will also experience direct hits ending in a new crater partially covering an old one.

In another 1976 study Peter Schultz investigated lunar craters that contained noticeable cracks and rift zones. He found that the observed fissures are manifestations of the past geologic activity on the Moon. These craters were classified by Schultz as volcanically modified impact craters. Floor-fractured craters are part of this group. The modification process of floor-fractured craters occurred after impact formation. When the Moon was still geologically active, it produced magma that rose close to its surface. The magma collected under impact craters and began to swell underneath the floors of the craters. The floors eventually developed cracks as the magma pushed it up. Figure 5 shows this process very well.

Figure 5: Depiction of igneous modification. The first stage is of a fresh impact crater with its normal morphology. In the next image, magma pool under the crater floor and starts to swell. The last shows a dramatic floor-lift with many cracks.



As a result of the igneous intrusion, the floors of the craters possessed many fractures and were uplifted due to the magma bulge underneath it. The depth parameter of floor-fractured craters was decreased due to floor uplift, and was changed more significantly by this type of modification than the other dimensions. Floor rise and cracks in floor-fractured crater, Lebegue, is seen in Figure 6. Generally, floor-fractured craters are old, and therefore underwent impact erosion like degraded. We wanted determine if this igneous form of modification would still be able to distinguish itself even if floor-fractured craters and degraded craters have morphologic similarities.

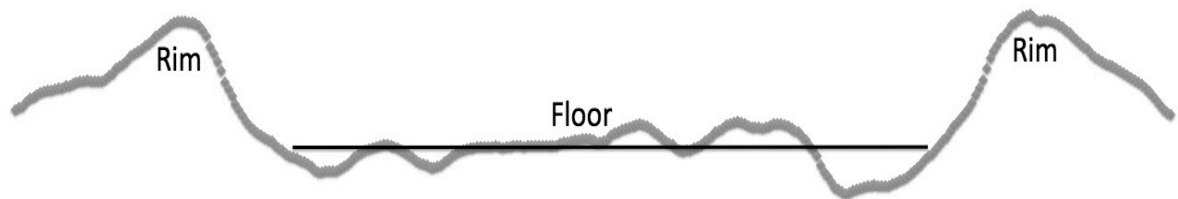
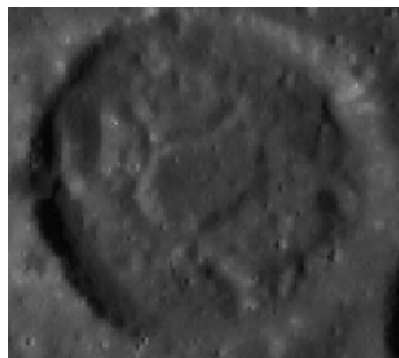


Figure 6a (above): Altimetry profile of floor-fractured crater, Lebesgue (km). The floor of crater is noticeably uplifted from magmatic intrusion. Also, both of the rims shown in this image are very well-defined, which might suggest that depth and rim measurements will be good parameters to analyze. 6b (below) shows the overhead view of Lebesgue.



We expect floor-fractured craters, which underwent unique igneous morphology, will exhibit specific parameter ratios that the other crater types will not possess.

METHOD

Using images from the Lunar Reconnaissance Orbiter (LRO) and topographic data from the Lunar Orbiter Laser Altimeter (LOLA), we were able to select craters to analyze by first visually examining their features and characteristics and obtaining necessary measurements of those craters for our dimensional ratios. Our measurement procedure was limited to very specific areas on the crater where we could obtain topographical information. We, therefore, needed to be aware of mountains, hills, or other craters on or around the craters that would prevent us from accurate data-collecting.

We also used Google Moon's Geologic maps. It provided us with better confidence in selecting craters based on visual features. Representing steeper slope in redder colors, and lesser slope angles in greens, the program served as a valuable tool in knowing the type of crater we were selecting. In areas not charted by geologic maps, like the terrae on the far side of the moon, we looked for white crater rays, in selecting fresh craters. To locate floor-fractured craters we used lunar maps that indicated areas where they are concentrated, like the edges of Oceanus Procellarum. Degraded crater selection was easier as we developed a better understanding of the visual crater characteristic after forming sample groups of the other two types of craters.

In order to develop measurement ratios, we began by selecting fresh and floor-fractured craters to study. We wanted to identify 40 to 50 fresh, floor-fractured, and degraded craters, initially, in order to have a definitive group of at least 25 craters for each type that are able to be measured according to our methods. This was done using Lunar Reconnaissance Orbiter Camera (LROC) images, accessible through the program, JMARS for the Moon. We sought to find craters between 5 to 30km in diameter, in an even size distribution.

In order to get the topographical information we needed to measure crater our parameters, we used data from the Lunar Orbiter Laser Altimeter (LOLA). LOLA, mounted on the LROC, orbits the Moon in parallel, longitudinal tracks while recording elevation changes of the lunar surface, which illustrates the topography. As it travels, it measures elevation by emitting a laser pulse consisting of 5 beams covering 50 by 50 meter area of the ground. LOLA tracks the amount of time it takes each laser pulse to reach the ground, and then reflect back to the spacecraft. The duration translates into topographical evaluations. Longer periods of travel by the lasers indicate lower elevations, while shorter time periods indicate higher elevations.

After determining the craters to be measured, we downloaded the topographical information obtained by LOLA through the Lunar Orbiter Data Explorer program. Once we had the topographies of each of our craters, we processed it using a system called "binning". From the raw LOLA information, we process it using a system that averages the amount of data, making it more manageable, and also converts the data from values of location in latitude and longitude coordinates into values of distance in kilometers. The data outputted from the binning for each crater was plotted on an excel chart, and the resultant image was a cross-sectional view

of a crater called a shapefile, which allowed us to measure our parameters. Figure 7 is an example of what a shapefile for a crater might look like.

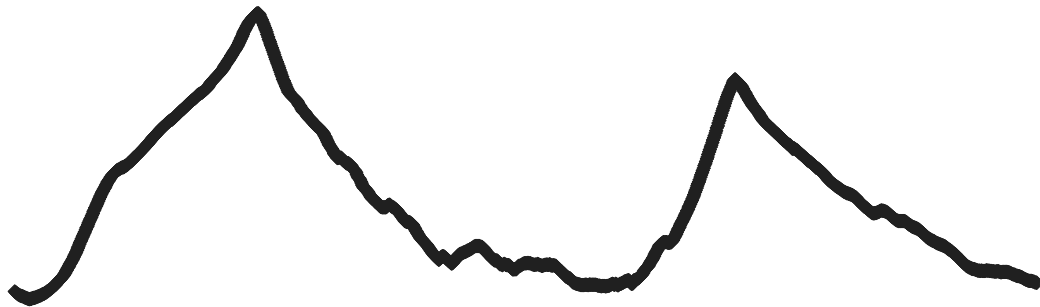


Figure 7: A shapefile of fresh crater Necho (33km). It is not a line, but made up of a series of many individual data points that illustrate the topography of the crater.

Using the distance and elevation values of the data points, we were able to calculate measurements according to the parameters.

RESULTS

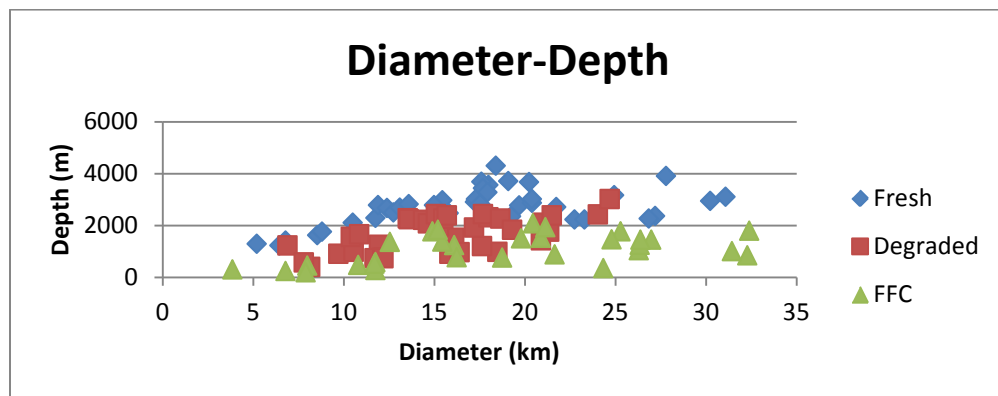


Figure 8: Plot of depth in meters to diameter in kilometer ratios for our fresh, floor-fractured, and degraded crater populations.

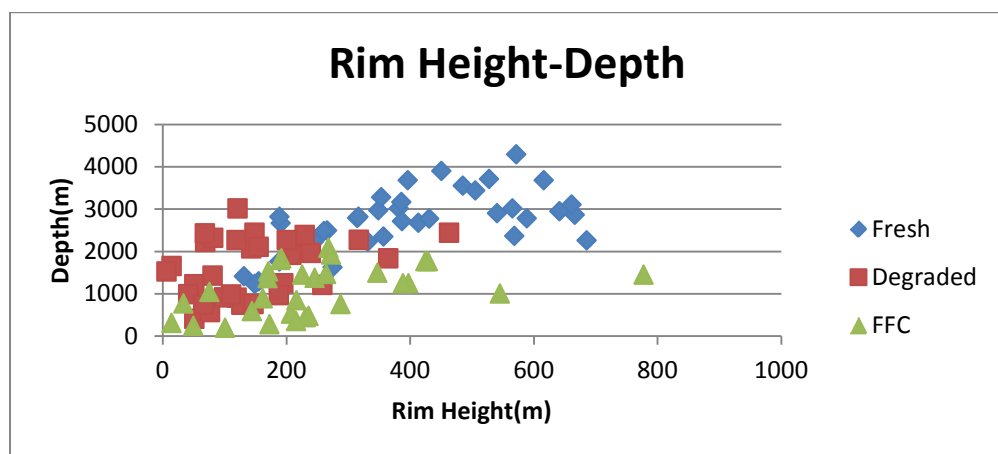


Figure 9: Plot of ratios between rim height in meters and depth in meters for our fresh, floor-fractured, and degraded crater populations.

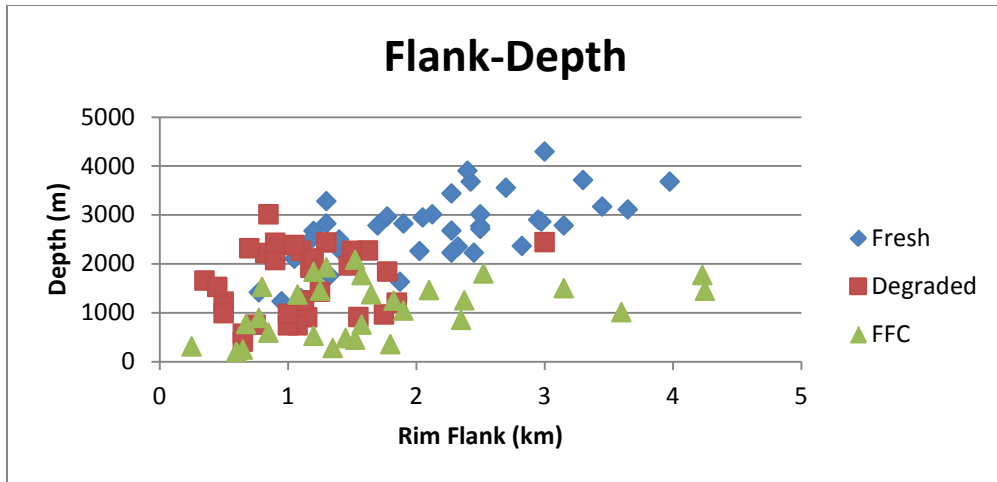


Figure: Plot of ratios between diameter in kilometers and rim flank in kilometers for our fresh, floor-fractured, and degraded crater populations.

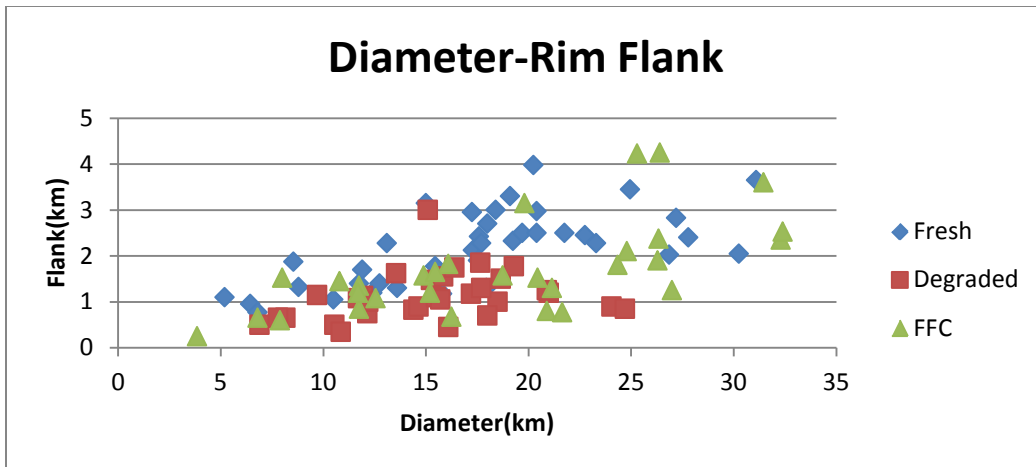


Figure 10: Plot of ratios between diameter in kilometers and rim flank in kilometers for our fresh, floor-fractured, and degraded crater populations.

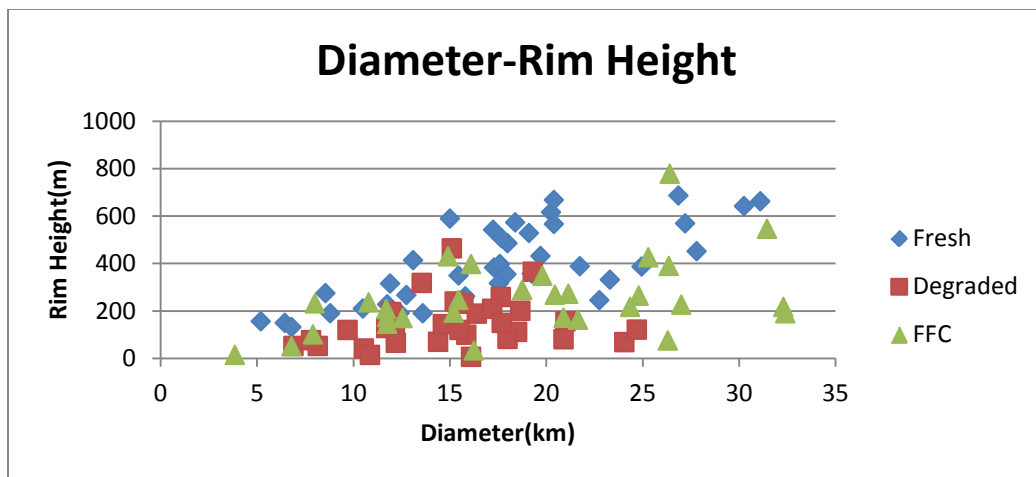


Figure 11: Plot of ratios between diameter in kilometers and rim height in meters for our fresh, floor-fractured, and degraded crater populations.

DISCUSSION

We found that the sets of parameters that showed the greatest amount of differentiation of floor-fractured craters from the fresh and degraded craters all included the depth parameter (figures 8, 9, 10). This is because the depths of floor-fractured craters were the only parameters that were significantly affected as a result of their period of magmatic intrusion.

The plotted ratios that showed the least observed separation of floor-fractured craters from the other crater types were all the parameter combinations that did not include a measure of depth (figures 11 and 12). This further determines that the differentiation is reflected by the igneous swelling causing reduction of crater depths that is more profound than shallowing due to ejecta fill.

In the future, a clearer understanding of measuring rim flank and rim height may improve the precision and accuracy of the results. Rim flank and height dimensions on craters are far less defined as diameter or depth. It was often a very qualitative process because the locations of breaks in slope for many craters are ambiguous, especially in older, more degraded craters with diminished rims. Many craters in our sample group of degraded and floor-fractured craters displayed total loss of their rims and therefore could not be measured accurately. Consequently those craters were not used to analyze rim parameters.

CONCLUSION

Ratioed parameters of crater measurements can show observed separation between fresh, degraded, and floor-fractured craters when plotted. Sets of crater dimension that have a component of depth, show some differentiation of floor-fractured craters from the other crater type reflective of their igneous modification.

In relation to NASA's Strategic Goal 2: understanding the Earth and the universe, which we live in, and NASA's Objective 2.2.1: understanding physical processes of the space environment, we used ratios of crater dimensions as a tool to identify if a crater is fresh floor-fractured or degraded in terms of their modification processes.

REFERENCES

Pike R.J (1976) Crater Dimensions from Apollo Data and Supplemental Sources. *The Moon* **15**, 473-474.

Schutz P.H. (1976) Floor-Fratured Lunar Craters. *The Moon* **15**, 241s.

EDUCATION IN 3 DIMENSIONS: USING INTERACTIVE SPHERICAL PROJECTION PRESENTATIONS TO TEACH ABOUT THE MOON

Brian P. James
School of Ocean and Earth Science and Technology
University of Hawai'i at Mānoa
Honolulu, HI 96822

ABSTRACT

NASA lists two of their current Strategic Goals as expanding our scientific understanding of the universe and sharing NASA's current mission with the public, educators, and students. This project aimed at taking the most recent data from the Lunar Reconnaissance Orbiter (LRO) and converting it into a format that is viewable on the Magic Planet and Science on a Sphere (SoS) projection systems. These spherical projection displays offer a unique way to view planetary and lunar data in 3 dimensions without distorting the image. The LRO, currently in orbit around the Moon, is collecting the newest and most detailed lunar data, most of which is not available in the proper format for spherical displays. The data converted in this project was assembled into a narrated, interactive movie aimed at educating high school students on the history of the Moon and the possibilities for future lunar exploration. This movie utilizes the exciting display format of the Magic Planet and SoS along with audience interaction via iClickers to create a memorable, education experience. The converted images as well as the completed movie will be made publicly available for educational use worldwide wherever the spherical displays are located.

INTRODUCTION

This project was created with the two key goals of expanding the database of lunar images available for spherical projectors, and utilizing those images to create an interactive educational presentation for display on those same projection systems. These spherical projectors offer a unique and memorable way to view objects in our solar system in 3-dimensions without distortion. There are two different display systems currently in common usage. The Science on a Sphere is the larger of the two. It is almost 6 feet in diameter and is a permanent installation, typically in museums, planetariums and universities. The Magic Planet (Fig. 1) is a smaller, portable spherical projector and was the focus of our project due to its availability and widespread usage in classrooms worldwide. Presentations between the systems are compatible since both display images with the same aspect ratio. Therefore, the images and slides created for one spherical projection system can be used on either the SoS or Magic Planet. With hundreds of these systems around the world, this means that the information we compiled is able to be shared on a global scale.



Fig. 1 Magic Planet spherical display projector.

Our data for this project was gathered by the Lunar Reconnaissance Orbiter. Prior to the LRO mission, the most recent lunar data was from Clementine, which completed its two month mapping mission in 1994. At the time, the images it sent back were astonishing in their detail. The high-resolution camera on-board was able to take photos with a resolution of 7 meters per pixel (Grayzeck, 2012). But as technology progressed, it became apparent that much better data could be gathered. The LRO, currently in orbit around the Moon, is continuously collecting the highest quality data. The images and data it sends back to Earth are a vast improvement over previous missions. The LRO's high-resolution camera can image the lunar surface at just 0.5 meters per pixel (MEM-TEK, 2012). This 14x increase in Resolution allows the Moon to be mapped in greater detail than ever before.

With 7 different instruments on-board (Fig. 2), the LRO is able to search for water ice, measure the surface slope and roughness as well as surface illumination, take high-resolution photographs, detect for radiation, and explore the chemical composition of lunar rocks. For our project, we focused on all of these criteria, with the exception of radiation, to produce maps and images for display on the SoS and Magic Planet systems. The raw data from LRO was converted to a compatible format using image editing software. The Magic Planet and SoS online communities both have a publicly shared database of image files available for display on

the projectors, with a noticeable lack of lunar data. Currently there are only two images of the moon available on these sites, and both date to the Clementine mission of 1994. The first stage of the project involved expanding this public database with our most recent LRO image files.

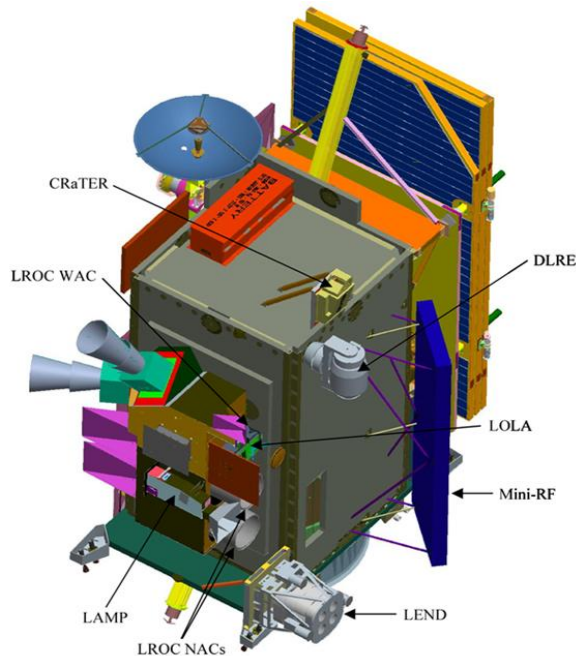


Fig. 2 LRO module with installed instruments labeled. [NASA]

The second part of our project was to create an interactive presentation that could be uploaded to the public sites as well. The movie uses images and animations with an overlaid audio track to teach about the Moon's origins, highlight the LRO mission and the latest data it is currently gathering, and to explore how this data helps NASA to plan for future lunar exploration. The projection systems are able to play animations and movies by converting a sequence of images into smaller .dds format files. These smaller files increase image load speeds and are then displayed at 30 frames per second to produce a seamless animation. The Magic Planet

software utilizes a script file to call on the sequence of audio tracks and image files, and link them together into a continuous movie. The interactive portion of the presentation was achieved through the use of iClickers. From the outset of our project, audience interaction was deemed a major priority. The spherical screens of the Magic Planet and SoS offer a unique way of viewing the lunar data, but as with any educational film, the content can become mundane to some. The interactivity element engages the audience and increases their retention and understanding of the material by creating fun quizzes where they can compare their results to others. The hand-held clickers feature five buttons that allow the audience to respond to questions from the presenter in real-time. Software for the clickers then allows the presenter to display results of the audience survey to show the popular votes or questions that the audience has chosen. This interactivity adds an additional stimulus to the presentation, making the information displayed more fun and memorable.

METHODS

The first step in the project was to convert images and data obtained by the LRO. The native format and resolution of the LRO data are not compatible with the Magic Planet projectors. ENVI, a mapping program, was used to resize the images and save them as .png image files in a 2:1 ratio. The projectors require this perfect 2:1 ration of image width to height in order to properly wrap the image around the spherical screen. When viewed in 2-dimensions, these images show intense distortion at the poles, but are distortion-free when projected in 3-D (Fig. 3). The ENVI software also enabled us to pinpoint locations on the images using the lunar coordinate system. Our team converted lunar data on illumination, surface roughness and slope, as well as the distribution of frozen water ice, titanium oxides, hydrogen, and helium. As all of us on the project were new to the ENVI program, it was easiest to use ENVI to resize the images and then do all image and color manipulation in Photoshop, with the end result being the same.

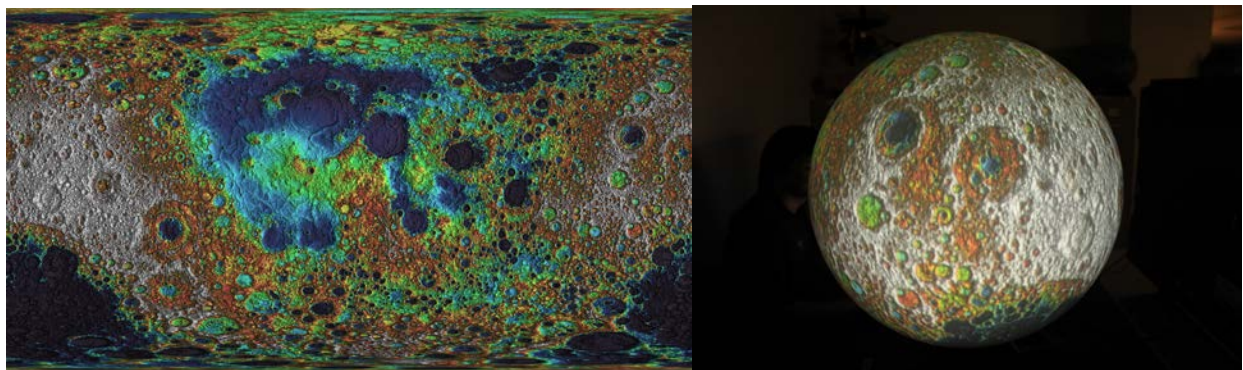


Fig. 3 Left frame shows image with distortion at the poles. Right frame shows the same image displayed on the Magic Planet with no distortion.

With all image files converted, the next step was to organize them into a cohesive movie. The Magic Planet display software uses an .xml script file to call each individual image or audio track in order. The script file allows control over image duration, frames per second, image rotation, animation sequences, and many other playback options. In order to make the movie more dynamic and interesting, intentional use was made of rotating the images, with preference

for animations over static images. The spherical screen of the Magic Planet is perfectly suited for rotation of the lunar data images. Latitude and longitude coordinates were specified in the script to rotate the image to key points on the maps. Animations were created in both Final Cut Pro and Photoshop. To import the animations into the Magic Planet, they were converted into a series of .jpg image files which were then further compressed into smaller .dds files. These small .dds images then played at a rate of 30 frames per second to produce a fluid animation on the spherical screen. Due to the heavy distortion at the poles of the projector sphere, most animations were created to be displayed in the equatorial region. The .dds files for each animation were stored in their own folder, and the folder itself was called by the script, initiating the animation sequence. For still images and audio files, the script called the file directly. Most image files used were obtained from NASA web sites by permission or from other public use image databases. A voice-over narration for the movie was recorded in Final Cut Pro. This narration was timed to coincide with the movie slides and provided the information that was presented in the movie. This narration was coupled with classical background music to create the final audio file.

Audience interaction was accomplished by the use of iClickers. These hand-held devices allow the audience to vote in real-time on questions proposed by the presenter. A short quiz was presented to the audience before the movie, asking questions about the Moon. The movie then gave information that answered those questions. It focused on the origin of the Moon and the data being gathered by the LRO mission. The initial third of the movie covered the early stages of the solar system and the formation of the moon. The second portion highlighted the LRO mission and the data it is currently gathering. The movie finished with an analysis of three different possible lunar base sites, analyzing the resources available at each and the drawbacks involved with each location. The movie concluded with a rotating image showing the contrast in detail between the Clementine data and the newest LRO data. The presentation continued by asking the audience the same questions from before the movie. The results from both “quizzes” were then shown on screen to allow the audience to see how their answers compared to others and how the results improved. Additionally, the audience was asked to consider all the criteria presented in the movie to choose the best site for a future lunar base.

RESULTS

Over 20 new maps and images were converted in our project for display on the Magic Planet and SoS systems. They cover a wide range of data being obtained by the LRO. Not all of the converted files were used in the presentation, with a total of 9 making it into the final cut. Due to slow processing speeds of the laptop with the Magic Planet display software, some of the more processor intensive animations had to be removed from the movie. The interactive movie was shown at the Hawai‘i Space Grant Consortium presentation symposium on April 28, 2012. The presentation met with enthusiastic reviews and support. Most audience members were seeing the Magic Planet for the first time and its unique display format immediately drew their attention. Additionally, the audience of mostly adults and college students took great joy in being able to be part of the presentation through the use of the iClickers. This bodes well since the target audience for the movie is a younger junior high or high school level group. The comparison of answers before and after the movie showed that the interactive format worked well, with the audience learning and retaining the information presented (Fig. 4). Showing the

presentation to a wider audience exposed some unseen flaws in the film, with a few slides lacking in-depth narration of the material being shown. Last minute difficulties resulted in the audio track being played simultaneously with the movie rather than being called by the script. This will have to be remedied before the movie is able to be presented on other Magic Planet displays.

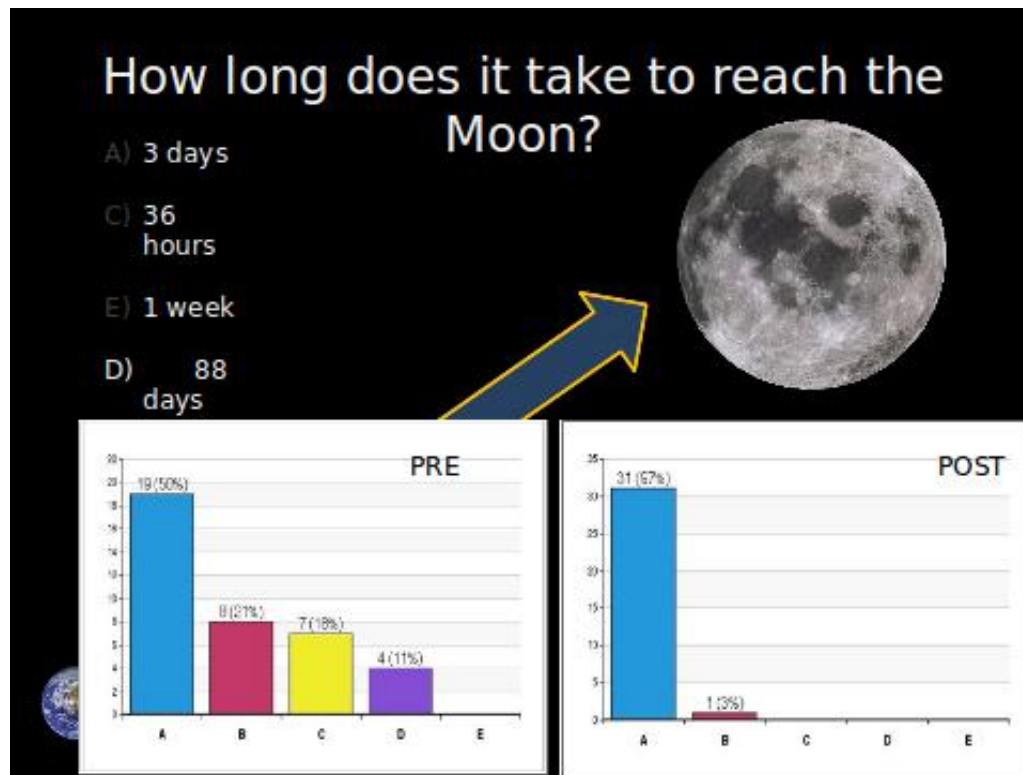


Fig. 4 Bar graphs showing before and after quiz results. The correct answer is A.

CONCLUSIONS

With over 20 images converted from LRO data, our project has greatly increased the number and quality of the images available for these spherical projectors. The images converted represent the most recent lunar data and are a great improvement on the Clementine data from 1994 that is currently available online for these projection systems. As predicted, the Magic Planet proved to be a perfect display system for this newest lunar data. The spherical format displays the lunar surface without distortion and offers a unique and engaging way to attract the audience's attention. The iClicker interaction allowed for immediate feedback to highlight what information was being learned by the audience and created another level of involvement for the viewer. A few minor fixes are necessary before the movie can be uploaded as a finished project, the most noticeable of which is the timing of the audio files within the Magic Planet script. This two semester long project was designed to meet two of NASA's Strategic Goals; to expand scientific understanding of our universe, and to share NASA with the public, educators, and students to provide opportunities to participate in NASA's mission and to foster innovation (Smith, 2012). These goals were both attained, and the information presented about one of NASA's most current missions was met with enthusiasm and great interest.

ACKNOWLEDGEMENTS

I would like to thank first and foremost Dr. Sarah Bean Sherman. She served as my mentor and advisor, and her dedication to making education memorable and exciting was the driving force behind this project. Thanks also go out to Korie Lum and Collin Au. Korie's expertise in Photoshop and Final Cut Pro made the movie images and animations far exceed what I would have been able to accomplish, lending a professional look to the finished presentation. Collin was our programming guru, revealing by trial and error the intricacies of the Magic Planet script language. And lastly, thanks to all those at the Hawai'i Space Grant Consortium for allowing me this opportunity to work first-hand with data at the forefront of NASA's mission objectives.

REFERENCES

- “Additional information about the LRO NAC images.” MEM-TEK. 2012. Web. 13 Jun. 2012
<http://apollo.mem-tek.com/LRO_NAC_Images_additional_info.html>
- Grayzeck, Ed. *Clementine High-Resolution Camera (HIRES)*. v. 4.0.20, National Space Science Data Center. 14 May. 2012. Web. 13 June. 2012.
<<http://nssdc.gsfc.nasa.gov/nmc/masterCatalog.do?sc=1994-004A&ex=06>>.
- Smith, Yvette. *Budget Documents, Strategic Plans and Performance Reports*. NASA. 13 Jun. 2012. Web. 13 Jun. 2012.
<http://www.nasa.gov/pdf/488471main_2011_Strategic_Goals.pdf>

COTS ADAPTABLE MODULE FOR ATTITUDE DETERMINATION IN CUBESATS

Tristan C. J. E. Martinez
College of Engineering
University of Hawai'i at Mānoa
Honolulu, HI 96822

ABSTRACT

The goal of this research proposal is to develop an inexpensive sun tracker platform and attitude sensor that can be used to test cubesats. Cubesats are satellites the size of a small cube of 10 x 10 x 10 cm. The design for this inexpensive platform and attitude sensor will be shared publicly through the Comprehensive Open-architecture Space Mission Operation System (COSMOS) enabling other institutions to develop their own space mission programs. Space rated sensors do not come cheap. For an educational institution wishing to incorporate space missions into their program, affording these types of sensors can be impractical given that the cost of the sensor is much greater than the cost of materials to construct the satellite. The University of Hawai'i is one such institution capable of designing, developing, and planning to launch cubesats in the near future.

INTRODUCTION

The University of Hawai'i has the capability of developing its own satellites and is also developing the capability of launching them into orbit through the efforts of the Hawai'i Space Flight Laboratory (HSFL) in collaboration with other entities. In order to run a space program, it is necessary to have the supporting infrastructure for the development of spacecraft. From this requirement, the Comprehensive Open-architecture Space Mission Operation System (COSMOS) was created in order to provide organizations with limited resources access to hardware and software tools to leverage their spacecraft development and mission operations efforts. These tools enable organizations to conduct their own space operations with limited funding.

Before satellites are ready to be launched into orbit, extensive testing is required to ensure proper operation of satellite components. Satellites are often outfitted with critical payloads tasked with experimental data collection. These instruments often require absolute attitude or information about the orientation of the satellite to effectively retrieve meaningful data. There are several methods for attitude determination in satellites. Most of which require very expensive hardware. Developing a module to determine absolute attitude using commercial-off-the-shelf (COTS) hardware would enable COSMOS and HSFL to keep in line with one of their primary objectives of providing fully functional hardware and software to operate a space program for low startup cost. In essence, HSFL would greatly benefit from having an inexpensive attitude sensor to test their cubesats with.

Satellite sun sensors use photo-diodes or photo-resistors as their main component. These devices output current or voltage proportional to the angle of incidence of light. Their highest reading will occur when the incident angle of light is perpendicular to the face of the device. As the incident angle changes, then so does the voltage or current output. This is the basic principle which sun sensors rely on for attitude determination. Most sensors used in satellite applications use the slit or pinhole method shown in Figure 1.

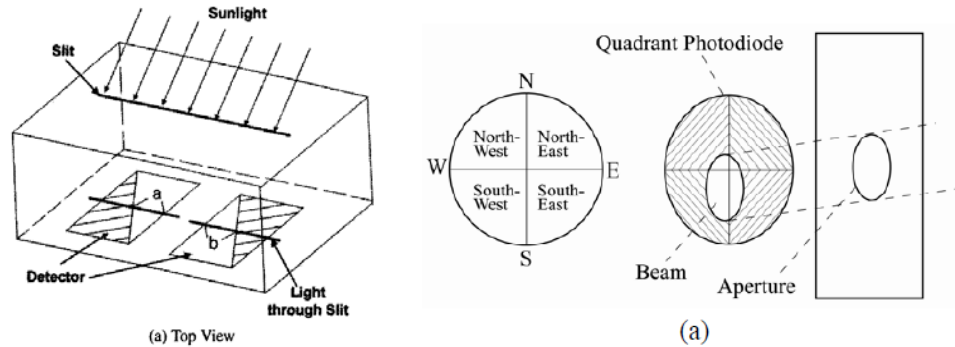


Figure 1: Pinhole and slit sun sensors

As the sun's light enters a container either through a slit or pinhole, a beam of light is cast down on an array of photo-resistors or photo-diodes. Depending on where the light is shown down on the array of photo sensitive devices, the angle to the sun can be calculated. In addition, these sensors are limited to two axes of determination. To fully determine the attitude of a spacecraft with respect to the sun, multiple sensors will need to be incorporated into the ADCS. Other sensors that could be included are additional sun sensors, magnetometers, earth horizon trackers or star trackers.

METHOD

During background research, a journal article was found detailing the use of the existing solar panels on a cube-sat as the sun sensor. This was perfect as we wanted to explore if the solar panels could be used for such a purpose. The article explained how three solar panels at perpendicular edges to each other could determine the sun position vector strictly from the current produced by the panels. A simulation of the response of having a solar panel array sun sensor would be needed to test its feasibility. A program was created using Processing and Arduino software that would collect the voltage readings from a solar panel into a text file using the Arduino Uno microcontroller. This program will be useful in collecting data automatically. Data would be collected over a range of solar panel positions with respect to the sun and used to construct a simulation for a solar panel array sun sensor. This simulation will allow us to design different configurations of panels by deriving a general equation for a multifaceted sun sensor. A simple three sided array of photo cells would be sufficient for a course sun sensor. However, a multifaceted sun sensor would give us better resolution for the sun position vector by effectively nesting three-sided photocell arrays on each other. This nesting scheme will give us multiple sun position vectors. By averaging these out, we can increase the accuracy of the sun sensor. As a first go around, test data was collected by hand for a single solar panel in sunlight. The following figure shows the voltage readings verses the azimuth and elevation of the solar panel. The data confirms the voltage output dependence of the solar panel to angle of incident light.

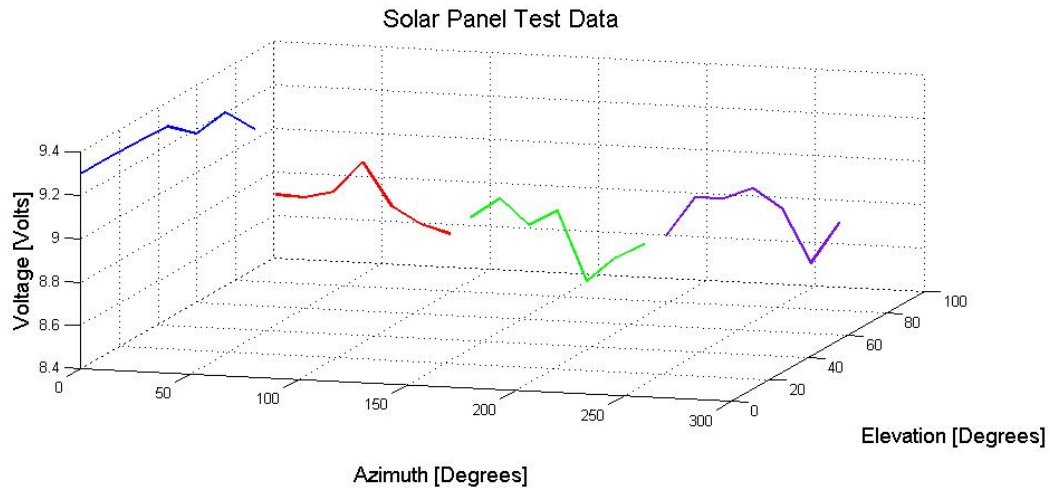


Figure 2: Voltage measurements for solar panel test

To automate the data collection process even further, the use of the satellite tracker mount would be involved. The satellite tracker mount was a senior mechanical engineering design project designed and built to track satellites through the sky autonomously. It has pan-tilt capabilities and can be controlled wirelessly. The tracker could be programmed to run through a predetermined set of positions very accurately in order to collect voltage readings from the sun sensor quickly.

MATERIALS

It was suggested that miniature photo cells should be considered in the design of the sun sensor. Two cheap miniature photo cells were chosen for testing that were relatively cheap and easily obtainable. They were the CPC1822 miniature photo cell and the BPW34 miniature photo cell pictured below, respectively.



Figure 3: Miniature photo cells considered.

The CPC1822 produces up to 4 volts and 50 microamps. The BPW34 produces up to 350 millivolts and 47 microamps. The figures show the electrical characteristics of the photo cells relative to incident light angle.

The Arduino Uno microcontroller was chosen to interface between the host computer and the photo cells because of its ease of use and availability. It is capable of analog-to-digital conversion with 10-bit resolution. The Uno is limited to only five A/D pins. This means at most the Uno can read from 5 photocells. For now, five photo cells are sufficient for a first prototype. The Arduino Mega has up to sixteen A/D pins if needed for a future prototype.

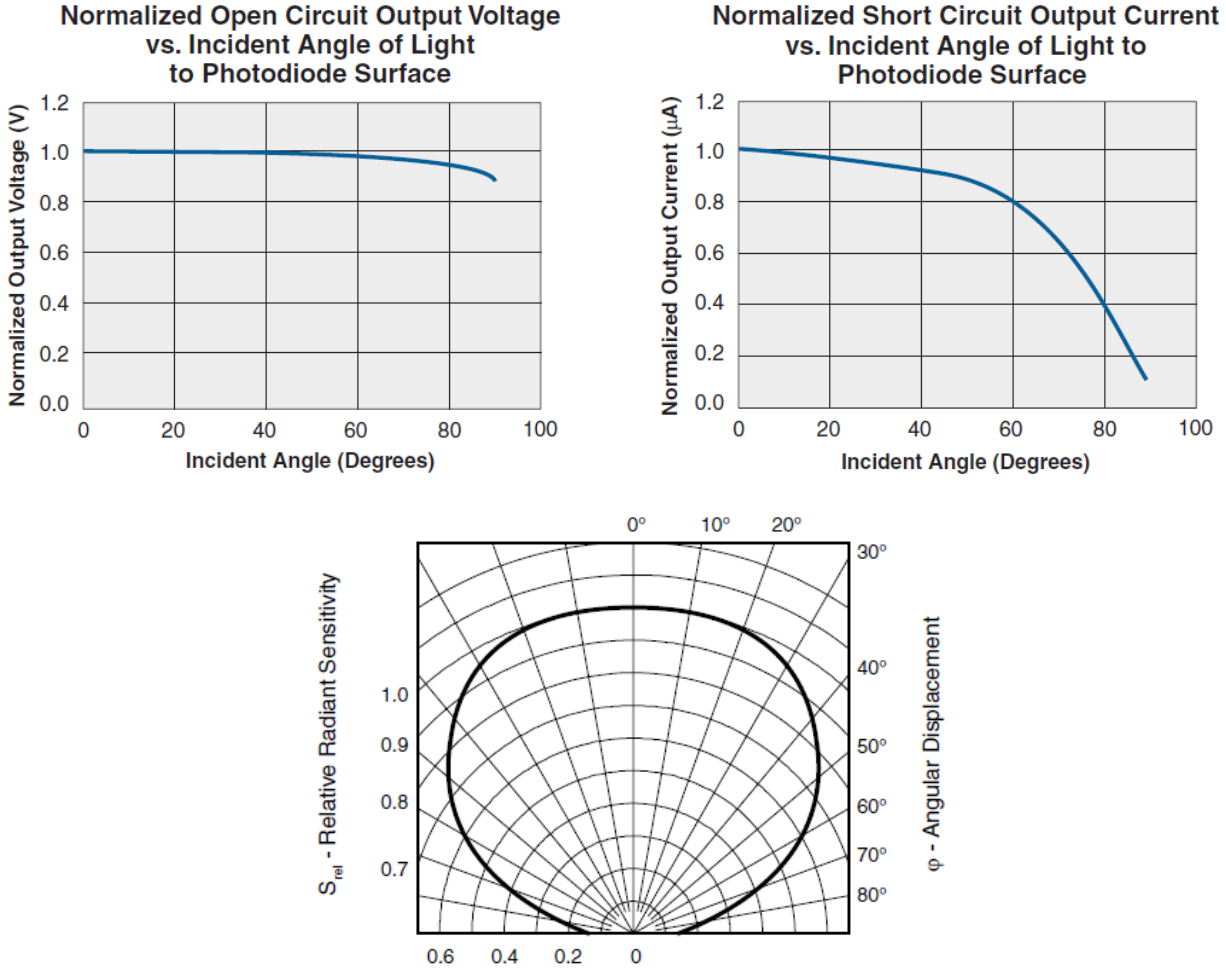


Figure 4: Electrical characteristic dependencies from incident light angles for photo cells.

TESTING

The CPC1822 was tested first with the Processing/Arduino data collection program. It was noticed that while covering the photo cell from the light the voltage reading expected should be around zero. The voltage readings from the Arduino would initially drop to zero but would then spike up and oscillate from zero and a higher voltage. In addition, when reading from multiple photo cells, there would be some linking between voltage readings. Meaning if one photocell was covered, either one or several others would respond to the change as well. It was first suggested that a simple pull-up resistor needed to be included because the circuit acted like an RLC circuit being under-damped. It was also speculated that the internal resistance of the photo cell was preventing the analog-to-digital converter in the Arduino from charging fully to read the correct voltage from the photocell. The internal resistance of the photo cell was measured to be 2.78 mega-Ohms. To address this, a voltage follower or buffer was included in the circuit setup. What it does is ensure that enough current is available for the A/D converter by using an operational amplifier. The buffer copies the voltage reading from the sensor and forces current to the copied output voltage. This setup would take care of the linking between photocells. Testing with only one buffered photo cell and the Arduino showed that the oscillations ceased. However, it was noticed that the readings were not very steady. The photo

cells were actually picking up AC voltage from the fluorescent lights in the lab. It was advised that the photocell circuit should contain some type of tunable filter to account for different lab testing conditions. A low-pass filter was chosen to clean out the noise. The low-pass filter would consist of an op-amp, capacitor and resistor. The capacitor would have a fixed capacitance but a trim-pot resistor would be used for variable resistance allowing for tuning the filter. The overall circuit would consist of a buffer and low-pass filter. A schematic of the circuit is shown.

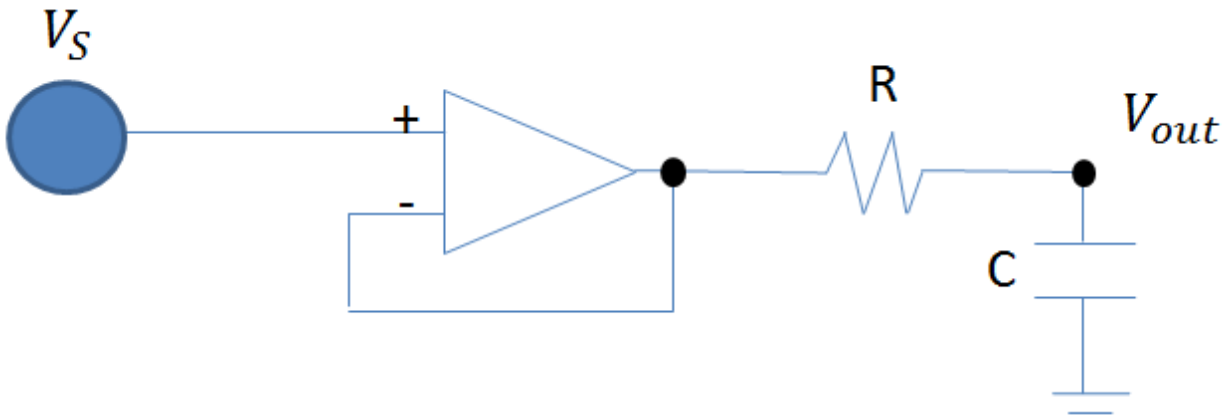


Figure 5: Buffer and Filter Circuit Schematic

The voltage source would be the photocell and be connected to the positive terminal of the op-amp. By tying together the negative input of the op-amp and the output, a voltage follower or buffer is created. The low-pass filter is the segment with the resistor, R , and capacitor, C . The buffered and filtered voltage is read as shown on the schematic, V_{out} . An oscilloscope was used to visually determine the effectiveness of the filter. The Figure 6 shows the buffered signal in pink and the buffered/filtered signal in yellow. From visual inspection, the noise in the signal is definitely reduced. Three photocells were rigged with buffers and filters, Figure 7.

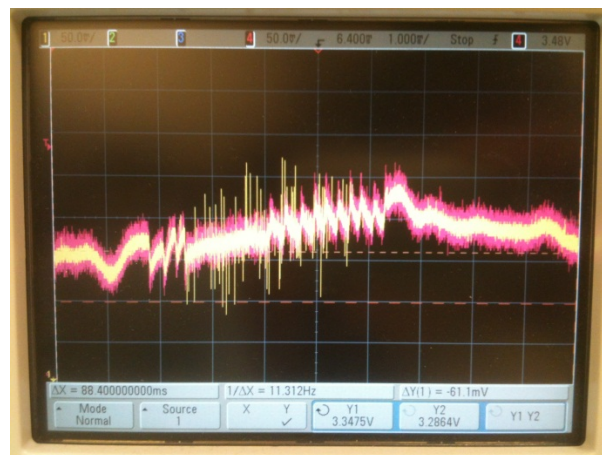


Figure 6: Buffered and filtered signals from photo cell voltage reading on oscilloscope.

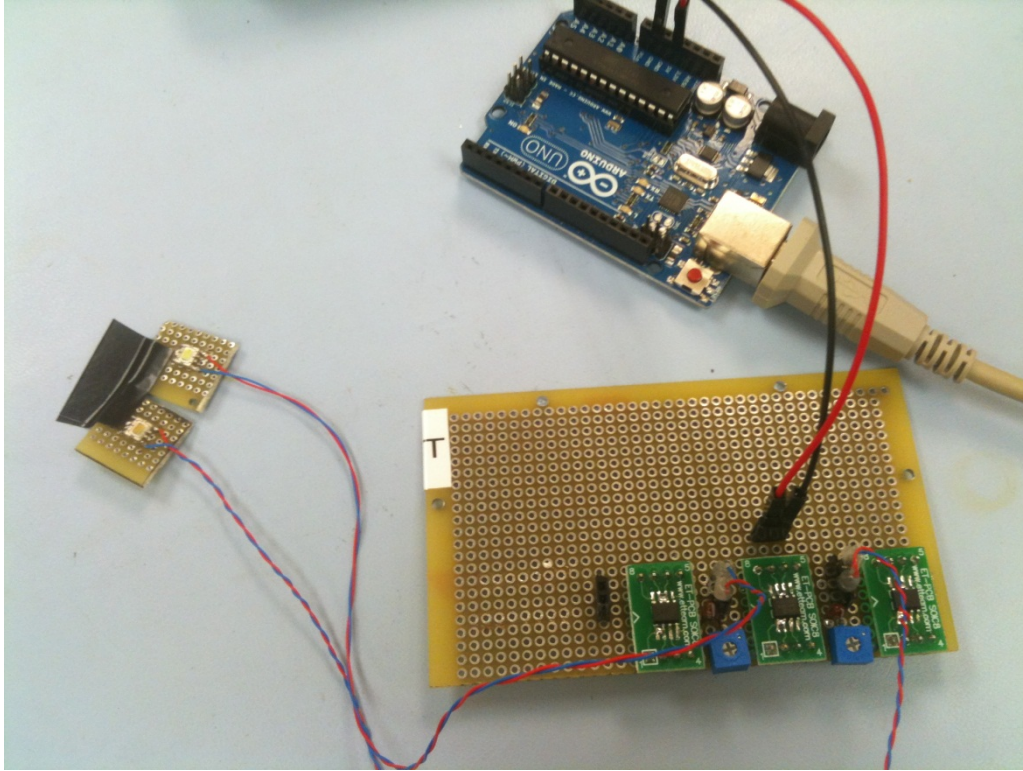


Figure 7: Circuit setup showing buffer/filter circuit for photo cells and Arduino.

CONCLUSION

To conclude, all the components are in place for data collection in order to produce a sun sensor simulation. For data collection, the photocells would need to be calibrated for the testing environment. The data collection Arduino would need to be mounted and integrated onto the satellite tracker mount. The next task would be to collect data from the 3-sided photo cell sun sensor and compare it to the light source position to determine the error associated with the photo cell sun sensor. Once errors are determined, simulations can be run to find the optimal nesting of 3-sided sun sensors to improve accuracy.

REFERENCES

- Chang, Y.K.; Kim, S.J.; Kim, S.O.; Moon, B.Y.; Oh, H.S.; Development of ultra-light 2-axes sun sensor for small satellite. *J. Astron. Space Sci.* **2005**, 22(1), 47-58.
- Chiang, C.M.; Chou, P.O.; Lee, C.Y.; Lin, C.F.; Sun Tracking Systems: A Review. *Sensors*. **2009**, 9, 3875-3980.

DESIGNING SPACE CRAFT MISSIONS TO NEOS

Reina M. Ojiri
Department of Mathematics
University of Hawai'i at Mānoa
Honolulu, HI 96822

ABSTRACT

This research involves the study of the trajectories of small Near-Earth Objects (NEO) in orbit around the earth. Our project consists of using computer simulations and an initial analysis of these trajectories provided by the Hawai'i Institute for Astronomy (IFA). We will be working within the two-dimensional case to identify NEOs based upon their proximity to the Earth-Moon equilibrium point L1 (EML1) and their velocities; using Matlab programming to validate our analysis. This initial analysis will allow for continued research to evaluate the three-dimensional case and to enable accurate simulations of space craft missions to these selected NEOs.

The primary purpose of this project will enable the simulation of space craft missions to rendezvous with NEOs that are temporarily captured by the Earth and Moon through gravitational interaction. The researchers at the IFA have numerically generated (and shared with us) over 16,000 simulated NEO trajectories, which will be the targets of our space missions. Based on computer simulations provided by the IFA, at any given time there are at least two or three small natural objects with a diameter anywhere from one to ten meters caught orbit around Earth. These NEOs usually stay in orbit around Earth for about one to six months. We will focus on the mathematical component consisting of guiding a spacecraft from an initial orbit (the geostationary orbit) to match the orbit of a NEO, known as an orbital transfer.

The National Aeronautics and Space Administration Authorization Act of 2008, Section 801 reaffirms the policy of surveying Near-Earth Asteroids and Comets as set forth in section 102(g) of the National Aeronautics and Space Act of 1958 (H.R. 6063). This Act focuses on the detection and survey of NEOs which directly relates to the serious and credible threat to human kind NEOs present, as an impact to Earth is one of the most costly natural disasters that can occur. Though this Authorization Act directly relates to national security, it has facilitated and increased interest in observing NEOs both locally and internationally. Thus in creating a program for the prevention or mitigation of impact catastrophes a comprehensive search for NEOs and a detailed analysis of their orbits and composition is needed.

In addition to national security, the data acquired from the NEOs will also expand our knowledge about the formation of the solar system, how such NEOs may have affected the Earth's atmosphere, climate, air quality, and surface changes, perhaps to the extent of identifying and investigating past and present habitable environments and life elsewhere in the solar system.

Therefore this project will focus on several of NASA's six Strategic Goals, particularly Strategic Sub-goals 3A, C, and D. Our research will aid in potential rendezvous which will allow for the study and possible retrieval of NEOs. Retrieval will enable us to expand our knowledge about the formation of the solar system, how NEOs and their interaction with Earth may have

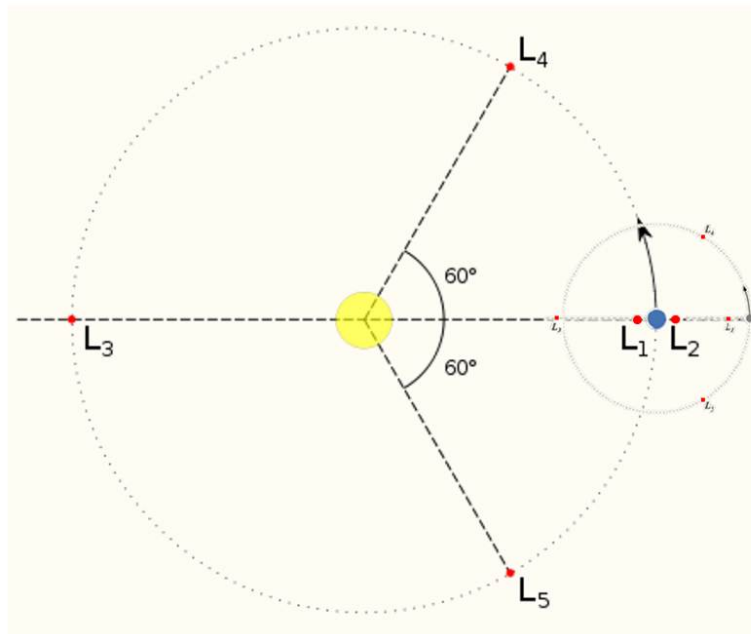
affected the Earth's atmosphere, climate, air quality, and surface changes in the past, or identifying and prompting future investigations of habitable environments and life elsewhere in the solar system.

The recent Hayabusa (Muses-C) mission a "Sample Return" mission, launched May 09, 2003 highly motivates our research. The main goals for the Hayabusa mission were the performance of an interstellar flight with newly developed ion engines, autonomous guidance and navigation, sample collection, and reentry into Earth's atmosphere. The targeted asteroid is the Itokawa, a stable Mars-crossing asteroid discovered in 1998 by the LINEAR project and officially named after Hideo Itokawa, a Japanese rocket scientist.

Though the main goals were technological in nature, one of the main successes of this mission was in its sample return. The minerals in the sample were identified as Ol (olivine); HPx (high-Ca pyroxene); Pl (plagioclase); Chm (chromite); and Tr (troilite) (Origin). Troilite is an iron sulfide mineral that is not normally found on earth but is abundant in meteorites originating from the Moon or Mars. The successful mineral collection from this asteroid has proven that a rendezvous is possible and that the information gained from possible capture and sample collection is valuable to our understanding of the universe.

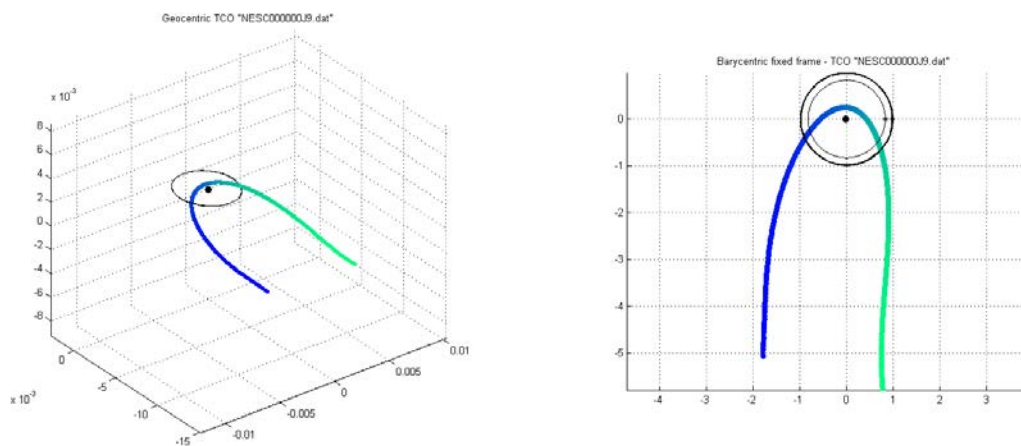
An initial analysis of the NEO trajectories by the IFA suggests that a NEO is usually captured somewhere near the Earth-Sun equilibrium point L1 (ESL1). Because of this, our initial project was to design an orbital transfer to the ESL1 point, and then modify our solution to transfer to the NEO as it passes near this point. However because the distance between the Earth and Sun is large, the precision needed to distinguish between the Earth and the ESL1 point was too great, making it difficult to accurately calculate and simulate an orbital transfer.

However after conducting an analysis of our own, it was discovered that many of the NEO trajectories also pass near the EML1 point. As the attempts to generate an orbital transfer from the Geostationary Orbit to the ESL1 point have not been successful, we have altered the objective of our project to utilize this EML1 point instead of the previously stated ESL1 point. This change was convenient for various reasons. First, the precision difficulties are alleviated since the distance between the Earth and Moon is significantly reduced than in the Earth-Sun case. Second, orbital transfers been completed to the EML1 point, thus this familiarity makes it a good candidate for our project. Finally, from a practical standpoint, the EML1 point is better than the ESL1, due to its familiarity and closeness to Earth.

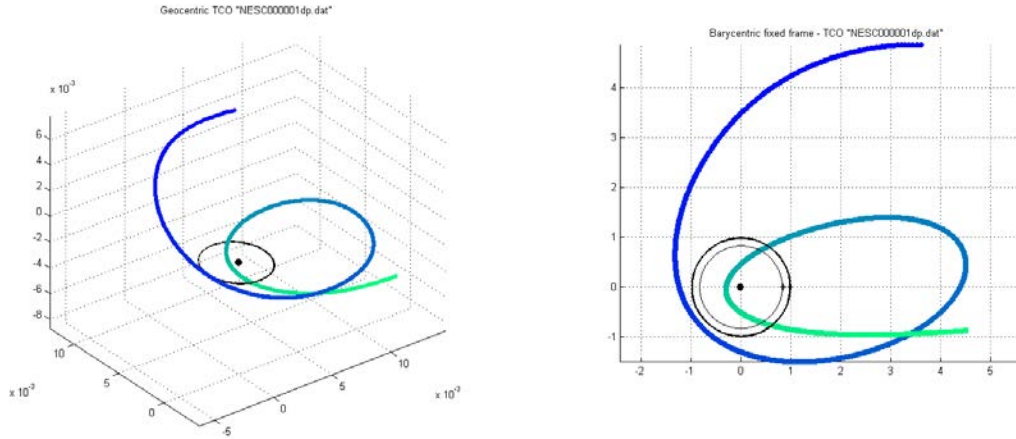


P.0 Lagrangian points of Earth-Sun and Earth-Moon.

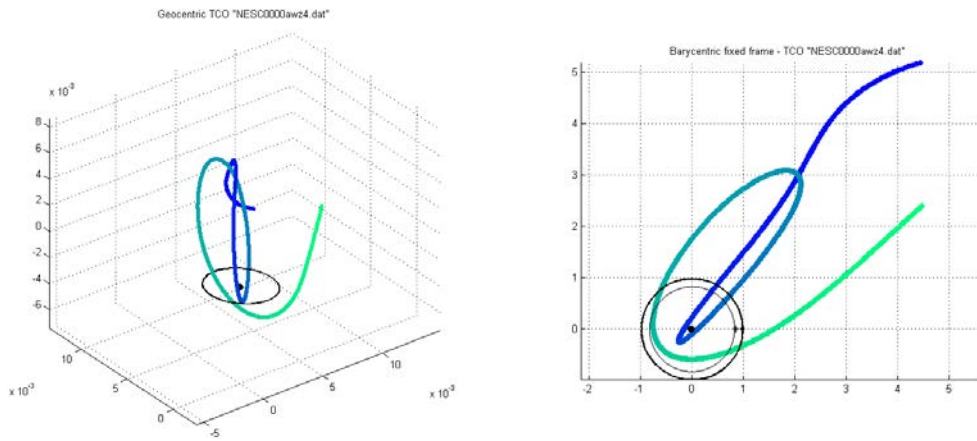
We will begin our work in the two-dimensional case, rather than three. Though the NEO trajectories are given to us in three-dimensions, we will project them to the xy -plane, ignoring the z -coordinate. Although these projections will no longer necessarily represent realistic trajectories, they will provide a good foundation for calculating optimal orbital transfers. From the foundations made within two-dimensional case, we will be able to look at NEO trajectories in three-dimensions which come near the EML1 point.



P.1 Depicts projection of generated orbit NESC000000J9 onto xy -plane.



P.2 Depicts projection of generated orbit NESC0000001 onto xy -plane.



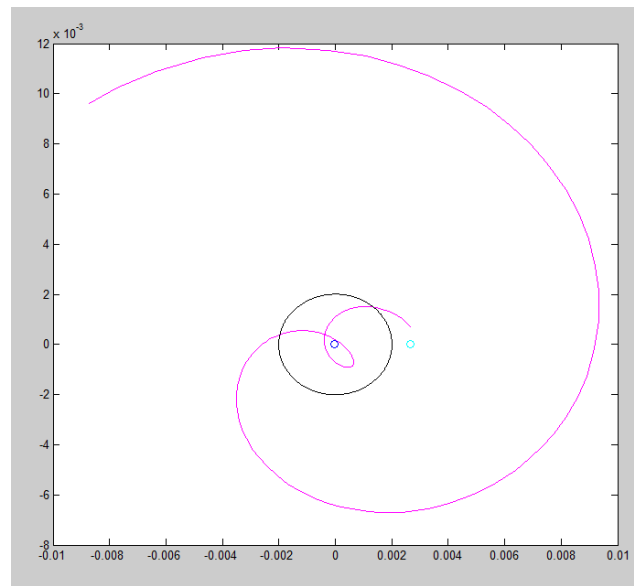
P.3 Depicts projection of generated orbit NESC0000awz4 onto xy -plane.

A recent paper analyzes “the number of revolutions by recording the longitudinal angle traversed during capture. The longitude is measured in a co-rotating ecliptic coordinate system where the line connecting the planet and the Sun forms a line of reference. At every timestep, the difference between the current and previous longitude to a counter which results in a negative angle for retrograde orbits (as seen from the north ecliptic pole) and a positive angle or prograde orbits (Granvik).”

Since we have begun our work with two-dimensions our approach to calculate the number of revolutions will be a slightly different method than that defined by Granvik. The data provided to us by the IFA begins at a set reference point for all trajectories. Thus using Matlab programming we took this initial point to create perpendicular planes at each timestep. Each subsequent timestep will then be analyzed; if the trajectory of our NEO passes through a previously made plane a counter of one will be assigned to the respective plane. Once one plane

has been traversed twice, with a counter of two, we have defined one revolution. This process is then repeated after each revolution.

Though working in two-dimensions causes greater variation and no longer represents realistic trajectories this method and analysis of the trajectories has helped us to gain a better understanding of the positioning of the NEOs with respect to the Earth and Moon and will help us recognize these discrepancies as we continue working with the third dimension. Working with Matlab has also allowed us to calculate the shortest distance from the EML1 during each revolution and the respective velocity of our NEO at that timestep. Thus we are able to create charts and visuals of our data as seen below.



P.4 Depicts projection of generated orbit NESC0000934f onto xy-plane.

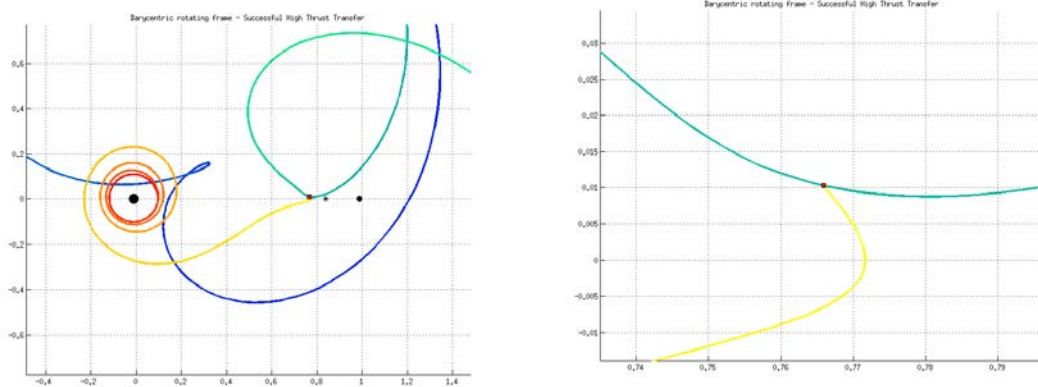
Name	Revolution No.	Minimum Distance (LD)	Velocity (LD/t)
NESC0000934f.dat	1	0.000887	-0.000506
	2	0.002410	0.000578

LD-Lunar Distance (Distance from the Earth to Moon)
t- nonstandard time unit (simplify calculations)

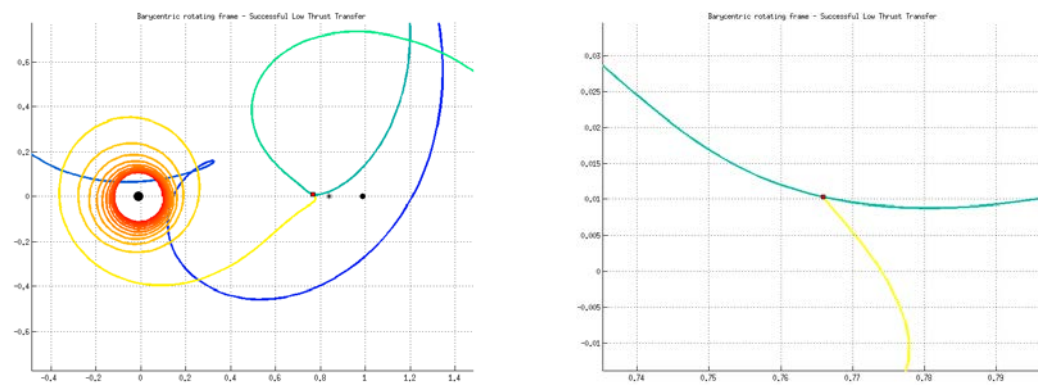
P.5 Depicts a chart for the number of calculated revolution, minimum distance for each revolution, and its relative velocities.

We then were able to filter and sort the data produced to find the trajectories that met specified requirements. Though we have not designated set criterion in selecting the best set of trajectories we will continue to review the data to see how the distances from the EML1 point and their velocities will affect our simulations.

This filtered and sorted data was used by Geoff Patterson, colleague and mentor, to conduct successful simulations using Hampath and CotCot programming. Some of his work, as seen below, depicts successful orbital transfers from the Geostationary orbit to the NEO itself to complete a successful rendezvous.



P.6 Depicts successful time optimal high-thrust orbital transfer (upper bound thrust set high)



P.7 Depicts successful time optimal low-thrust orbital transfer (upper bound thrust set low)

Since we have currently changed the method of the analysis of our project we have begun selecting and analyzing the best set of captured objects based upon their velocities and distance from the EML1 point. Though we have not completed a full analysis of the data within the two-dimensional model, once we have completed this we will continue our analysis to incorporate the three-dimensional model.

ACKNOWLEDGEMENTS

I would like to acknowledge Dr. Monique Chyba, Dr. Gautier Picot, Geoff Patterson, the Institute for Astronomy, and Hawai'i Space Grant Consortium for their assistance and mentoring.

REFERENCES

- "Asteroid and Comet Impact Hazards Spaceguard Survey." *NASA Ames Space Science Division*. PDF file.
- "Close-Up on the Asteroid Itokawa-The Achievements of Hayabusa's Scientific Observation." *JAXA: Japan Aerospace Exploration Agency*. 2007-2001. Web. 25 November 2011. http://www.jaxa.jp/article/special/hayabusa/_sp3/index_e.html
- Granvik, Mikael; Vaubaillon, Jeremie; and Jedicke, Robert. "The population of natural Earth satellites." 8 August 2011.
- "H.R.6063 National Aeronautics and Space Administration Authorization Act of 2008." *National Space Society*. 04 May 2009. Web. 25 October 2011. <http://www.nss.org/resources/library/planetarydefense/HR6063.html>.
- Picot, Gautier. "Shooting and Numerical Continuation Methods for Computing Time-Minimal and Energy-Minimal Trajectories in the Earth-Moon System Using Low Propulsion." *Discrete and Continuous Dynamical Systems Series B*. Volume 17, Number 1, January 2012: 245-269.
- "Three-Dimensional Structure of Hayabusa Samples: Origin and Evolution of Itokawa Regolith." *Science*. 26 August 2011. Vol 333 no. 6046 pp 1125-1128. Web. 25 November 2011. http://www.spring8.or.jp/en/news/_publications/press/_release/2011/110826_2

DEVELOPMENT OF A DEPLOYABLE 3U CUBESAT SOLAR PANEL ARRAY

Nathan K. Walsh
College of Engineering
University of Hawai'i at Mānoa
Honolulu, HI 96822

ABSTRACT

The primary goal of this project is to design, fabricate, and test a deployable solar array for a 3U CubeSat. The deployable mechanisms will adhere to the design restrictions of the standardized 3U CubeSat. The mechanisms will consider the capabilities of the Attitude Determination and Control System (ADCS) to ensure a smooth deployment. A crucial aspect of this project is based on the material selection and design to ensure safe operating throughout the life of the CubeSat. To achieve an effective design, structural analysis methods was applied in addition to failure criteria methods.

The design process was broken down into three main phases: Parameter definition, Design Concept, Design Analysis. Parameter Definition provides data and background research defining the parameter constraints. By defining all the working parameters an effective design envelope can be established so the mechanism does not interfere with other subsystems. The Design Concept, outlines the deployment design and the how the constraints were taken into consideration. The Design Analysis section provides data on the static analysis using finite element analysis.

The final hinge mechanism meets all design requirements with a safety factor greater than 2.5. From the integration to the structure to the deployment angle, the panel deployment system has been designed to meet a wide range space missions. The resulting design provides an efficient product that attaches to a 3U CubeSat with the ultimate goal of increasing power generation.

INTRODUCTION

CubeSats have eased the way for space accessibility and payload development. The primary goal of this project is to design, fabricate, and test a deployable solar array for a 3U CubeSat. Increasing the power generation capabilities of the CubeSat will help to provide on future missions. This project will provide a product that increases the potential of the 3U CubeSat through a more effective means of solar collection.

CubeSats are a class of pico-satellites typically deployed into low Earth orbit. The primary advantages of CubeSats are the low cost, standard infrastructure and quick launch capabilities.

CubeSats make space accessible to a larger audience that originally could not participate. Payload variance and development increases when platforms are easily available and cost

effective. Systems that previously required mating to a piggyback satellite have the option to utilize the CubeSat standard as the structure.

Standardization of the CubeSat makes it possible to create a highly flexible bus that serves as a multi-purpose testing platform. Through the use of CubeSats, academic institutions, the private industry, and government entities can test preliminary payloads to determine space worthiness. Standardization also enables quick exchange of payload modules, ease of interchangeability and lower cost due to volume production.

As microprocessors and computing technology continue to shrink in size, the power requirements for components remain steady. More data processing can therefore be done onboard prior to data transmission. Payload and data transmission capabilities are also limited if power generation is insufficient. Deployable Solar panels increases the capacity of power generation. Orientating the panels to face perpendicular to the sun significantly increases output power from the solar cells. By increasing the power generation on a CubeSat can increase its potential. Consequently, the power capacity of a CubeSat is as important as ever for a given CubeSat.

In the realm of satellites, solar panels are often the sole source of power generation. Expanded capacity of power generation significantly increases the capabilities of a CubeSat bus. Processing power, data transmission, and data collection potential are all dependent on the power capacity. With an increased power generation capacity, missions have the potential to accomplish more.

METHODS

Background Research

Background research was first conducted to ensure sufficient understanding of the project. The research explored existing panel deployment systems, deployment configurations and defined the deployment parameters for this project. The proposed deployment system shall be in accordance with CubeSat standards. CubeSats are strictly by Cubesat Design Specifications published by California Polytechnic State University [1].

Deployment angle and configuration varies one spacecraft to another depending on the power capacity required, orbit orientation, and payload. While deployment systems are available commercially, they are often custom systems and therefore expensive. They can also be difficult to integrate onto a generic off the shelf CubeSat because of the specialized mounting brackets.

With a better understanding of the design problem, the parameters and requirements of the project were then established. This included defining mass and volume budgets, and the deployment configuration. Figure 1 illustrates the physical dimensions required of 3U CanSats.

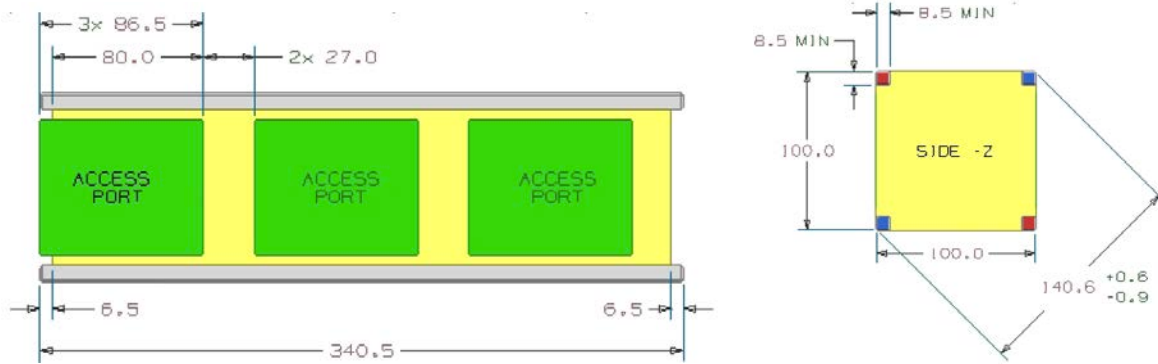


Figure 1: CubeSat dimensions as defined according to CDS [1]

Since the panel deployment configuration can vary from mission to mission, the deployment system will be designed to be versatile. This is accomplished by sizing the mechanism to fit along the short side of the CubeSat, while being deployable on all four sides. The hinge can be adapted to fit either face by changing the torsion spring. For the purposes of this project, the system will accommodate a deployment angle of 90 degrees.

Due to the possibility of jitter disturbing other subsystems or the payload, the design shall attempt to avoid introducing excessive jitter into the spacecraft. A complete understanding of what is expected of a deployment system and how it's integrated onto the bus is crucial to the success of the system and the overall success of the mission.

Conceptual Design

The Conceptual Design process began with brainstorming ideas and researching current designs that would satisfy all parameter requirements. Despite the wide variety of commercially available deployment systems, I was unable to find or configure one that fit the requirements for this project. Faced with designing a custom deployable, it took many attempts before a design emerged that fit all parameters.

There are many deployable systems that were reviewed. A rubric was created to list all the attributes and design features the deployable must meet. Some of the main attributes the deployment mechanism must have was light weight, low profile, simple movement and versatility. A versatile deployment design was priority for this project. A versatile design encompasses ease to adapt the system to various structure types, configurable deployment angles, and ease of integration.

A spring loaded hinge design satisfied the majority of the attributes. A hinge was chosen because of its simplicity, low profile, light weight, and versatility. The simple movement of a hinge eliminates the need for gears, linkages, or any complex motion. This design features a low profile and incorporates a custom torsion spring. The spring characteristics, including spring constant, are determined by the weight of the solar panel, weight of the hinge, and the torsion required keeping the panel stable when fully deployed.

A unique feature of this design allows for the parametric adjustment of the hinge geometry and spring configuration for the final deployment angle. The configuration shown

above deploys the array to a final angle of 90 degrees as defined by the project requirements. The material selected for the hinge is 6061 Aluminum. Aluminum is a durable material that has a high strength to weight ratio. This alloy is commonly used and machinable, making it ideal for use in prototyping.

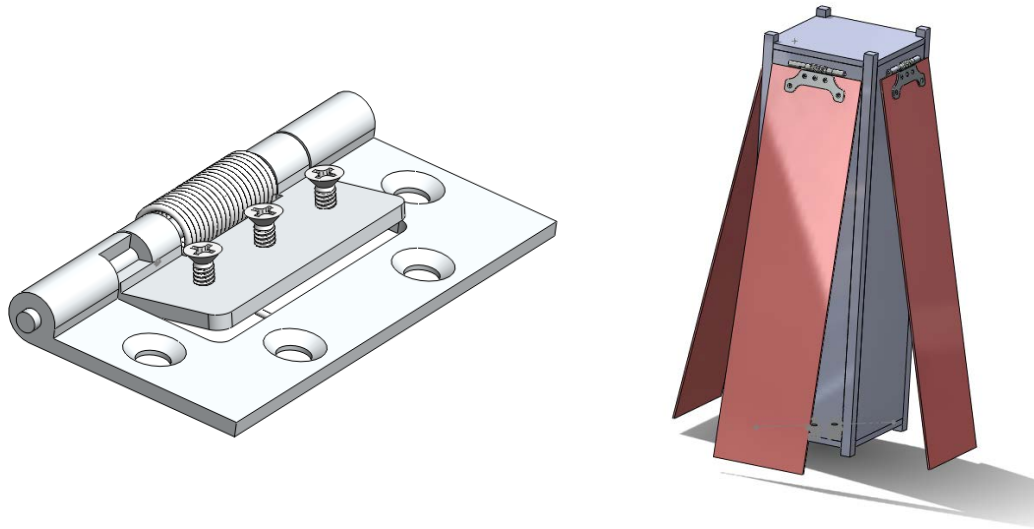


Figure 2: Left: Isometric view of the hinge. Right: Side profile cut away view of deployment hinge. The top bracket show above is intended to sandwich the panel together.

The other half of the array system is the release mechanism. The release mechanism is responsible for deploying the array from the initial launch configuration and is currently in the draft preliminary design phase. The current concept involves monofilament fishing line and nichrome wire. The panel will be secured in the launch phase using the fishing line. When the panel needs to be deployed, a current will be applied to the nichrome wire, causing it to heat up and cut through the fishing line. This releases the hinge-spring mechanism, effectively deploying the panel array. This type of release mechanism has been previously used in other CubeSats for a variety of deployables.

Design Analysis

Currently, static finite element analysis (FEA) is being employed to evaluate the design. FEA is a numerical method of evaluating how a component will react to loads and stresses. The FEA simulation tools packaged with SolidWorks are being used in this analysis.

Loading conditions for the solar panel were based off of the weight and dimensions for COTS 3U solar panels manufactured by Clyde Space (part number SP-L-S3U0016-CS) [2]. Additional factors considered in the analysis include the hinge material and torsion forces from the spring.

Figure 1 shows the stress gradient of the hinge at the final deployment angle. As shown, the greatest load would be on the material surrounding the contact faces of the hinge, thus creating the largest stress concentration. This is expected because it is where the torsion force

from the spring is applied. The maximum local stress is 97.9 MPa. The typical yield strength of 6061 aluminum is 276 MPa giving the component a safety factor greater than 2.5.

The material and thickness of the inner hinge is partially driven by the required fastener size and thread type that secures the panel to the hinge. The hinge must be thick enough to ensure that a sufficient number of threads are engaged. Fastener selection is in turn, driven by the required pullout load for the screw. However, thickness also affects the spring specification and overall profile. The material must not be too thick and overdesigned. The correct balance between the hinge thickness and the screw is essential for a reliable design. Highlighted in Figure 3 are the combinations that will satisfy the required loading and material thickness.

Diameter(mm)	Nominal Shank		Pitch Diameter		Thread	
	Diameter(mm)	Pitch	(mm)		Engagement(mm)	Ath (mm^2)
1.69418	2.1844	0.017857143	2.172801445		0.4064	0.005250854
1.69418	2.1844	0.017857143	2.172801445		0.635	0.008204459
1.69418	2.1844	0.017857143	2.172801445		0.8128	0.010501708
1.69418	2.1844	0.017857143	2.172801445		1.016	0.013127135
1.69418	2.1844	0.017857143	2.172801445		1.27	0.016408919
1.69418	2.1844	0.017857143	2.172801445		1.5748	0.020347059
1.69418	2.1844	0.017857143	2.172801445		1.5875	0.020511149
1.69418	2.1844	0.017857143	2.172801445		2.000000001	0.025840817
1.69418	2.1844	0.017857143	2.172801445		2.032	0.02625427
1.69418	2.1844	0.017857143	2.172801445		2.286	0.029536054
1.69418	2.1844	0.017857143	2.172801445		2.999999994	0.038761226
1.69418	2.1844	0.017857143	2.172801445		3.175	0.041022297

Figure 3: #2-56 Screw and hinge thickness matrix. The shaded region highlights the material with sufficient pull-out strength that will allow for the stripping of the screw rather than the hinge material.

$$A_{th} = 0.33 * p * d_p * L_e \quad [1]$$

Ath = shear area of threads

Le = Thread Engagement

p = Pitch

n = Threads per unit length

Dn = Nominal shank diameter

Dp = Pitch diameter

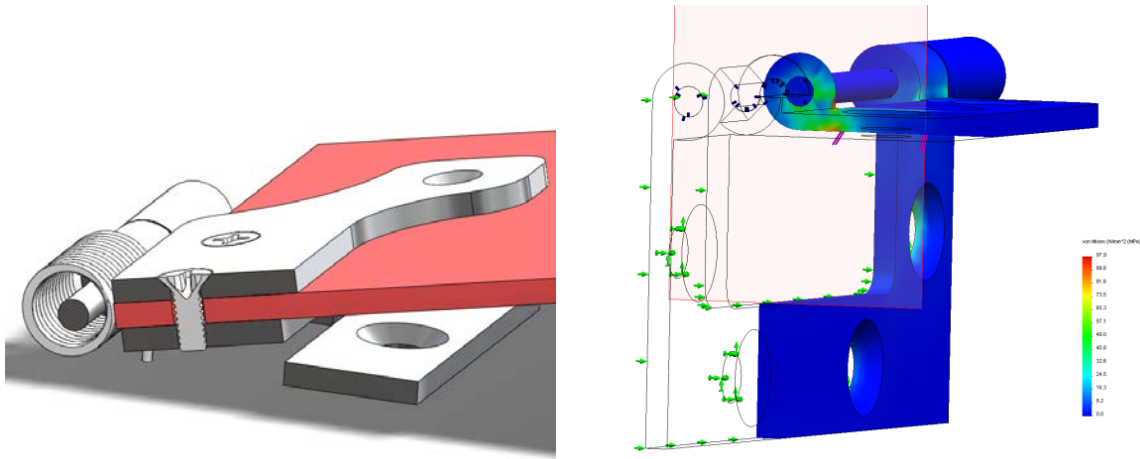


Figure 4: Left shows a cutaway view showing thread engagement. Right

Increasing the thread engagement of the screw allows for a larger shear area thus increasing the pull-out strength. Referencing Figure 3 and the estimated loading based on the Clyde panels a minimum thread engagement of 2 mm is required with a #2-56 UNC fastener. Analysis shows that three #2-56 UNC fasteners will be sufficient for a 2 mm thick inner hinge.

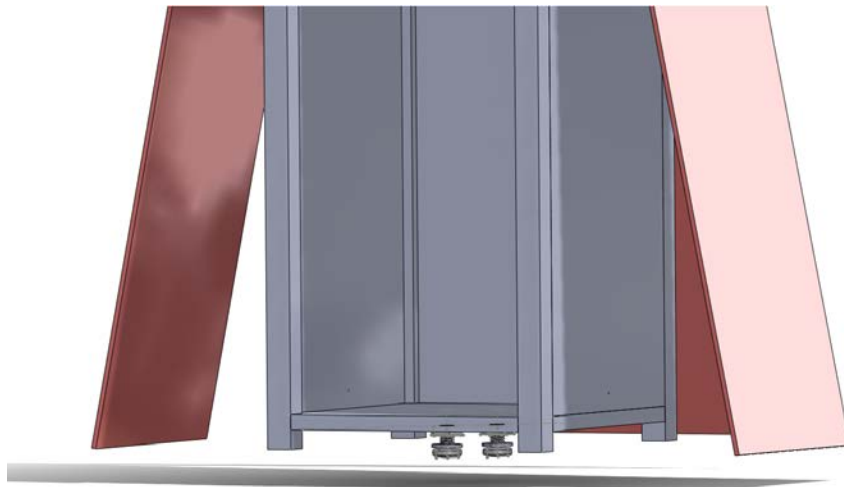


Figure 5: Release mechanism uses Nichrome burn wire and monofilament fishing line to deploy the panels

The panel release mechanism uses nichrome burn wire and monofilament line to deploy the panels. Nichrome wire is a reliable, non-mechanical method of releasing deployments. Nichrome wire is a tested space standard for small scale deployments. The nichrome wire is placed across the fishing line, providing a slight contact stress for thermal conductivity. When a current is applied to the nichrome it heats up burning trough the fishing line triggering the deployment. The advantages of using a burn wire for deployment eliminates the possibility of a

freeze up of a mechanical moving part such as a motor or a spring loaded mechanism. Nichrome wire heats up quickly and effectively. Additional analysis of current draw must be researched to ensure proper integration to the satellite's electrical system. Optimal sizing must be taken into consideration as well. The wire must be thick enough to be mechanically strong, but thin enough to reduce current draw. The most reliable method of fastening nichrome is through mechanical crimps. For these connections vibration and strength testing will need to be conducted.

CONCLUSION

This report provides the design for a panel deployment system, encompassing the deployment hinge and burn wire release mechanism. The final design meets all the design parameters required of a 3U CubeSat in accordance with the CubeSat Design Specifications [1]. Major attributes taken into consideration include: stand-off height, light weight, simple mechanical motion and adjustable deployment angles. Static testing shows the design exceeds the loading conditions with a safety factor of 2.5. Additional work still needs to be done to continue the detailed analysis of the hinge under dynamic loading.

ACKNOWLEDGEMENTS

I would like to say a huge, Mahalo to my mentor Lance Yoneshige for all of his patience and assistance in helping me with the modeling and analysis tools.

I must thank the Hawai'i Space Grant Consortium for allowing me to perform this design project. It was a great experience to be able to get involved in engineering design as an undergraduate student.

Finally I must thank Mars and the entire HSGC office staff for their patience and assistance. It was not always easy to meet deadlines and requirements during the semester when I had many other obligations. Their help with the logistical portion of the fellowship is greatly appreciated.

REFERENCES

- [1] California Polytechnic State University, CubeSat Design Specifications (CDS) (2009), Rev. 12, p. 20.
- [2] Clyde Space Retrieved 05/05/2012, from <http://www.clyde-space.com/documents/2625> p. 3.
- [3] Barrett, *Fastener Design Manual*, NASA RP-1228, (1990) p. 21.

AIR BEARING ADCS TEST BED

Daniel E. Wukelic
College of Engineering
University of Hawai'i at Mānoa
Honolulu, HI 96822

ABSTRACT

The Hawai'i Space Flight Laboratory (HSFL) designs, tests and builds small satellites. To properly test satellites, a diverse testing facility is required. In building up their testing facility infrastructure, HSFL acquired an air bearing to test Attitude Determination and Control Subsystems (ADCS). The focus of this work was to develop a satellite test bed interface for this air bearing. The first step was to research components of the ADCS and design a test bed to meet any requirements of testing. The second step was to build a prototype in order to prove the concepts used in the test bed. Finally, the full-sized test bed was built, tested and is now ready for use in the HSFL testing facilities.

INTRODUCTION

The Hawai'i Space Flight Laboratory is an entity located on campus at the University of Hawai'i at Manoa dedicated to advancing the research and development of satellites in Hawai'i. They already have a large infrastructure in place aiding in the design, manufacturing, testing and launching of small satellites. HSFL can test the structural integrity of a satellite or the strength of fasteners using their large electromagnetic vibration table. They can also test the Thermal Control Subsystem (TCS) of a satellite using an Intlvac thermal vacuum test chamber capable of simulating environmental conditions encountered in a Low Earth Orbit (LEO). These integration and testing facilities are located in either standard rooms or clean rooms with 10,000 particles per cubic meter of air. Despite the dynamic infrastructure already in place, HSFL needs several more test beds to verify the other satellite subsystems.

Satellites have a tendency to tumble in space, which is undesirable for most missions. There are many disturbances, both spacecraft-induced and environmental, that contribute to the overall moment experienced by a satellite. For example, the sloshing of propellant in fuel tanks, the motion of a mechanism or thrust imbalances are spacecraft-induced, whereas atmospheric drag, solar radiation pressure, gravity gradients and magnetic field disturbances are considered environmental factors. The orientation of a satellite in space has an obvious effect on payload pointing and exposure, power generation, antenna pointing as well as thermal effects. In order to sense and adjust satellite orientation, satellites depend on the Attitude Determination and Control Subsystem (ADCS).

ADCS consists of two parts, sensors to determine the attitude of a satellite and devices to control the attitude. There are many different types of ADCS sensors. Sun sensors and star sensors gather light to provide an accurate assessment of the satellites orientation relative to the sun and stars. Magnetometers measure the magnetic field of the earth or the change in magnetic field to determine the orientation and motion of a satellite. Other sensors such as gyroscopes use

changes in inertial attitude to keep track of a satellite's orientation. These sensors are very interesting and still require much testing, however they are the focus of a different Space Grant Fellowship.

The focus of this fellowship is on the attitude control devices and developing a test bed to verify these devices. Depending on the altitude of a satellite's orbit, there are many different attitude control devices that can be used. Satellites below 1000 km can utilize magnetic torquer rods to align with the magnetic field of the earth. Above this altitude, satellites often depend on spin stabilization (Sellers). Flywheels use conservation of angular momentum principles to maintain stability or rotate a satellite as desired. Thrusters can also be used but generally are not practical for small satellites. Before launching a satellite, HSFL needs to be able to test and validate the attitude control devices on board. This creates a rather unique problem because attitude control occurs in all three axes in the frictionless environment of space. This means that the ADCS test bed must simulate these aspects of space as accurately as possible in order to properly test the attitude control devices.

Traditional bearings provide the necessary rotation for a test bed; however they involve a fair amount of contact between metal pieces that results in unwanted friction. In order to satisfy this need for a nearly frictionless apparatus, HSFL acquired a spherical air bearing. The spherical air bearing is able to rotate 360 degrees, tilt 45 degrees and support a 200 kg load. This apparatus consists of a pedestal, a bowl and the hemi-spherical bearing itself. High-pressure air from an air compressor comes out of valves in the bowl, creating a thin layer of air between the bowl and bearing. Figure 1 below shows the range of motion of the air bearing along with the gap between the bowl and bearing. The gap as illustrated has been exaggerated to be more visible. The actual separation is nearly imperceptible.

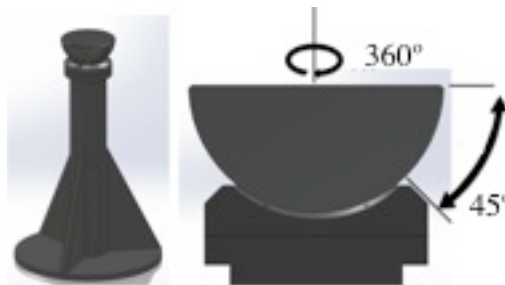


Figure 1: The entire air bearing (left) and a cross section of the bowl and bearing (right)

METHOD

Although the air bearing is a key acquisition in creating an ADCS test bed, it alone cannot satisfy all the requirements of the project. If a satellite or some of its components were mounted directly onto the air bearing, the assembly would most likely tip over and damage the test subject and/or the bearing. To fix this, an interface was needed between a satellite and the air bearing. This test bed must be able to host a variety of small satellites; therefore it must have a generic hole pattern to connect to any satellite. In addition, the air bearing is manufactured with specific mounting holes, so the apparatus must have matching attachment points.

While designing and building a small satellite, great care is taken in placing components to keep the satellite well balanced, however this is not always possible. As a result most satellites are not perfectly balanced, meaning that the center of mass is not located exactly at the geometric center of the satellite. Since an effort is usually made to minimize this error, it is assumed that the center of mass will be located within 20% of the satellite radius from the geometric center. Table 1 below shows the calculations done in order to determine the worst-case scenario center of mass location for various small satellites. Figure 2 defines the satellite body variables used in equations 1 through 4 below.

$$C_Z = \frac{1}{2} \text{height} \quad (1)$$

$$a = C_Z \times 20\% \quad (2)$$

$$b = a + C_Z \quad (3)$$

$$c = \frac{1}{2} \text{width} \times 20\% \quad (4)$$

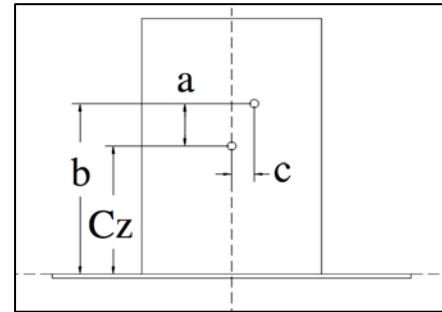


Figure 2: Satellite Layout

Satellite	Mass (kg)	Height (cm)	Width (cm)	Width Description	C_Z (cm)	a (cm)	b (cm)	c (cm)
CubeSat	1.33	10	10	square base	5	1	6	1
3U CubeSat	4	34.05	10	square base	17.03	3.41	20.40	1
HiakaSat	40	36.83	67.31	Circumscribed	18.42	3.68	22.10	6.73
HawaiiSat-1	85	73.66	67.31	Circumscribed	36.83	7.37	44.20	6.73

Table 1: Center of mass calculations for various satellites

When an unbalanced satellite is placed on the air bearing apparatus, the center of mass is not directly above the center of rotation, creating a moment that causes the assembly to tip over. Figure 4 below shows the unbalanced satellite placed on the air bearing apparatus along with the induced moment that causes a rotation of the assembly. In order to balance the assembly and prevent it from tipping over, a counterweight can be placed on the opposite side of the vertical axis. When the horizontal counterweight is located properly, the center of mass of the entire assembly, including the satellite, mounting plate and counterweight, will be aligned above the center of rotation. A vertical counterweight must also be used to position the center of mass of the assembly vertically on the center of rotation.

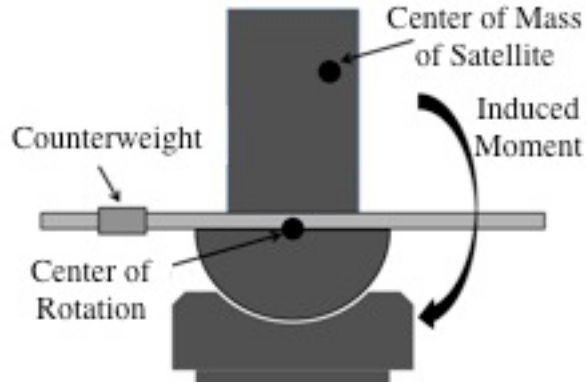


Figure 3: Satellite Air Bearing Assembly showing induced moment

The required weight and position of each counterweight can change dramatically dependent on the satellite. In order to accommodate a wide variety of small satellites, the test bed had to be highly adjustable in every dimension. Calculations were done to figure out the maximum distance that a given counterweight would have to be from the center of a satellite in order to balance the assembly. These calculations were taken into account while designing the test bed so that every small satellite being developed at HSFL could be tested.

The air bearing came with specifications for operation and maximum operating limits. In order to provide a safe apparatus, all of these factors had to be taken into account while designing the test bed. The most critical value for safe operation and to avoid ruining the air bearing was the maximum loading. While operating at 50 psi, the maximum loading according to the Nelson Air Corporation is roughly 200 kg. It can be assumed that the company built a safety factor into this value and that the air bearing can safely handle the maximum loading. Using this limit, a mass budget then had to be created, dictating certain aspects of the design. The largest satellite being developed at HSFL would be the limiting factor. Table 3 shows a mass budget for HawaiiSat-1, the large 85 kg satellite. The estimated mass of the test bed frame as calculated using SolidWorks was 35 kg. This left 80 kg for use as adjustable weights on the test bed.

Mass Budget	
Object	Mass (kg)
Test Bed	35
HawaiiSat-1	85
Adjustable Weights	80
Total	200

Table 2: Mass Budget for ADCS Test Bed

DESCRIPTION OF APPARATUS

With the general structure concept established, ideas had to be solidified and brought to life. The air bearing, test bed and several satellites were modeled using SolidWorks to create three-dimensional images of the apparatus. Figure 5 below shows the original design of the ADCS Test Bed, fully dimensioned and mounted on the air bearing with weights on each arm. The hole patterns and dimensions will be discussed in a later section.

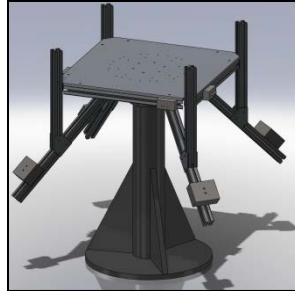


Figure 4: Design for ADCS Test Bed shown on air bearing

PROTOTYPE

Before moving forward and building the final model, mentors Lance Yoneshige and Miguel Nunes suggested that a prototype be made as proof of concept. If a scaled down prototype worked, then the full size test bed would also work. A half-sized prototype was then designed using SolidWorks and constructed from c-channel aluminum. This material is light and inexpensive, yet still strong enough to accomplish the required task. Since the prototype would be too small to fit on the air bearing, it was decided to use a standard metal bearing with 360 degree rotation but only about 20 degrees of tilt. Despite being somewhat inefficient, the metal bearing shown in Figure 6 would still be suitable for proof of concept testing.



Figure 5: Metal bearing (left), slots in arms (center) and prototype frame (right)

The prototype didn't need a top plate like the full sized test bed because no large satellites would be attached to it. Instead, a cross shape was used that provided structural support to the frame and also allowed mock satellites or test weight to be attached. Each arm had to be milled down the center (as seen in the center photo above) to serve as attachment points for the counterweights.

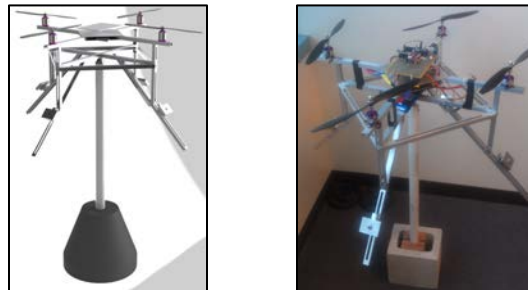


Figure 6: SolidWorks model (left), real prototype with quadcopter (right)

The first payload used to validate the concepts used on the prototype was a quadcopter being developed by mentor Miguel Nunes. The quadcopter is mostly symmetrical, but has several electrical components that place the center of mass away from its geometric center. By

carefully positioning the counterweights, the prototype with the quadcopter payload was successfully balanced. It is easy to tell when the system is balanced because when it is released, the system does not rotate by itself in any direction, no matter what orientation it is placed in. Figure 7 above shows the SolidWorks model of the quadcopter on the prototype along with the actual assembly.

FINAL DESIGN

As a commonly used metal in the aerospace industry, aluminum was selected as the building material. Aluminum is fairly strong, despite being less dense than most metals. This is appealing because it is possible to achieve a given strength while minimizing mass. Aluminum is also very easy to machine, and since there were many pieces to be made, it cut down on the manufacturing time. Aluminum is significantly easier to cut, drill and tap than steel and doesn't require special equipment. Finally, aluminum is resistant to destructive corrosion. This is especially important in Hawai'i because of the extremely humid environment where unprotected metal corrodes very quickly. It would be dangerous for both the satellite and the test bed operator if the apparatus suffered significant corrosion damage.

With a material chosen, the next step was to design the interface between the air bearing and a variety of satellites. In order to provide a solid base to connect satellites, test bed arms and mount on the air bearing, a half-inch aluminum plate was acquired from a local manufacturer. The plate was a 70 cm by 70 cm square, with the corners cut off. The air bearing has 6 threaded holes in a hexagonal shape with a 3 inch radius for mounting. Countersunk clearance holes with the same hexagonal pattern were centered on the plate to connect to the air bearing. More holes had to be drilled for various brackets and a very specific pattern was chosen for mounting satellites.

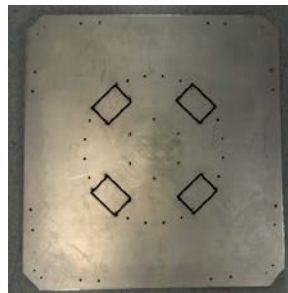


Figure 7: Top Plate of Test Bed with holes drilled

The release of a satellite from the launch vehicle is critical to mission success. A common apparatus used to release a satellite is the Lightband. The details of how a Lightband works are irrelevant to this research, however being able to accommodate this apparatus on the test bed is important. HawaiiSat-1 and HiakaSat, two small satellites being developed at HSFL, both interface with a 15 inch Lightband. Therefore, the test bed must have the same mounting hole pattern as the launch vehicle, 24 clearance holes spaced evenly on a 15 inch diameter. There are holes located on the corners of the traced rectangles in Figure 8 used to mount the arms to the plate. These mounting holes interfere with the Lightband pattern and as a result, the blocked holes were never drilled, leaving four clusters of four holes to connect the Lightband. Despite the decrease in attachment points, there are still enough for a firm connection. The smaller satellites

being developed at HSFL do not use the Lightband but a simple adaptor can be made so that they may be mounted using the same holes.

Arms had to be constructed in order to hold the counterweights away from the center of rotation of the system. The arms could not be oriented vertically because when the test bed tilts, arms of a useful length would come into contact with the air bearing's pedestal. It was important while designing the test bed to minimize any additional unnecessary mass that was added to the system. As a result, it was desirable to minimize the weight of each arm, yet still be strong enough to hold up to 20 kg extended horizontally. Internet searches and conversations lead to the use of extruded aluminum for the arms of the test bed. The hollow profile shown in the center of Figure 9 below minimizes the weight of each arm while still maintaining strength. The slots on the side of each arm also allow the counterweights to be easily attached and adjusted using machine screws and square nuts that fit snugly and slide in the slots.

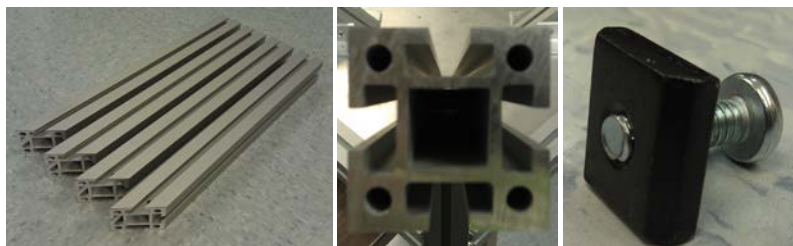


Figure 8: Arms with angled cut (left), extruded aluminum profile (center) and square nut (right)

In order to fasten the arms to the top plate of the test bed, custom brackets were made. The corner brackets were made from angled aluminum while the triangular brackets were cut from 1/4" thick plates of aluminum. The custom hole patterns had to match those on the top plate and the fasteners had to be strategically positioned so they would not get in the way of mounting a satellite.



Figure 9: Brackets used to secure arms of test bed

The test bed was assembled while inverted before being flipped over for final integration with the air bearing. A custom lift was made by mentor Lance Yoneshige that aids in placing the test bed on the air bearing pedestal. No full sized satellites have yet been tested on the platform, although it is ready for use when the time comes. Figure 11 shows the stages of assembly and the final test bed installed on the operating air bearing.



Figure 10: Stages of construction (left and center) and the test bed in motion (right)

PROCEDURE

There are two methods to balancing the satellite air bearing assembly. One technique is a mathematical approach, whereas the other is a visual computer aided guess and check approach. Both work well however the purely mathematical approach is a little quicker.

In order to balance the test bed using mathematics, you must first know the mass and center of mass of the satellite and test bed individually. Since the center of mass cannot be measured easily for most things, it is important to make a SolidWorks model that is as accurate as possible. Material properties can be added to the computer model and SolidWorks will provide the mass, center of mass and moment of inertia information needed. To simplify things, the origin is defined as the center of rotation, located at the interface between the air bearing and the test bed. Moment equations can then be used to balance the system. In order to be fully balanced the sum of the moments has to equal zero as seen in Equation 5. Equations 6 through 8 are then solved for the location of the center of mass (C) of each counterweight where mass (m), moment (M), and gravity constant (g_0) are known while the horizontal weights (hw) and vertical weights (vw) are noted via subscript.

$$\Sigma M = \Sigma F_i x_i = 0 \quad (5)$$

$$\Sigma M_x = g_0(m_{\text{sat}}C_{x,\text{sat}} + \Sigma m_{\text{hw},i}C_{x,\text{hw},i}) = 0 \quad (6)$$

$$\Sigma M_y = g_0(m_{\text{sat}}C_{y,\text{sat}} + \Sigma m_{\text{hw},i}C_{y,\text{hw},i}) = 0 \quad (7)$$

$$\Sigma M_z = g_0(m_{\text{sat}}C_{z,\text{sat}} + m_{\text{tb}}C_{z,\text{tb}} + \Sigma m_{\text{hw},i}C_{z,\text{hw},i}) = 0 \quad (8)$$

In order to avoid doing math, there is a guess and check method that uses SolidWorks. With an assembly composed of the satellite, test bed, counterweights and air bearing, SolidWorks can then provide center of mass information about the entire system. If the center of mass of the system does not match the center of rotation, the system is unbalanced by definition and the counterweights can be adjusted. By repeating this process until the system is balanced, the locations of each counterweight are then known.

RESULTS

There are no definite results to report in terms of numbers, values or charts. The results of the ADCS Test Bed are more abstract. The success of the project was dependent on whether it could serve as a fully functioning test bed for the ADCS of any satellite being developed at HSFL. Although there are currently no fully functioning satellites at HSFL ready to be tested, the

test bed has proven its functionality with mock satellites on a small-scale prototype and is ready for full-scale use with the final model. The test bed has been mated to the air bearing and successfully demonstrates the full range of motion required for testing.

CONCLUSION

Testing every sensor, component and system of a satellite is essential during the design process and assembly. At HSFL there is a large infrastructure in place to test most of the subsystems of small satellites. With the completion of this fellowship, it is now possible for HSFL to test the actuators and control mechanisms of the Attitude Determination and Control Subsystem of a satellite. The concepts used by the test bed were first verified using a half-scale prototype, which lead to the construction of a full-scale apparatus. The test bed and the air bearing have been mated and verified that the full range of motion required can be met. The Air Bearing ADCS Test Bed is now ready for use in the test centers of the Hawai'i Space Flight Laboratory.

ACKNOWLEDGEMENTS

I would like to thank a few key people and groups that made this fellowship possible. A special thank you to the Hawai'i Space Grant Consortium for giving me the opportunity to do this research and funding the project. Thank you to Lance Yoneshige, my main mentor, who taught me everything I know about SolidWorks analysis and machining metal. He was a tremendous help whenever I had a question or problem and provided great leadership. Thank you to Miguel Nunes, co-mentor of the project, who always pushed me to outdo myself and really get creative. His persistent questioning required in depth knowledge of the subject and clear understanding of how the system worked. Thank you to Dr. Sorensen, I learned almost everything about ADCS from his Astronautics class. Thank you to all the staff in the Space Grant Office who were always available and friendly when I dropped in to ask a question. And finally, thank you to Roy Tom for his precision machining skills on the larger pieces of the project.

REFERENCES

Sellers Jerry John (2003) Understanding Space: An Introduction to Astronautics. McGraw-Hill

FINAL REPORT FOR SOFTWARE INTERNSHIP AT NOVASOL

Kale A. Y. Nakata
College of Engineering
University of Hawai'i at Mānoa
Honolulu, HI 96822

ABSTRACT

During my internship at NovaSol I was able to experience work in a software department of a Technical Company. Since I have had some experience with databases and my interest in software, my boss assigned me to facilitate the transition of database software. This report contains what I have learned during the internship.

INTRODUCTION

NovaSol is a company that was founded as an Innovative Technical Solutions in October 1998. NovaSol specializes in the research, engineering development, and productization of next-generation active and passive optical systems. The department that I was personally working in was the software department. The workplace was secure with locked doors. I was assigned a temporary pass on the first day of work. The person that I reported to was Keith Nakanishi who is the Director of ISR Software. Mr. Nakanishi placed me in a cubicle near his and was always there to answer my questions.

I have done some work with databases in past internships but not nearly in this magnitude. The size of the databases that I have worked on have been very small and consisted on only a few members. The databases that I was to be working on during the internship did not consist of much members but the size of the project files were a lot bigger. The amount of people working on a project at NovaSol isn't that big but the availability of encompassing for more users is an important aspect of software development.

TASKS

1. Migrate VSS Databases

Team Foundation Server Provides tools to effectively manage software development projects. The old software used by NovaSol was VSS and will not be supported in the upcoming year. Due to this, Mr. Nakanishi has decided to make the move to TFS. TFS has a lot of good features that can be utilized.

Since the software was new to me the first task was to read up and learn about the basic commands and operations of Team Foundation Server. My boss bought an informational book about TFS for the both of us. The beginning of the internship consisted of learning how to set up the framework and use the basic commands. The structure of TFS can be easier explained by looking at the breakdown in Figure 1.

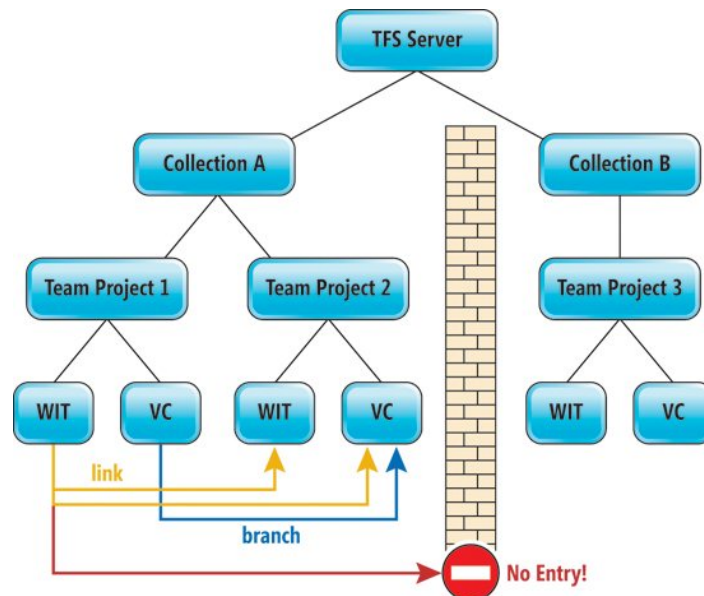


Figure 1. TFS levels

As shown in Figure 1, the top-level of this database structure is the TFS server which branches into collections. These collections can be set up to contain many different projects. This type of organization aids in project development. Once the general framework was set up I could assign users with specific privileges. The user's privileges could be for the entire collect or just for a specific project. This is very useful so that users only have access to the data that they are allowed. For the databases that I migrated the only user that was set to be active was Mr. Nakanishi's administrative account.

The VSS databases needed to be migrated to a selected TFS collection. TFS has a migration tool that would take VSS projects and convert them to TFS projects. The book along with steps found on the internet made the migration process go fairly smoothly. I ran into a couple of problems, one being I ran into was the physical memory on the computer that I was doing the migrations with.

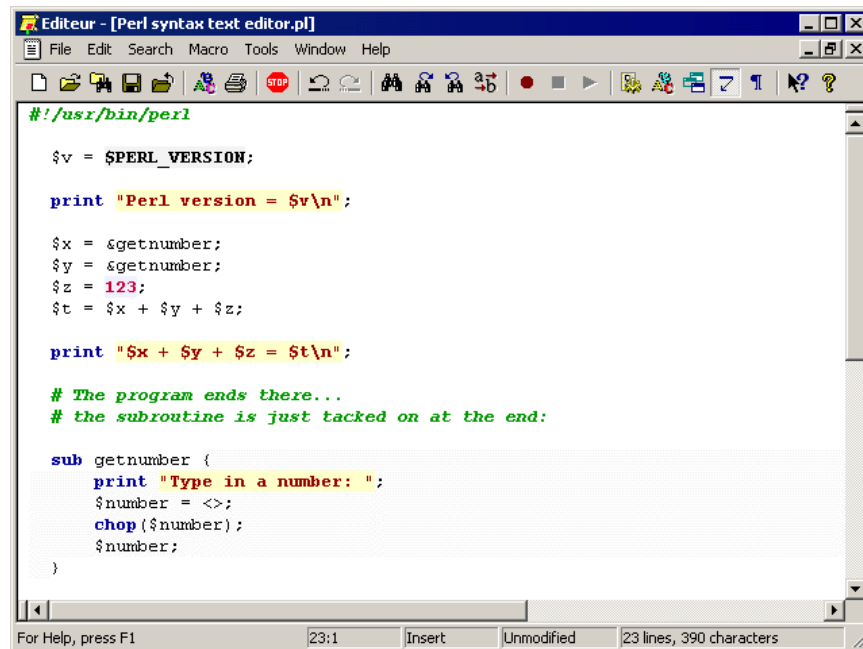
2. Create a Migration Guide

The second task I was assigned was to create a migration guide for my boss to use to migrate future projects. Since I was performing the migration on several databases I could word the process better. This was also useful since while performing the first couple migrations, I encountered a lot of problems. One of the problems was that I did not have all of the required permissions such as administrative privileges. The finalized migration guide contained tips that I had found as well as useful links.

3. Edit Nightly Build Script

Another important task that was assigned to me was to edit the nightly build script. A nightly build script is run every night. This builds certain projects that are specified in the build script. Projects can contain a large amount of source code, so a full build could take up to an hour depending on the size of the project. These builds are an important part of software development since developers need to know if the code that they have edited will work correctly.

The build script is written in Perl. Perl is a general-purpose dynamic programming language. A sample of Perl code is depicted in Figure 2.

The image shows a screenshot of a text editor window titled "Editeur - [Perl syntax text editor.pl]". The window has a menu bar with "File", "Edit", "Search", "Macro", "Tools", "Window", and "Help". Below the menu bar is a toolbar with various icons. The main text area contains the following Perl code:

```
#!/usr/bin/perl

$v = $PERL_VERSION;

print "Perl version = $v\n";

$x = $getnumber;
$y = $getnumber;
$z = 123;
$t = $x + $y + $z;

print "$x + $y + $z = $t\n";

# The program ends there...
# the subroutine is just tacked on at the end:

sub getnumber {
    print "Type in a number: ";
    $number = <>;
    chop($number);
    $number;
}
```

The status bar at the bottom of the window displays "For Help, press F1", "23:1", "Insert", "Unmodified", and "23 lines, 390 characters".

Figure 2. Sample Perl Code

This was the first time I have experienced using Perl. Although the syntax is unique, the general layout is similar to basic C. The main changes that I needed to make to the nightly build script were to create a subroutine that used TFS utility commands and figure out what TFS commands correlated to the VSS commands. To do this I manually used the TFS commands in the command line. Once I was sure that I found the correct TFS command I replaced it with the old VSS command. The most difficult part of this task was that in order to complete the replacement I needed to understand what the original script was doing. This tested my understanding of Perl as well as my understanding of the scripts algorithm.

OUTCOMES

This internship let me experience work in software environment. I was not able to complete the migration of all of the databases assigned to me due to space and time limitations. The migration guide that I created should be sufficient to complete the migration process of the remaining database. The biggest skill that was enhanced during this internship was the ability to adapt and learn. There were a lot of things that I needed to learn to complete my daily tasks such as learning Perl.

Version control was something that I learned during the internship. Version control in respect to programming is the management of changes to a program. The use of version control is very important as a software developer. This allows the developer to roll back to a previous working build. I have had the experience in the past where I was working on a program with a group of people and a member made a change to the program. The change although small caused an error and that error took a long time to get rid of. This problem mainly occurred

because we did not have a previous version to roll back to. TFS keeps track of changes made to a project and provides the option to roll back. I used this feature while learning the different command codes.

CONCLUSIONS

I was able to complete most of the assigned tasks.

1. Migrate VSS databases to TFS
2. Create a Migration guide
3. Edit the Nightly Build Script

From this internship I gained a lot of information about how software development is used to complete projects. There was a lot of software and command line commands that I used which were new to me. Besides the knowledge that was learned from completing my assigned tasks I gained a lot from talking to my boss and fellow workers. They gave a lot of good advice that I will take with me as I prepare to enter the workforce after graduation. I had a great semester working at NovaSol.

ACKNOWLEDGEMENTS

I would like to thank:

- Keith Nakanishi, Director of ISR Software for allowing me to work for him and being a great boss
- Jennifer Arthur, Office Manager for helping me with the initial forms and tour of the workplace
- All of the workers at NovaSol, for being very friendly and making my time working enjoyable
- Stewart Burley, for forwarding my application to the correct place
- Hawaii Space Grant Consortium, for sponsoring my internship and providing me with this great opportunity
- The University of Hawaii

REFERENCES

NovaSol Website (2011): Home Page
<http://www.nova-sol.com/>

NovaSol WebSite (2011): Company Page
<http://www.nova-sol.com/>

CONTROL DESIGN FOR A SMALL SATELLITE REACTION WHEEL FOR ATTITUDE CONTROL

Zachary K. Lee-Ho
College of Engineering
University of Hawai'i at Mānoa
Honolulu, HI 96822

1 INTRODUCTION

Historically, space based scientific research has been driven by large satellites that take several decades to develop and require a specified launch vehicle in order to be deployed. These factors drive the cost of missions for large spacecraft significantly high and infer a long development time to complete such a mission. Alternatively, small satellites' have significantly shorter development time and lower cost implication, making them an attractive option to conduct scientific research and other space based missions. In addition, small satellites can be added as a secondary payload to a multitude of different launch vehicles increasing the number and variety of possible launches. The physical laws that govern small satellites' motion and dynamics in space coupled with orbit insertion errors and unmodeled forces can greatly affect the attitude dynamics due to their small moments of inertia [1]. Small satellite's limited physical stature restricts their ability to carry certain payloads, generate power and store energy. Thus, to execute some adequate scientific experimentation or credible surveillance a reliable attitude determination and control system (ADCS) with a small physical and power profile is required.

1.1 Hawai'iSat Spacecraft Bus and Control Scheme

Small satellites are categorized based on their overall mass, such that a microsatellite is classified as weighing between 10 to 100 kg, nanosatellites between 1 and 10 kg and picosatellites 1 kg and below [2]. Hawai'iSat is a Low Earth Orbit microsatellite being developed at the University of Hawaii. Hawai'iSat shown in figure 1 will be placed in a sun-synchronous orbit at 98 degrees inclination at a 500 – 600 km altitude range. The objective of Hawai'iSat is to demonstrate its ability to accommodate and support various types of payloads and validate the satellite technology developed at the University of Hawai'i. The ADCS will be responsible for accommodating each individual payload's pointing requirement(s) and placing Hawai'iSat in the desired attitude during each specified mission mode. Attitude is the relative orientation of a body-fixed coordinate frame to an inertial frame, which in the case of Hawai'iSat is geocentric. Hawai'iSat is an octagonal cylinder in shape and approximately 80 kg in mass. The ADCS is comprised of actuators, sensors and a dedicated computer stack for data acquisition and processing of the estimator and control scheme. The attitude actuators are three magnetic torquers and a reaction wheel [1].

The Hawai'iSat control law employs Morse functions which are Lyapunov-like functions on $SO(3)$ nonlinear configuration space [1], enabling asymptotic tracking of a desired trajectory almost globally. Sizing of the feedback gains for the attitude and angular velocity are based on the attitude and angular velocity tracking errors, ensuring that the control torques are within the saturation constraints of the actuators. The control law is continuous with respect to the trajectory tracking error to eliminate chatter that may occur in sliding control systems. A

description of the control scheme in its entirety can be seen in the AIAA GNC 2009 literature entitled by Dr. Amit Sanyal and Zachary Lee-Ho.

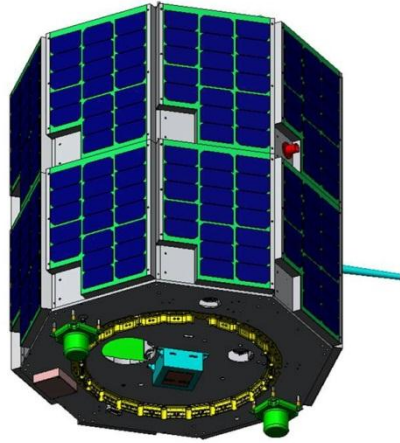


Figure 1: External view of Hawai'iSat

1.2 Reaction Wheel

External torques acting on the body of the spacecraft augments the angular momentum of the entire spacecraft. In the absence of active attitude control, the body accumulates angular velocity increasing the spacecraft's overall angular momentum and resulting in a change of attitude of the spacecraft. Reaction wheels are momentum exchange devices that provide continuous smooth actuation, allowing for very accurate attitude control for moderately fast maneuvers [3]. The reaction wheel serves as an internal rotating actuator that when accelerated produces an angular torque. The angular torque produce does not affect the overall spacecraft momentum but instead transfers the momentum change to the spacecraft. A gradual net increase in reaction wheel speed represents a net increase in system momentum due to the effects of external torques. A typical reaction wheel assembly consists of a rotating flywheel suspended on ball bearings and driven by an internal brushless DC motor.

1.3 Motivation

There are various motivations for developing an in-house reaction for small satellite purposes. Financially the in-house reaction wheel provides a significant cost reduction to the current commercial off the shelf options. The Sinclair Interplanetary Company supplies the best option with regards of quality, reliability and inexpensiveness actuators for microsatellites available commercially. However, even the cheapest commercially available reaction wheels for microsatellites bear a price tag of 25K USD each. This high price for actuation can limit a programs ability to afford 3-axis stabilization and thus limit the ability to perform significant scientific research. Financial viability of a mission is often the most constraining requirement in a satellite project. Thus an increase in actuator size or number can cripple a project and deem a mission not financially feasible. Therefore an in-house reaction wheel makes the access to space cheaper and more feasible. An inexpensive in-house reaction wheel allows a project to increase the number actuators or actuator size without setting it back financially, thus ensuring the effectiveness of the attitude control law. Mathematical singularities can be minimized through the use of the rotation representation $SO(3)$ and Lyapunov stability techniques but a satellite's

ability to achieve a desired maneuver can be hampered significantly by the number or size of actuators on the spacecraft. Thus, heightened maneuverability made available by inexpensive actuation extends the types of space-based scientific research that can be made possible.

2 MOTOR CONTROL

The tracking system for the DC motor will be evaluated assuming an infinite-time/horizon case and therefore will be time-invariant. In the infinite horizon problem the control law, u , is not constrained. Synthesis of the controller is an iterative process performed through adjustment of the gains until the desired goals are achieved. In addition, if any of the states are uncontrollable and/or unstable then the corresponding performance measure V will become infinite and would not make sense physically. Therefore, the system depicted by state space form of the plant must be completely controllable. The controllability matrix $[BAB \dots A^{n-1}B]$ must be nonsingular or contain n linearly independent column vectors to deem the system completely controllable.

2.1 Inner-loop Control for Reaction Wheel

In this section, the inner-loop control law will be introduced. Inner-loop control is defined as a smaller internal feedback control loop within a larger feedback control loop. The objective of the control law will be to take the desired angular velocity for the reaction wheel derived by the Hawai‘iSat ADCS and convert it to an acceptable input to be given to the DC motor. In accord with basic properties of a DC motor, the electromotive force, v_{emf} is proportional to the angular velocity $\dot{\theta}$ of the motor

$$v_{emf} = K_s \dot{\theta} \quad (1)$$

where speed constant and armature current i_a is proportional to the torque, τ , at the shaft

$$\tau = K_\tau i_a \quad (2)$$

given the torque constant K_τ . The goal of this research will be to construct an Lyapunov stable control law that takes the desired reaction wheel torque derived by the Hawai‘iSat control law and translates it into a usable voltage input to generate the desired torque for the spacecraft. Stability of the inner loop control law ensures that the desired reaction wheel torque for the satellite bus is achieved. An unstable system could result in an erratic torque production by the actuator putting excessive strain on the system; instability could also result in over actuation, excess consumption of electrical power and saturation of the actuator at an accelerated rate. Analysis of the inner-loop control law will begin with the introduction of the free-body diagram for the DC motor given in figure 2. The corresponding differential equation for the motor’s dynamical properties is derived

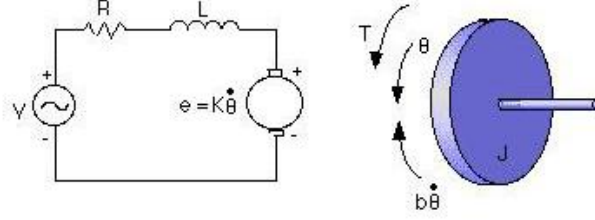


Figure 2: Electric circuit of armature and free body diagram of the rotor

from Newton's law of motion that defines the product of the rotor's inertia, J_m , and angular acceleration, $\ddot{\theta}_m$, is equivalent to the summation of the torques acting on the motor shaft. The resulting equation for the motor's dynamical properties is

$$J_m \ddot{\theta}_m = -b\dot{\theta}_m + K_\tau i_a \quad (3)$$

The electric circuit of the motor is defined by

$$L_a \frac{di_a}{dt} + R_a i_a = v_a - K_s \dot{\theta}_m \quad (4)$$

where K_s is the speed constant, R_a is the armature resistance, and L_a is the inductance of armature.

2.2 State Space Representation of DC Motor

The set of all states of a dynamical system are termed the state space of the system [4]. The state space equation for the linear system the system output is given by:

$$\dot{x} = Ax + Bu \quad (5)$$

$$y = C^T x \quad (6)$$

where A, B, and C are matrix functions of time with continuous entries. The vectors x , u , y denotes the system state vector, system input or control and system output respectively. Taking the differential equation 3 and 4 of the DC motor, the state space representation of the system is obtained. The state variables, x for the DC motor are taken to be angular velocity and armature current of the motor. The output of the system, y , will be the angular velocity of the wheel measured by the Hall-effect sensors and the input into the system, u , will be a given voltage input. Solving for the respective state variables of the system, the differential equations 3 and 4 are rearranged to achieve the following:

$$\begin{aligned} \ddot{\theta}_m &= -\frac{b}{J_m} \dot{\theta}_m + \frac{K_t}{J_m} i_a \\ \dot{i}_a &= -\frac{R_a}{L_a} i_a + \frac{1}{L_a} v_a - \frac{K_e}{L_a} \dot{\theta}_m \end{aligned}$$

These equations are then put in state space format to yield the following

$$\begin{bmatrix} \ddot{\theta}_m \\ \dot{i}_a \end{bmatrix} = \begin{bmatrix} -\frac{b}{J_m} & \frac{K_t}{J_m} \\ -\frac{K_e}{L_a} & -\frac{R_a}{L_a} \end{bmatrix} \begin{bmatrix} \dot{\theta}_m \\ i_a \end{bmatrix} + \begin{bmatrix} 0 \\ \frac{1}{L_a} \end{bmatrix} v_a \quad (7)$$

and the output is given by

$$\omega = \begin{bmatrix} 1 \\ 0 \end{bmatrix}^T \begin{bmatrix} \dot{\theta}_m \\ i_a \end{bmatrix} \quad (8)$$

2.3 Transfer Function Representation of DC Motor

Derivation of the respective Transfer Function (TF) for the DC motor beings by taking the Laplace transform of the state space equations for the system and the system output, given in (5) and (6) to attain the following

$$sX(s) = AX(s) + BU(s) \quad (9a)$$

$$Y(s) = CX(s). \quad (9b)$$

Solving in respect to the state vector, $X(s)$, the system equation becomes

$$X(s) = (sI - A)^{-1}BU(s) \quad (10)$$

where I is the identity matrix of same dimension as A . The state vector, $X(s)$ is substituted into the output function attains the following

$$Y(s) = C(sI - A)^{-1}BU(s)$$

and then respective TF is given as

$$\frac{Y(s)}{U(s)} = C^T(sI - A)^{-1}B$$

Now substituting in the values for A, B, C from the state space equations (7) and (8)

$$\begin{aligned} \frac{\Omega(s)}{V_a(s)} &= \begin{bmatrix} 1 \\ 0 \end{bmatrix}^T \left(s \begin{bmatrix} 1 & 0 \\ 0 & 1 \end{bmatrix} - \begin{bmatrix} -\frac{b}{J_m} & \frac{K_t}{J_m} \\ -\frac{K_e}{L_a} & -\frac{R_a}{L_a} \end{bmatrix} \right)^{-1} \begin{bmatrix} 0 \\ \frac{1}{L_a} \end{bmatrix} \\ &= \begin{bmatrix} 1 \\ 0 \end{bmatrix}^T \left(\begin{bmatrix} s + \frac{b}{J_m} & -\frac{K_t}{J_m} \\ \frac{K_e}{L_a} & s + \frac{R_a}{L_a} \end{bmatrix} \right)^{-1} \begin{bmatrix} 0 \\ \frac{1}{L_a} \end{bmatrix} \\ &= \frac{K_t}{(J_m L_a) s^2 + (R_a J_m + L_a b) s + (R_a b + K_e K_t)} \end{aligned} \quad (11)$$

An alternative approach to attain the respective TF for the DC motor is to derive the TF directly from the motor dynamical and electric circuit differential equations given by (3) and (4). The Laplace transform of the differential equations (3) and (4) are attained as follows:

$$\begin{aligned}
J_ms^2\Theta_m(s) - J_ms\Theta_m(0) - J_m\Theta'_m(0) + bs\Theta_m(s) - b\Theta_m(0) &= K_t I_a(s) \\
L_as I_a(s) - L_a I_a(0) + R_a I_a(s) &= V_a(s) - K_e s\Theta_m(s) + K_e \Theta_m(0)
\end{aligned}$$

Assuming $\Theta_m(0) = 0$, $I_a(0) = 0$, the equations are simplified and solved with respect to I_a .

$$I_a(s) = \frac{1}{K_t}(J_ms^2 + bs)\Theta_m(s) \quad (12a)$$

$$I_a(s) = \frac{1}{(L_as + R_a)}(V_a(s) - K_e s\Theta_m(s)) \quad (12b)$$

Setting equation (12a) equivalent to (12b) and then some rearranging the angular position-to-voltage transfer function is given by

$$\begin{aligned}
\frac{1}{K_t}(J_ms^2 + bs)\Theta_m(s) &= \frac{1}{(L_as + R_a)}(V_a(s) - K_e s\Theta_m(s)) \\
\left(\frac{J_ms^2 + bs}{K_t} + \frac{K_e s}{L_as + R_a}\right)\Theta_m(s) &= \frac{1}{L_as + R_a}V_a(s) \\
\frac{\Theta(s)}{V_a(s)} &= \frac{K_t}{s((J_ms + b)(R_a + L_as) + K_e K_t)} \quad (13)
\end{aligned}$$

and the transfer function for angular velocity-to-voltage is

$$\frac{s\Theta(s)}{V_a(s)} = \frac{\Omega(s)}{V_a(s)} = \frac{K_t}{((J_ms + b)(R_a + L_as) + K_e K_t)} \quad (14)$$

Applying the equation (3) for the motor's mechanical torque the transfer function (13) is translated into a torque-to-voltage transfer function exhibited by

$$\frac{\tau(s)}{V_a(s)} = \frac{[J_ms^2 + bs]K_t}{s((J_ms + b)(R_a + L_as) + K_e K_t)} = \frac{(J_ms + b)K_t}{(J_ms + b)(R_a + L_as) + K_e K_t} \quad (15)$$

3 OUTPUT TRACKING CONTROL FOR SISO

The problem of returning the system to its zero state is considered in this section. The error is defined as the difference between the reference input and the system output, and the desired output given by

$$e = r - y \rightarrow 0 \quad \text{as} \quad t \rightarrow \infty \quad (16)$$

and assumes the tracking error goes to zero given an infinite amount of time. Additionally, the Laplace transform for the tracking error is given by

$$R(s) - Y(s) = E(s) \quad (17)$$

The Lyapunov controller looks to track a desired trajectory over some time interval while using the minimum expenditure of

control effort. The Lyapunov candidate used to derive a control law that asymptotic stabilizes is given by

$$\begin{aligned} V &= \frac{1}{2} e^T P e \\ &= \frac{1}{2} (\tilde{y} - y)^T P (\tilde{y} - y) \end{aligned} \quad (18)$$

assuming P is a scalar, denoted as p , then (18) becomes

$$\begin{aligned} V(x, \tilde{y}) &= \frac{1}{2} p (\tilde{y} - y)^2 \\ &= \frac{1}{2} p (\tilde{y} - Cx)^2 \end{aligned} \quad (19)$$

The time derivative of the Lyapunov candidate is taken and the system state equation (9b) is substituted in, giving the following

$$\begin{aligned} \dot{V} &= \frac{1}{2} (\tilde{y} - y)^T p (\dot{\tilde{y}} - \dot{y}) \\ &= \frac{1}{2} (\tilde{y} - Cx)^T p (\dot{\tilde{y}} - C\dot{x}) \\ &= \frac{1}{2} p (\tilde{y} - Cx)^T (\dot{\tilde{y}} - CAx - CBu) \end{aligned} \quad (20)$$

Asymptotically stable tracking of the output requires the expression (20) be negative definite. For \dot{V} to be negative definite in $y - \tilde{y}$, sufficient condition is obtained as:

$$p (\tilde{y} - Cx)^T (\dot{\tilde{y}} - CAx - CBu) = -g (\tilde{y} - Cx)^2 \quad (21)$$

where $g > 0$ is a scalar control gain parameter. Therefore, based on the assumption that $CB \neq 0$, we obtain the output feedback tracking control law.

$$\begin{aligned} \dot{\tilde{y}} - CAx - CBu &= -\frac{g}{p} (\tilde{y} - Cx) \\ u &= (CB)^{-1} \left[\frac{g}{p} (\tilde{y} - Cx) + \dot{\tilde{y}} - CAx \right] \end{aligned} \quad (22)$$

This control law ensures exponential tracking of the desired output signal \tilde{y} .

4 CONTROL LAW APPLICATION TO SINCLAIR RW

4.1 Reaction Wheel Model

The Sinclair reaction wheel will serve as a baseline for designing the in-house reaction wheel. Some basic characteristics desired for the in-house reaction wheel, is the ability to produce a nominal torque of 2 mNm and minimal angular momentum of 30 mNm-sec. The reaction wheel is equipped with three hall-effect sensors to detect the position of the rotor magnets. The system characteristics of the Sinclair reaction wheel will be determined by evaluating its step response. The time-domain specifications of a step response are defined as

- Rise time, t_r , is the time it takes for motor to go from 10% to 90% of the desired velocity.
- Settling time, t_s , is the time it takes for the motor transient response to decay within 2% of the desired velocity
- Overshoot, M_p , is the maximum velocity reached divided by the final velocity desired, expressed as a percentage.
- Peak time, t_p , is the time it takes to reach the maximum overshoot.

The damping ratio, ζ , and natural frequency, ω_n , of the reaction wheel are approximated utilizing the time-domain specifications

$$\zeta = \frac{\beta}{\sqrt{1 + \beta^2}} \quad \omega_n = \frac{\omega_d}{\sqrt{1 - \zeta^2}} \quad (23)$$

where $\beta = \left| \frac{\log M_p}{\pi} \right|$ and the damped natural frequency, $\omega_d = \frac{\pi}{t_p}$. The damping ratio and natural frequency were then used to derive the characteristic equation for the Sinclair reaction wheel. The transfer function of the system takes the form of

$$T(s) = \frac{\omega_n^2}{s^2 + 2\zeta\omega_n s + \omega_n^2} \quad (24)$$

There is a 0.217 sec time delay which occurs during the first initial input to the reaction wheel. Given a 100 rad/sec command, the output of the step command to the Sinclair reaction wheel was plotted and can be seen in figure 4. When determining the system's time dependent characteristics the time delay is accounted for by subtracting the time delay from the overall rise time, settling time and peak time. From the plot, the time-domain specifications of the reaction wheel show a 5.11% overshoot, M_p , rise time of 1.84 seconds, T_r , settling time of 4.25 seconds, T_s , and peak time, T_p , of 2.87 seconds for the system.

Table 1: Sinclair Interplanetary reaction wheel specifications

Motor Properties	Units	
------------------	-------	--

Nominal speed	rpm	5600
Nominal torque	mNm	2
Rotor inertia	gcm^2	5.1
Mechanical dimension	$\text{mm} \times \text{mm} \times \text{mm}$	$50 \times 50 \times 40$
Mass	g	185
Operating temperature	$^{\circ}\text{C}$	-40 to +70
Control method		Speed or Torque
Supply voltage $+V_{cc}$	V	3.4 to 6.0

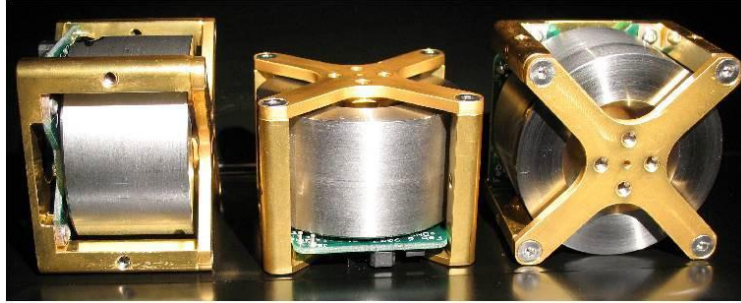


Figure 3: Image of Sinclair reaction wheel

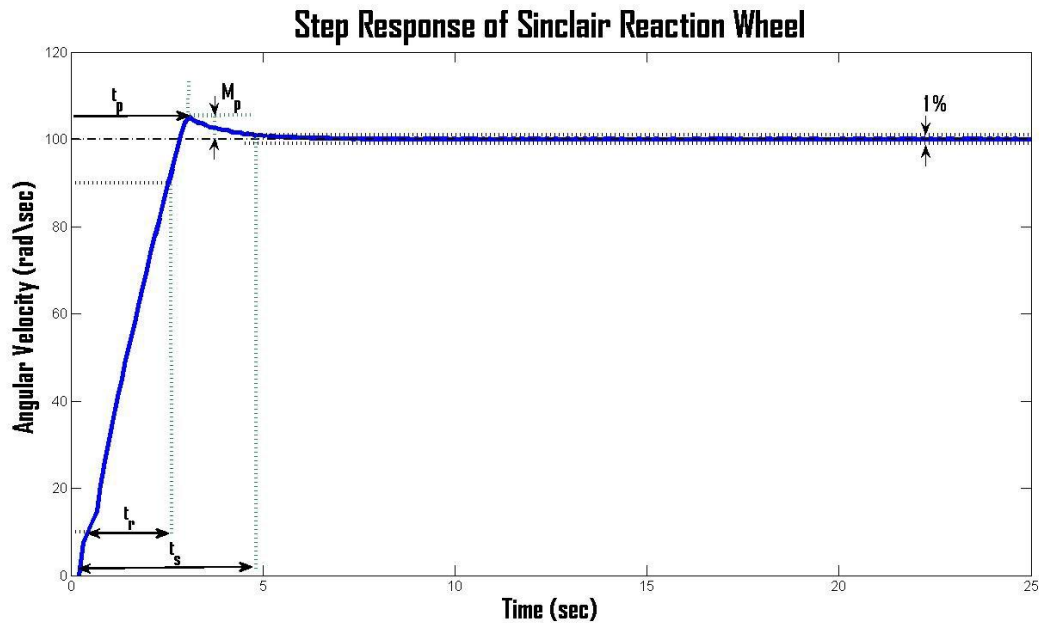


Figure 4: Step Response of Sinclair reaction wheel given a 100 rad/sec angular velocity command

The time-domain specifications are then used to derive the transfer function for the reaction wheel that is given by the following

$$T(s) = \frac{2.2805}{s^2 + 2.0766s + 2.2805} \quad (25)$$

The figure 5 shows the step response to 100 rad/sec command for the reaction wheel and reaction wheel model that is derived using the transfer function (25). The reaction model has 5.11% overshoot, rise time of 1.38 seconds, settling time of 3.97 seconds and peak time 2.88 seconds for the system. One note when developing a controller, the increase in the natural frequency is often correlated to increase in rise time, the lowering of the damping ratio is related to the increases in the overshoot of the step response and the moving of the poles to the left in the s-plane will minimize settling time.

5 CONCEPTUAL DESIGN OF IN-HOUSE REACTION WHEEL

5.1 Reaction Wheel Motor

Selection of the proper motor is an important aspect when ensuring the reliability of the actuator, minimizing power consumption and achieving the best performance. The major components making up the reaction wheel, in which performance of the wheel is dependent on, are the motor, flywheel and controller. Most direct current motors fall under two categories Brush Direct Current (BDC) and Brushless Direct Current (BLDC) motors. The basic components that make up a DC motor consist of the rotor, stator, field magnets, windings, bearings and the shaft.

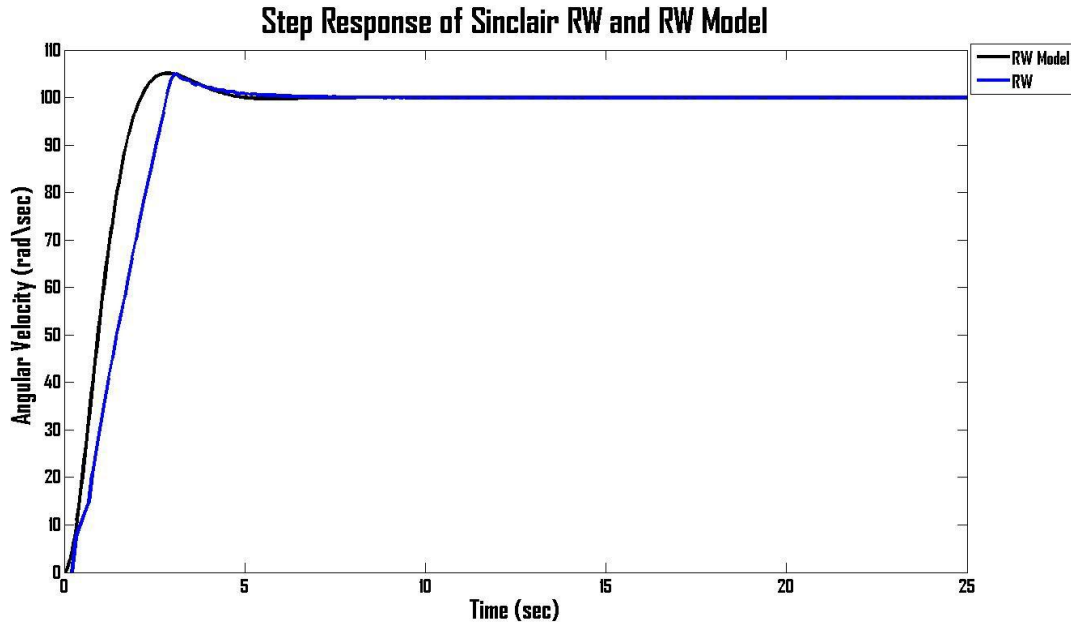


Figure 5: Step Response for a 100 rad/sec angular velocity command of the Sinclair reaction wheel and reaction wheel model

5.1.1 Brush Direct Current Motor

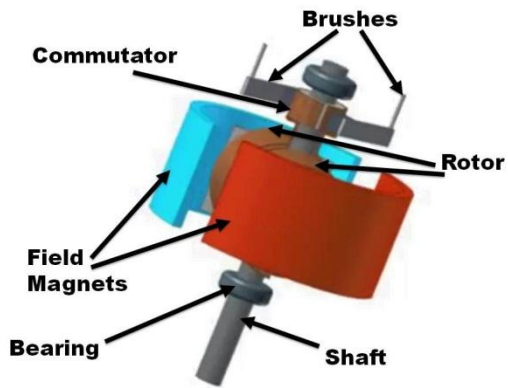
In the BDC motor, current is supplied to the rotor windings by the commutator through spring loaded carbon brushes. A diagram of the BDC motor is displayed in figure 6. Polarities of the electrically separated windings are varied as contact with the carbon brushes is broken and reconnected as a result of the rotor's rotation. Rotation of the rotor is an effect of the polarity from the windings being repelled by the field magnets on the outer stationary stator ring.

5.1.2 Brushless Direct Current Motor

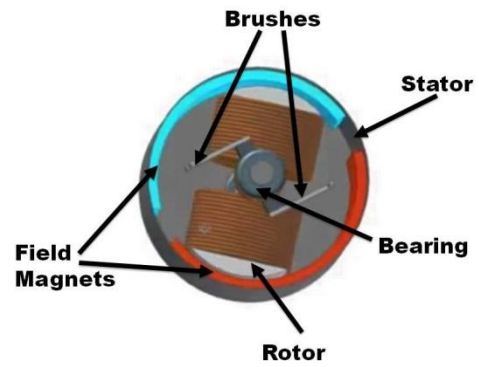
BLDC motors operate structurally inverse to that of the BDC motor. The structural arrangement of the BLDC motor is shown in figure 7. Unlike the BDC the inner windings of the BLDC remain stationary throughout the motor operation and is referred to as the stator. The outer ring lined with field magnets rotates during operation of the motor and is referred to as the rotor. Carbon brushes and the commutator are eliminated from the structural configuration in BLDC motors. Instead, current is supplied to the stator coil windings by an electronic controller. Commutation logic and switching electronics convert the rotor position information attained by an internal hall sensor or similar sensor, to the correct excitation for each stator phase.

5.1.3 Motor Selection

The absence of the commutator and carbon brushes in BLDC motor, minimizes power loss and enables the motor to be more efficient than its brush counterpart. Higher attainable speeds, higher torque outputs at high speeds and improved heat dissipation increases the attractiveness of BLDC motors as a solution. The Maxon EC-20 flat BLDC motor was selected to administer the desired angular velocity by the in-house reaction wheel. A Solidworks Computer Aided Design (CAD) for the Maxon EC-20 flat motor is displayed in figure 8. Maxon's EC-20 flat BLDC motor was primarily selected based on its compact volume, low mass, and similar torque output to that of the Sinclair reaction wheel. Additional mechanical and electrical circuit properties of the BLDC motor can be observed in table 2. Assuming armature inductance and resistance are 3.54Ω and 0.424 mH respectively. Figure 9 shows the open loop step response of the DC motor for a 100 rad/sec angular velocity command. The open loop step response has a steady state error.

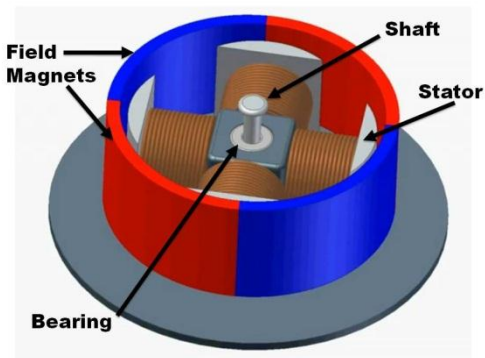


(a) Isometric view

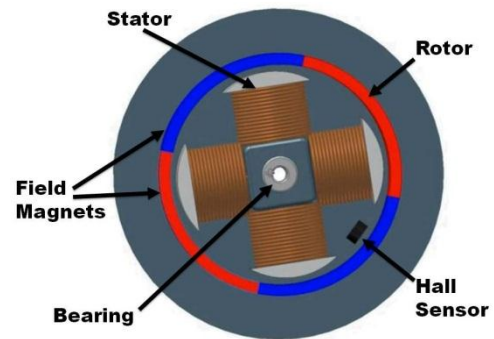


(b) Top view

Figure 6: Views of Brush DC Motor [5]

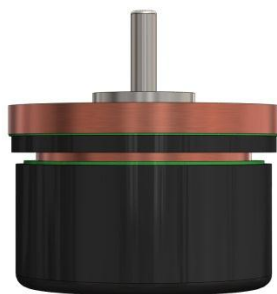


(a) Isometric view

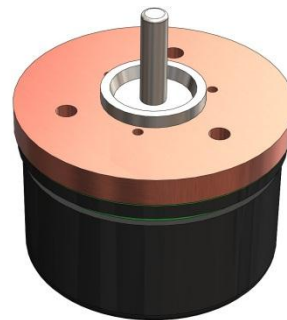


(b) Top view

Figure 7: Views of Brushless DC Motor [6]



(a) Front View



(b) Isometric View

Figure 8: CAD rendering of 9V Maxon EC 20 flat motor

Motor Properties	Units	Maxon EC 20 flat brushless motor
Nominal voltage	V	9.0
No load current	mA	68.3
Nominal speed	rpm	5480
Nominal torque	mNm	8.2
Nominal current	A	0.934
Stall torque	mNm	22.4
Speed constant	rpm/V	1080
Rotor inertia	gcm ²	5.1
Terminal inductance	mH	0.424
Terminal resistance	Ω	3.54
Viscous friction coefficient	Nm/(rad/sec)	6.1003e-7
Mechanical dimension	diameter(mm), height(mm)	21.2, 21.4
Mass	g	22
Operating temperature	C	-40 to + 100

Table 2: Maxon EC 20 flat brushless motor specifications

6 FLYWHEEL

The flywheel is a rotating cylindrical shaped mass used to store or transfer momentum. The flywheel refers to the wheel itself that is attached to the rotating shaft of the BLDC motor. Energy transfer of the reaction wheel is based on the spinning of the flywheel, it stores energy as its speed is increased and releases energy as the is speed decreased.

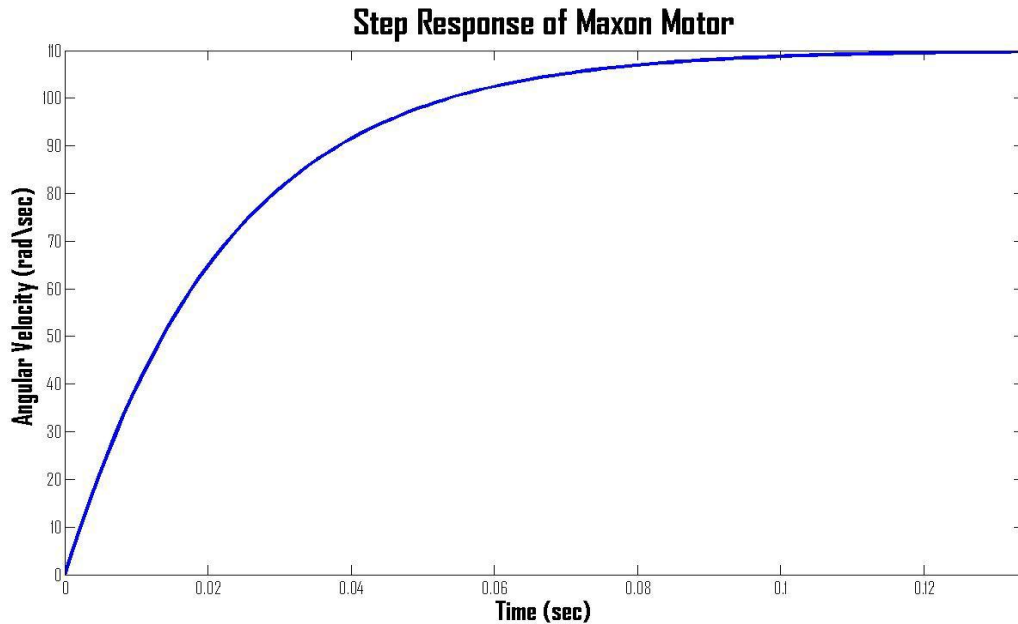


Figure 9: The open loop step response of the Maxon EC 20 flat motor angular ω (rad/sec)

6.1 Material Selection

Components on the spacecraft must be able to withstand an extreme range of temperatures, electrons and electrically charged atoms experienced in orbit at an altitude between 500 and 600 km. Aluminium 606T6 was selected to fabricate the flywheel notably because of its low cost, ease to machine, strength-to-weight ratio and resistance to corrosive atmospheres. Aluminium 6061 alloy comprised of Magnesium and Silicon, is the least expensive of the heat treatable alloys. The T6 signifies that the alloy is heat treated and then artificially aged to strengthen the alloy, while still maintaining its excellent inherit weldability and formability properties. The Sinclair reaction wheel's flywheel and housing is comprised of Aluminium 6061 T6 as well, making the 6061 alloy a very reliable and proven material used consistently in space applications.

6.2 Mass Moment of Inertia

By spinning the flywheel in a precise way, the satellite will rotate in the opposite direction as result of the conservation of momentum law given by

$$h = I\omega \quad (26)$$

where h is the angular momentum, I is the moment of inertia about the axis of rotation and ω is the angular velocity. Moment of inertia is dependent on the total mass of material used and the distance of the material from the axis of rotation. The most efficient flywheel design places a majority of the efficient flywheel design places a majority of the flywheel mass far from the axis of rotation. Therefore, the basic geometry selected for the flywheel consists of a thick outer ring and thin inner disk that is displayed in figure 10. The Sinclair reaction wheel assembly's total moment of inertia is $5.12 \times 10^{-5} \text{kg m}^2$ and will serve as the design requirement for the in-house reaction wheel's flywheel. A rough approximation of the mass moment of inertial for the flywheel can be calculated by evaluating the inner disk and outer ring separately, then superimposing the tow inertias together.

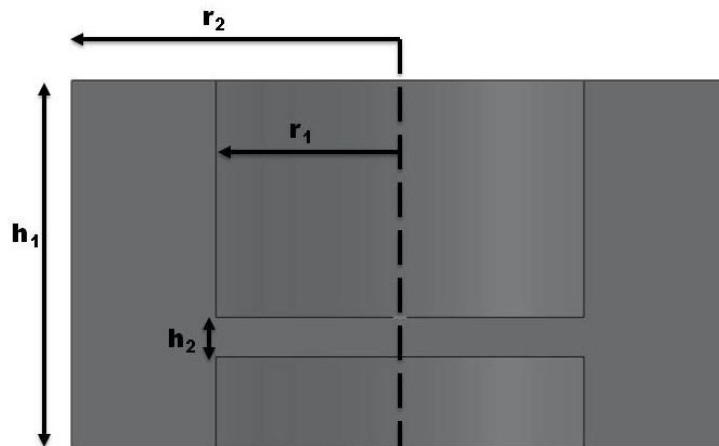


Figure 10: Cross section of in-house flywheel

The mass moment inertia of a disk is given by:

$$I_{disk} = \rho \frac{\pi}{2} h_2 r_1^4 \quad (27)$$

The mass moment of inertia of a ring is given by:

$$I_{ring} = \rho \frac{\pi}{2} h_1 (r_2^4 - r_1^4) \quad (28)$$

where ρ signifies the material's density and the remaining variables are defined in the figure 10. Summing equations (27) and (28) yields the total mass moment of inertia for the flywheel.

$$I_{flywheel} = \rho \frac{\pi}{2} [h_1 (r_2^4 - r_1^4) + h_2 r_1^4] \quad (29)$$

Solidwork models of the flywheel exhibited in figure 11 convey the mass moment of inertia to be $5.843 \times 10^{-5} \text{ kg m}^2$ and to have a total mass of 106.88 g, based on the assumption that the density of Aluminium 6061 T6 is 2.70 g/cm^3 .

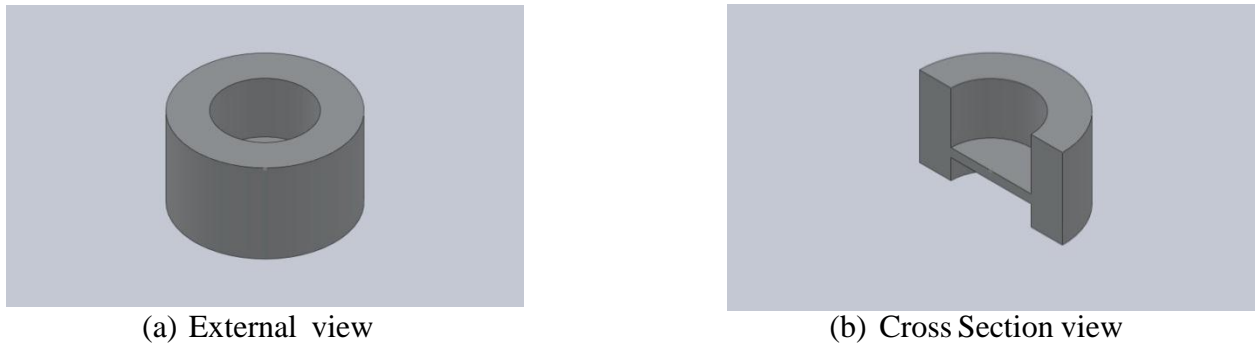


Figure 11: Isometric Views of the flywheel

7 NUMERICAL SIMULATIONS OF THE INTER-LOOP CONTROL LAW FOR IN-HOUSE REACTION WHEEL

The block diagram in figure 12 is of the Lyapunov controller derived for the reaction wheel system. Working with a single input single output system the Lyapunov tracking control law must be in terms of u , \tilde{y} and y .

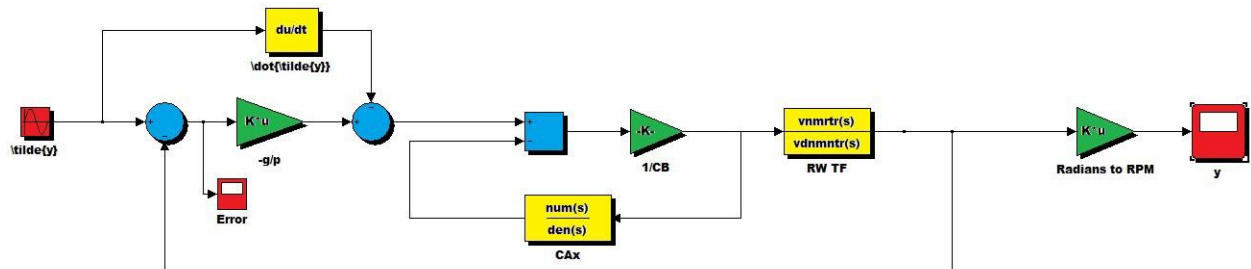


Figure 12: Block diagram of reaction wheel system with Lyapunov stable controller

Therefore, the term CAx from the Lyapunov control law in equation 22 is rearranged to be expressed in terms of u , \tilde{y} and y . The translation of CAx begins with equation (10)

$$X(s) = (sI - A)^{-1}BU(s)$$

Expanding equation (10) further, the following is attained

$$\begin{aligned} X(s) &= \left(\begin{bmatrix} s + \frac{R_a}{L_a} & \frac{K_t}{J} \\ -\frac{K_e}{L_a} & s + \frac{b}{J} \end{bmatrix} \right) \begin{bmatrix} 0 \\ \frac{1}{L_a} \end{bmatrix} U(s) \\ &= \frac{1}{(s + \frac{b}{J}) \left(s + \frac{R_a}{L_a} \right) + \frac{K_t K_e}{J L_a}} \begin{bmatrix} \frac{K_t}{J L_a} \\ \frac{(s + \frac{b}{J})}{L_a} \end{bmatrix} U(s) \end{aligned} \quad (30)$$

then multiplying the matrices

$$\begin{aligned} CAx &= \begin{bmatrix} 0 \\ 1 \end{bmatrix}^T \begin{bmatrix} -\frac{b}{J} & \frac{K_t}{J} \\ -\frac{K_e}{L_a} & -\frac{R_a}{L_a} \end{bmatrix} \frac{1}{(s + \frac{b}{J}) \left(s + \frac{R_a}{L_a} \right) + \frac{K_t K_e}{J L_a}} \begin{bmatrix} \frac{K_t}{J L_a} \\ \frac{(s + \frac{b}{J})}{L_a} \end{bmatrix} U(s) \\ &= \frac{-\frac{K_e}{L_a} \frac{K_t}{J L_a} - \frac{R_a}{L_a} \frac{(s + \frac{b}{J})}{L_a}}{(s + \frac{b}{J}) \left(s + \frac{R_a}{L_a} \right) + \frac{K_t K_e}{J L_a}} U(s) \\ &= \frac{[-J R_a L_a s - (K_e K_t + R_a b)]}{L_a [J L_a s^2 + (b L_a + J R_a) s + (b R_a + K_t K_e)]} U(s) \end{aligned} \quad (31)$$

Figure 13 represent the decomposition of the CAx given an input of u and achieving an output of CAx . A1, A2, A3, and A4 in the diagram represents the elements in the 2×2 system matrix of the reaction wheel system. Respectively those values are $-\frac{b K_t}{J}$, $-\frac{K_e}{L_a}$ and $-\frac{R_a}{L_a}$.

7.1 Computation of Control Gains

The Lyapunov controller requires some selection of the scalar gains g and p in order to implement the inner-loop control law. These gains are combined as ratio between the two gains to form a single scalar gain, $-\frac{g}{p}$, which will be refer to as the Lyapunov gain for the purposes of this paper. The tuning of the single Lyapunov gain provides a level of simplicity rather than having to tune multiple gain values analogous to that of the proportional-integral-derivative control law techniques. The Lyapunov gain was tuned until the desired output tracking was achieved and the output error ($\tilde{y} - y$) was minimized sufficiently. The steady state error of the system is highly dependent on the tuning of the Lyapunov gain. A closer look at the correlation between the output tracking error and gain size will be expressed later in Section 7.3.

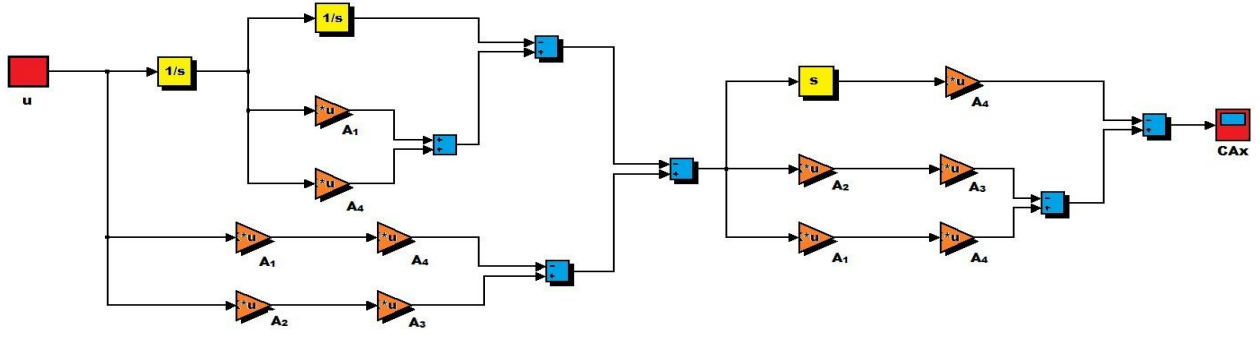


Figure 13: Block diagram of the term CAx

7.2 Desired Trajectory Determination

In deriving the Lyapunov control law, knowledge of \tilde{y} and $\dot{\tilde{y}}$ are required. The scalars \tilde{y} and $\dot{\tilde{y}}$ represents the desired angular momentum and its time derivative for the reaction wheel derived by the Hawai'iSat ADCS controller. In evaluating the Lyapunov controller, two different cases of \tilde{y} were used to simulate various desired angular momentum profiles that may potentially be given by the ADCS controller. The first case used to evaluate the system is of a sinusoidal angular velocity profile. The second case was derived by the Hawai'iSat ADCS when simulating the momentum desired by the reaction wheel during a detumble maneuver. The objective of the detumble maneuver is to stabilize the spacecraft after initial tip-off and is seen as the most actuating intensive maneuver during the spacecraft's entire mission duration. The computation of desired angular velocity time derivative, $\dot{\tilde{y}}$, requires some knowledge of the function for the angular velocity profile. The function for the velocity profile is found by using the 'polyfit' function in MATLAB, which fits a polynomial function to the angular momentum time plot generated by the ADCS control code, seen in figure 14. Given the coefficients of the line used to estimate the desired angular velocity for the reaction wheel, \tilde{y} , and the respective time derivative of the desired angular velocity, $\dot{\tilde{y}}$, is given by:

$$\tilde{y} = (2.4836 \times 10^{-11}) tx^4 - (1.1173 \times 10^{-8}) tx^3 + (1.7980 \times 10^{-6}) tx^2 - (1.2217 \times 10^{-4}) tx - 3.4290 \times 10^{-4}$$

$$\dot{\tilde{y}} = 4(2.4836 \times 10^{-11}) tx^3 - 3(1.1173 \times 10^{-8}) tx^2 + 2(1.7980 \times 10^{-6}) tx - (1.2217 \times 10^{-4}) \quad (32)$$

An alternative solution for attaining the time derivative of the angular velocity is to use the derivative block in Simulink.

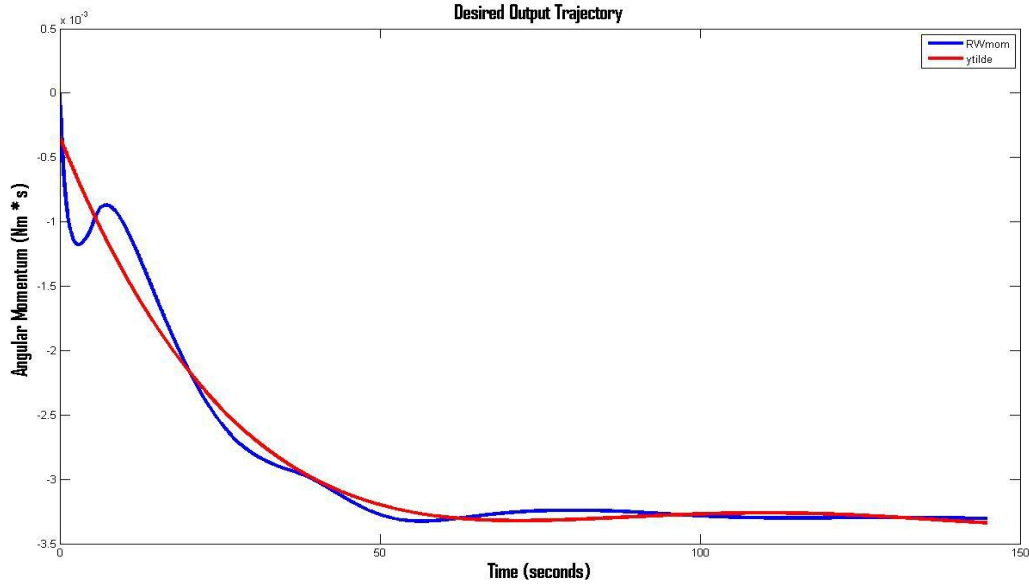


Figure 14: Plot of the Hawai'iSat reaction wheel angular momentum and \tilde{y}

7.3 Numerical results

Figure 15 is a simulation demonstrating the Lyapunov control law's ability to follow a sinusoidal angular velocity profile with an amplitude of 5000 rpms. Figure 15 displays the input \tilde{y} superimposed on the output y of the reaction wheel system, demonstrating complete tracking of the desired angular velocity. The second case requires the Lyapunov controller to track the angular velocity profile generated by the Hawai'iSat. This case demonstrates the controller's ability to track less predictable velocity profiles which will be typical during the spacecraft mission. The plot of error magnitude for the Lyapunov control law, tracking a sinusoidal output is shown in figure 17. Using a $3.0e10$ Lyapunov gain value which results in steady state error of $\pm 4.5351e - 5 (rad/sec)$. Similarly to the previous case the error magnitude for the Lyapunov control law, tracking an angular velocity profile generated by the Hawai'iSat ADCS is shown in figure 18. Using a $3.0e4$ Lyapunov gain correlated to steady state error of $\pm 2.1816e - 5$.

Through additional simulations a correlation between error magnitude and gain size was discover, a segment of those values can be seen in 3 and a plot of relationship between error size and gain value is shown in figure 3.

8 REACTION WHEEL CONTROLLER GRAPHICAL USER INTERFACE

The reaction wheel controller graphical user interface (GUI) was constructed as means to construct a controller for a DC motor and rapidly simulate both open-loop and compensated closed-loop characteristics of the system. Given basic motor specifications like motor inertia, terminal resistance, terminal inductance, etc. the GUI can construct a Lyapunov stable or proportional-integral-derivative type variation controller for a variety of motor types from various vendors.

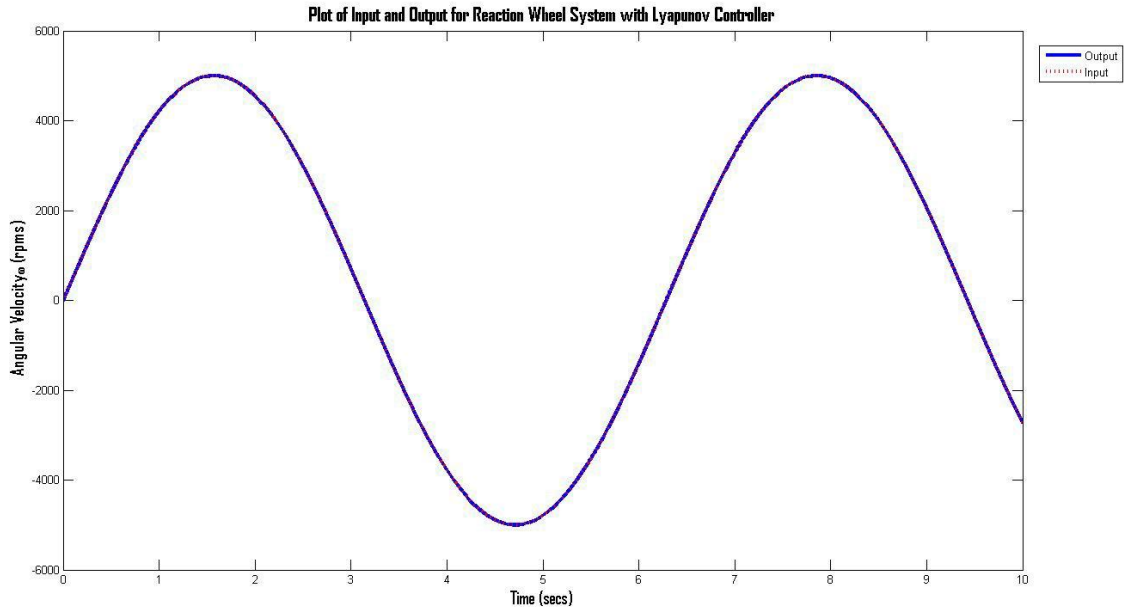


Figure 15: Plot of the Lyapunov controller tracking a sinusoidal angular velocity profile with $3.0e10$ gain value

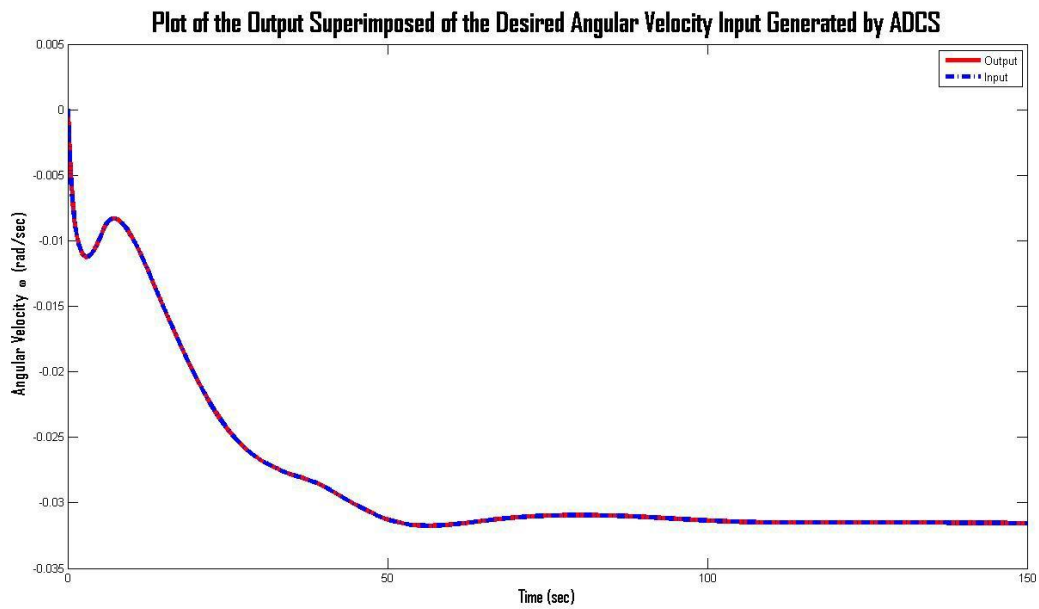


Figure 16: Plot of the Lyapunov controller tracking the desired angular velocity using a $3.0e4$ gain value

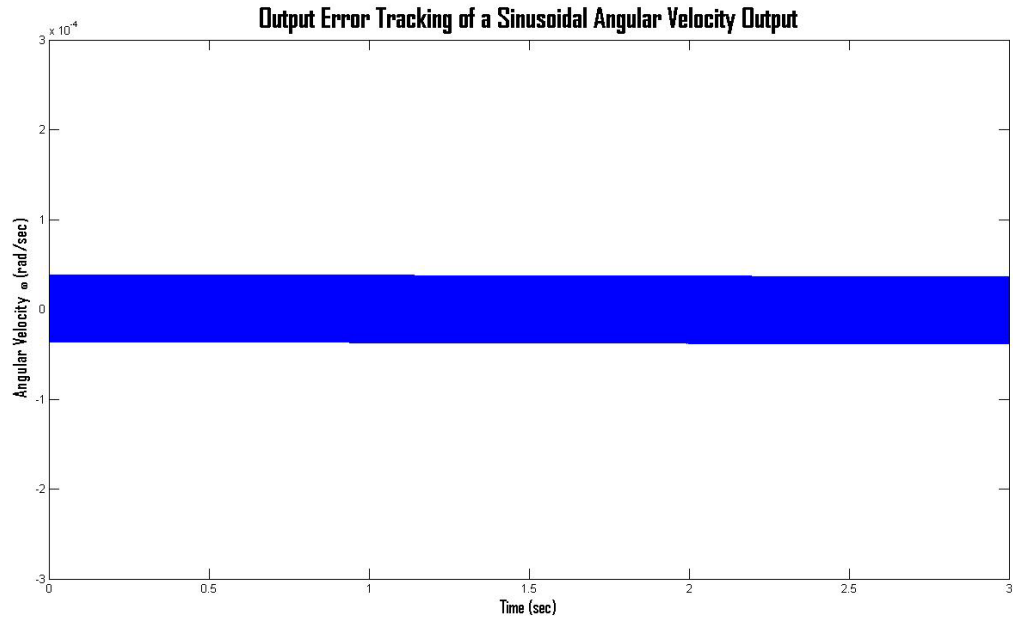


Figure 17: Plot of the error magnitude for Lyapunov controller tracking using $3.0e10$ gain value while tracking a sinusoidal output

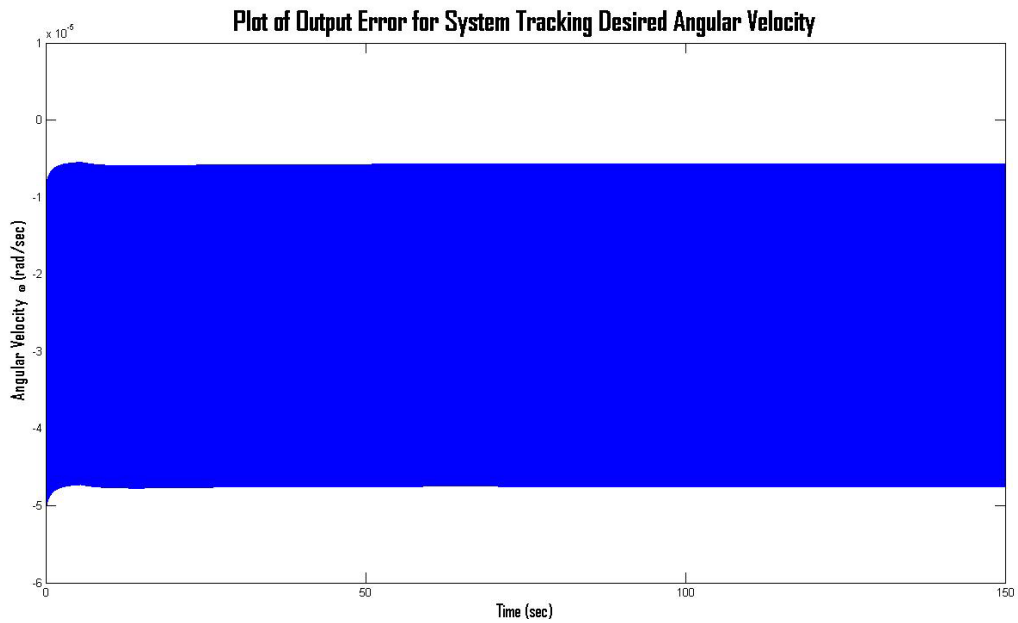


Figure 18: Plot of the error magnitude for Lyapunov controller tracking using $3.0e4$ gain value while tracking a sinusoidal output

Gain	Output Error $\omega(rad/sec)$
$3.0e3$	9.4941
$3.0e4$	0.9558
$3.0e5$	0.1077
$3.0e8$	0.0025
$3.0e10$	0.00024725

Table 3: Relationship between maximum error size and gain value of the system tracking a sinusoidal output

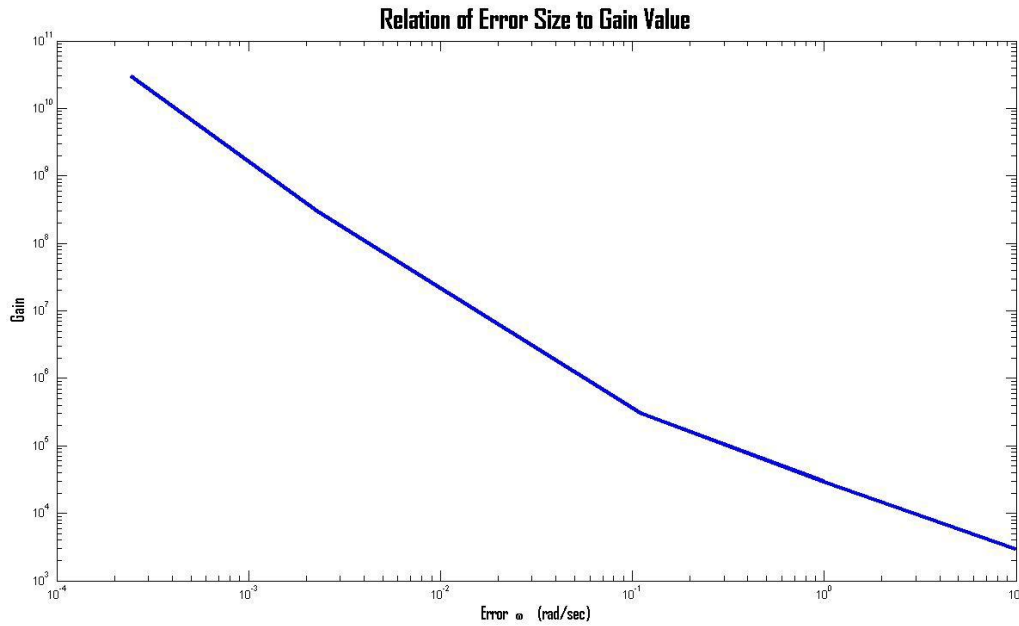


Figure 19: Plot of the error size relative to the Gain Value

The Reaction Wheel Controller GUI, seen in figure 20, allows one to input the specifications of a desired motor by clicking on the respective field and inputting the correlated value. The default values in each field is of the Maxon EC-20 flat motor, the motor used as the focus of this document. After specifying the motor properties, plots of the system's open-loop step response, bode plot, root locus or Nyquist plot can be generated by selecting the check box to respective plot name. After necessary fields are filled and desired plots are selected, the pressing of the "Evaluate System" push button will generated the respective plots and compute the transfer function of the uncompensated system. Once the transfer function of the system is computed and displayed in the lower left field, a Lyapunov stable or proportional-integral-derivative variation type controller can be selected to compensate the open-loop system by pressing the respective button.

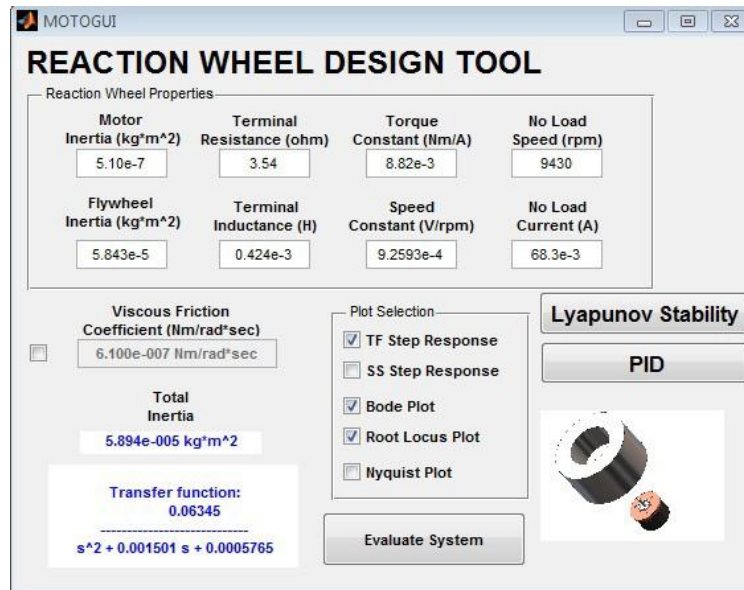
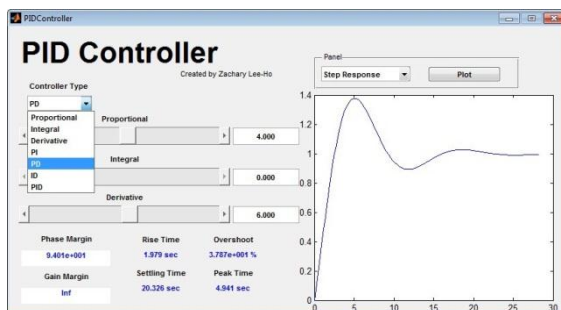


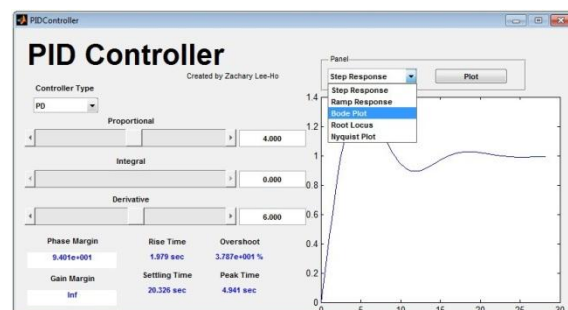
Figure 20: Reaction Wheel Controller Design GUI

8.0.1 PID Controller GUI

When selecting the PID controller, the user is transported to PID Controller GUI window shown in figure 21 a) and b). Implementing the proportional-integral-derivative type of controller requires selection of the desired controller form the controller pop-up menu shown in figure 21 a). The selection of a particular controller will activate the scroll bar to modify the respective gains for that corresponding controller. The remaining gains not used in the selected controller will be disabled to prevent any addition of undesirable gains. After the desired controller is selected, the gains for the respective controller can be adjusted. The corresponding step response for that compensated system with selected gain values can be seen in the plot window of the GUI in the bottom right. In addition, as the gain values are modified properties of the respective system such as phase margin, rise time, overshoot, etc. are given in the fields located at the bottom of the GUI.



(a) Controller type togglebox



(b) Plot togglebox

Figure 21: PID Controller GUI window

When the desired compensated system is achieved, plots of the system characteristic can be generated by selecting the desired plot from the plot pop-up menu and pressing the plot button shown in figure 21 b).

8.1 Lyapunov Controller GUI

Analogous to the PID GUI, the Lyapunov Controller GUI shown in figure 22 is displayed when the Lyapunov Stability button is pressed in the opening Reaction Wheel Design Tool GUI. The Lyapunov GUI enables the user to construct a Lyapunov controller by modifying a single Lyapunov gain value until the desired response is achieved. The GUI displays the block diagram of the Lyapunov controller constructed for the reaction wheel assembly for this document.

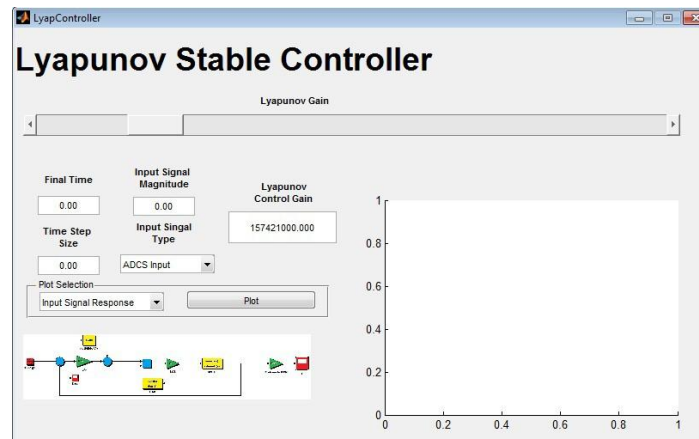


Figure 22: Lyapunov Controller GUI window

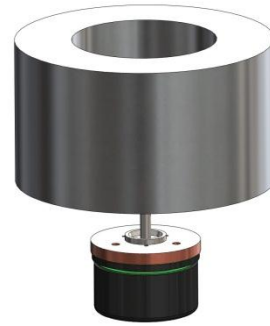
Similar to the PID Controller GUI, the Lyapunov GUI allow the user to generate characteristic plots of the Lyapunov stable system by selecting the desired characteristic plot and pressing the plot button. The signal response to a chosen input can be seen generated in the plot field in the bottom right of the GUI.

9 CONCLUSION

This document discusses the construction of a Lyapunov asymptotically stable control law for a reaction wheel system. The control laws takes an angular velocity input derived by the Hawai'iSat ADCS and asymptotically tracks the output to generate the desired torque for the spacecraft. Using a commercial off the shelf reaction wheel from Sinclair Interplanetary as a baseline, a brushless DC motor with comparable performance specifications was select and flywheel geometry was designed. The Reaction Wheel Design Tool GUI allows the application of the Lyapunov controller to various motor types from different vendors. In addition, the GUI enables a comparison of the Lyapunov controller with traditional proportional-integral-derivative controllers. The combination of readily available hardware found commercially, simple machining and the Reaction Wheel Design Tool GUI provides an inexpensive solution to acquire reliable precise control authority capabilities for small satellite missions.



(a) Exploded Side View



(b) Exploded Front view

Figure 23: Solidworks rendering of reaction wheel assembly

9.1 Future Work

Additions to the work presented in this document can be made to enhance the research performed and address potential issues that may occur during development or during the satellite's mission. A discretization of the control law and the ability to discretize control laws using the Controller Design GUI. Discretizing the reaction wheel controller using the GUI will allow the option to modify the constant time size sampling to meet design and hardware requirements. Then to validate the research presented, control scheme into the hardware discussed in this document will be done. A scheme for managing momentum of the reaction will need to be develop. The gradual net increase in reaction wheel speed, represents a net increase in system momentum due to the effects of external torques. External torques acting on the body of spacecraft augments the angular momentum of the entire spacecraft. The accumulated momentum is transferred to the reaction wheels. A continuous accumulation of excess momentum transferred to the reaction wheel will eventually result in the wheel approaching its momentum saturation limit. Momentum must be “dumped,” or the wheel's synchronous speed would eventually be exceeded and unable to perform a desired actuation [7].

REFERENCES

- [1] Amit K. Sanyal and Zachary K. Lee-Ho. Attitude tracking control of a small satellite in low earth orbit. In *AIAA Guidance, Navigation, and Control Conference*, number AIAA-2009-5902, Chicago Illinois, August 2009.
- [2] John Stark Peter Fortescue and Graham Swinerd. *Spacecraft Systems Engineering*. John Wiley & Sons Ltd., 3rd edition, 2003.
- [3] Marcel J. Sidi. *Spacecraft Dynamics & Control A Practical Engineering Approach*. Cambridge University Press, 1997.
- [4] Sanjay P. Bhat and Dennis S. Bernstein. A topological obstruction to continuous global stabilization of rotational motion and the unwinding phenomenon. *Systems & Control Letters*, (39):63–70, 2000.
- [5] Giorgos Lazaridis. How dc motors are made and how they work. PCBheaven electronic workbench, March 2010. <http://pcbheaven.com/wikipages/HowDCMotorsWork/>.
- [6] Giorgos Lazaridis. How brushless motors work. PCBheaven electronic workbench, March 2010. <http://pcbheaven.com/wikipages/HowBrushlessMotorsWork/>.
- [7] Patrick H. Stakem. Passive magnetic momentum wheel unloading. *Journal of Spacecraft and Rockets*, 14(6):335-338, 1977.

A CROSS-EXAMINATION OF SATURNIAN KILOMETRIC RADIATION EMISSION OBSERVED BY CASSINI AND ULYSSES

Robert M. Albarran
Department of Astronomy and Physics
University of Hawai'i at Hilo
Hilo, HI 96720

Saturnian Kilometric Radiation (SKR) is an auroral radiation of Saturn that has been observed by the Voyager 1 and 2, Cassini and Ulysses spacecraft. Previous studies show that the SKR periodicity varies with time; it was not locked to a fixed rotation period for Saturn. In this study, we compare radio observations from the Cassini and Ulysses spacecraft to determine a geometric model for the SKR emission. We localize peak SKR frequencies within Saturn's magnetosphere via models governed by the Cyclotron Maser Instability (CMI). Subsequently, by correlating spacecraft signals and triangulating detection times, we use the CMI model with Saturn's offset dipole model to survey SKR emission cone orientations through time. Such radio data reduction will allow for further constraint of the SKR rotational modulation. Ultimately, we examine the question - Is the SKR source location fixed in Saturnian longitude or Local Time (LT)?

In October of 1990, the Space Shuttle Discovery (STS-41) launched the Ulysses spacecraft along the plane of the Solar System towards Jupiter. In 1992, Ulysses used its plutonium Radioisotope Thermal Generator (RTG) and a Jovian gravitational assist to assume a near-polar orbit around the Sun; with perihelion at ~ 1 AU and an aphelion at ~ 5 AU. Among the ten instruments aboard Ulysses designed to study the Sun at various latitudes is the Unified Radio and Plasma Wave Experiment (URAP). URAP consists of six sub-instruments optimized to study radio sources and plasma-waves in the solar environment and interplanetary medium. As a whole, the URAP experiment allows us to define dynamic spectra for frequencies up to ~ 900 kHz, a range that engulfs the local electron cyclotron frequency and SKR peak frequencies from 100-400 kHz.

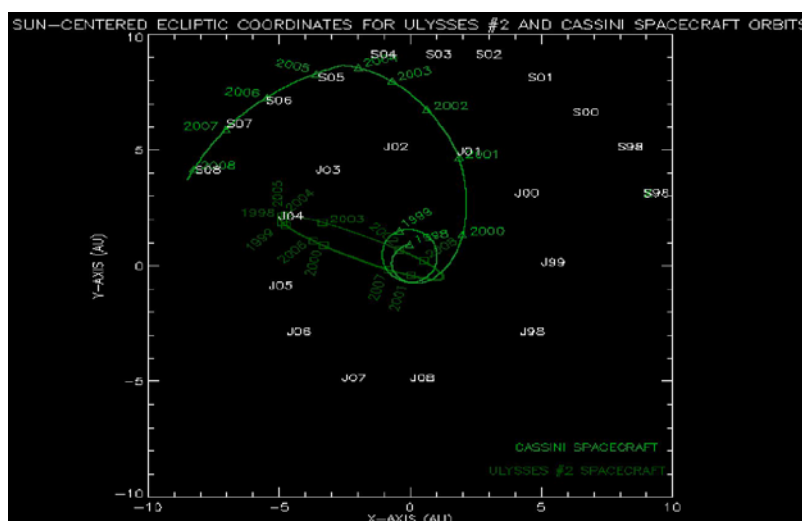


Figure 1: Trajectory plots for Saturn (SYY), Jupiter (JYY), Ulysses and Cassini.

In October of 1997, the Cassini spacecraft was lifted by a Titan/Centaur rocket to be inserted into orbit around Saturn's equatorial plane in July of 2004 (see Figure 1). Also powered by the natural decay of plutonium, Cassini uses its suite of instruments to image, map, and spectrally analyze the Saturnian system. Among these resides the Radio and Plasma Wave Science (RPWS) instrument designed to primarily study radio sources and plasma temperature and density variations in the Saturnian neighborhood. Similar to the URAP experiment, the RPWS instrument allows us to determine the amplitudes and directions of radio signals over the SKR peak frequency range. In our investigation, we compare and contrast dynamic spectral plots of URAP and RPWS observations across various times and spacecraft vantage points (see Figures 4 and 5). Moreover, we perform succinct correlations between each spacecraft's recorded intensity level and time of detection to construct a geometric concept of the SKR.

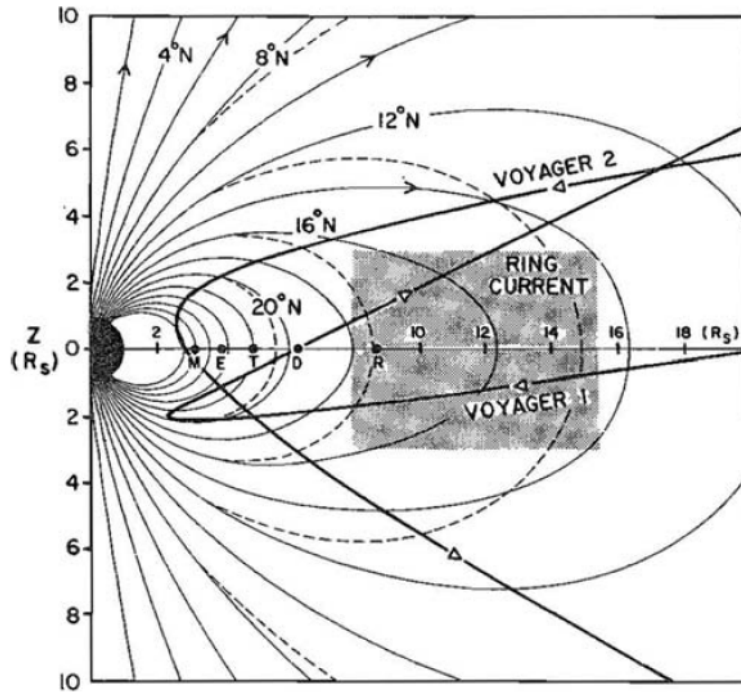


Figure 2: Magnetic field lines and ring current projection onto meridian (in Saturnian Radii) of the dipole model. Moons referenced by first letters along $Z=0$. (Connerney et al. 1983).

To properly scrutinize the complexities of the emission periodicity and location, we assign magnetic field lines of Saturn (see Figure 2) with the SKR frequencies they produce. Usually occurring in regions of low plasma density, the cyclotron maser instability (CMI) is an instability in Saturn's magnetosphere whereby a cyclotron frequency proportional to the magnetic field strength is emitted as radiation. The CMI involves electromagnetic waves that act to organize the cyclotron motions of electrons along a magnetic field line so they resonate with the original electromagnetic wave. The emission inherits the conical pattern of the CMI; the source cone axis of a given frequency aligns with a respective magnetic field line. In the case of electrons, the cyclotron frequency is given by: $B(\text{nT}) = 28 f_{ce} (\text{Hz})$, where $B(\text{nT})$ is the magnetic field strength in nT and f_{ce} is the electron cyclotron frequency in Hz. As we assign peak frequencies along magnetic field lines of Saturn's offset dipole axis, we locate sources of lower frequency SKR towards the equator (where the magnetic fields are weaker) and higher frequency

sources towards the poles. Accordingly, we find the source location for a given SKR frequency to assume a dependency on latitude. This fact is considered when using geometric arguments to describe the rotational modulation of the SKR.

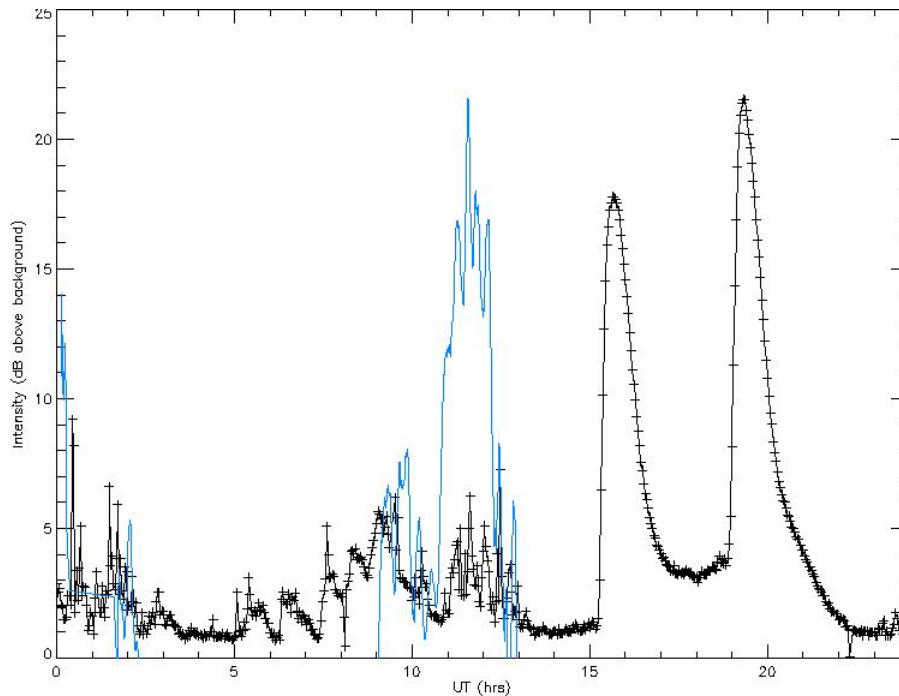


Figure 3: An intensity (dB) versus time (UT) plot of 7/12/2006. URAP and RPWS signals shown with SKR at UT~1-2hrs and UT~8-10hrs.

The spacecraft positions and dynamic spectra are manipulated with the computer language Interactive Data Language (IDL). Using IDL, we graphically represent large numerical data sets and create trajectory plots for Saturn, Jupiter, Ulysses and Cassini (see Figure 1). Since the URAP and RPWS instruments locate the direction of the radio emission, we are able to reference spacecraft observations to defined locations of Saturn, Jupiter and the Sun. More importantly, we measure the angular extent between the Saturnian longitudes of Cassini and Ulysses, at a given date, and account for the difference in time taken for a local source to rotate across that angle. In this manner, the orientation of the SKR emission may be interpolated with respect to the System III rotation rate; as the SKR source rotates it will be seen by one spacecraft and then the other, assuming they were at an equal distance from Saturn. This time delay is referred to as the rotational time delay and is used to determine SKR constraints in Saturnian longitude and periodicity.

Despite the angular separation in longitude of the two spacecrafts, a given SKR radio burst would reach Cassini before Ulysses, as it is closer to Saturn. This time delay in observation is referred to as the propagational time delay. When we sum the rotational time delay and the propagational time delay, for a certain event, and compare this to the SKR time separation seen in the dynamic spectra, we find that the total time is not fully explained; there is a residual delay. In other words, the SKR source location is localized and rotating with Saturn.

As we continue to isolate events, we will implement a sophisticated signal analysis to more precisely define the time delays. Subsequently, we will shift the time axes of Cassini's intensity to the right by a previously derived time-step (e.g. 144s). As more multiples of this time-step are applied, the amount of signal from Cassini will begin to overlap in time with the signal from Ulysses (see Figure 3). When multiplying these two SKR signal levels and summing over all similar products through n time-steps per frequency, ideally, we will have a quasi-Gaussian curve that peaks at a value corresponding to a time delay. The peak value in the curve is referred to as the total time delay, given by $dt_{\text{total}} = dt_{\text{prop}} + dt_{\text{rot}} + dt_{\text{resid}}$, where dt_{total} is the total time delay, dt_{prop} is the propagational time delay and dt_{rot} is the rotational time delay. By such signal analysis, the total time delay serves as a measurement of "maximum correlation" in coherent contrast to the calculated propagational and rotational time delays. Their difference (ie. dt_{total} minus $dt_{\text{prop}} + dt_{\text{rot}}$), referred to as the residual time delay dt_{resid} , inherits a quantification of possible symmetry between SKR emission cone orientation and spacecraft geometric detectability. The Saturnian magnetic dipole model, adjusted to CMI equations, along-side long-term (ie. on temporal order of a decade) spacecraft kinematic coordinates at millisecond time resolution enables us to correlate all peak frequencies over all pertinent detections. Such an engagement serves subtle insight into the underpinnings of SKR variability.

We have shown that the source locations for distinct SKR frequencies are latitude-dependent and the SKR sources are rotating with Saturn. It is yet to be shown the cause and quantity of the radio source drift and SKR rotational modulation. Consecutively, we continue to expand on our investigation and perform the aforementioned statistical analysis of the SKR signal levels. For a particular event catalogued in Local Time (LT) and Universal Time (UT), the total, propagational, rotational and residual time delays, frequencies and magnetic field lines will prove useful for continued in-depth studies of the SKR emission geometry. Such parameters, when compiled over time will allow us to unravel constraints concerning the relationship of the SKR and the various complexities of the Kronian system.

ACKNOWLEDGEMENTS

Special thanks to the research team, Robert MacDowall (Planetary Magnetospheres Laboratory Chief, NASA Goddard Space Flight Center), Melissa Guzman (NASA Lunar and Planetary Science Academy) and Roger Hess (NASA Goddard Space Flight Center). Extended gratitude to those in the Solar System Exploration Division at NASA Goddard Space Flight Center and the NASA Lunar and Planetary Science Academy for being patient with my questions. Deep appreciation to the Hawai'i Space Grant Consortium for making this opportunity a reality.

REFERENCES

- Galopeau, Patrick, Mohammed Boudjada, Alain Lecacheux (2007) Spectral features of SKR observed by Cassini/RPWS: Frequency bandwidth, flux density and polarization. *J. Geophys. Res.* **112**, A7.
- Galopeau, Patrick, Alain Lecacheux (2000) Variations of Saturn's radio rotation period measured at kilometric wavelengths. *J. of Geophys. Res.* **105**, A6, 13,089-13,101.
- Gurnett, et al (2002) The Cassini Radio and Plasma Wave Investigation. Department of Physics and Astronomy, University of Iowa.
- Stone, et al (1992) The unified radio and plasma wave investigation. *Astronomy and Astrophysics Supplement Series.* **92**, 291-316.

FIGURES

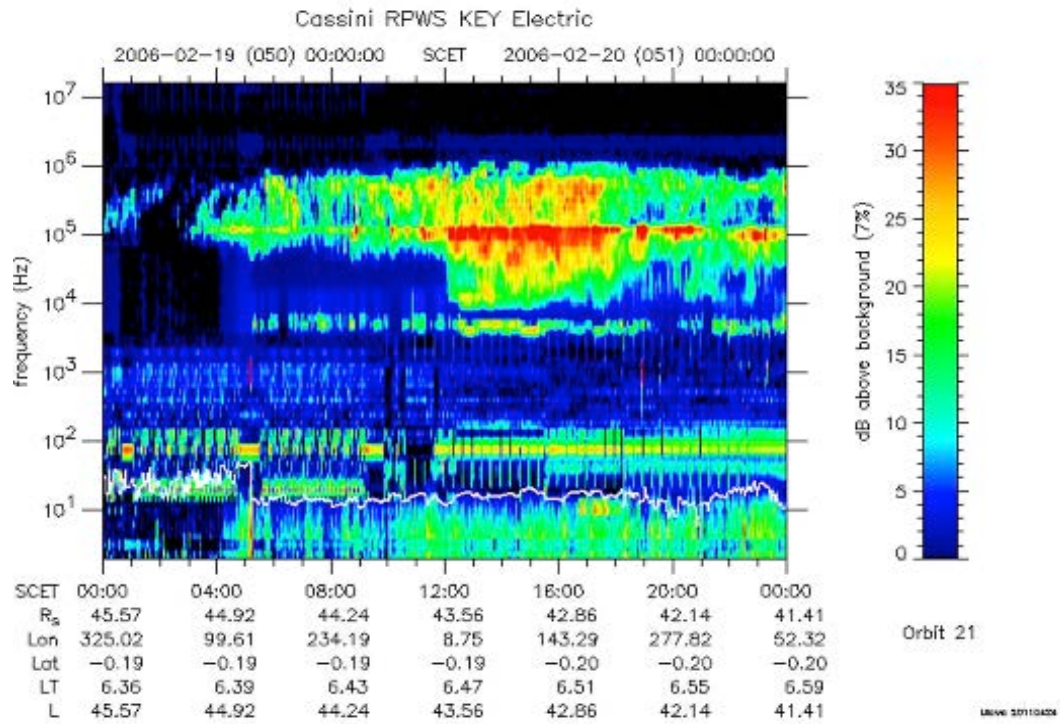


Figure 4: Cassini RPWS dynamic spectra (frequency, Hz versus time, UT) for particular SKR event.

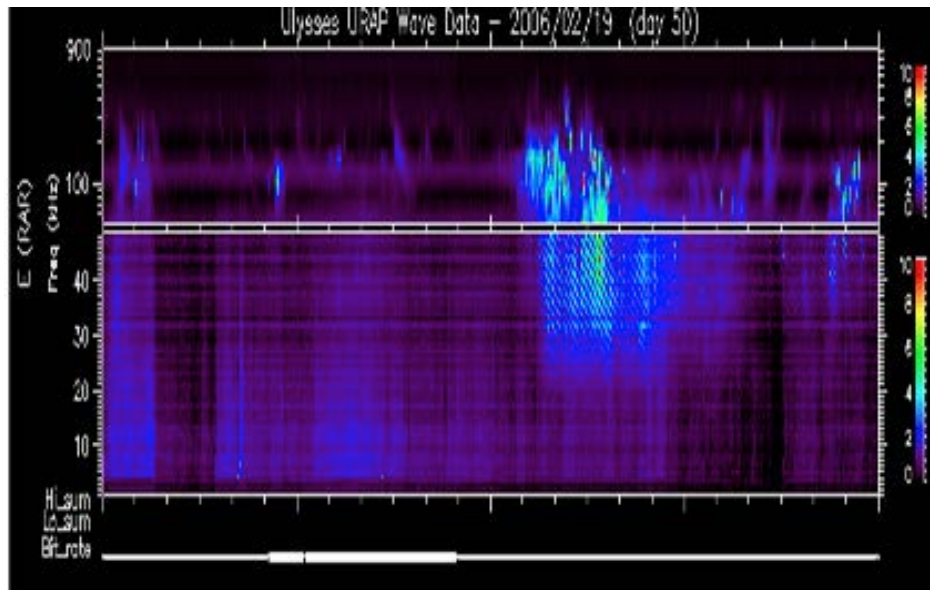


Figure 5: Ulysses URAP dynamic spectra (frequency, Hz versus time, UT) for particular SKR event.

SIMULATIONS AND GUIs: A NEW LOOK TO RADIO SCIENCE

Michael R. C. Andonian
Department of Mathematics
University of Hawai'i at Mānoa
Honolulu, HI 96822

ABSTRACT

This paper serves to discuss the development of a graphical user interface (GUI) designed for a C-programming demodulation software tool. This demodulation software tool was created to recover pertinent science data from a radio science experiment. The GUI was designed with the intention to simplify the analysis aspect of acquiring radio science data. Moreover, within this paper will be an overview of a set of simulations of a remote ground location uplink with the International Space Station. Using these simulations, we can determine times and dates an uplink is plausible, as well as the length of link and direction an antenna should be pointed. Lastly, we discuss briefly the modification and use of a link budget analysis tool, CCSDS-DCT and the remote operation of a Radio Science Receiver to call to New Horizons.

INTRODUCTION

For the last eighty years or so, astronomers and researchers have understood that visible light offered humankind only a tiny glimpse of information of the universe, plausibly comparable to the space visible light occupies on the electromagnetic spectrum. Radio waves constitute a large portion of the EM spectrum and as such are significant to the process of acquiring knowledge of the vast universe we live in. The Radio Science Systems Group (RSSG) entirely devotes itself to the analysis of radio wave phenomena and developing tools to assist in the study. Through this analysis, one can discover the compositions of atmosphere, gravitational fields, temperature, etc. of a celestial body in question. Most recently the RSSG has been implementing a Radio Science Receiver (RSR) in the Deep Space Network (DSN). The RSR is an open-loop receiver with the primary task of supporting radio science experiments. It does so by locating the spacecraft on a mission, using user uploaded tuning frequencies and trajectory prediction parameters, and measuring various changes to the carrier signal such as changes in frequency, amplification, and/or polarization. As of now, when radio science data is received, it is down converted before heading off to the RSR. In the RSR, the signal is digitized, decimated to a lower sampling rate, runs through a signal processor which extracts phase and frequency information of the signal, and finally shipped off to a data processor which provides a user real-time monitor data and spectrum plots. Along with the RSR, it would be nice to have a demodulation tool that could potentially offer a real-time analysis of the carrier signal; an example of this real-time analysis would be an immediate temperature profile of the celestial object under study yielded from the carrier signal as it is acquired by the RSR. Computer software of this nature is typically accessed through a Graphical User Interface (GUI), an interface which allows a user to "point and click" and view displays while data is processed in the background. Along with three other projects to be discussed, developing a GUI for a demodulation software tool had been the primary goal for this summer's internship at the Jet Propulsion Lab.

RSR GUI

The design and software for the RSR GUI has changed considerably over the course of the summer. To summarize, the RSR GUI implements a demodulation tool on a digitized radio signal received from a spacecraft through the Deep Space Network (DSN). As with all GUIs, instead of running the demodulation process and analysis in the command line of a machine, the user can simply "point and click", selecting values for parameters to be used and specific modules of the tool to be run. Initially it was believed the GUI would be built using MATLAB's GUI creator while a few other ideas were considered as well, most notably a web-based interface. Ultimately, we chose to use the Qt Software Development Kit (SDK) for its versatility between platforms.

At this stage in time, the GUI is capable of running through a pre-analysis process. This process includes selecting the demodulation processes the user would like to run, inputting parameters to be used in the analysis, and loading a data file, each task located in a window separate from the main window where these selections may be made. When selecting demodulation processes, a dialog window presents eight check boxes corresponding to eight steps in the full analysis method. Figure 1 below provides an image of the dialog window in which the user may select a desired combination of demodulation processes to be executed.

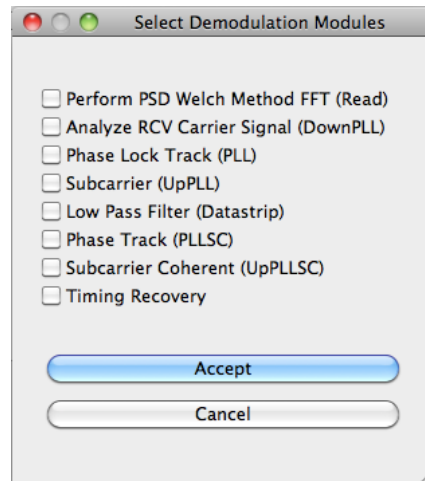


Figure 1. *Demodulation Window*. Dialog window where the user selects steps of the demodulation process to be run.

For whatever reason, time efficiency most likely, the user may decide not to run the entire demodulation process; the option to not run the entire analysis is available via these eight check boxes. However, each module (with the exception of the first, "Read" module) of the demodulation process is dependent on other modules. In the dialog window, the modules have been arranged to reflect the order in which the full demodulation process is carried out. With the exception of the first module, every module is dependent on all the preceding modules, calling upon calculations from these modules. For example, referring to Figure 2 below, if the user wishes to run the demodulation process only up to the Low Pass Filter, all the preceding modules will be automatically selected as the "Low Pass Filter" module requires information and calculations from them.

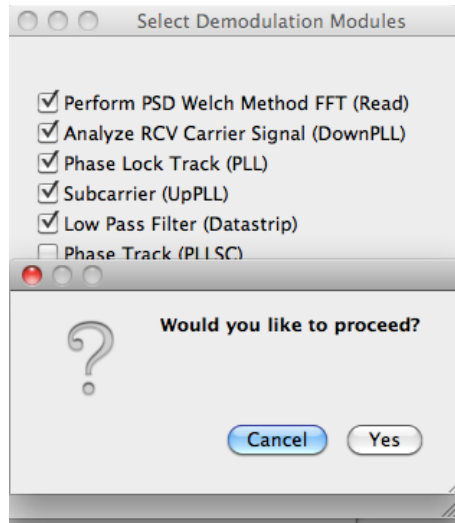


Figure 2. *Demodulation Selection*. Each module is dependent on the preceding one. Upon agreeing to proceed, a makefile calling upon the selected modules is written.

With a given combination of check boxes, an integer is assigned to said combination and passed back to the main screen. The main screen then takes this integer and automatically creates a makefile that calls on the analysis modules selected. If no modules are selected, an error message will appear. If the user would like to choose specific parameters of the demodulation process, such as the sampling rate or low pass filter bandwidth, they may do so in another dialog box seen in Figure 3. Here, all the parameters of the demodulation process are listed and may be altered. The dialog only accepts integers and can always be reset to default numbers.

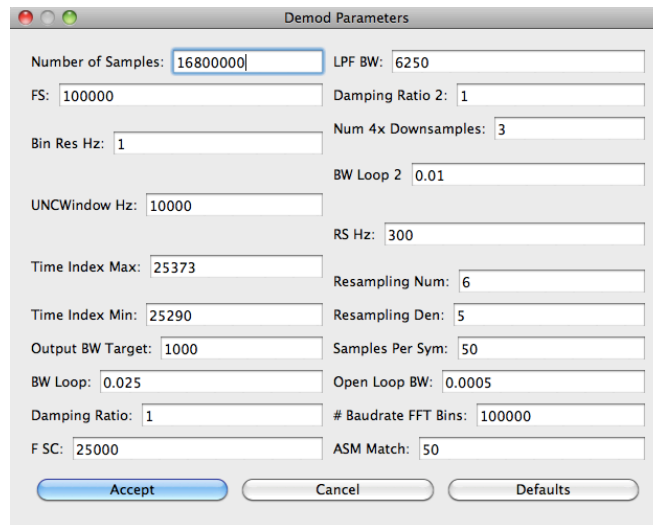


Figure 3. *Demodulation Parameters*. Dialog window which accepts integer values for parameters to be used in the demodulation process.

When the user accepts the values inputted, a file is generated with these parameters recorded and is later called when the analysis is run. Lastly, the GUI is capable of accessing other applications which in the future will mean the GUI will call on an application to run the analysis utilizing the demodulation module and parameter files. Unfortunately, the GUI is quite far from a finished product, as much more needs to be coded.

S.O.A.P. SIMULATIONS

SOAP is an analysis program used primarily for simulations and visual displays, although it is capable of performing certain levels of calculations. The primary task was to also model and simulate a link analysis between any remote ground terminal and ISS. The secondary task using SOAP was to model and simulate a three-way link analysis between the White Sand Ground Terminal (including a site in New Mexico and Guam), any TDRS, and ISS. The ground terminals chosen were the University of Hawai'i at Manoa and the University of Idaho. Both models will be discussed shortly but first one must understand how SOAP works.

In order to build an effective and useful model, one has to know how to interpret the values of certain parameters. Thus, familiarity with the software as well as the underlying orbital mechanics was absolutely essential. In particular we learned how to interpret NORAD two-line element (TLE) sets used for satellite tracking and confirm that an object placed into the model situation was located where the NORAD data implied it should be located. TLEs contain all the parameters required to completely define a Keplerian orbit and more.

The process in which SOAP handles the TLE sets will be discussed lightly, but a more in-depth description is given in Hoss. SOAP takes these TLE sets and input them into simplified general perturbations (SGP) models. In general, SGP models calculate the orbital state vectors containing positions and velocities of a given satellite's TLE set. The positions (x, y, and z) correspond to the three-dimensional location of the satellite relative to the Earth-centered inertial coordinate system and the velocities correspond to the velocity of the satellite in the x, y, and z directions. These six-dimensional state vectors are repeatedly updated through the SGP model, which accounts for perturbations of the satellite caused by the gravitational forces of the Earth, Sun, and Moon. A simulation clock drives the simulation from a user-defined epoch and cycles forward (or backward) in user-defined time steps. Quite simply, when a step forward (or backward) in time is taken by the simulation clock in SOAP, the SGP models predict and update the orbital state vectors of a satellite through the information given by the TLE sets, resulting in a display of the satellites new location.

To perform any significant radio link analysis, one would have to build a suite of platforms, sensors, transmitters, and receivers. When developing this part of the simulation and analysis, it was absolutely crucial to understand SOAP's concept of coordinate systems. Basically, every object generated in SOAP (planets, satellites, etc. and even views) requires a coordinate system so SOAP and the object can compute its position (and velocity if necessary) in the simulation relative to Earth, space, and other objects.

Once the model was set up properly, one can run a simulation and perform a desired analysis. Again, for this project we developed two different scenarios simulating an S-band radio

uplink to the ISS. The first scenario was simply a direct uplink from an arbitrary remote location on the surface of Earth. Both the University of Hawai'i at Manoa (UHM) and the University of Idaho were chosen as these remote locations. Figure 4, located at the end of this section, provides an image from a SOAP scenario of a radio uplink at 2.025 GHz between UHM and ISS. From these two locations, an S-band signal is emitted towards the ISS as it passes over. Once the link closes, the display of SOAP shows a green line between the ISS and the location. Using a variety of tools offered in SOAP, two significant analyses were conducted both of which are motivated by the fact that the ISS currently "zips" by overhead. First, we were able to generate a list of dates and UTC times a link between UHM and the ISS would be closed over a one-week span. It would be useful then to know before conducting an experiment when the ISS would fly overhead of UHM and how long one would be able to maintain a signal, i.e. perform an experiment. The second analysis we went after was to determine the rate of elevation change of the ISS relative to a ground viewer at UHM. One could then use this information to ensure their radio antenna could track the ISS across the sky. Overall, this information provides useful to an amateur radio scientist or university with a portable RSR wishing to perform tracking, ranging, and other radio science experiments involving the ISS.

The second scenario was a bit more complicated, involving quite a bit of creativity, which would later be implemented on the first scenario as well. This scenario was a three-way uplink originating from two White Sands Ground Terminals, one in New Mexico (WSGT) and the other in Guam (GSGT). At specific Ku-Band frequencies, WSGT would be in constant link with TDRS-3, and 6 and GSGT in constant link with TDRS-7. In addition, we also simulated an S-band uplink from WSGT to TDRS-9. The reason these links are never lost is due to the fact that the entire TDRSS is geostationary, therefore links can be established, ideally, at any given time. Next, links had to be established between each of the TDRSs and the ISS, each of which were at S-band frequencies. Here is where the creativity came into play. Initially, it was assumed that an antenna, in this case a module to be attached to the ISS next year called CoNNecT, could only receive signals from the bow and not from the sides, the solar panels contributing to blockage of the radio signal. However, for transmitters and receivers SOAP only projects a cone into space where a link can occur, complicated structures representing a field of vision (FOV) cannot be built. To overcome this problem, there were three different receivers built and can be described using cones. One FOV constructed was a cone with a 75-degree central angle facing "forward". The other two FOV represented areas where the solar panels would block the signal. Using Boolean logic, these three FOV were intersected to yield the true FOV. Visually, this was even more difficult to accomplish, but still completed. This method was later integrated into the first scenario. Our analysis included only dates and UTC times a three-way link was closed. The simulation is using carrier waves only, no modulated signals, and provided an excellent means of visualizing the three-way link.

There was discussion of a third scenario, but SOAP is not capable of simulating such a scenario. The third scenario was to simulate a ranging experiment between UHM and ISS. Ranging not only informs a ground station on the distance a particular satellite is from the station, but also where the satellite is located in space. Having amateur radio scientists (in collaboration with JPL) range remotely from anywhere on the planet with ISS would only help improve the ability to accurately pinpoint its location in space. Although SOAP was not capable of simulating a ranging experiment, one could easily determine times the experiment could be

performed by using SOAP's analysis capabilities. Figure 6 provides the results of such an analysis along with the lengths of each ISS pass over UHM for a one week period from August 24th, 2011 at 12:00 UTC to August 31st, 2011 at 12:00 UTC.

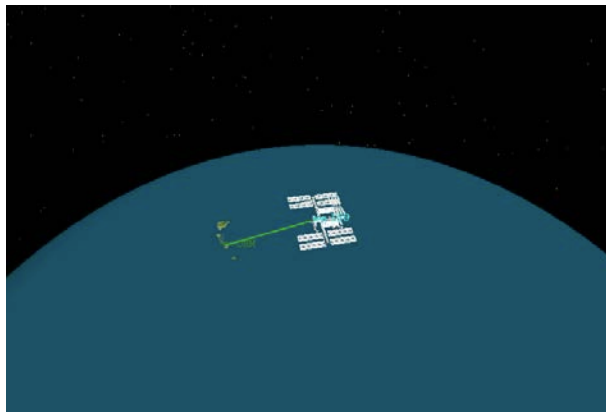


Figure 4. *SOAP Scenario 1*. S-Band uplink from UHM to ISS

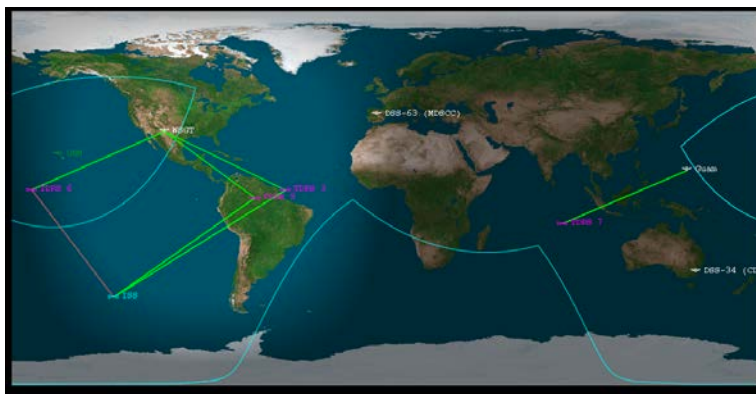


Figure 5. *SOAP Scenario 2*. Three-Way Radio Link from WSGT to TDRS-3 and 9 to ISS. Link between TDRS-6 and ISS is actually a red link, it does not exist.

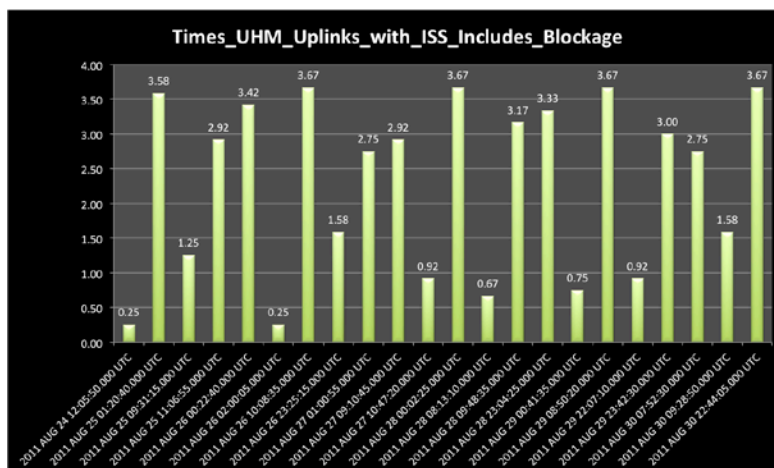


Figure 6. *SOAP Scenario 3*. Dates, Times, & Lengths of closed link Radio Uplink, UHM to ISS.

CCSDS LINK BUDGET

The third project assigned over summer involved working with a radio science software tool called the Consultative Committee for Space Data Systems link Design Control Table (CCSDS-DCT). The CCSDS-DCT is primarily used to gauge the capabilities of a telecommunications link, for both proposed and existing missions. For links in existence, the CCSDS-DCT can critique the performance of said link under changes to original conditions. One of the first tasks we were given this summer was to convert the CCSDS-DCT from Excel 2003 to MATLAB. The reason this conversion was desired stemmed from the inability to run the software developed in Excel 2003 with subsequent versions of Excel. There were two real problems, the first being Microsoft had discontinued a specific add-in the CCSDS-DCT utilized and the second turned out to be a compatibility issue. However, this compatibility issue turned out to be a difference in the syntax used for the macros in Excel 2003 and Excel 2011. In addition, third-party software was developed to account for Microsoft's elimination of the specific add-in used by the CCSDS-DCT. With this tool up and running, the ensuing task involved performing a link analysis with the CCSDS-DCT based on actual Cassini data. Although this Cassini data has already been processed, the main point is to understand how the tool operates by mimicking data results (such as range), learning what forms of data and parameters are interesting to radio scientists, and to discover the differences between the two fields of telecommunications and radio science. Although converting this tool seems like a trivial task, its significance lies in the capabilities of the tool itself. This significance is discussed thoroughly in the conclusion.

OPERATION OF RSR WITH NEW HORIZONS

The last task assigned had been the operation of the RSR located in Canberra, Australia remotely from JPL as it makes a weekly connection test with New Horizons. As mentioned before, the RSR operates as an open-loop controller, which, more or less, means that the system performs with minimal input from a human user. Open-loop controllers need only the current state of system (or initial parameters) as a model computes the desired output. In the case of the RSR, predict files containing information on a spacecraft's last known location and velocities act as the current state of the system. The RSR then internally updates the location of the spacecraft using these predict files and the correct model for predicting a given spacecraft's location. Next, the RSR begins to emit a radio signal in hope of link with the spacecraft. We will be operating the RSR by retrieving these data predict files for the New Horizons spacecraft and hand these files off to the RSR. From here, New Horizons will be located using the model for location the spacecraft and a link will be established. However, we will not be performing any science or an analysis on the established link.

CONCLUSION

Working this summer with the RSSG seemed to be three very separate tasks but in fact all three tasks directly relate to each other. In fact, one could consider all three projects a mock of a real radio science experiment, which can be broken down into three phases. The first phase was to use SOAP to visualize and plan a radio science experiment from an arbitrary remote location. Regarding SOAP, the project was finished in its entirety. The intention of the SOAP project was

to visualize two different scenarios of a radio link with the ISS. With the first scenario, the goal was to determine whether or not an amateur radio scientist with a portable RSR could perform a radio science experiment with the ISS. To do this, a link would need to be established between a remote location and the ISS. We performed two analyses on the link to yield dates and times a link could be established at any point in the future, the duration of these links, and lastly the speed an antenna would have to be able to rotate in order to maintain a lock with the ISS. Once we knew a radio science experiment could be performed from, say, the University of Hawaii at Manoa, we could use this information in the second phase of our mock radio science experiment.

The second phase of our pseudo radio science experiment would be the analysis of the link. This task would be accomplished using the CCSDS-DCT. With CCSDS-DCT we attempted to mimic the results of tests already performed with Cassini as a task. But in the context of a pseudo radio science experiment, this would be the phase where we could answer any number of questions of our link. For example, "Is the link transmitting with sufficient power?", "Were all the losses accounted for and if not which losses need to be accounted for?", or "Does the emitted signal reach ISS with adequate gain?" are all questions that could be answered using the CCSDS-DCT. Once these questions have been answered and the link between UHM (or Idaho) and the ISS can be considered a capable link for radio science experiment, one would move on to the final phase of the experiment, data processing.

With the knowledge of how to operate the RSR remotely, data acquisition remotely only becomes an issue of permission. Even better, with a portable RSR, a radio science experiment could be executed at a given time and date provided by the SOAP simulations. During the data processing of this mock radio science experiment, one could use the GUI we were developing to decode and run a demodulation analysis of the carrier signal. Unfortunately, as mentioned before, the RSR GUI has quite a ways to go until it can be considered "finished". At this stage, the GUI is only capable of accepting user inputs and preparing for the analysis. The GUI does not however, actually execute the analysis. Our group came to a consensus that the GUI would call an application (it is currently capable of this) that would run the analysis. Moreover, once the analysis is complete, any user would like to see an immediate display of results of the analysis. This could be as simple as frequency-amplitude plot, the point is the user would not have to search for the results. Ultimately, it would be great if the GUI could be used as real-time data is collected, projecting a display, most likely of the signal, as close to real-time as possible. Yet, the GUI does not have the capability to display information at this point in time.

ACKNOWLEDGEMENTS

First and foremost, thank you to the Hawai'i Space Grant Consortium; without the HSGC, I would have no experience to speak of or individuals to thank. My utmost thanks and gratitude goes to the California Institute of Technology and the Jet Propulsion Lab. Having the opportunity to spend ten weeks at two institutes spearheading the advancement of humankind's understanding of the universe opened the door to amazing insights and interactions. I met brilliant individuals, forged strong bonds, truly saw the dedication and passion required being a successful scientist and colleague, and learned more about the type of research and projects both Caltech and JPL are responsible for. I'd like to thank everyone in the education office at JPL for their efforts in making students outside of Caltech feel welcome and keeping us on track with

what seemed like “weekly” progress reports. Also, I'd like to thank David Orozco, Melissa Soriano, and Sel Kayalar for all the help they provided myself and my partner this summer. A warm thank you to everyone in the Radio Science Systems Group for treating us like family and offering their support. Thank you to my partner Carlos Gonzalez of the University of Idaho for all his effort and providing feedback. We worked tirelessly from dawn until dusk, but had a great time in the process. I must also thank Dr. Monique Chyba for always providing me the opportunities to be successful. She casually asked me one day if I'd like to spend a summer at JPL, and I cannot express how grateful I am that she would even think to offer me such an opportunity. Thank you to Sami Asmar, the supervisor of the Radio Science Systems Group. Sami is truly a generous man who opened his arms to the interns, offering his expertise, guidance, and the occasional joke. Lastly, a special thank you to my mentor Kamal Oudrhiri. He not only worked diligently with my partner and I, but trusted us as though we were his own colleagues. Kamal's kindness will never be forgotten. Thank you to everyone who had a hand in providing me with a fantastic summer experience at the Jet Propulsion Lab.

REFERENCES

- Andre, P., et al. (2009) A Deep Space Network Portable Radio Science Receiver. Tech Briefs. Retrieved May 8, 2011 from <http://www.techbriefs.com/component/content/article/6341>.
- Asmar, S., et al. (2003) Reducing cost with autonomous operations of the Deep Space Network radio science receiver. 5th International Symposium on Reducing the Cost of Spacecraft Ground Systems and Operations. Pasadena, CA.
- Hoots, F.R., Roerich, R.L., (1980) Models For Propagation of NORAD Element Sets, Space Track Report No. 3, Aerospace Defense Command, USAF.
- Johnston, D., Asmar, S., Chang, C., Estabrook, P., Finely, S., Pham, T., Satorius, E. (2004) Radio Science Receiver Support of the Mars Exploration Rover Landings. Third ESA International Workshop on Tracking, Telemetry and Command Systems For Space Applications. Darmstadt, Germany.
- Jongeling, A., Finley S.G. (2004) Radio Science Receiver Standard Formatted Date Unit (SFDU). Documented owned by M.J. Connally, Jet Propulsion Laboratory.
- Radio Science Systems Group. (2011) Retrieved May 4, 2011 from <http://radioscience.jpl.nasa.gov/>.
- Stodden, D., Coggi, J., Paget, J., Phan, M., Swartz, R. (2010) SOAP Version 13 User's Manual Rough Draft. Aerospace Corporation. El Segundo, California.

LUNAR MICRO ROVER CAMERA SYSTEM DEVELOPMENT

Adria S. Fung
Robotics Engineering
Worcester Polytechnic Institute
Worcester, Massachusetts 01609

ABSTRACT

The objective of my internship at NASA Ames Research Center Robotics Academy is to develop a Camera System flexible enough to allow the user to switch seamlessly between Navigation mode and Recording mode. One task was to determine how many packets the link could drop before the image became too distorted for the human operator to drive. Another task was to explore image compression techniques for low bandwidth connections but still be able to drive the rover. Basics in Electronics and C Programming were taught in order to achieve this objective. A commercially available IP webcam mounted on a rover testbed was used to determine teleoperation capabilities with two Linux-based computers connected via Ethernet mimicking a lossy environment.

INTRODUCTION

The NASA Ames Robotics Academy comprises of FIRST (For Inspiration and Recognition of Science and Technology), VEX, and Botball students and alumni as well as members interested in the field of Robotics. The Ames Robotics Academy was started by NASA Civil Servant, Mark Leon, an avid FIRST emcee at various Robotics Competitions. The Robotics Academy is one of several ways NASA is cultivating STEM (Science, Technology, Engineering, and Math) leaders, focusing more on college and high school level students.

The Lunar Micro Rover is the ongoing project at NASA Ames Robotics Academy. The goal of the project is to create inexpensive Lunar Micro Rovers capable of enduring the Lunar environment. The mission involves deploying two Micro Rovers to the moon by 2012, each capable of carrying out specific objectives such as Micro-Payloads, Lunar Exploration, Extended Deployment, and Tele-Operation. Members of the Robotics Academy are assigned to their specific subgroups: Structural Integrity System, Power Control System, Communications System, Command and Data Handling System, Rover Avionics System, Camera Payload System, Thermal Control System, Radiation Mitigation System, and Rover Simulators. For my internship, I was assigned to the Camera System.

The Camera System consists of two subsystems: imaging hardware and software and compression hardware and software shown in Figure 8. The camera will be used during tele-operated mode to provide a live feed to the human drivers. It will also be used to record high-resolution pictures while on the lunar surface. The camera must be 1.3 megapixels or greater, have a low power draw 5W or less, a small form factor, a 100G or more shock-resistant rugged enclosure, capable of operating in a -40 to 85 degrees Celsius temperature window, have scalable bandwidth outputs, and utilize a standard lens mount.

METHODS

The first test done on the prototype camera was on a commercially available rover test bed with verified mobility capabilities. The rover and camera were controlled by web interface operated by servers in a remote Academy office. Packet loss and latency was controlled by the aforementioned servers. The group's hypothesis was that the image quality would degrade as packets were dropped. Ultimately, the image quality of the video feed did not change; instead the speed of the stream did slow down significantly when the amount of packet drops increased. It was concluded that additional steps needed to be taken to ensure the image quality would degrade more gracefully and maintain a more even frame rate.



Figure 1: The Rover testbed used to simulate packet loss and driving

Photo by Adria Fung

The second test was done through a handheld video camera connected to a computer via FireWire. A Linux-based computer running VLC Media Player served as the media streamer. With the three computers the group had at its disposal, all had some minor problem that inhibited the testing. For example, one computer had a FireWire port, but was not able to connect to another computer via Ethernet cable. The handheld video camera was removed from testing, and a laptop webcam was used instead; however, one of the computers did not recognize its own webcam when operating under Linux. This method had proven itself to be overly complex for the test required, and so additional work on this test was abandoned.

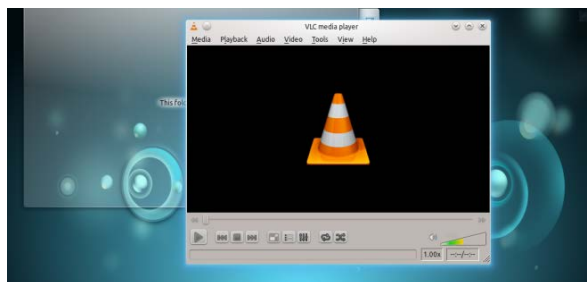


Figure 2: VLC Media Player in Linux

Screenshot by Adria Fung

DEVELOPMENT

The Camera System subgroup was tasked with determining how best to compress the driving image but still allow the human operator to drive the rover on the moon. Many different image compression techniques were tested to see whether the image could be used for driving, despite large amounts of image data being removed. The use of a black and white image instead of a color image allowed us to compress the on-disk size of each image by a factor of 24 over a raw RGB image. Additional lossless compression techniques allowed further compression. Four different methods of converting a full-color RGB image to a black and white binary image are shown.



Figure 3: Original Image

Photo by Camera subgroup



Figure 4:
Floyd Steinberg Dithering

Figure 5:
Edge Detecting

Figure 6:
Thresholding

Figure 7:
Randomized Dithering

Photos by Camera subgroup

RESULTS

Each method had significantly different results. Of the methods described, Floyd-Steinberg Dithering was chosen because it most fully represents the original picture using only two colors.

In pseudocode:

```
for each y from top to bottom
  for each x from left to right
```

```
oldpixel := pixel[x][y]
newpixel := find_closest_palette_color(oldpixel)
pixel[x][y] := newpixel
quant_error := oldpixel - newpixel
pixel[x+1][y] := pixel[x+1][y] + 7/16 * quant_error
pixel[x-1][y+1] := pixel[x-1][y+1] + 3/16 * quant_error
pixel[x][y+1] := pixel[x][y+1] + 5/16 * quant_error
pixel[x+1][y+1] := pixel[x+1][y+1] + 1/16 * quant_error
```

DISCUSSION

The Camera System is still in the development stage. Streaming the video feed over the radio is an ongoing work in progress. Fully utilizing the subsampling and compressing capabilities of the camera and frame grabber board are being investigated. Matlab is being used to explore additional compression techniques, such as Run-Length, Huffman, or LZW Encoding. It is still in discussion whether or not to compress the image in JPEG, PNG or JBIG format, or to use a video file format like MPEG or MJPEG.

CONCLUSION

Dithering and image compression have both been completed. Floyd-Steinberg Dithering was chosen because it utilizes only two colors; black and white, rather than gray scale, therefore, reducing the amount of data being sent from the moon to Earth. It proved to depict the image more truly than other techniques while requiring less bandwidth than a comparable grayscale image.

ACKNOWLEDGEMENTS

I would like to thank NASA Ames Robotics Academy for the opportunity to meet and work with many different people. I would also like to thank Mark Leon, Drew Price, Guy Chriqui, and Jenny Yang for organizing this project and making it one of my most memorable summers. I would also like to thank my Camera Payload team, Dane Bennington and Rob Rucker, for their continuous guidance in this program. I would also like to thank Art and Rene Kimura and the Hawai'i Space Grant Consortium for their support in allowing me to participate in this internship.

FIGURES

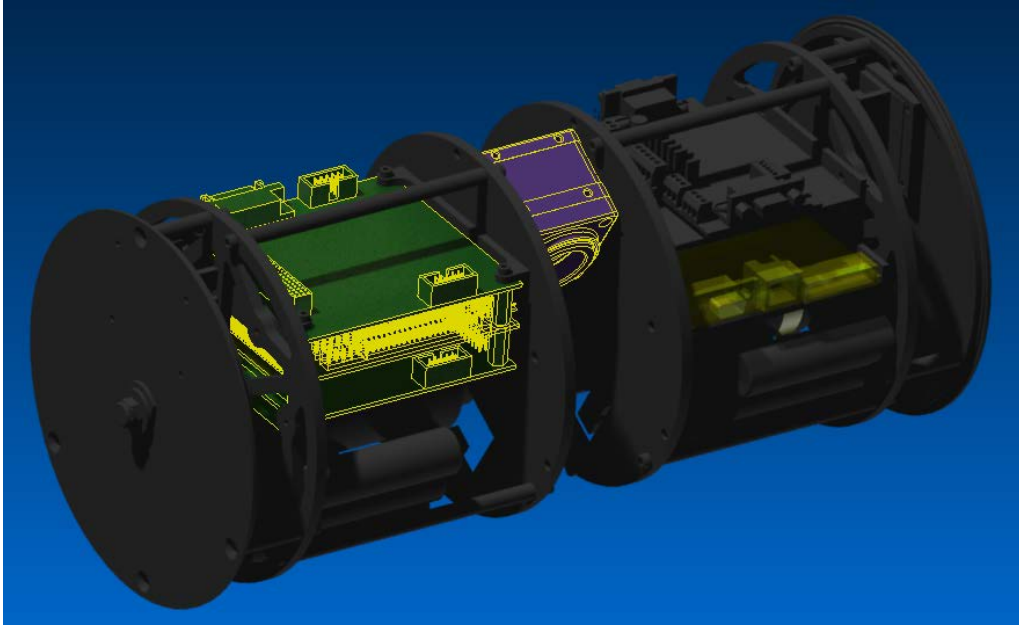


Figure 8: Camera subsystem in the Rover

Drawn by NASA Ames Robotics Academy

LADEE DECOMMISSIONING IMPACT DISPERSION ANALYSIS

Arlen M. Kam
Department of Aeronautics and Astronautics
Stanford University
Stanford, CA 94305

ABSTRACT

The Lunar Atmosphere and Dust Environment Explorer (LADEE) will spend 100 days in an equatorial science orbit around the Moon. After the propellant has been depleted, during the decommissioning phase of the mission, LADEE will deorbit and impact the lunar surface. The non-uniformity of the Moon's gravity distribution will cause orbit perturbations, and analyzing the trajectory of the decommissioning phase of LADEE will provide important information on acceptable orbital parameters at the end of the science phase. Using MATLAB in connection with the STK Astrogator to propagate the deorbit trajectory allows for dispersion generation to vary the apoapsis altitude, periapsis altitude, argument of periapsis, and longitude of the ascending node. Analysis of the resulting array of possible impact sites provides the probability of impacting near existing Apollo sites, which need to be preserved as historic sites. Using this information, mission designers can identify certain combinations of orbital parameters to avoid before decommissioning in order to be certain to miss Apollo sites on impact. The probability of impacting within 0.5 degrees of an Apollo site was 0.0161%, however the impact distribution showed that the Apollo 15 and 17 sites are in areas of high densities of impacts.

LADEE

LADEE will launch in May 2013 and take scientific observations while in an equatorial orbit around the Moon for 100 days. While most lunar orbiting mission use a polar orbit, an equatorial orbit is necessary for LADEE, as a key goal of the mission is to take observations of the rise of lunar dust at the day/night terminator.

PROJECT GOALS

Orbit maintenance maneuvers will be carried out throughout the science phase of the LADEE mission. The ideal orbit is a 50km x 50km equatorial orbit, but non-uniform characteristics of the Moon's gravity cause orbital perturbations that make it difficult to maintain this orbit. Thus, at the end of the science phase and the beginning of the decommissioning phase, the orbital parameters could be vastly different from this 50km x 50km nominal orbit.

Creating dispersions of the orbital parameters just prior to the decommissioning phase and propagating the uncontrolled orbits down to impact produces a map of potential impact sites. Finding the probability of hitting an existing Apollo site enables identification of those certain orbital parameters to avoid before the decommissioning phase. The decommissioning phase of the LADEE mission will allow the observatory to deorbit and impact the lunar surface. While the decommissioning phase will likely still execute orbit maintaining maneuvers, this analysis operates on the assumption that there will be no orbit corrections during this phase.

Apollo landing sites on the lunar surface are historically and politically significant not only for America, but for the entire world. Preserving these sites is important, therefore completing an impact analysis is important for any lunar mission that plans to deorbit and impact the lunar surface.

MATLAB AND STK ASTROGATOR

One of the major goals of this project was to use MATLAB to drive STK, thus the details of that connection is important to include here. The propagator used in the STK Astrogator is a lunar model that uses the LP150Q gravity field model to the 50th degree, and also takes into account the effects of solar radiation pressure and Sun and Earth third body forces. The simulation was set to propagate until the altitude equals zero.

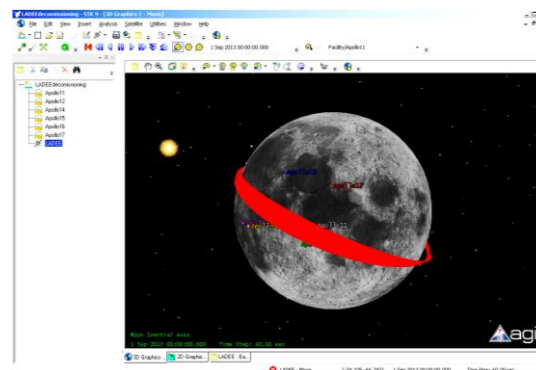


Figure 1: Deorbit simulation in STK

Once the connection between MATLAB and STK is established (instructions for that can be found on the STK website), use the following MATLAB commands to set initial orbital parameters, run the simulation, and obtain output values.

To set value: `stkExec(conid,'Astrogator */Satellite/LADEE SetValue
MainSequence.SegmentList.Initial_State.InitialState.Keplerian.PeriapsisAltSize
50 km')`

To run simulation: `stkExec(conid,'Astrogator */Satellite/LADEE RunMCS')`

To get value: `stkExec(conid,'Astrogator_RM */Satellite/LADEE GetValue
MainSequence.SegmentList.Propagate.FinalState.Mixed_Spherical.Latitude')`

DISPERSION GENERATION

Varying altitude of apoapsis, altitude of periapsis, longitude of ascending node, and argument of periapsis allows for an extensive range of possible orbits. Using nested for loops in MATLAB, every orbit is propagated in STK and the resulting longitude and latitude of the impact site is recorded.

Table 1: Parameter variations

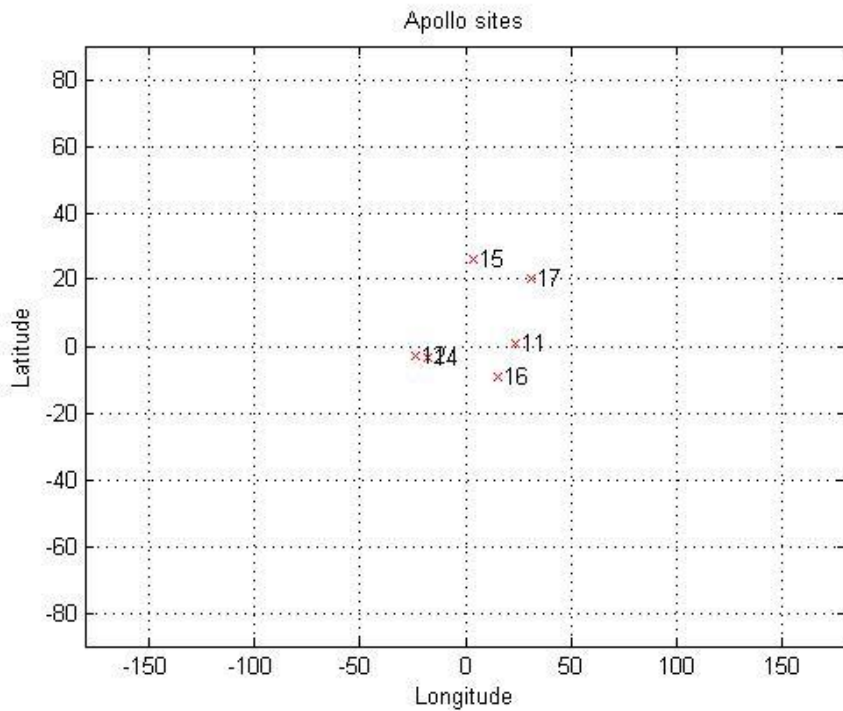
	Altitude of Apoapsis (km)	Altitude of Periapsis (km)	Longitude of Ascending Node (degree)	Argument of Periapsis (degree)
Range	50-150	15-50	0-359	0-359
Step	25	5	30	30

RESULTS

Any impacts that come within a certain distance of an Apollo site are recorded along with the orbital parameters that caused that impact. The plot of the impact sites shows a pattern in the gravity distribution near the equator

IMPACT PATTERN

Here we can see clear areas with higher densities of impacts, which could be caused by patterns in the Moon's gravity distribution.

**Figure 2: Map of Apollo sites**

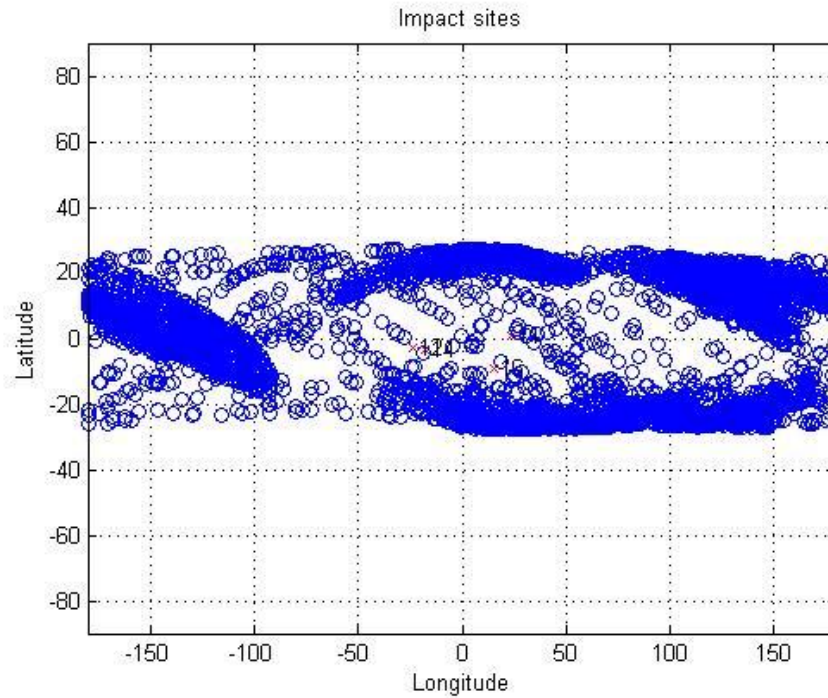


Figure 3: Scatter of 6228 unique simulations

NEARBY IMPACTS

Only one impact came within 0.5° of Apollo sites out of 6228 simulations, which makes for a near hit probability of 0.0161%. However, both the Apollo 17 and Apollo 15 sites are in areas of high densities of impacts while all other Apollo sites are in an area of fewer impacts.

Table 2: Near impacts within 0.5 degrees

Latitude (deg)	Longitude (deg)	Periapsis altitude (km)	Apoapsis altitude (km)	LAN (deg)	Argument of periapsis (deg)	Apollo
20.34	31.07	50	100	30	0	17

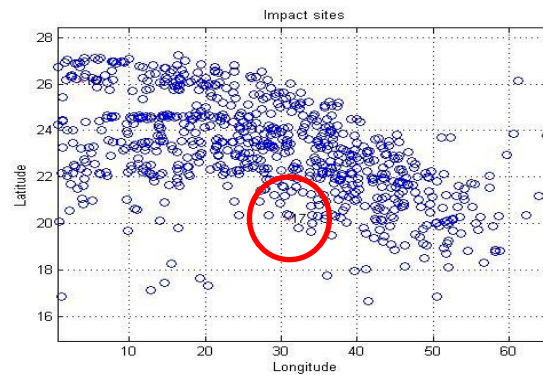


Figure 4: Apollo 17 location

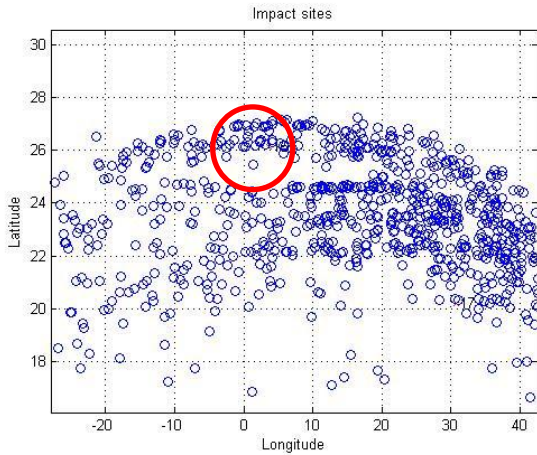


Figure 5: Apollo 15 location

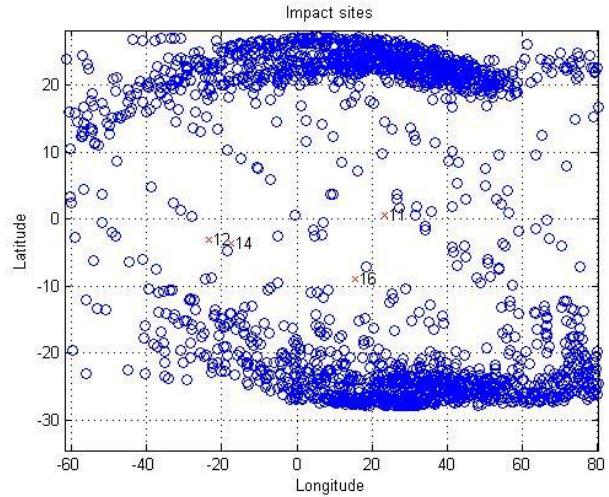


Figure 6: Apollo 11, 12, 14, 16

CONCLUSION

The probability of impacting near an Apollo site is 0.0161%, which shows that it is highly unlikely that LADEE will disturb a historic Apollo site. The only nearby impact happens near the Apollo 17 site, which is near the edge of an area that exhibits a high density of impacts. The Apollo 15 site is also in a region with a high density of impacts. By identifying these high density areas and the orbital parameters that end up propagating into these areas, the orbit prior to decommissioning can be manipulated to avoid those certain parameters.

A clear pattern emerged from the plot of the impact sites (Figure 3). This is probably due to patterns in the Moon's gravity distribution due to terrain, rock composition, third body effects, and others. Observing the perturbations of LADEE's orbit could provide valuable information on the specifics of this gravity distribution pattern.

FUTURE WORK

This simulation used the stopping condition of altitude = 0, which does not take lunar terrain into account. This can be improved upon by requesting the lunar terrain model from STK and incorporating this data into the simulation, which would give more accurate information on the impact locations.

While a cursory hypothesis was presented above to explain the pattern in the impact plot, further analysis on the Moon's gravity distribution could provide better explanations for this phenomenon.

ACKNOWLEDGEMENTS

Dr. Butler Hine has been a valuable resource for LADEE information and an incredible mentor. Laura Plice, Anthony Genova, and many others provided important guidance and support throughout the summer.

This project could not have been possible without the NASA Ames Academy and funding from the Hawai'i Space Grant Consortium.

REFERENCES

NASA Ames/GSFC. (2011). *LADEE Mission Critical Design Review*.

Wertz, J., & Larson, W. (1999). *Space Mission Analysis and Design*.

LUNAR MICRO ROVER PROJECT

Carissa C. Nakao
College of Engineering
University of Hawai'i at Mānoa
Honolulu, HI 96822

ABSTRACT

The objective of my internship at the NASA Ames Research Center was to help create the next and improved version of the Lunar Micro Rover, or LMR-Alpha. This project has been going on for many years, and our mission was to construct a Lunar Micro Rovers from a family of interoperable modular subsystems capable of supporting a variety of technical objectives such as supporting Micro-Payloads, Lunar Exploration, Extended Deployment, and Tele-Operation. The current way of lunar exploration with humans being sent into space will become obsolete with the start of small robots being sent into space. Also, by taking out the human aspect of space exploration, you take out the human error/risk that can occur during a space mission. This project is the start of whole new revolution in creating an economical and efficient way to have space and planetary exploration. This project is only limited to the extents of our imaginations and is powered by our creativity in the world of science and engineering. Being in the structural group, our objective was to design and modify the previous lunar micro rover designs to bring the success rate of the rover higher.

INTRODUCTION

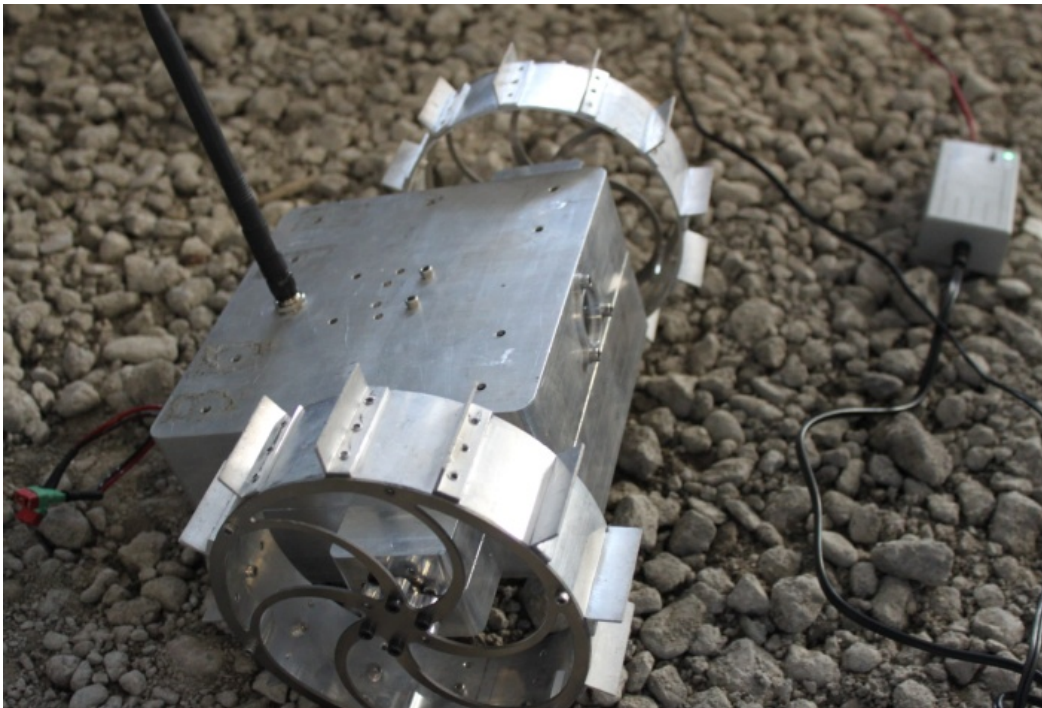
The Lunar Micro Rover Project was started in 2006 by Mark León and has been an ongoing project since. This program is focused towards current and past participants of FIRST (For Inspiration and Recognition of Science and Technology), Botball, and VEX robotics. This project tests the skills that the students have learned from their respective robotics program and incorporate their skills into a project that teaches them useful skills towards their futures. This is the next step from these robotics programs to help incorporate new young minds and to further inspire new young minds in the fields of science, technology, engineering and math (STEM Fields).

The main objective of this project is to create a micro lunar rover that is efficient, low weight (defined as less than 10kg by JPL) and under \$500,000. The cost and weight are very important aspects of this project because the cost to send things out into space are based on the weight and that the amount that it would take to build the rover needs to be economical and not an outrageous price.

This project was split up into many different groups and from there we carried out individual goals and solved problems that would all be towards one project. Each group was split based on a specific variable of the rover (example: camera group, thermal group, power systems group, etc.) I worked with the structural team, where our goal was to create a rover that was more efficient than the last prototype and completely change the design of the chassis.

Throughout the years, the rover has drastically changed in size, shape and functionality. With each prototype, the design and rate of success has always gone up from year to year because many changes are tested and made. The rover project started in 2006, but now has a completely different design compared to the past. Each year, the work would be continued from the previous years, the flaws with the design would be taken into account and the proper changes were made. This transformation process is the product of trial, error and testing throughout the years of this ongoing project.

The moon itself has a much different climate and atmosphere from that of the Earth. The time it takes for the moon to go through one “day” is worth the amount of about 27 days in Earth time. There is almost no tilt in the axis of the moon unlike the earth, causing weather conditions to be harsh. The area where the equator should be would be extremely hot while that by the polar caps would be cold. The area that does not see the sun (darker side) is known to have freezing temperatures. During this project, we had to keep all this in mind to try to create a rover that could withstand all of the physical barriers.



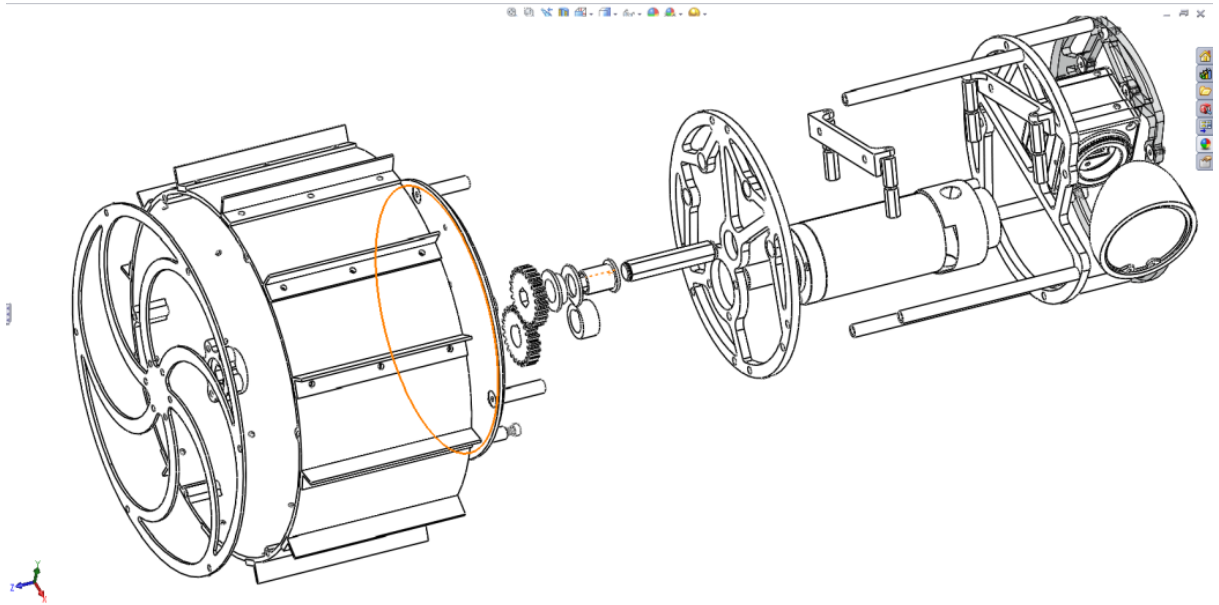
Above is a picture of the 2010 LMR Design.
This prototype was presented to General Pete Worden, NASA Ames Research Center director.
(Summer 2011)

Photo Credit: Carissa Nakao

METHOD

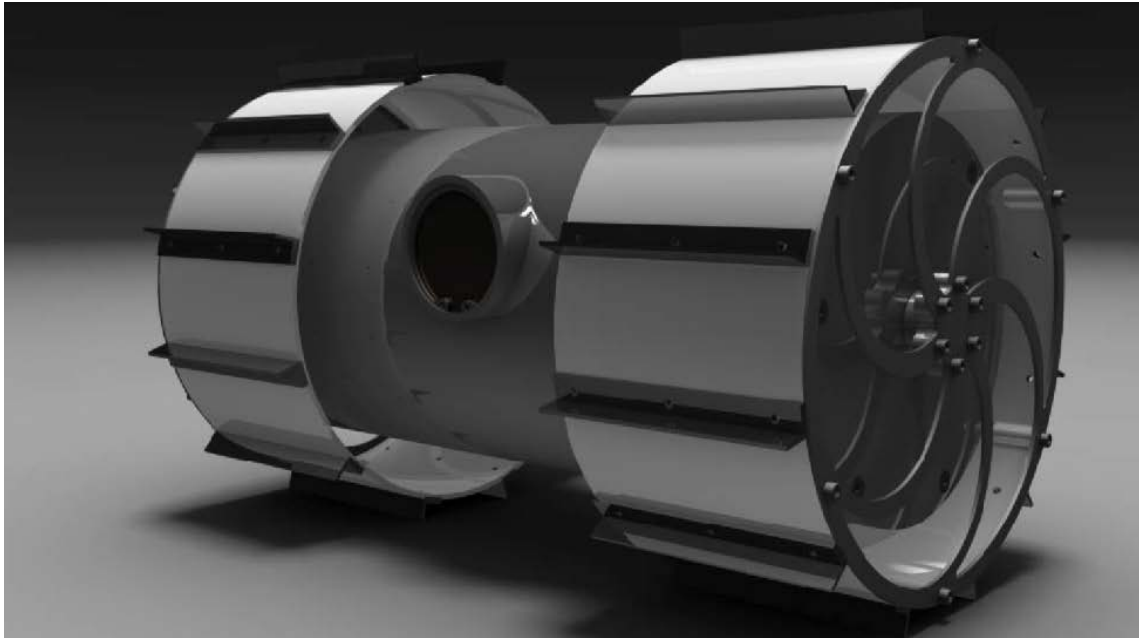
It was decided that in the new design, the rover would have a cylindrical base instead of the previous rectangular base. This would prevent the new rover to have the flaw that the one last year had. The previously used rectangular base was flawed in design because it was not able to travel on the moon's terrain. The base of the rover would get caught up on rocks and craters and the previous design made it hard to turn because the skid would dig up regolith. It was tested that last year's rover would not be able to carry out its mission with its current design. The design of the wheels was kept the same because they performed efficiently in the previous design. They were also kept the same because they were a good thermal mitigation and provided a small suspension system.

To create the model of the new and improved lunar micro rover, the structural team designed the model of it on a program called Solidworks. This program is a 3D design program that you can literally design anything you can imagine. Solidworks is also very useful because it gives you the ability to run simulations within the program and test the strength of the design with a pressure/force test (will show the maximum force that that certain structure/material can take).



Above is an exploded version of the LMR 2011 Rover

Photo Credit: Cara Lai



Above is the 3D designed 2011 LMR

Photo Credit: Structural Team

DISCUSSION

I was not able to see the final result and testing of the rover this year by the end of my internship. But I believe that the new design will have a much more positive result with that of be more efficient on the moon's terrain. Because of my inexperience and knowledge in the mechanical engineering field, I was not allowed to CAD or personally design the rover (being right out of high school). Despite this, I was able to learn how to use Solidworks through the tutorials and I know have the knowledge to CAD future projects.

ACKNOWLEDGEMENT

I would like to thank everyone at the NASA Ames Research Center and everyone that was on this Lunar Micro Rover project for such a great experience. I would like to also thank Art Kimura and Mark León giving me the opportunity and allowing me to participate in this internship. I would especially like to thank Marcia Rei Sistoso and the Hawai'i Space Grant Consortium for funding my internship and for making this whole experience possible. This summer was a huge learning opportunity for me and has changed the way I look at the world of engineering. I would like to give a warm Mahalo to everyone who was involved in this program.

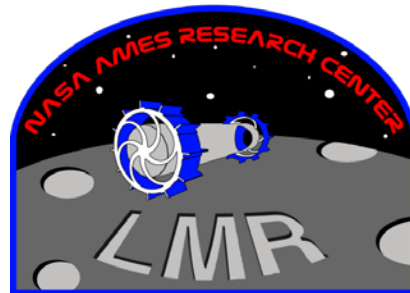
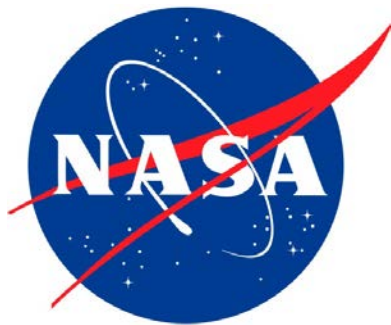


The 2011 LMR Interns

Photo Credit: Carissa Nakao

REFERENCES

- "Lunar Micro-Rover Project." *Lunar Micro-Rover Project*. N.p., n.d. Web. 3 Aug. 2011. <<http://lmr.nasa.gov/>>.
- "Lunar Application of a Micro-Rover | Lunar Science Forum 2011." *Welcome | Lunar Science Forum 2011*. N.p., n.d. Web. 3 Aug. 2011. <<http://lunarscience2011.arc.nasa.gov/lunar-application-micro-rover>>.
- "File:Nasa-logo.gif - Wikipedia, the free encyclopedia." *Wikipedia, the free encyclopedia*. N.p., n.d. Web. 3 Aug. 2011. <<http://en.wikipedia.org/wiki/File:Nasa-logo.gif>>.
- "Hawai'i NASA Space Grant Consortium." *Hawai'i NASA Space Grant Consortium*. N.p., n.d. Web. 5 Aug. 2011. <http://www.spacegrant.hawaii.edu>



DEFENSE APPLICATIONS IN HYPERSPECTRAL REMOTE SENSING

James M. Bishop
School of Ocean and Earth Science and Technology
University of Hawai'i at Mānoa
Honolulu, HI 96822

INTRODUCTION

This summer I worked at Nova-Sol Hawai'i as an Image Analysis intern doing hyperspectral remote sensing. Nova-Sol is a defense contractor that specializes in optical communications and surveillance. My main responsibility was to take data collected by a short wavelength infrared (SWIR) camera and identify targets of interest using both matched filters and anomaly filters. The main tools I used for this job were Matlab and Envi as well as some devices in the optics lab. Nova-Sol's SWIR sensor is a new product and a large part of my task involved adjusting the Matlab code to read the SWIR data as well as providing calibration data to apply to the image cube. I am a senior in the department of Geology and Geophysics and have taken courses in Matlab and Remote Sensing which benefited me in my job with Nova-Sol. I also did a remote sensing project through Space Grant using radar which introduced me to Envi and remote sensing.

ADJUSTING THE IMAGE PROCESSING CODE

My initial task at the Nova-Sol was to familiarize myself with the Matlab algorithm that processed the image cube, applied radiometric calibration, and then did the match and anomaly filtering. This Matlab code is simulating the real time code that is used in conjunction with the sensor. Because Matlab is a higher level computing language than the C code that is used in the real time system and it is faster to write code in. The Matlab code makes it easier to test different approaches to processing the image cube and getting correct target matches than the C code. The C code is used with the real time system because it is less demanding computationally than the Matlab code. The person that wrote the Matlab algorithm was leaving exactly one week after I arrived at the job which meant I had a limited amount of time to ask him questions about how to run the code before he left. I learned as much as I could while he was there, took lots of notes, and processed a lot of data to familiarize myself with running the algorithm.

The algorithm as I received it was set up for a very near infrared sensor (VNIR) and so I began adjusting the code to process the SWIR data that would be arriving soon. The SWIR data was of different spatial and spectral dimension which meant that I had to adjust the Matlab code accordingly. Some of the calibration files were named differently so I adjusted the code to read the appropriate files. I also wrote some code that applied bad pixel interpolation. The code would read in a file that had ones where pixels were bad and zeros where pixels were good. Then it would interpolate by taking the weighted average of the value of the nearest adjacent pixels and apply that to the bad pixel(s). The code was written so that it could run in both the spectral and spatial dimension. I adjusted the algorithm so that when it was run it would save a JPEG image that had the location of the anomaly or matched filter detections circled in red with the thresholding parameters included in the title of the image.

IMAGE CALIBRATION

One of the duties I was assigned was taking flats. Flats are obtained in the optics lab by shining a light of known luminance on the camera and then looking at how each of the pixels in the image reads that light level. If one of the pixels is reading that light level higher or lower than the amount of light that is actually emitted a coefficient is applied to the pixel to calibrate it. The exposure time of the camera affects the amount of light coming in so a range of exposure times need to be calibrated for. The device I used in the lab to generate light was an integrating sphere in which one end the lens of the camera was fixed and at the other end was a light source. The inside of the sphere was coated with a white substance that had nearly perfect reflectance. The light would shine in one end and be reflected all over the sphere so that the focal plane array in the camera was receiving light from every possible angle in order to simulate a real life situation. For every different exposure time I would choose 13 different luminance levels. Three of the levels would be at or above the light saturation level for a given exposure time, and the remaining ten would decrease almost to zero in regular intervals. While I worked all the lights had to be off and the room had to be essentially pitch black so that there would not be any foreign light contamination. The other data I provided with each exposure time was a measure of the dark noise before and after the set of light levels was taken. Dark noise is photons of light that are given off by the camera itself. Finding the dark noise is important because this energy needs to be subtracted from the total amount of signal in order to determine how much of the signal is true radiance. Once I collected the flats and darks in the lab I would provide that to one of my coworkers who generate the coefficients to be applied to each of the pixels. This process is called a non uniformity correction (NUC). Without applying a NUC the image would look noisy (Fig. 1) and it would make the filtering process unreliable. Figure 2 is a plot of DN level versus Band. Each line is a different luminance level. The top couple of lines are flat because they have saturated the pixels at those bands, meaning the DN of those pixels are at their maximum.



Figure 1. The image on the left has not had a non-uniformity correction (NUC) applied. Notice the horizontal striping and grainier look compared to the image on the right. The NUC is useful in more than just creating a clean looking image, it makes it possible to make much more reliable detections on targets of interest.

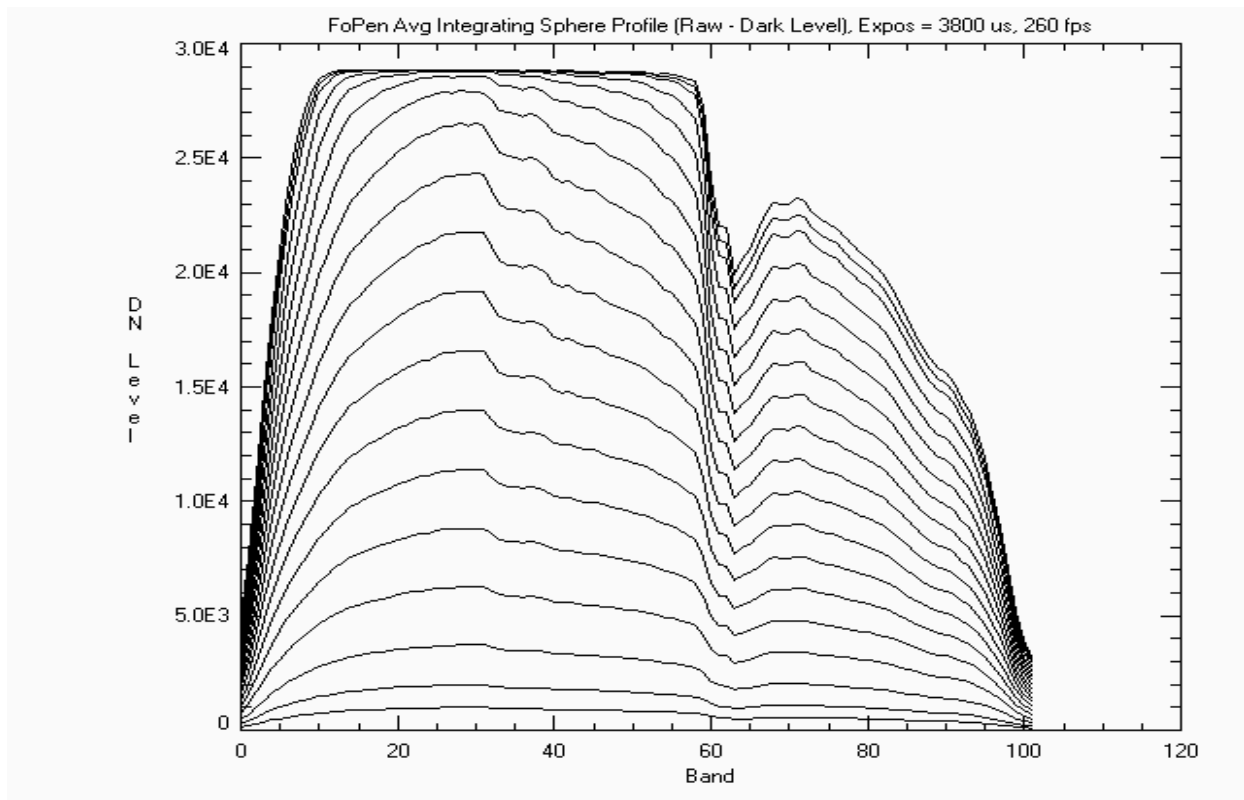


Figure 2. This is a plot of DN level versus band. Each line is a different luminance level. The highest few levels saturate the pixels at certain bands.

SWIR CAMERA TESTING

During my internship Nova-Sol had a test of its SWIR camera for a potential customer. The test area simulated the conditions in which the camera would be used by the customer and on the ground were various targets of interest that the customer was interested in being able to identify. The test area and the targets are sensitive information so I am unable to go in to more specific details. My main responsibility was to use the SWIR data acquired at the test location and the Matlab algorithm to identify various targets of interest at the test location. The camera was attached to a small airplane and flown over the test area at approximately 1000 and 2500 ft above the ground. Nova-Sol sent a team from Hawai'i to the test location to run the tests and collect spectra of the targets using a handheld spectrometer. The handheld target spectra are used in the match filter to try to detect the targets of interest. Once the team returned I took the handheld spectrometer data and formatted it so that it could be read by the Matlab code. The handheld spectrometer data is of much higher spectral resolution than the SWIR camera and so the resolution of the handheld data had to be reduced to match that of the camera.

The SWIR sensor Nova-Sol was testing acquired light from ~850 nm to ~1600 nm. In this range atmospheric moisture absorbs certain frequencies of light. The wavelengths that are absorbed provide little or no signal to the camera and the signal that is received is primarily dark noise. In the SWIR camera the spectral pixels are binned into groups called bands, and these bands are basically a wavelength interval. The SWIR camera had 102 bands from 850 to 1600 nm. Not all of these bands were usable because of atmospheric absorption. Figure 3 is a plot of spectral irradiance versus wavelength. The direct circumsolar radiation is the amount of sunlight that passes through the atmosphere and reaches the earth's surface. At certain wavelengths irradiance drops low or non-existent. These bands have to be omitted or they will negatively affect the matched filtering process.

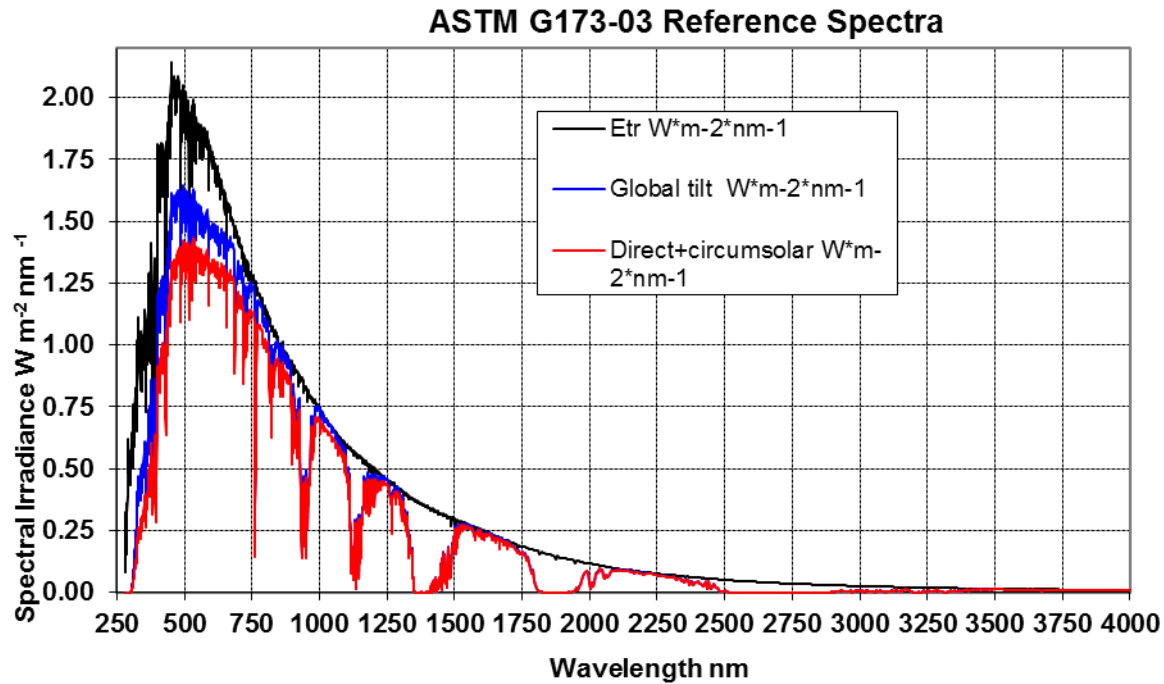


Figure 3. Direct circumsolar is the amount of sunlight reaching the earth's surface. The sharp troughs at approximately at 900, 1100, and especially 1300 nm means there is very little signal for the sensor to detect. Bands that correspond to these wavelengths must be omitted.

Once the data from the test area came in I began applying anomaly and matched filters to see how well targets of interest were detected. A large part of the process was pre-processing the data. The entire image cube may have been 15 to 20 thousand lines long and the area where targets place maybe only in a fraction of that area. I would reduce the size of the cube to the area I needed to reduce the computational burden and have the algorithm run faster. When running a detection on targets of interest it is important to have the algorithm detect the target while also keeping the number of false detections to a minimum. The algorithm had designed in a way to adjust the thresholding parameters to allow for more or less detections. Part of my job was to adjust the thresholding value so that the target was detected while at the same time keeping the false detections to a minimum. Some of the targets of interest were much easier to detect with fewer false alarms than other targets. By looking at the spectra of the targets collected by the handheld spectrometer it was possible to see qualitatively why some targets were easier to detect than others. The targets that were easily detected often had some peaks or troughs in their spectra that made them stand out from the background spectra.

While I am not allowed to discuss the specifics of the targets that were or were not detected I will say that some of the targets that were of higher priority were able to be detected accurately. Some of the targets were just too small for the spatial resolution of the camera. Some of the targets that were difficult to detect may have been difficult because they had a similar spectral signature to other objects in the scene. One of the targets in particular looked very similar in color to other objects in the scene when displaying a false color image. No matter what red, green, and blue band combination was chosen to display the image the target looked similar to background objects. This would cause the target to blend in statistically with similar

looking background object, thus making it difficult to detect or result in false alarms on the much larger background object.

CONCLUSION

Overall the internship was an enjoyable and useful experience. I learned a lot about remote sensing and about programming using Matlab that I think will help me in my future. I was able to see how a finished remote sensing image is actually made and all the different parameters that may affect the quality of the data. I learned various techniques for calibrating an image in order to get reliable information. My co-workers at Nova-Sol were all really friendly and extremely helpful and knowledgeable. Keith Nakanishi, Brian Hill, and Selwyn Yee provided me with excellent guidance for problem solving and were great at filling me in on all the things I didn't understand.

ACKNOWLEDEMENTS

I would like to thank Nova-Sol for giving me the opportunity to work with them. I would also like to thank the Hawai'i Space Grant Consortium for helping to support during this internship.

OPTICAL COMMUNICATIONS AT NOVASOL

Amber K. R. Imai
College of Engineering
University of Hawai'i at Mānoa
Honolulu, HI 96822

ABSTRACT

Summer internships teach students how to apply the knowledge they have gained through their college courses in a real world setting. At NovaSol, I was able to apply many skills learned in the classroom, as well as learn about optics and optical communication.

Optical communication is a complex field that has many components. Within the course of this internship, I learned about free-space optical communication, fiber optics, optical signal noise, design concepts, troubleshooting, and testing of the Compact and Sub-Compact.

INTRODUCTION

NovaSol is a Hawai'i based engineering contractor which specializes in optics. The Optical Communications (Op Comm) group is currently working on the Free-Space Optical Communications Compact Interrogator, a compact version of the original Dual Mode Optical Interrogator (DMOI) which will be explained in greater detail below. The Compact and the new Sub-Compact is currently the main focus of the Op Comm group.

This report will cover the fundamentals of optical communication. I will discuss the benefits and limitations of using optical communication, and the projects that I worked on during the course of this internship.

MODERN OPTICAL COMMUNICATIONS

Optical communication is defined as a means of communication which utilizes the visible and infrared section of the electromagnetic spectrum. It is one of the newest, most advanced forms of communications and employs shorter wavelengths, thus higher frequencies, which allow a higher volume of information to be transmitted over a single channel. This is one of the advantages optical communication has over microwave and radio communication. To transmit an optical signal, a laser or high-intensity light-emitting diode (LED) is used to generate a pulse wave. Lasers are used for long distance communications because they are a high intensity focused beam of light, where as LEDs are used for short distances due to the losses due to the light being less focused. Pulse waves are received and processed by a photodiode, a semiconductor that converts light energy into either a voltage or current, which can then be interpreted by the rest of the circuit. [1]

NovaSol's Op Comm group focuses on free-space optical communications, using an infrared laser. Free-space point-to-point optical links are good for relatively short direct-view implementations such as theirs. Misty rain, fog, and dust can greatly affect the stability of the

link between the links, as demonstrated during one of the field tests. Fog and dust have particle sizes that are a few microns in size can completely block the laser beam, making it difficult to keep a stable connection. Misty rain weakens the strength of the beam by distorting the light as it passes through the droplet. However, this form of communication is great for ensuring a secure connection between a minimum of two points, which is not as easy to hack when compared to radio and microwave communication making this application ideal for military usage.

DMOI, COMPACT, AND SUB-COMPACT

The DMOI project started in 2002 when NovaSol was awarded a multi-year contract by the Naval Research Lab (NRL) to develop a free-space optical communication system. DMOI's project objectives is to develop a low powered optical laser link for a family of high bandwidth "last mile" communication systems between ships, planes, and ground units. It was big, bulky and required a engine hoist to lift. By utilizing new technology, DMOI was reduced to the Compact Interrogator, which weighs in at 30 lb and is a little smaller than a cubic foot.

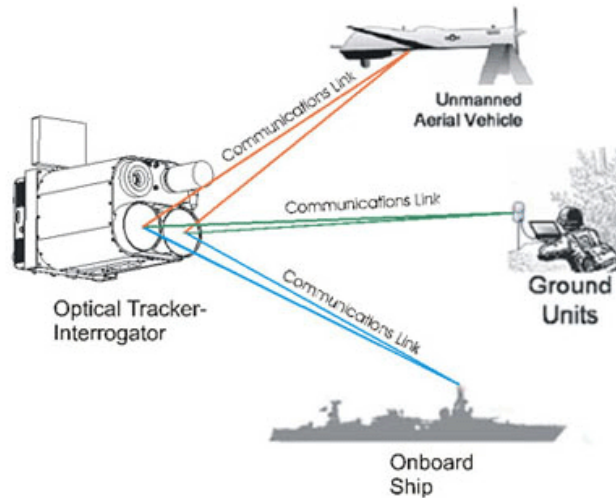


Figure 1: DMOI and the overall objective of the interrogator units designed and built by NovaSol.
Photo Credit: NovaSol

The Compact is the current model which was demonstrated to NRL this summer. Like DMOI, the Compact has 2 modes of operation; retro mode and direct mode. In direct mode two interrogators, the ground station and the mobile station, communicate with each other directly using infrared lasers. Retro mode is used when the unit "transmits a laser beam to a remote unit that modulates a data stream onto the beam and reflects it back to the unit" [NovaSol website]. This mode relies on retro-reflectors to take in light and reflect it out in the same direction that it entered. Data can be encoded into the returning light beam using a modulator thus creating a two way link to send and receive data. [2]

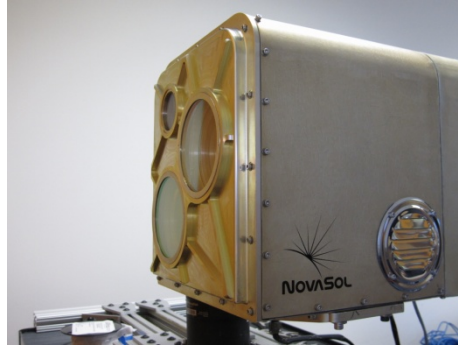


Figure 2: The Compact Interrogator on one version of the gimbal during testing
Photo Credit: Amber Imai

The Sub-Compact is NovaSol's newest optical interrogator. It is much smaller than the Compact and weighs just 16 pounds. Using the latest technology, this is the smallest unit that can be made with all of the functionality of the Compact and DMOI.

FIBER OPTICS

The first thing that I was tasked with was learning about fiber optics. There are many types of fibers and connectors, each with a different purpose and different physical properties associated with them. At the core of each of these cables is a very fine piece of silicon glass, therefore these cables must be treated with care.

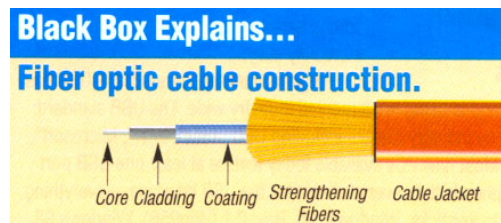


Figure 3: Layers of a fiber optic cable
Photo Credit: ARC Electronics

Within the fiber cable, there are layers. A buffer or jacket is the outer-most layer and covers the entire cable to protect the glass fiber. It is usually layered with Kevlar or some other stiffening material to ensure the fiber does not break. Just below that is the cladding which keeps light confined to the core. The core of the cable determines many major properties of the cable, such as mode, bandwidth, and transmission rate. A single mode cable has a very thin core, usually with a diameter between eight and 10 microns. This cable carries a higher bandwidth, but requires a light source with a narrow spectral width. It also provides a higher transmission rate, eliminates distortion from overlapping light pulses, which helps to provide the least signal attenuation. Multi-mode cables have a larger core diameter, usually between 50-100 microns. Multimode fibers provide high bandwidth at high speeds, however they cannot be used for long distances as the multiple paths of light can cause signal distortion at the receiving end. [3]

“Single mode fiber”
single path through the fiber

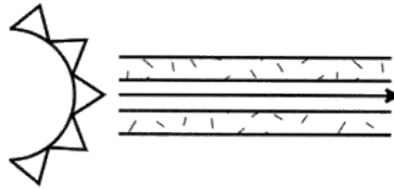


Figure 4: How a single mode fiber optic cable transmits light
Photo Credit: ARC Electronics

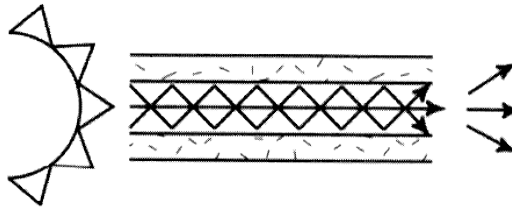


Figure 5: How a multi mode fiber optic cable transmits light. From this figure it is easy to see why the single mode cable has less distortion at the receiving end. Photo Credit: ARC Electronics

CIRCUIT ANALYSIS

Simulation Program with Integrated Circuit Emphasis (SPICE) is a general purpose analog electronic circuit simulator used to check the circuit design and predict the circuit's behavior. I used a free version of TINA SPICE, Texas Instruments version of SPICE, to simulate a circuit with an avalanche photodiode to determine which segment of the circuit noise was coming from. The circuit is from the modem used for the interrogators. After modeling the circuit, it was discovered that we were unable to do the noise simulation as previously planned, as a full version of TINA SPICE must be purchased in order to run this section of the simulation with optical components.

MOTION SIMULATOR

In order to test the Compact Interrogators in the past, NovaSol employees needed to rent a small fishing boat for the day in order to test their system. To avoid needing to rent a boat in the future, we worked on constructing a motion simulator which was designed in advance. The motion simulator is made out of 80/20 aluminum and two Aerotech motors to simulate the pan and tilt of the boat. The GUI was made using Microsoft Visual Studio and was coded in C Sharp, the programming language of choice at NovaSol.

Constructing and programming the motion simulator took well over a month due to modifications that were needed to the parts, problem solving when the parts did not fit as they should have in the drawing, and changing the code. By the last day of the internship, we had written the code for a manual and simulate mode and the structure was fully assembled. The tilt motor was incorrectly tuned; therefore it needs to be sent back to Aerotech to be fitted for the appropriate weight.

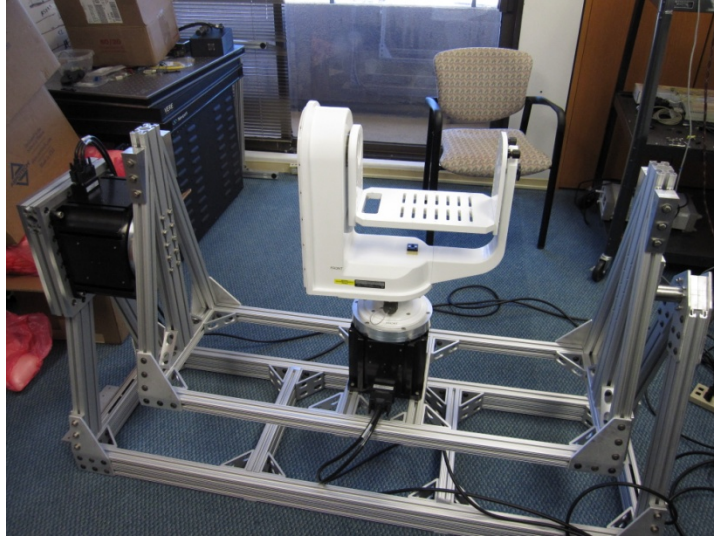


Figure 6: “Boat side” gimbal on completed motion simulator.
Photo Credit: Amber Imai

CONCLUSION

Optical communication is a complex field. Over the summer, my knowledge of optics and optical communication has grown tremendously through both online research and practical application. NovaSol’s Compact Interrogator served as a great platform to learn about this upcoming technology, as well as many of the components that go into it.

ACKNOWLEDGEMENTS

I would like to thank the Hawai‘i Space Grant Consortium and NovaSol for providing me with this amazing opportunity. Additionally, I would like to thank all of the Optical Communication staff at NovaSol for working with me and helping me to understand many of the things I was tasked with. It has been an amazing experience.

REFERENCES

- [1] Optical Communications. Answers.com ReferenceAnswers.
<http://www.answers.com/topic/optical-communication>. Last updated 2011. Accessed on August 6, 2011.
- [2] NovaSol main website. NovaSol. <http://www.nova-sol.com>. Last updated 2007. Accessed on August 6, 2011
- [3] Fiber Optics. ARC Electronics. <http://www.arcelect.com/fibercable.htm>. Accessed on August 6, 2011

INTERNSHIP AT INNOVATIVE TECHNICAL SOLUTIONS (NOVASOL)

Kevin Shin
College of Engineering
University of Hawai'i at Mānoa
Honolulu, HI 96822

ABSTRACT

For my internship with NovaSol, there wasn't a specific project assigned for the duration of the internship. Instead, my task was to assist the Optical Communications (OpComm) group with various tasks related to the research and development of their Compact Interrogator. Such tasks included adding to and improving the existing graphical user interface (GUI) which controlled the hardware involved, provide support during field tests, and to help construct and design software for a machine that simulated a boat's movement on the open water. This machine eliminated the need to actually go out to sea to conduct field tests for the interrogators. Microsoft Visual Studio was used to modify GUI elements and to design the software to run the boat simulator machine. C Sharp was the language of choice for these object-oriented tasks.

INTRODUCTION

NovaSol is a Hawai'i-based company founded in October of 1998 that provides products to clients in the defense industry. They specialize in a variety of optical systems and our role was to help with the development of Free Space Optical Communication systems. I was under the direction and guidance of Dr. Eric Saint Georges (Principal Investigator) and Stanley H. Uecke (Project Manager), and worked with Amber Imai (Intern – University of Hawai'i at Manoa) during my time here. Due to nature of the clientele being part of major defense organizations, I will not go into detail of their current projects and will only discuss the general purpose and uses.

Traditional radio-frequency communication systems are vulnerable to interference and interception. So there are places, such as the battlefield, where they should not be used. Using optical communication systems solves this problem as optical communications relies on transmitting data through a light source.

The Compact Interrogator (Figure 1) was the current project of the OpComm group. The interrogator uses a laser to acquire either another interrogator to send and transmit data or to acquire and transmit data to a reflecting device. They had successfully tested a larger, bulkier alpha unit with the Naval Research Laboratory (NRL) prior to our arrival. The compact unit delivers stronger performance in a noticeably smaller and lighter package providing more flexibility and mobility with these units.

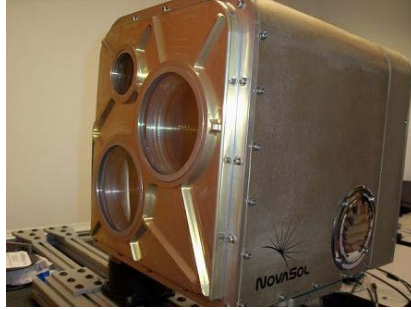


Figure 1: Compact Interrogator

The interrogator sits upon a two-axis gimbal (Figure 2) that allows for movement of the unit to scan for targets. This also serves to stabilize the unit in a moving environment such as a boat. To control this, a GUI was developed to allow the user to control the many factors of the interrogator and its pointing direction as well. This GUI was the one I worked with to modify and add features to during the first half of my internship.



Figure 2: Gimbal

Approaching the date of the demonstration for NRL of the compact units, many field tests had taken place. The majority of the field tests involved two different interrogators both at a static position. One field test actually involved the renting of a fishing vessel to use one of the interrogators out at sea to communicate with the other in a static position. This was the proposed use for the interrogators and simulated the setup of the actual demonstration. However, this process proved tedious, tiresome for everyone involved, and took the timespan of an entire day. Another detrimental factor to the field test was that the ocean and weather were uncontrollable and that day, the conditions were less than favorable. A solution to having labor-intensive field tests was to build a boat motion simulator. The designs were done and the order was already placed. For the second half of the internship, we constructed the machine and developed the software to control it.

SKILLS

Being unfamiliar with the C Sharp programming language, I first had to research the language to figure out how to use it for the task assigned. The current code was also studied for examples on using some of the library commands in the C Sharp language. The more complicated concepts such as threading, and delegates were explained to me by Stanley Uecke. To gain familiarity with the language, I was given the task of changing the units of coordinates given from the GPS antennas from degrees and minutes to just degrees. I had to study the code and follow along in order to make the necessary changes. I had just finished a programming course, prior to this internship, so calculations in programming were not too difficult.

The GPS antennas were used along side with the interrogators because, they were supposed to be capable of tracking and acquiring the other interrogator unit just using GPS coordinates. The antennas sent back strings of information through a serial port that had to be decoded for information. When I started my internship, some of these strings were parsed already but there were still others that contained important location information that were not decoded yet. This was my next task. Stanley Uecke gave me the website where I could find the information on what the strings meant, and the code he used to parse the strings. Using this I was able to decode strings that contained information such as how many satellites were in view from the current position and the satellite positions as well. I also worked on other components of the GUI but those were just modifications that provided more convenience for the user.

Field tests required much preparation and a usually a whole day's worth of work. Interns were responsible for making sure that they ran smoothly with minimal nontechnical problems. This meant keeping a checklist of the tools and hardware needed, making sure spare parts were on hand, and instructions for setup were clear and present. The testing did not always run smoothly though but they the majority of the time.

The last test was especially tiresome with one of the interrogators being tested out at sea. Conditions on that day were choppy and resulted in the queasiness of the crew on board the ship. Besides the hard work that was put into conducting such a test, there was also the factor of the expensive equipment being showered with the salt-laden ocean water. When it was over, salt encrusted itself into many of the small crevices on both the interior and exterior of the interrogator and other equipment.

The problem of trying to conduct such a field test was solved with the boat simulator (figure 3), our final task. The boat simulator design implemented the use of two rotary stage motors, one for the panning motion (horizontal), and one for the tilt (vertical). These would simulate the panning and tilting orientations that would be felt on a boat. The frame was made of aluminum parts and the designs were done by Dave Breitweiser (Senior Optical Engineer).

In order to operate the motors, software had to be written. Using a sample file from the files that came with the motors and the controllers, we (the interns) developed our own GUI application (Figure 4) that would control the motors. Elements of the GUI included feedback from each motor about the current position (degrees), the amount of current flowing to the motors (amps), and other basic information of the motors. There were also the basic buttons that were needed to connect the devices, and the enable them. There was a manual mode that allowed for testing of the individual or both motors, and a method to get data from a saved text file with

recorded information of the boat during from the actual demonstration. This last function provided a more realistic simulation of the motion of a boat.



Figure 3: The Boat Movement Simulator

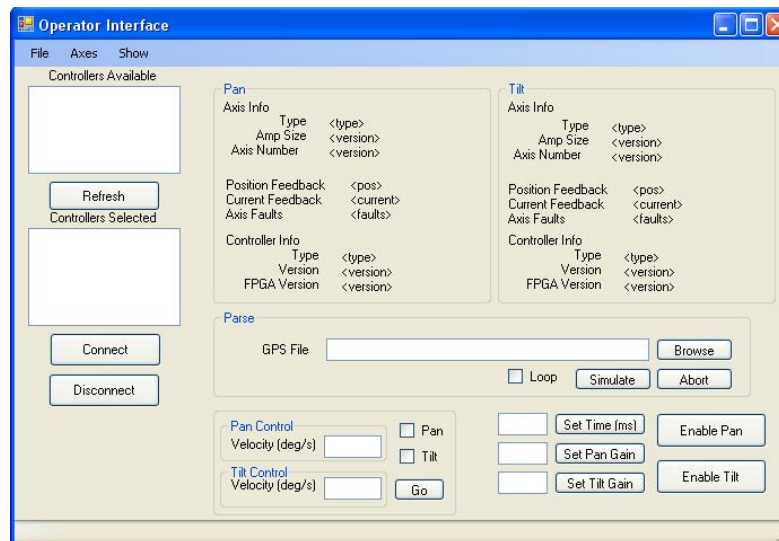


Figure 4: Operator Interface GUI

OUTCOMES

This being my first internship, I didn't know what to expect. I had no idea what was to be expected of me and the difficulty of the work that I'd have to do. Luckily most of my tasks were doable and if there was something I couldn't figure out, the people at NovaSol helped me out. Through this internship, I was able to experience what it's like as an engineer in the private sector.

Along the way, I also gained new skills. I learned how to use C Sharp and to program graphical user interface (GUI) applications. Before this, I had not used programming to create useful software that is needed for the operation of a machine or system. Doing so allowed me to explore different areas of programming such as object-oriented programming and though I am majoring in mechanical engineering, I would like to learn more about software and programming.

Even if I did not design the boat motion simulator, I still learned a little about mechanical design. As we were building it, I could see how some parts would fit well into place while, we had to come up with solutions for parts that didn't fit into the angled areas.

Overall, this internship exposed me to different areas of engineering and I learned a little about each. This was a helpful starting point for me to discover what exactly I'd like to do as an engineer. Having some experience from a high-tech company, I am now confident to experience other areas as well in different environments.

CONCLUSION

This internship has provided me with a foundation for me to base other experiences on. I learned to program software, built and programmed a structure from scratch, and work alongside real engineers as they developed a product that could possibly used more commercially in the future. Being exposed to technologies that I previously had not even known existed, I am now even more excited to become an engineer so that some day I will be working directly to develop new technology.

ACKNOWLEDGEMENTS

I would like to thank everyone on the OpComm team including my mentors Dr. Eric Saint Georges and Stanley H. Uecke for extending this enriching opportunity to me and providing advice and instilling knowledge. Also from the OpComm team I'd like to thank John Sender, Aldrick Nago, Selwyn Yee, and although the following people aren't a part of the OpComm team, they helped me at various times during my stay, James Mock, Dave Breitweiser, and Jennifer Arthur. Everyone at NovaSol helped to create a welcoming atmosphere that made working here enjoyable and I'm thankful for that.

I would also like to thank the people at the Hawai'i Space Grant Consortium who made my experience possible and I hope to partake in more of the programs offered.

STRUCTURAL OPTIMIZATION OF SPACE SYSTEMS USING GENETIC ALGORITHMS

John G. Furumo
College of Engineering
University of Hawai'i at Mānoa
Honolulu, HI 96822

The common engineering practice of design followed by analysis, while effective, is far from nominal due to its iterative nature. While it is practically impossible to remove all iteration from the design process due to the high stakes involved and demanding design requirements, design optimization can greatly streamline the process. Cutting-edge optimization software such as Altair's Optistruct and NASA's X-TOOLSS use gradient-based algorithms and genetic algorithms, respectively, to produce optimal designs satisfying specified requirements. The application of these tools to structural optimization of satellite payloads is an important proof-of-concept study that will guide future payload and space system development. My research has sought to apply the optimization process in parallel with the conventional design process that is currently underway developing the next generation of FASTSAT microsattellites. Decades of flight heritage have conveyed well-suited structural member configurations such as ortho-grid and iso-grid panels that maximize strength and stiffness while minimizing mass. The optimization process driven by Optistruct demonstrated a new and unconventional structural layout that saved mass and volume over the original FASTSAT-HSV02 design while maintaining structural strength and integrity. Future X-TOOLSS optimization can further enhance the process, yielding global optimum configurations for satellite structures.

NOMENCLATURE

CAD	= computer-aided design
FEA	= finite element analysis
X-TOOLSS	= eXploration Toolset for Optimization Of Launch and Space Systems
MSFC	= Marshall Space Flight Center
FASTSAT	= Fast, Affordable, Science and Technology SATellite
SLS	= Space Launch System
LEO	= low earth orbit
LV	= launch vehicle
ESPA	= EELV Secondary Payload Adapter

INTRODUCTION

The preliminary stage of aerospace vehicle and systems development is usually divided between design and analysis phases. This was true for past generations of engineers relying on drafting and hand calculations as well as modern engineers utilizing computer-based CAD and FEA tools to fulfill the same purposes of design and analysis. For large-scale and complex projects, the design and analysis process generally becomes highly iterative in nature. In such cases, designs must be verified by analysis after each revision. While tedious and time-

consuming, this method has proven to be highly effective. Even the most highly coordinated efforts, however, still suffer from delays and setbacks due to this design-analysis iteration.

Design optimization is a new process that serves to effectively combine the design and analysis phases, achieving goals of both in a single step. Cutting-edge software tools such as Optistruct, part of Altair's HyperWorks suite, and NASA's X-TOOLSS allow designers to perform elements of CAD and FEA simultaneously. Such tools yield designs or guidelines to design that meet specified design requirements from the start, thereby eliminating the need for analysis afterward to verify the design. While design optimization has great potential, it is difficult to apply to complex designs as the large quantity of degrees of freedom involved makes it difficult or impossible to find a single optimum configuration. As a result, optimization tools are usually focused on small scale or component-level studies.

RESEARCH PURPOSE

The ES22 Thermal & Mechanical Analysis Branch has an interest in optimization as it relates to their common duties of verifying space system design iterations. With the cancellation of the Ares program and the delays in the start of the SLS program, ES22 has been focused more on payload instead of vehicle systems. One example of a payload that that ES22 has worked on recently is the FASTSAT microsatellite that was designed and fabricated at MSFC. FASTSAT provides a cheap and accessible platform for scientific instruments as part of NASA's new focus on reducing mission costs and development time by creating smaller and cheaper payloads for LEO. The first generation, FASTSAT-HSV01, was launched last year and has performed so well that a second generation, FASTSAT-HSV02, is now on the drawing board. Figure 1 shows FASTSAT-HSV01 in the clean room prior to launch. Design group ES21 is currently finalizing the FASTSAT-HSV02 design while ES22 is providing design verification through structural and thermal analysis. Figure 2 below shows the current iteration of the FASTSAT-HSV02 CAD model created by ES21.



Figure 1: FASTSAT-HSV01 [1]

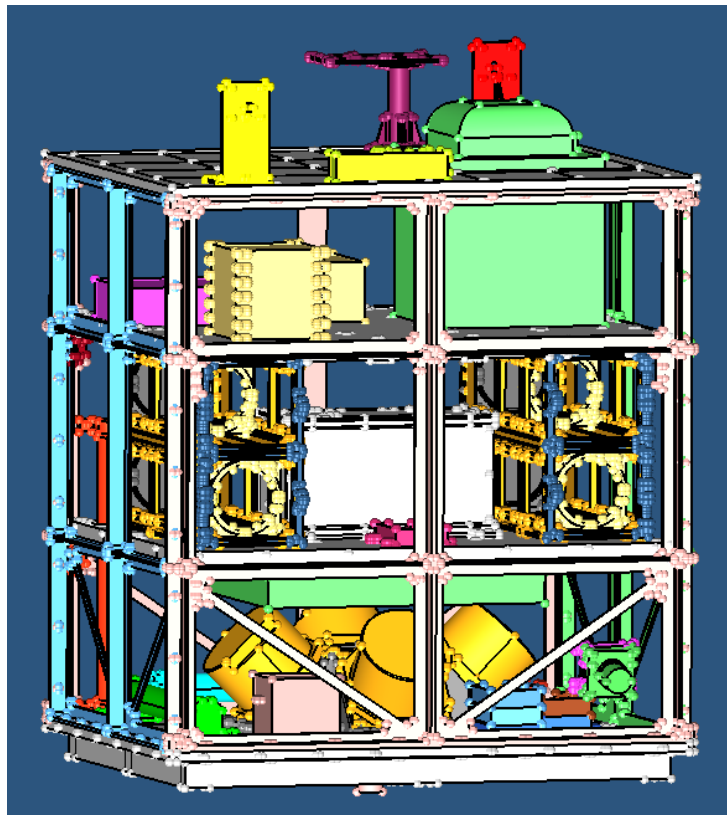


Figure 2: FASTSAT-HSV02 CAD model

My research sought to apply the optimization process in parallel with this conventional development process now being carried out by ES21 in concert with ES22 as a proof-of-concept and guide for future design optimization. In particular, my objective was to optimize the structural design of the satellite, with the goals of minimizing structural mass while maintaining structural strength and stiffness. This was performed by a previous ES22 intern for FASTSAT-HSV01 [2], demonstrating the capability of the optimization toolset. The hope of my mentor was that I would be able to replicate the process and document it so that it could be applied to future projects from the start.

METHODOLOGY

The first step of the structural optimization process was performed using the aforementioned Optistruct solver from Altair Engineering. Optistruct utilizes gradient-based optimization methods to converge on a design satisfying given requirements. These studies are performed on FEA models which contain important information that define the simulation. These include boundary conditions such as constraints and loading conditions. For the case of the FASTSAT-HSV02 FEA model, the loading condition considered was a lateral 15 G static acceleration representing the launch loads. The dynamic conditions of the launch environment can be encapsulated by a single static acceleration [3]. As a microsatellite-class payload, FASTSAT mates to the LV via an ESPA ring payload adapter as a secondary payload which is mounted laterally with relation to the rocket's direction of travel, hence the direction of the loading condition simulated [4]. The LV interface ring serves as the constraints for the model, the points which remain fixed and unable to move.

For these optimization studies, there are several parameters that must be defined by the user. The first of these is a design objective. This is the overarching goal that the solver seeks to achieve through the simulation. For the purpose of the structural optimization of FASTSAT-HSV02, the design objective was to minimize mass, minimize volume, or minimize compliance. Because the only design material considered was 7075-T6 Aluminum, an isotropic material, mass and volume would be minimized simultaneously. Compliance is the inverse of stiffness, and so minimizing it would maximize the stiffness of the overall structure. One of the drawbacks of Optistruct is that only one design objective can be sought at a time.

Another user-specified property of the optimization study is the design variable. This is the property of the model that Optistruct varies in order to meet the design objective. For structural optimization, the design variable depends on the type of optimization being performed. For this project, both a topology optimization and a gauge optimization study were performed.

TOPOLOGY OPTIMIZATION

A useful first iteration of structural design optimization is a topology optimization. This is used with a 3-D FEA model comprised of solid elements. Topology will show load-paths through a structure and indicate areas of greatest stress. The design variable for a topology study is element density. In order to satisfy the design objective, the solver will vary the density of the model elements. Topology is useful because it will reveal where extra structural material is needed in order to shore up the structure, and vice-versa where material can be shaved off to

lighten the structure. Figure 3 below shows the FEA model I created for topology optimization using Pro-E and HyperMesh. The only components meshed for FEA and optimization are the structural members. The internal components have been modeled as point masses connected to the structural elements via rigid bodies.

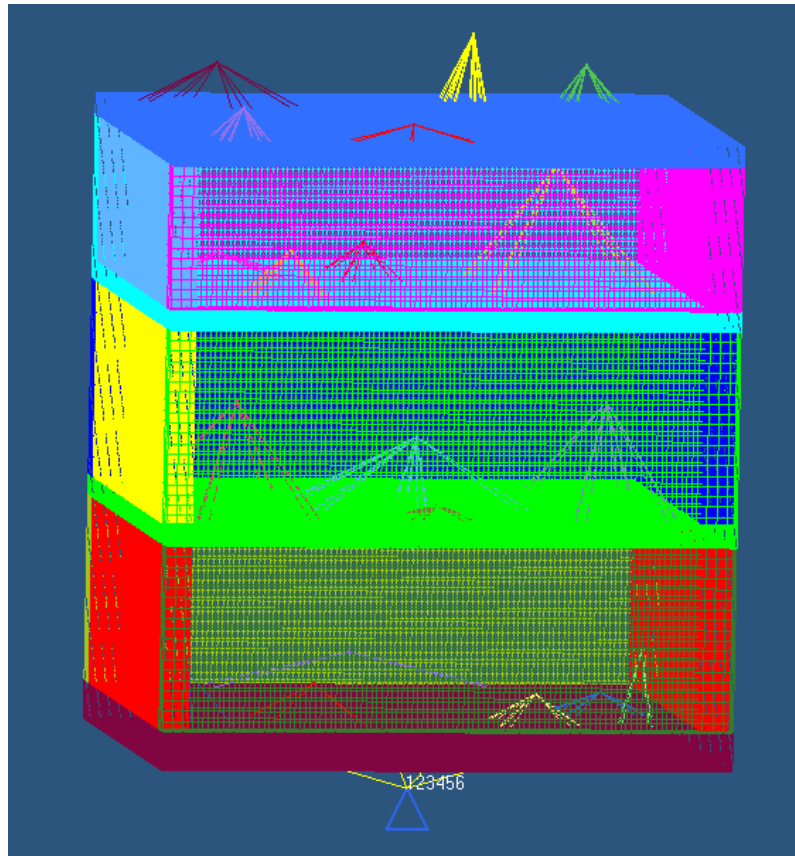


Figure 3: Topology model of FASTSAT-HSV02

I created this model by taking the structural components of the CAD model in figure 2 and wrapping the members in a solid design envelope. This provided the design space for Optistruct to work with to create the optimum pattern of material density.

GAUGE OPTIMIZATION

A higher fidelity study was performed with a gauge optimization. This utilizes an FEA model comprised of 2-D shell elements. For such an optimization, element thickness or gauge is the design variable. This is a more useful optimization tool because it takes an existing design and varies specific properties such as component dimensions, yielding a more realistic and applicable solution. Figure 4 below shows the gauge optimization model used, an adaptation of the dynamics model for FASTSAT-HSV02.

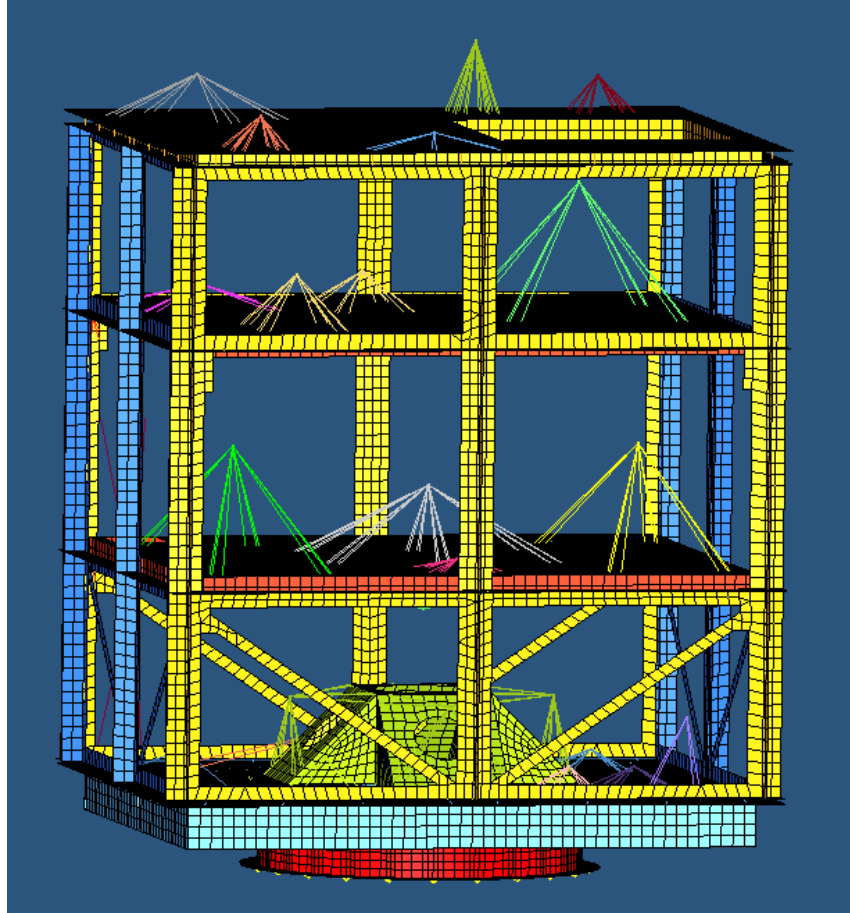


Figure 4: Gauge optimization model of FASTSAT-HSV02

Once again only the structural members are meshed for analysis, and the internal components are modeled as point masses. As can be seen in figure 4, the structural elements are comprised of 2-D shell elements instead of the 3-D solid elements used for the topology model seen in figure 3.

X-TOOLSS

NASA's X-TOOLSS software engine is a powerful solver that can be used to drive optimization problems as well. It utilizes genetic algorithms to vary input parameters for an objective function, the output of which is judged based on a fitness calculation function which in turn influences how the solver selects the next iteration of input values. Figure 5 below shows a flow chart illustrating the X-TOOLSS process.

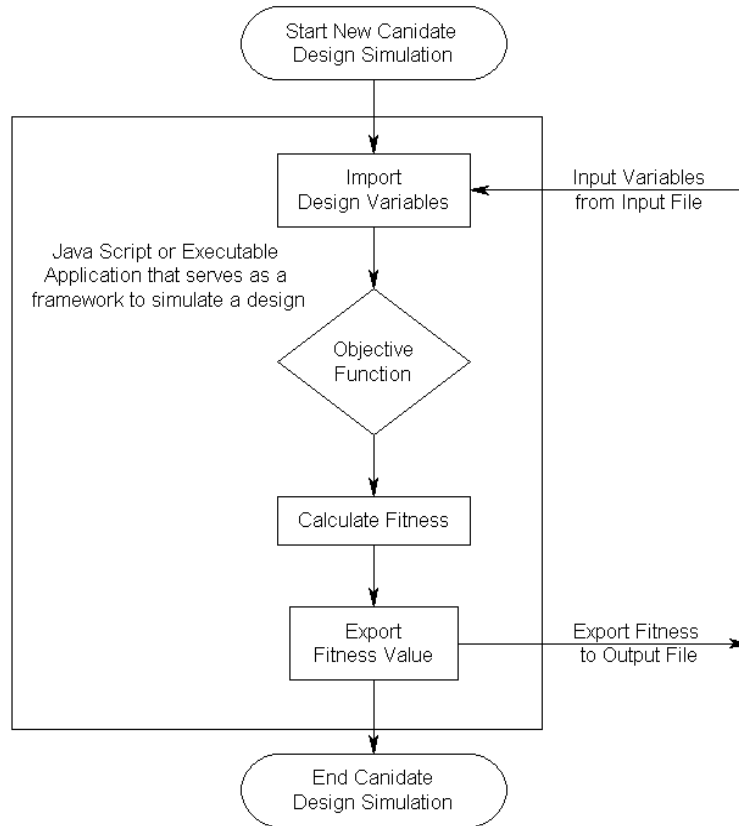


Figure 5: X-TOOLSS functionality flow chart

For structural design optimization, the objective function can be an FEA simulation or an optimization study. The design variables input would likely be structural member dimensions or materials. After running the objective function, the fitness calculation function parses the simulation output file for important parameters such as stress and mass in this case since the objective is to minimize mass and stress. By varying design parameters X-TOOLSS will converge on an optimal design. For a specified population size, the program will find the weakest candidate design based on the fitness calculation and remove it from the pool. After a set number of generations, the process selects the best candidate in the pool based on the same fitness calculation. By using X-TOOLSS to drive the gradient-based optimization process of Optistruct, the optimization process is augmented greatly. The use of genetic algorithms to create random inputs helps prevent the process from converging on local optima and instead ensures that the process will find the global optimum of the design space.

RESULTS

Figure 6 shows the results of the Optistruct topology optimization study. Shown in red are the areas of maximum element density, with blue showing areas of minimum element density. These correspond to areas of maximum and minimum stress, respectively. As expected, the greater stresses are found nearer the LV interface ring located at the bottom of the figure. While this topology result may not possible to manufacture in real life, it does however serve as a useful guide to the overall layout of the satellite structure, showing where more material and strength are needed.

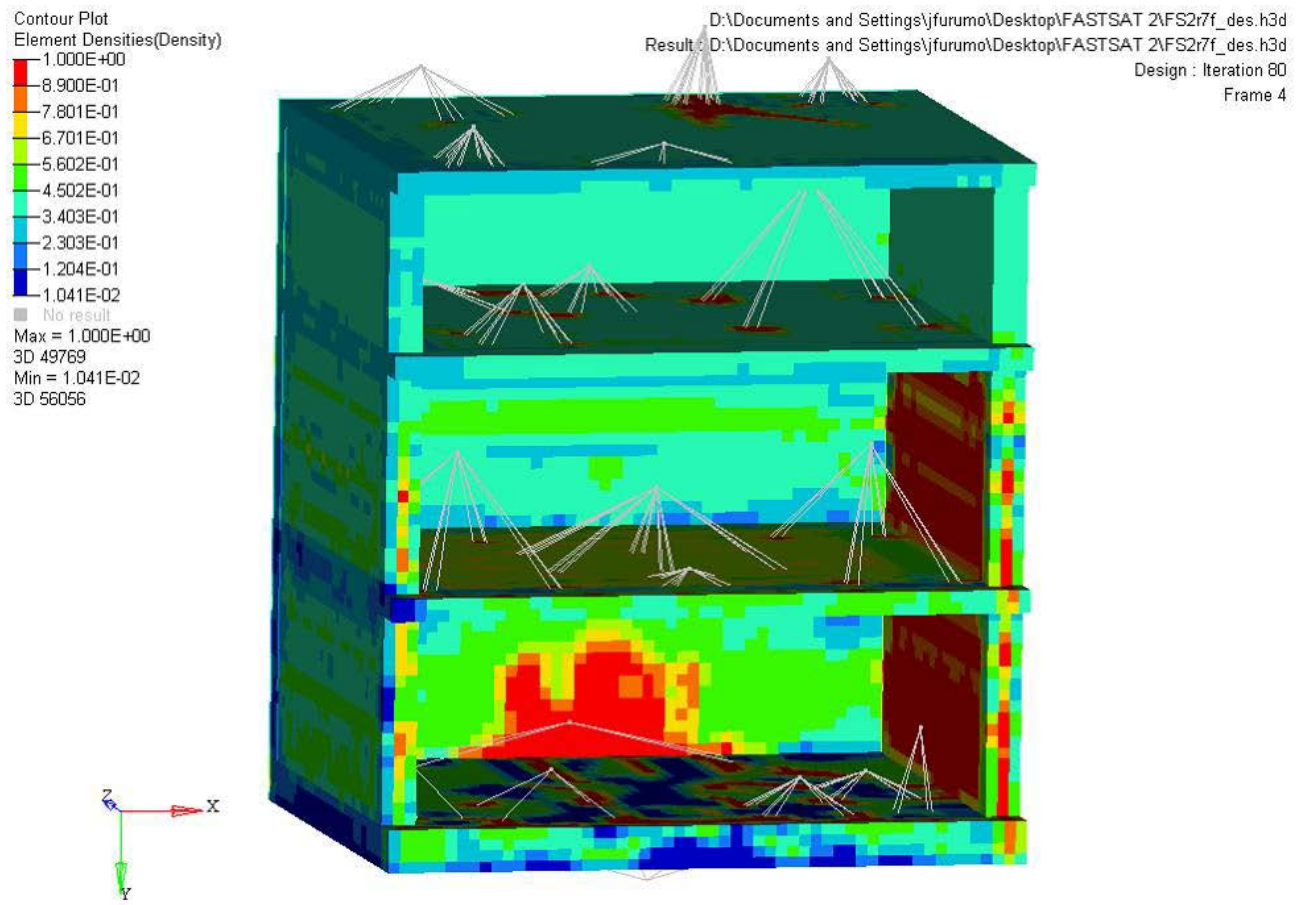


Figure 6: Topology optimization results

This topology study reduced 358 lbm from the starting design envelope. While this doesn't necessarily mean that there is 358 lbm of actual satellite mass that can be removed, it illustrates the topology process and shows how it reaches the design objective by reducing mass. Figures 7 and 8 below show two iterations of the gauge optimization study. Figure 7 shows the 0th iteration of the gauge optimization, effectively the starting configuration of the model. Figure 8 shows the 7th and final iteration of the optimization. Once again, red areas represent thicker components and blue areas represent thinner components. As can be seen, the model becomes thinner over the optimization iterations, reducing the mass of the structure. The overall mass reduction of the gauge optimization study was 101 lbm. Again, this doesn't necessarily represent that much mass savings over the actual design, but does demonstrate the capability of the optimization process.

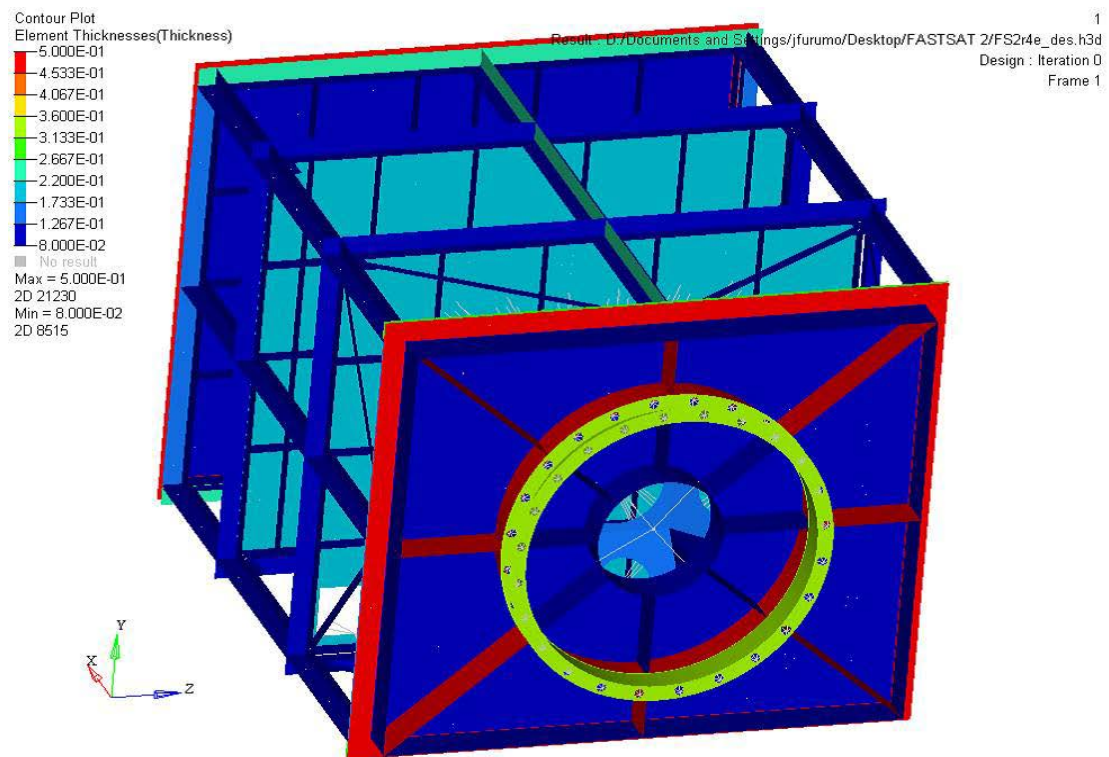


Figure 7: Gauge optimization iteration zero

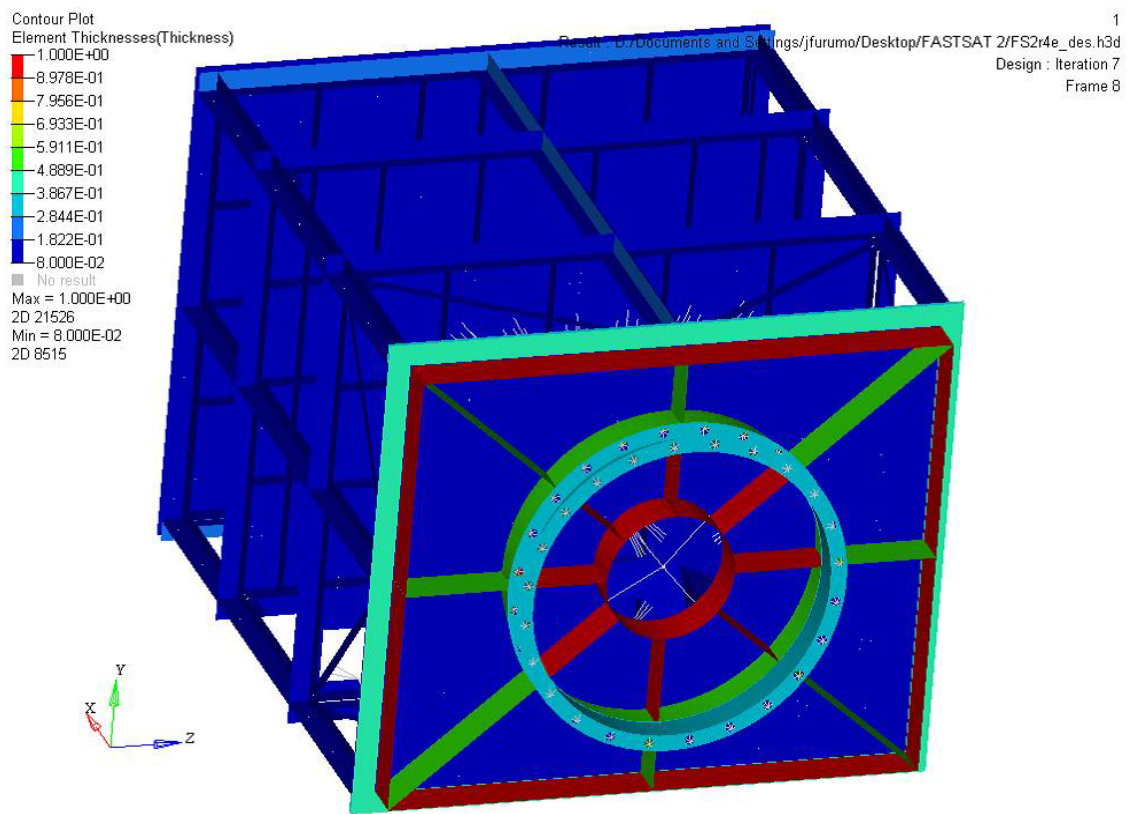


Figure 8: Gauge optimization iteration 7

CONCLUSIONS

While useful results were obtained from the topology and gauge optimization studies, sufficient time was not available to obtain useful results from the X-TOOLSS optimization study. The X-TOOLSS setup process is still in development and not entirely user friendly, especially to a novice user such as myself. As is true with all computer analysis, more refining is needed to increase the fidelity of the models to an acceptable degree that will match physical test results. That being said, it is still obvious that the optimization process is a useful tool that augments the traditional design process. Topology optimization provides a great preliminary study that guides the overall design shape and form while gauge optimization is useful for refining a later design iteration. Both methods effectively and usefully blur the line between design and analysis, streamlining the overall engineering process.

REFERENCES

- [1] NASA, “NASA’s FASTSAT Satellite Readies for Shipment to Alaska”. Press release, available online: <http://www.nasa.gov/centers/ames/news/releases/2010/10-63MR.html>
- [2] Moore, Erin. “Structural Design of a Satellite Bus using Finite Element Based Optimization” April 1, 2011. Western Michigan University
- [3] Parsons, David, “Preliminary MicroSat Loads”. June 8, 2011.
- [4] USAF, “Evolved Expendable Launch Vehicle Secondary Payload Adapter Rideshare Users Guide”. May 2010.